East Asian climate and sedimentary dynamics along submarine canyons since the last glaciation in the northeastern South China Sea

Bertaz Joffrey

Thèse de doctorat

NNT : 2023UPASJ019

East Asian climate and sedimentary dynamics along submarine canyons since the last glaciation in the northeastern South China Sea

Climat est Asiatique et dynamiques sédimentaires de deux canyons sous-marins au nord de la Mer de Chine du Sud depuis la dernière période glaciaire

Thèse de doctorat de l'université Paris-Saclay et de Tongji University

École doctorale n° 579, Sciences Mécaniques et Energétiques, Matériaux et Géosciences (SMEMAG) & School of Ocean and Earth Science
Spécialité de doctorat : Géosciences
Graduate School : Géosciences, climat, environnement et planètes
Référent : Faculté des sciences d'Orsay

Thèse préparée dans les unités de recherche **GEOPS** (Université Paris-Saclay, CNRS), et **School of Ocean and Earth Science** (Tongji University), sous la direction de **Christophe COLIN**, Professeur, et la co-direction de **Zhifei LIU**, Professeur

Thèse soutenue à Shanghai, le 06 septembre 2023, par

Joffrey BERTAZ

Composition du Jury

Membres du jury avec voix délibérative

Zhimin JIAN Professeur, Tongji University	Président
Stephan STEINKE Professeur, Xiamen University	Rapporteur & Examinateur
Xufeng ZHENG Professeur, Hainan University	Rapporteur & Examinateur
Franck BASSINOT Chercheur au CEA-Saclay, LSCE/IPSL	Examinateur
Andrew Tien Shun LIN Professeur, National Central University	Examinateur

同济大学 TONGJI UNIVERSITY

université PARIS-SACLAY

博士学位论文

(学术学位)

南海东北部末次冰期以来东亚气候与海底峡谷沉积动力过程

姓　　名：Joffrey BERTAZ

学　　号：1990023

学　　院：同济大学海洋与地球科学学院

巴黎萨克雷大学气候与环境科学实验室

学科门类：理学

学科名称：海洋科学

论文研究方向：海洋地质

指导教师：刘志飞 教授

Christophe COLIN 教授

二〇二三年九月

同濟大學
TONGJI UNIVERSITY

université
PARIS-SACLAY

A dissertation submitted to Tongji University and Université Paris-Saclay
in conformity with the requirements for the degree of Doctor of Natural Science

East Asian climate and sedimentary dynamics along submarine canyons since the last glaciation in the northeastern South China Sea

Candidate: Joffrey BERTAZ

Student Number: 190023

School/Department: School of Ocean and Earth Science

École Doctorale n° 579, SMEMAG

Discipline: Natural Science

Major: Ocean Science

Research Fields: Marine Geology

Supervisor: Prof. Zhifei LIU

Prof. Christophe COLIN

September, 2023

南海东北部末次冰期以来东亚气候与海底峡谷沉积动力过程

乔睿

同济大学&巴黎萨克雷大学

université PARIS-SACLAY

ÉCOLE DOCTORALE
Sciences mécaniques et énergétiques, matériaux et géosciences (SMEMAG)

Title : East Asian climate and sedimentary dynamics along submarine canyons since the last glaciation in the northeastern South China Sea

Key words : sediment transport, physical erosion, chemical weathering, East Asian monsoon, typhoon activity, Taiwan..

Abstract : Taiwan is under the regime of the East Asian monsoon system and affected by numerous typhoons (3 to 4 events per year) controlling the regional moisture transport pattern. Sediment transfer along the southern margin of Taiwan is mainly realized by several submarine canyons playing a key role in terrigenous sediment redistribution to the deep sea (e.g., turbidity currents). However, past climatic (monsoon, typhoon) and hydrological (sea level, oceanic currents) variations recorded in sediments deposited on the levees of submarine canyons are still not well established over the late Quaternary. In this study, sedimentological, mineralogical, and geochemical analyses were investigated on two long CALYPSO cores retrieved from the submarine canyon systems. Cores MD18-3569 (located on the bank of the Penghu Canyon) and MD18-3574 (located on the levee of the Gaoping Canyon) were investigated in order to (i) identify the sediment provenance, (ii) reconstruct the chemical weathering and erosion history of South Taiwan drainage basins, and (iii) determine the frequency and intensity of past typhoon activities associated with climatic changes in South Taiwan since the last glaciation.

Sediments of Core MD18-3569 are characterized by major proportions of illite and chlorite, moderate smectite, scarce kaolinite, and 87Sr/86Sr (0.7187 to 0.7213) and εNd values (-11.63 to -10.89), which allow us to constrain to Southwest Taiwan rivers as the unique source of the sediments deposited on the eastern bank of the Penghu Canyon since the last glaciation. The dominant illite-chlorite and elemental compositions (e.g., chemical index of alteration) indicate that sediments experienced a moderate chemical weathering in agreement with high denudation rates of SW Taiwan linking to strong uplift (~10 mm/yr). We demonstrated that the long-term change in chemical weathering of SW Taiwan soils is mainly driven by changes in monsoon and typhoon rainfall and environmental changes (e.g., vegetation cover) over the past 32 kyr.

The sediments of Core MD18-3569 consist of clay and fine silt (~13 μm) indicating the Penghu Canyon receives low amount of coarse sediment (<25%) from Taiwan rivers because it is not directly connected to rivers. Grain size variations and End member modelling indicate coarser grain size occurred during the last glacial period and finer grain size happened during the Holocene. There is a transition period from 10.7 to 10 ka, when the coarse sediment content (EM2) dropped from ~40% to nearly 0%. This period was concurrent to the Melt Water Pulse Event-1C, a rapid marine transgression that significantly changed the land-sea configuration (flooding of the Taiwan Strait) and potentially disconnected the Penghu Canyon from Taiwan river systems. During the Holocene, sediments derived from Taiwan rivers are prevailing (>80%) though the larger distance between the Penghu Canyon and Taiwan river mouths during the high sea-level stand.

Core MD18-3574 records numerous turbidity currents triggered by typhoons (~70% of turbidity currents, 3-4 events per year) in the Gaoping Canyon over the past 4 ka. High resolution XRF core scanning, hyperspectral imaging, grain size, and bulk mineralogy were utilized to characterize fine characteristic laminations preserved on the studied levee. Dark and coarse levels have been associated to the deposit of turbidity currents. A total of 2400 dark laminae, mostly associated with typhoon events, have been identified for the last 4.2 ka. Typhoon frequency recorded in the Gaoping Canyon has decreased since 4 ka (in link with the cooling of western Pacific Ocean and surrounding marginal seas). After 1.5 ka, cold periods are characterized by low frequency and strong typhoon intensity. We have then suggested that typhoons are affected by La Niña like conditions of El Niño Southern Oscillation strengthening the Pacific Walker Circulation and winter monsoon winds.

université PARIS-SACLAY

ÉCOLE DOCTORALE
Sciences mécaniques et énergétiques, matériaux et géosciences (SMEMAG)

Titre : Climat est Asiatique et dynamiques sédimentaires de deux canyons sous-marins au nord de la Mer de Chine du Sud depuis la dernière période glaciaire

Mots clés : transfert sédimentaire, érosion, altération chimique, mousson est asiatique, typhons, Taiwan.

Résumé : Le climat de Taiwan est contrôlé par les précipitations de la mousson est asiatique et des typhons (3 à 4 par an). Les transferts sédimentaires le long de la marge sud de Taiwan se produisent majoritairement par le biais de plusieurs canyons sous-marins jouant un rôle clé dans la redistribution de sédiments terrigènes aux bassins profonds (ex : courants de turbidité). Mais les impacts des variations climatiques (mousson, typhons) et hydrologiques (niveau marin, courants) passées sur la sédimentation des levées de canyons sous-marins ne sont toujours pas bien établis pendant le Quaternaire. Des études sédimentologiques, minéralogiques et géochimiques ont été effectuées sur deux carottes CALYPSO. Les carottes MD18-3569 (située à l'est du Canyon Penghu) et MD18-3574 (située sur la levée du Canyon Gaoping) ont été étudiées dans le but (i) d'identifier la source des sédiments ; (ii) reconstruire l'altération chimique et l'érosion des sols du sud de Taiwan depuis la dernière période glaciaire (iii) reconstituer un enregistrement de l'activité turbiditique du Canyon Gaoping associée à la fréquence et intensité des typhons au sud de Taiwan depuis 4.2 ka.

Les sédiments de la carotte MD18-3569 sont caractérisés par des proportions majeures d'illite et chlorite, modérée de smectite, faible de kaolinite, et des valeurs de 87Sr/86Sr (0.7187 to 0.7213) et εNd (-11.63 to -10.89) permettant d'identifier les rivières du sud-ouest de Taiwan comme la seule source des sédiments déposés sur la levée du Canyon Penghu. L'abondance d'illite et chlorite et la composition chimique (ex : Indice d'altération chimique) indiquent une faible altération chimique, en accord avec l'important taux de dénudation et soulèvement de Taiwan (~10 mm/yr). Nous avons également démontré que les variations à long terme d'altération chimiques des sols du SO de Taiwan sont contrôlées par les changements des précipitations de mousson et typhons et environnementaux (ex : couvert végétal) depuis 32 ka.

Les sédiments de la carotte MD18-3569 sont constitués de silts fins et argiles indiquant que le Canyon Penghu reçoit peu de sédiments grossiers provenant des rivières de Taiwan. Les variations de granulométrie et modèles d'End-members révèlent une granulométrie plus grossière pendant la dernière période glaciaire et plus fine durant l'Holocène. Une transition s'est produite entre 10.7 et 10 ka, la granulométrie moyenne a diminué de 40% et la fraction grossières a chuté de 40 à 0%. Cet intervalle est simultané au Melt Water Pulse Event-1C, une rapide transgression marine qui a bouleversé la configuration terre-mer (inondation du détroit de Taiwan) et potentiellement déconnecté le Canyon de Penghu des rivières taiwanaises. A l'Holocène, les sédiments dérivant de Taiwan sont majoritaires car la distance entre le canyon et les rivières est plus importante.

La carotte MD18-3574 enregistre de nombreuses turbidites, provoquées par les typhons, se produisant dans le Canyon Gaoping au cours des derniers 4 ka. L'étude, à haute résolution par XRF core scanning et imagerie hyperspectrale, granulométriques et minéralogiques, de lamines ont permis de caractériser la dynamique sédimentaire de la levée. Les niveaux sombres et grossiers sont associés aux dépôts turbiditiques. 2400 dépôts turbiditiques ont été identifiées (majoritairement associés aux typhons) au cours des derniers 4.2 ka. La fréquence des typhons enregistrés par le Canyon Gaoping a diminué depuis 4 ka (en lien avec le refroidissement des SST de l'Océan Pacifique ouest). Après 1.5 ka, les périodes froides sont associées à des typhons plus rares mais plus intenses. Nous suggérons que l'activité des typhons est affectée par les températures de surfaces du Pacifique les conditions La Niña-like de El Niño Southern Oscillation renforçant la circulation de Walker et la mousson d'hiver affectant le mouvement des typhons.

université PARIS-SACLAY | ÉCOLE DOCTORALE Sciences mécaniques et énergétiques, matériaux et géosciences (SMEMAG)

论文题目：南海东北部末次冰期以来东亚气候与海底峡谷沉积动力过程

关键词：沉积物搬运，物理剥蚀，化学风化作用，东亚季风，台风活动，，全新世，台湾.

摘要：台湾位于东亚季风气候区，同时受到台风活动的强烈影响。台湾南部的沉积物主要经由多条海底峡谷通过不同方式（如浊流）向南海深海搬运。然而，这些海底峡谷堤岸和堤坝晚第四纪沉积记录的气候（季风、台风）与水文（海平面、洋流）变化过程尚未得到充分的认识。本研究选取南海东北部台湾岸外澎湖峡谷堤坝 MD18-3569和高屏峡谷堤岸 MD18-3574两根活塞柱状长岩芯，开展高分辨率沉积学、矿物学和地球化学分析，旨在：（1）明确沉积物的来源；（2）重建台湾南部流域的化学风化和剥蚀历史；（3）确定末次冰期以来台湾南部与气候变化相关的台风活动频率与强度。

MD18-3569岩芯取自澎湖峡谷东侧堤坝，晚第四纪以来沉积物中的粘土矿物主要为伊利石和绿泥石，其次为蒙脱石，以及少量的高岭石。根据陆源碎屑全岩和粘土粒级（<2 μm）87Sr/86Sr（0.7187~0.7213）和 εNd 值（－11.63~－10.89）可以发现，台湾西南部河流是澎湖峡谷东岸末次冰期以来沉积物的唯一来源。以伊利石-绿泥石为主导和元素组成特征（如化学蚀变指数 CIA）表明沉积物经历了中等程度化学风化，与台湾西南部强烈隆升导致高剥蚀速率（~10 mm/yr）相符。研究结果还表明，在过去32 ka，台湾西南部土壤的化学风化长期变化主要受季风和台风降雨以及环境变化（如植被覆盖）的共同影响。

MD18-3569岩芯沉积物主要由粘土和细粉砂（~13 μm）组成，表明澎湖峡谷并没有直接与台湾河流相连，因而从河流中接收到的粗粒沉积物含量较低（<25%）。粒度分布特征和端元模型结果显示，较粗的粒度组分出现在末次冰期，而较细的粒度组分出现在全新世时期。早全新世10.7~10.0 ka 期间存在一个过渡期，粗粒沉积物含量从~40%降低到接近0%。该时期与融冰水事件 MWP-1C 同时发生，代表一次快速的海侵事件，显著改变了海陆格局（台湾海峡被淹没），导致澎湖峡谷与台湾河流系统的连接断开。全新世期间，虽然高海平面时期澎湖峡谷与台湾河口的距离较远，但台湾河流沉积物的贡献仍占主导地位（>80%）。

MD18-3569岩芯沉积物主要由粘土和细粉砂（~13 μm）组成，表明澎湖峡谷并没有直接与台湾河流相连，因而从河流中接收到的粗粒沉积物含量较低（<25%）。粒度分布特征和端元模型结果显示，较粗的粒度组分出现在末次冰期，而较细的粒度组分出现在全新世时期。早全新世10.7~10.0 ka 期间存在一个过渡期，粗粒沉积物含量从~40%降低到接近0%。该时期与融冰水事件 MWP-1C 同时发生，代表一次快速的海侵事件，显著改变了海陆格局（台湾海峡被淹没），导致澎湖峡谷与台湾河流系统的连接断开。全新世期间，虽然高海平面时期澎湖峡谷与台湾河口的距离较远，但台湾河流沉积物的贡献仍占主导地位（>80%）。

MD18-3574岩芯取自高屏峡谷西侧堤岸，记录了高屏峡谷4 ka 以来由台风触发的大量浊流事件（约占浊流的70%，每年3~4次）。采用高分辨率 X 射线荧光（XRF）岩芯扫描、超高光谱成像、粒度和全岩矿物学分析，对该堤岸沉积岩芯中保存的纹层特征加以分析，认为暗色、粗颗粒纹层与浊流活动有关。在过去4.2 ka 中，总共识别出2400个暗色层，大部分与路径台湾的台风活动密切相关。统计结果发现，距今4 ka 以来，高屏峡谷记录的台风频率有所减少，这与西太平洋及周边边缘海的降温有关。1.5 ka 以来，台风频率降低，但强度加大。研究同时显示，全新世以来的台风活动受到拉尼娜现象的影响，如厄尔尼诺-南方涛动（ENSO）加强了太平洋沃克环流和冬季风

Contents

Chapter 1 General introduction

1.1 Motivation

The South China Sea is the marginal sea which receives the highest amount of riverine terrigenous sediment worldwide, 1600 Mt/yr representing about 8% of the global sediment discharge to the ocean (Milliman and Farnworth, 2011). The fluvial drainage systems of northern South China Sea amount to 291 Mt/yr (Taiwan: 176 Mt/yr, South China: 102 Mt/yr, Luzon: 13Mt/yr) (Milliman and Syvistki, 1992; Dadson et al., 2003; Liu, Z.F. et al., 2009; Zhang et al., 2012).

Taiwan margin consists of the narrow Gaoping shelf and slope at the south, and the wide and shallow Taiwan Strait in the west. The Gaoping slope is characterized by the presence of many submarine canyons delivering high amounts of sediments from Taiwan rivers to the deep-sea and the Manilla Trench system (e.g. Gaoping and Penghu canyons). The Gaoping Canyon is directly connected to the Gaoping River mouth, which discharges about 50Mt/yr of sediments to the sea through the canyon via turbidity currents (Zhang et al., 2018). Rivers from south and south-west Taiwan discharge sediments to Taiwan Strait and western Gaoping slope. Canyons like Penghu Canyon are not directly connected to rivers at present time; thus, their sediments transport dynamics remains unclear. In last decades, monitoring and in situ studies showed that the actual fluvial terrigenous inputs and sediment redistribution by turbidity currents, surface and deep circulation from Taiwan to the northern South China Sea is controlled by climatic forcings such as Asian monsoon and typhoons (Fang et al., 1998; Zhang et al., 2018). Active submarine canyons are efficient pathways and storage features for organic matter and carbon (Canals et al., 2006; Allen and de Madron, 2009; Masson et al., 2010; Liu J.T. et al., 2016). For this reason, studies of their sedimentary dynamic in link with climatic forcing are important for the understanding of carbon cycle with climate changes.

Climate of East Asia is dominated by the East Asian monsoon system and influenced by the tropical cyclone (typhoon in the Pacific Ocean region). The East Asian monsoon, as part of the global monsoon system, controls the moisture and heat transport in the western Pacific Ocean and East-Southeast Asia (Wesbter, 1987). The East Asian monsoon consists in a seasonal shift in wind directions during summer and winter (Wesbter, 1987). During the winter season, the Asian continent cools faster than the Pacific Ocean and marginal seas. This results in the formation of a high atmospheric pressure cell over Siberia. Such high-pressure

fields on the continent determine a pressure gradient which in turn results in the onset of cold and dry winds from northern latitudes (Webster, 1987). The inter-Tropical convergence zone (ITCZ) and the precipitations are located on northern Australia and Indonesian arc during winter. Inversely, during summer, oceans heat faster than the continent and high-pressure atmospheric cells are formed above the ocean. This leads to the formation of warm and moist northward winds from oceans to the East Asia continent and a northward shift of ITCZ and precipitation front to the South China, Philippines, and Taiwan regions (Webster, 1987). In addition, concurrently to the wet summer monsoon, typhoons affect the Philippines, Taiwan, the coastal South China and the northeast Asia inducing intense episodic precipitations. Taiwan is affected by 3 to 4 typhoons per year causing critical damages (Liang et al., 2017). Typhoons are generated in western and central Pacific and western marginal seas at tropical latitudes and their tracks are largely controlled by the regional atmospheric circulation (Emmanuel, 2003, Chan, 2005). The summer season, when strong East Asian summer monsoon and typhoons occur, accounts for more than 80% of the yearly precipitation on Taiwan (~2500 mm, Dadson et al., 2003).

Such precipitation patterns imply that sediment fluxes from rivers to sea are largely controlled by the seasonal precipitation variations. Numerous studies based on marine sediments have investigated the impacts of East Asian monsoon and typhoon rainfalls on the sedimentary redistribution from source-to-sink at different time scales (Boulay et al., 2005, 2007; Colin et al., 2010; Liu Z.F. et al., 2010a, 2016; Zhao et al., 2018). Paleoclimatic studies conducted in the East Asia region have demonstrated the link between the monsoon system and glacial-interglacial cycles (Wang et al., 2001; Dykoski et al., 2005; Cheng et al., 2016). During warm interglacial periods, the summer monsoon was enhanced, and East Asian climate was more humid. On the contrary, during cold glacial periods, the winter monsoon was dominant and aridification of East Asia is observed. To date, there is no consensus on the impact of monsoon variations on the chemical weathering conditions in East Asia. Studies have shown that in large draining basins, the intensification of summer monsoon precipitation might enhance the chemical weathering of sediments (Sang et al., 2022) (Fig. 1-1). However, studies of small mountain river sediments in Taiwan suggest that the stronger summer monsoon precipitations increase the runoff and erosion, reducing the sediment residence time in river basins and then chemical weathering (Zhao et al., 2017) (Fig. 1-1).

Paleo-typhoon activity is intense in the East Asian region, particularly during the Holocene (Yu S.W. et al., 2017; Yue et al., 2019). The paleo-typhoon variations have been

demonstrated to be controlled by El Niño Southern Oscillation (Zhu et al., 2017). Past reconstructions of typhoon activity during the Holocene have shown stronger typhoon frequency during the early and the Late Holocene (Chen et al., 2012; Zhu et al., 2017). Gaoping submarine canyon is an ideal area to study paleo-typhoon records because its head is connected to the Gaoping River mouth. Under such conditions, the suspended-sediment concentration of the river plume from Gaoping river sediment discharge can generate turbulent hyperpycnal flows in the canyon during major flood events such as those of typhoons.

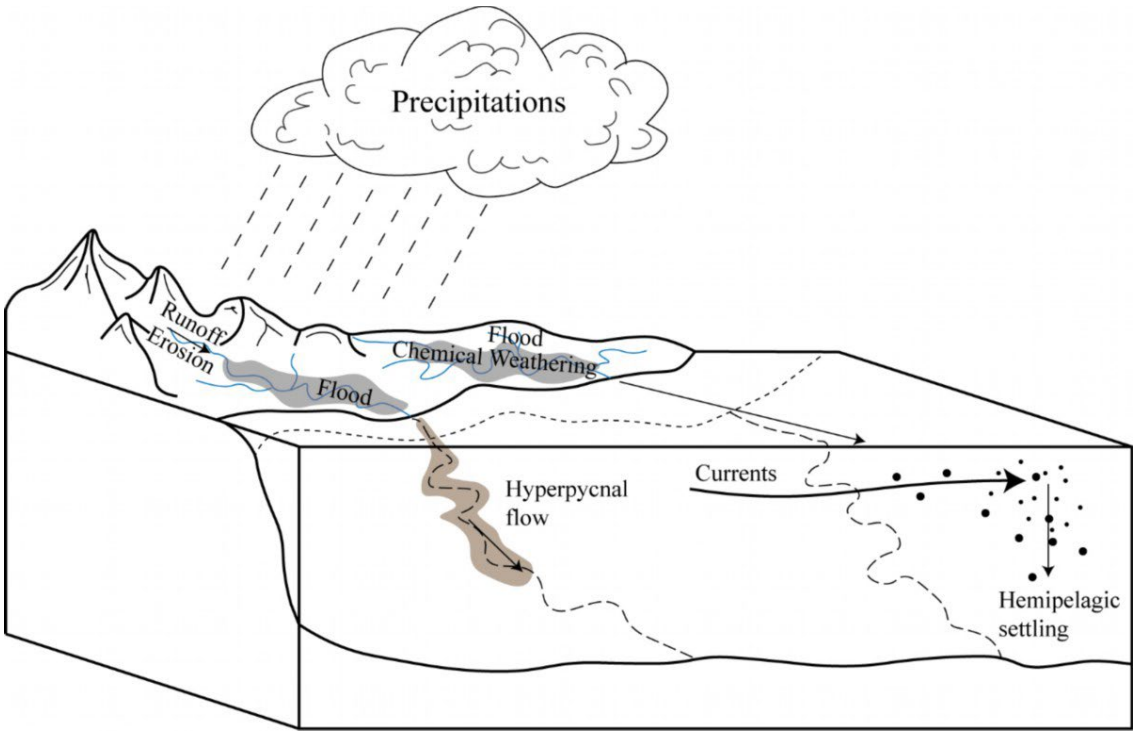

Figure 1-1. Representation of source to sink processes on a continental margin, highlighting river connected and not connected submarine canyon that control sedimentary dynamics.

East Asian climate is also an important control of the South China Sea surface current circulation. The seasonal reversal of the monsoon winds induces a reversal of main surface current directions (Fang et al., 1998; Hu et al., 2000). The South China Sea is only connected to the western Pacific Ocean through the deep Luzon Strait. In general, surface, and deep-water masses of the Philippines Sea inflow to the South China Sea through the Luzon Strait, and South China Sea intermediate water masses outflows to the Philippines Sea (Yuan, 2002; Caruso et al., 2006; Tian et al., 2006; Gan et al., 2016; Zhu et al., 2019). In addition, the glacial-interglacial sea level fluctuations also modify the South Chin Sea hydrology. In high sea level phases, shallow straits (<100 m of water depth) like the Taiwan Strait connect the

SCS to adjacent seas. During glacial low sea level stand (-120 m), these straits are emerged. Such changes of the hydrology have important effects on the detrital sediment redistribution of the South China Sea (Wang et al., 1997).

The South China Sea is an interesting area to study source to sink process:

(1) Due to the contrasted mineralogical and geochemical signatures of the sedimentary sources of the northern SCS, many studies have combined clay mineralogical assemblages (clay fraction) and geochemical (Nd and Sr isotopes) to trace sediments provenance variations in link with climatological and hydrological fluctuations at different time scales (Liu Z.F. et al., 2004, 2005, 2007a, 2008; 2009; 2010; 2016; Colin et al., 2010; Zhao et al., 2018; Nayak et al., 2021).

(2) The clay mineral assemblages and major elements can be used to reconstruct the chemical weathering history of sediments deposited in the SCS in link with east Asian monsoon rainfall variations (Hu et al., 2012; Clift et al., 2014; Liu Z.F. et al., 2016; Zhang et al., 2017; Sang et al., 2022).

(3) Grain size investigations can be conducted to determine the impacts of changes in hydrodynamic conditions, current strength and sea level fluctuations on hemipelagic sedimentation (McCave et al., 1995a; Stow and Tabrez, 1998; Boulay et al., 2003; Xu et al., 2017) and submarine canyon activities (Mulder et al., 2003; Liu J.T. et al., 2009; Hsiung et al., 2021).

The objective of this study is to reconstruct the dynamics of sediment transports from lands (South Taiwan) to the Northern SCS with a source to sink approach and establish the climatic control (paleo-typhon, paleo-monsoon, sea-level changes). In detail, our objectives are (i) to assess the role of the East Asian monsoon and typhoon rainfall on the erosion and chemical weathering of South Taiwan since the last glacial period; (ii) to establish the activity of the Penghu submarine canyon and potential climatic control (sea-level changes, rainfall); (iii) to reconstruct, on the base of high-resolution stratigraphy frameworks, the late Holocene temporal changes of turbidity-current activities of the Gaoping submarine canyon which permit us to reconstruct paleo-floods of the Gaoping river (paleo-typhoon).

For this study two long Calypso cores collected during the Hydrosed cruise on the levee of the Gaoping submarine canyon and on the bank of the Penghu submarine canyon (south margin of Taiwan). The two canyons are characterized by different land-sea configurations.

Their studies are complementary and required to establish the dynamic processes of sediment transfers from Taiwan, Taiwan Strait and South China to the Northern margin of the SCS.

We have then conducted radiocarbon dating, mineralogical analyses (XR diffraction on clay-sized fraction and bulk sediments), geochemical analyses (XRF, XRF core scanning, Nd-Sr isotopes) and sedimentological analyses (hyperspectral imaging, laser grain size and carbonate content) to: (i) determine sedimentary provenances of the sediment deposited on the levee of Penghu Canyon (clay minerals analyses and Nd-Sr isotopic composition) and sedimentary dynamic (grain size) in link with sea level fluctuations and oceanographic conditions; (ii) reconstruct weathering processes affecting the SW Taiwan (clay mineralogy and major elements composition) associated with climatic changes since last glaciation; (iii) constrain sedimentary dynamic of the Gaoping Canyon levee and obtain a high resolution record of turbidites deposit through time to reconstruct the typhoon activity since late Holocene (grain size, XRF core scanning, hyperspectral imaging).

The results of all investigations performed as part of this thesis are organized in five chapters. This thesis is articulated in six chapters:

The first chapter is a general introduction of this study. The second chapter will introduce the climatic and geological background of the studied area and the materials and methods used for this study. This first chapter is divided into four sub-chapters. First, the sedimentary settings of the northern South China Sea region will be assessed to present the geology of the Southeast Asian regions and the present sedimentary dynamic with a particular focus on Taiwan and the northern South China Sea margin. Then, the climatic settings of the East Asia domain will be introduced presenting the present and past features of East Asian monsoon system, the El Niño Southern Oscillation and typhoons and their impacts on the sedimentary dynamics of the studied region. The oceanographical settings of the northern South China Sea and their control on present and past sediment redistribution from rivers to deep sea will be presented as well. Finally, the study strategy with the cores sampled and investigated and the methodologies used in this work will be presented.

The third chapter of this manuscript will focus on the identification with mineralogical (clay mineral assemblages of illite, chlorite, smectite and kaolinite) and geochemical investigations (Nd-Sr isotopic compositions) of the provenance of the hemipelagic sediments deposited on the eastern bank of the Penghu Canyon and its changes since the last glacial period (last 32 ka) from Core MD18-3569. Taiwan appears to be the unique source of eastern

Penghu Canyon levee since the last glaciation. In addition, as there are no major provenance changes, geochemical composition (major elements: Chemical index of alteration, Al/Na, Al/Si) and clay mineralogical ratios (smectite/illite+chlorite, kaolinite/illite+chlorite) permit us to reconstruct the chemical weathering history of the sediments from SW Taiwan rivers basins. The chemical weathering proxies should indicate the impacts on SW Taiwan soil weathering from climatic forcing (east Asian monsoon and typhoons rainfall) since the last glacial period.

The fourth chapter will be focused on the grain size study of the eastern Penghu Canyon sediment since the glacial period (last 32 ka). Sediments deposited on eastern Penghu Canyon are mainly hemipelagic clays and fine silts, without visible turbiditic activity. Sediment provenance from SW Taiwan is constant since last glaciation, but the deglaciation sea level rise changed drastically the land sea configuration of the Taiwan Strait and Penghu Canyon. The canyon is thought to be connected to rivers draining the strait during low sea level periods. The grain size record will allow to reconstruct the hydrodynamic conditions and terrigenous sediment redistribution controlled by climatic forcings and glacial-interglacial sea level fluctuations. End-member modeling approaches have been used in order to better understand the coarse and fine sediments transport processes modulated by the sea level rise. In this chapter we aim to identify a potential canyon-river disconnection during the deglaciation based on grain size results.

The sixth chapter aims to present the study of the late Holocene turbiditic frequency recorded on the western levee of the Gaoping Canyon. The Gaoping Canyon activity is interpreted to be directly controlled by typhoon activity (~70% of turbidites on the levee are triggered by typhoons). The core MD18-3574, collected on the western levee of the Gaoping Canyon, presents numerous fine laminations (2-25mm) indicating it records the strongest events from the canyon. This will be investigated using an approach combining the scanning of a highly laminated sediment core with non-destructive and high-resolution methods, hyperspectral imaging and XRF core scanner to obtain relative sedimentological and geochemical information. In addition, the high-resolution grain size measurement of a core section and the mineralogical investigation of identified laminae will allow to characterize the turbiditic deposit and reconstruct their frequency. Thus, we aim to reconstruct the paleo typhoon frequency in the south of Taiwan since 4 ka and understand the link between Taiwan typhoon activity and regional climatic changes (monsoon, ENSO).

1.2 Sedimentary context of the northern South China Sea

The South China Sea is a semi-closed marginal sea of the Western Tropical Pacific region. The SCS is ranging from 0° to 23° N and from 100° to 121° E (Fig. 1-2).

The SCS is the largest western Pacific marginal sea (3.5 million km²). It is limited to the west by China and Indochina Peninsula (Vietnam, Cambodia, and Thailand), at the south by Malay and Indonesian (Borneo and Sumatra) islands, at the east by Philippines archipelago (Luzon and Palawan) and at the north by Taiwan island.

The SCS shelves present contrasted morphologies. The South China and the Sunda shelves correspond to passive margins and are large and shallow (<200 m depth). Inversely, the Indochina and northeastern and eastern SCS shelves are very narrow and not well developed with very steep slopes characteristic of active margins. The northeastern and eastern SCS is characterized by the presence of the Manilla Trench. Manilla Trench is a N-S axis trench boarding Philippines archipelago and originating from a submarine canyon system converging from South China and Gaoping (South Taiwan) slopes. The central SCS is a deep-sea basin with sea floor at bathymetry ranging from 3000 to 4000 m. The SCS average depth is around 1200 m. The Manilla Trench presents the deepest water depth up to 5400 m.

The SCS is directly connected to the Western Pacific only through the deep Luzon (also called Bashi Strait) Strait. The Luzon Strait is a north-south strait located between Luzon and Taiwan islands (Fig. 2.1). The deepest sill of Luzon Strait reaches 2400 m. It permits water mass exchanges between the SCS and the Western Pacific (Hu et al., 2000). The northern SCS is connected to the East China Sea by the shallow Taiwan Strait (Fig. 2-1) separating Taiwan to China block (maximum water depth of 60 m). The Karimata and Mindoro Straits are connecting the Southern SCS to the Java and Sulu seas (Fig. 2-1) and are characterized by shallow water depths (respectively <50 and 200 m.

The SCS is the convergence zone of three tectonic plates: at the west and north the Eurasian continental plate, at the east the Philippines Sea oceanic plate and at the south the Indo-Australian plate. Such tectonic context results in an active tectonic development of the east SCS trenches and Indonesian and Philippines' extrusive magmatism (Katili, 1975; Yumul et al., 2003). It results also in a rapid uplift of Taiwan (~10 mm/yr) and Borneo (~5 mm/yr) (Huang., 1997; Hall, 2002, 2013; Ching et al., 2011).

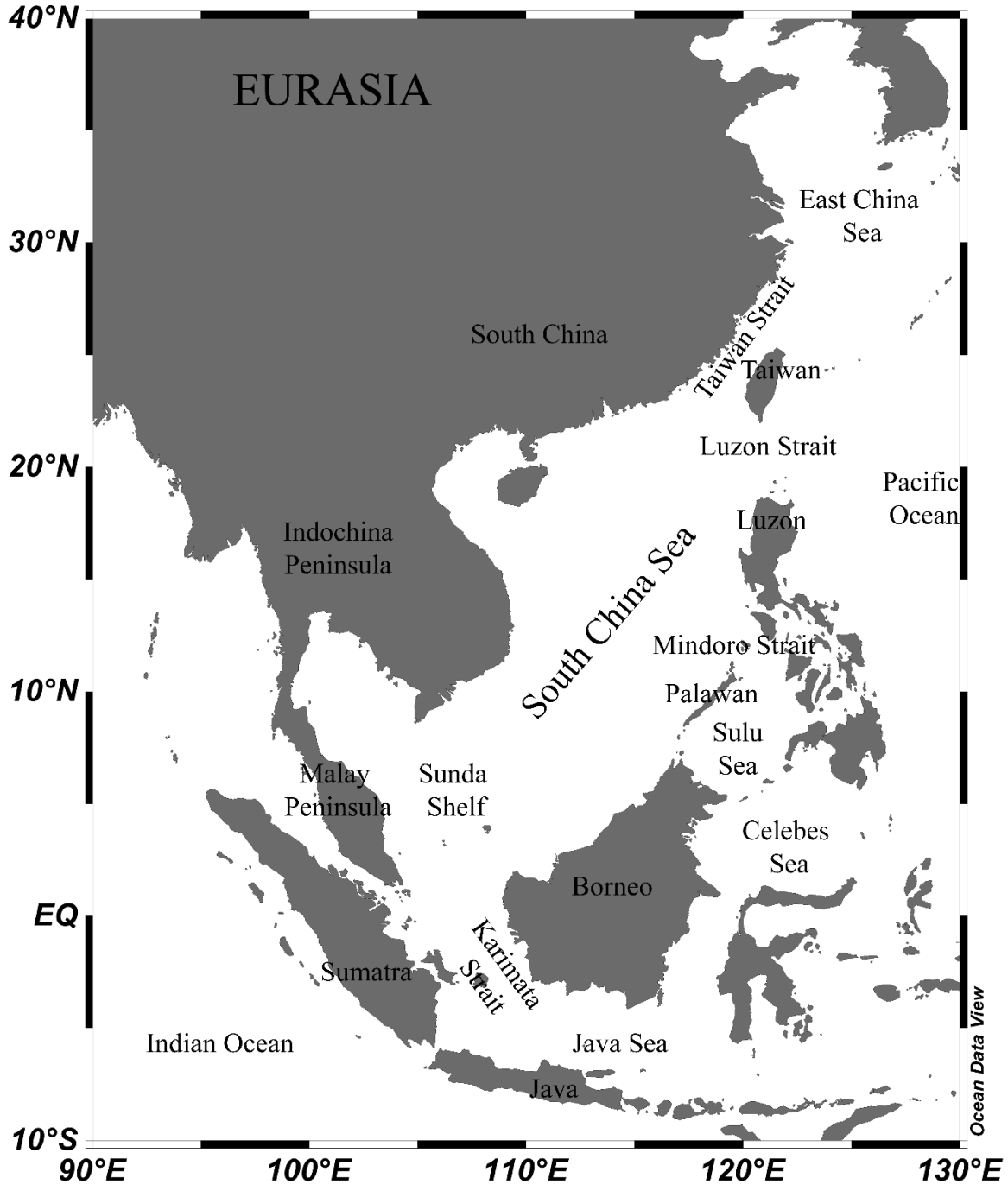

Figure 2-1. Map of Southeast Asia centered on South China Sea

The SCS is surrounded by large rivers that discharge large amount of sediment (~1600 Mt/yr) (Mekong River, Red River and Pearl River (Milliman and Syvitski, 1992; Milliman et al., 1999; Milliman and Farnsworth, 2011; Zhang et al., 2012;). However, sediments deposited in the northern SCS derived from the three land masses surrounding the region. To the west of northern SCS, the South China is drained by rivers including the Pearl Rivers which flow into the western SCS and Taiwan Strait (102 Mt/year). At the northern SCS, small mountain rivers

of south and south-west Taiwan discharge sediments (176 Mt/year) to the northern SCS and Taiwan Strait. At the east of the SCS, many rivers draining the volcanic Philippines archipelago discharge small amounts of sediments (13 Mt/year) to the northeastern SCS.

1.2.1 Geology of Taiwan

Taiwan is located in an active tectonic region where a triple subduction-collision has been occurring since the Miocene (Huang et al., 1997). At the south of Taiwan, the SCS oceanic crust (Eurasia plate) is subducting below the Luzon volcanic arc forming the Manilla Trench oriented north-south following the subduction axis (Yang et al., 1996). At the east, the Philippines Sea plate subducts beneath the Eurasia plate forming the Ryukyu Trench (Yang et al., 1996). Taiwan is the accretion prism of the crust subducted in the arc-continent collision forming the orogenic belt, the Central Range (Lester et al., 2013). The subduction caused a significant uplift 7-20 mm/yr (Hsieh and Knuepfer, 2001; Ching et al., 2011) and Taiwan emerged between 11 and 4 Ma (Hsieh et al., 2022; Zhang et al., 2023). Taiwan is composed by Eocene-Oligocene to Quaternary sedimentary rocks and Cenozoic metamorphic rocks.

Taiwan is drained by small mountain rivers with small and steep draining basins (Liu J.T. et al., 2009). Due to the intense tectonic activity coupled to heavy rainfall and their steep profiles, south-west Taiwan rivers are highly incising bedrocks (5-16 mm/yr). These rivers discharge about 176 Mt/yr of suspended sediment to the SCS and Taiwan Strait (Dadson et al., 2003). More specifically, eleven major rivers drain the southwest Taiwan (Fig. 1-3), including four rivers with annual sediment discharge higher than 10 Mt/yr. These four rivers are, from north to south, Zhuoshui (54.1 Mt/yr), Tsengwen (25.1 Mt/yr), Erhjen (30.2 Mt/yr) and Gaoping (49 Mt/yr) rivers (Dadson et al., 2003). Tsengwen and Erhjen river mouths are the closest river mouths to the Penghu Canyon head (~100 km). Gaoping River is directly connected to the head of the Gaoping Canyon.

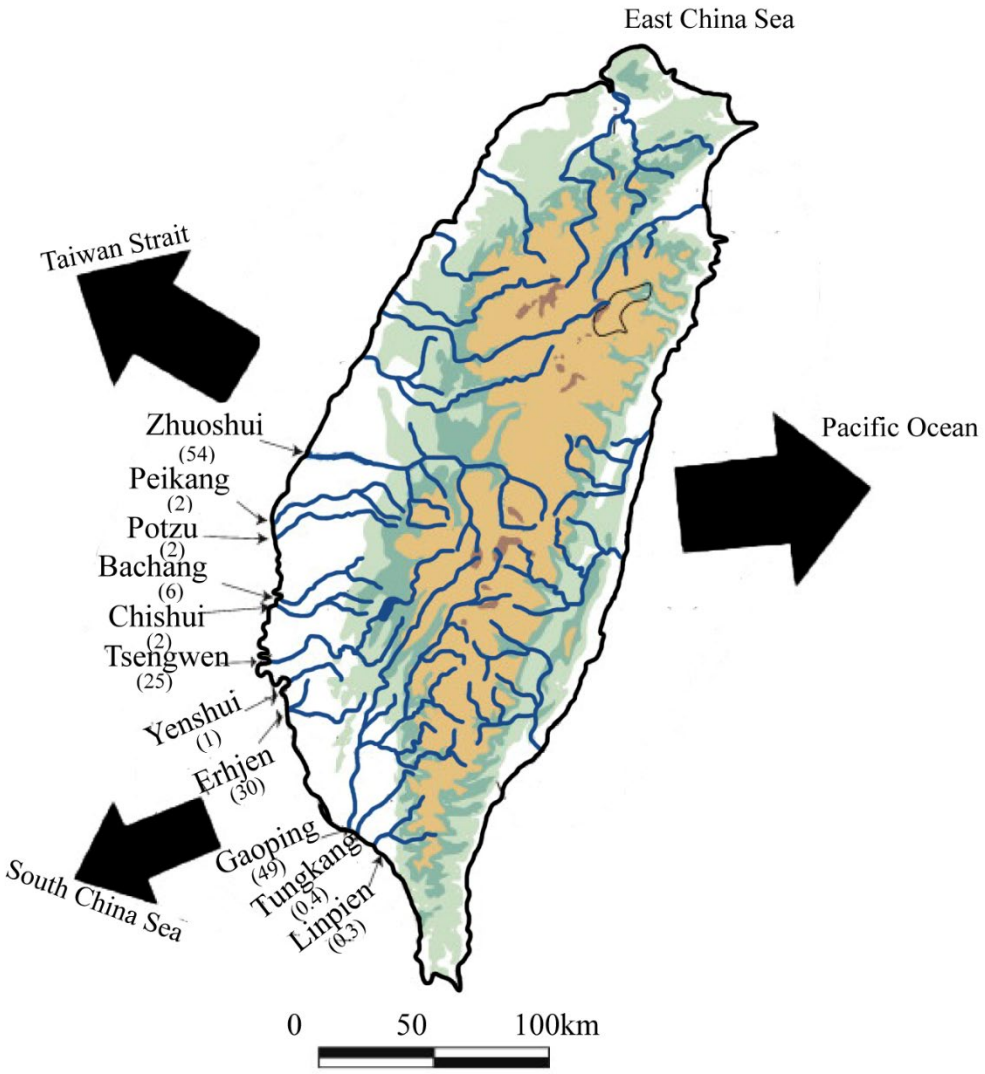

Figure 1-3. SW Taiwan rivers map and sediment discharged to SCS and Taiwan Strait (modified from Dadson et al., 2003; Liu J.T. et al., 2009).

1.2.2 Geology of Luzon Island

Luzon is an island located at the south of Taiwan, it is the northern island of Philippines archipelago and the only one directly surrounding the SCS. Luzon is the result of the collision between Eurasian Plate and Philippines Sea Plate. The collision results in a subduction forming the East Luzon Trough and Manilla Trench, respectively at the east and west of Luzon. Northern Luzon's volcanic activity produced andesitic and basaltic deposits in the southern part of the island from the Pliocene to Quaternary (Commission for the Geological Map of the World, 1975; Durkee and Selmer, 1961) (Fig. 1-4.).

Luzon is drained by numerous small rivers and four major river drainage systems (Fig. 2.3). Most of the largest rivers transport ~5 Mt/yr of sediments (e.g. Agno ~4.7 Mt/yr; Pampanga ~3.5 Mt/yr; Angat ~4.6 Mt/yr). In present time, the western Luzon rivers contribute

a total of 13 Mt/yr of sediment to the eastern SCS which is considerably less than the other regional sediment sources (Liu Z.F. et al., 2009).

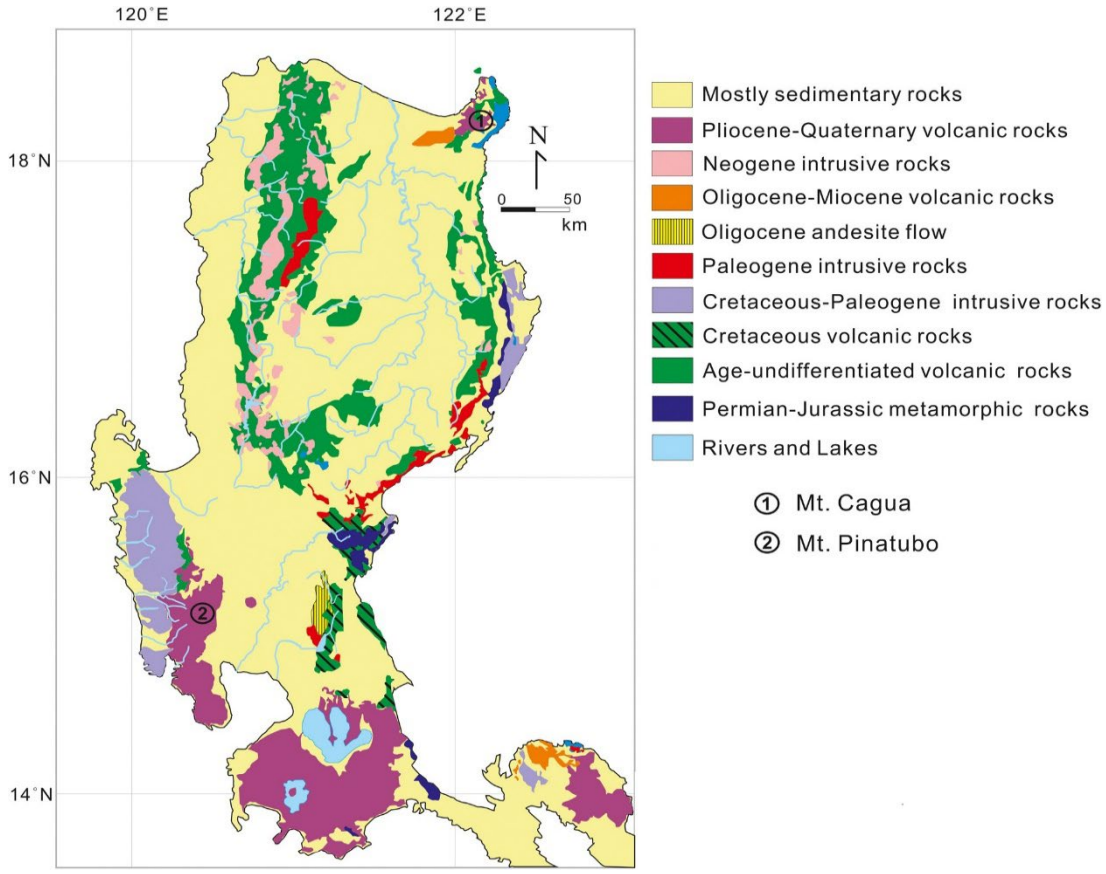

Figure 1-4. Geological map of Luzon Island (modified from Tsai et al., 2019).

1.2.3 South China: Pearl River draining system geology

The South China Block is a Mesozoic cratonic block of the Eurasian Plate. South China is divided in two sub-blocks separated by the Jiangshan–Shaoxing (JSF) and Ziyun Luodian (ZLF) faults systems, at the north the Yangtze craton and in the south the Cathaysia block (Wang et al., 2013) (Fig. 1-5). South China is mainly composed of Paleozoic-Mesozoic igneous, sedimentary and carbonate rocks. The rivers draining the South China discharge a total of 102 Mt/yr of sediments (Liu Z.F. et al., 2016). The largest river draining the South China block is the Pearl River and covers more than 450 000 km² (the third largest river in China). The river flows southeastward through the craton Paleozoic-Mesozoic rocks and discharges 84.3 Mt/yr of suspended sediment to the SCS through the Pearl River delta (Zhang et al., 2012). The other south China rivers discharge significantly less sediment to the SCS Pearl River with an average suspended sediment flux of less than 10 Mt/year, (e.g. Jiulong (3.1 Mt/yr); Han (10 Mt/yr) rivers) (Milliman and Fanworth, 2011).

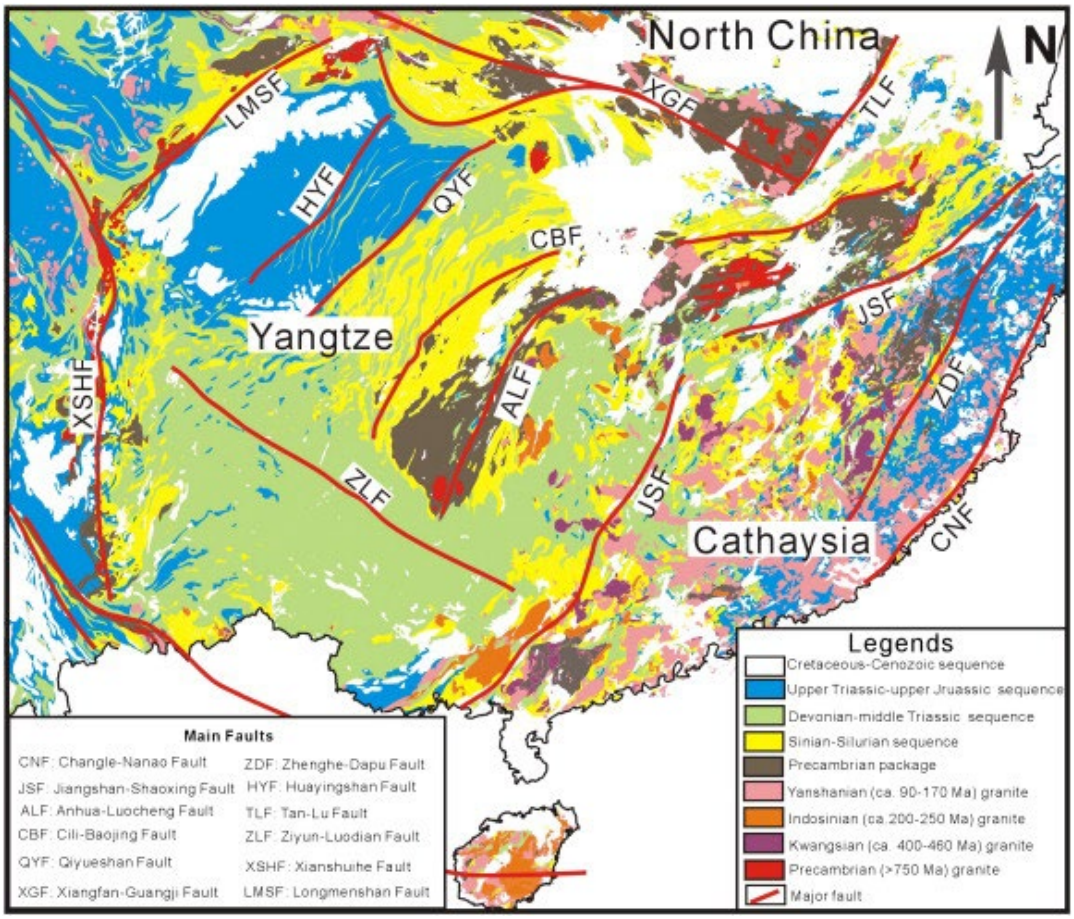

Figure 1-5. Simplified geological map of South China (from Wang et al., 2013; Zheng et al., 2013).

1.2.4 Northern SCS sediment provenance identification

River basins around the South China Sea are characterized by very contrasting environmental and geological settings resulting in very different chemical weathering conditions. Thus, the sediments transported from the land masses to the SCS through the river draining system have very contrasted mineralogical and geochemical signatures. Several studies have focused on the identification of sediment provenance using clay mineral assemblages and isotopic compositions of the rivers draining the southeast Asian domain.

Liu Z.F et al. (2016) showed that clay mineral assemblages in the northern SCS are an interesting proxy to determine the main source of sediments due to their very contrasted mineralogy. Four groups of clay minerals (illite, chlorite, kaolinite and smectite) have been identified in sediments of the SCS (Fig. 1-6).

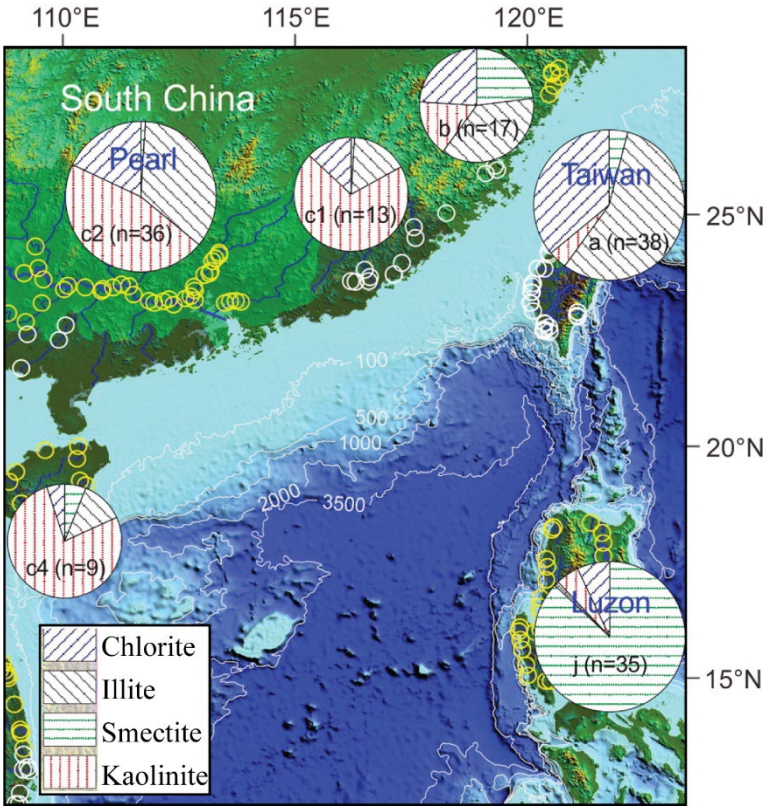

Figure 1-6. Average clay mineral assemblages of fluvial drainage systems around northern SCS (modified from Liu Z.F. et al., 2016)

Illite and chlorite are considered primary minerals and result mainly from intense physical erosion and moderate chemical weathering of metamorphic (i.e., muscovite or biotite) and granitic parent rocks, but can also be derived from reworking of sedimentary rocks (Chamley, 1989). In the northern SCS, illite and chlorite derive from the same processes and sedimentary sources (e.g. Liu Z.F. et al., 2007b, 2016a; Liu et al., 2010; Hu et al., 2012). llite and chlorite are abundant in Taiwan (56% and 36% respectively) (Fig. 1-6) (Liu Z.F. et al., 2007b, 2010, 2016). Taiwan region is characterized by rapid uplift and important seasonal precipitation which induces significant physical erosion, which is the prevailing factor for illite and chlorite formations (Huang et al., 1997). In addition, illite and chlorite contents are low (less than 20%) in volcanic provinces around the SCS.

Smectite (and mixed-layer) minerals result from the bisialitization of ferromagnesian aluminosilicates (leaching of mobile elements). Smectite is considered a secondary mineral produced by the chemical weathering of parent aluminosilicates and ferromagnesian silicates under warm and seasonally contrasted climatic conditions (Chamley, 1989). Smectite could also be produced in a large amount from the weathering of volcanic provinces (andesitic and to basaltic rocks) under low to moderate chemical weathering (McKinley et al., 1999).

Smectites are the dominant clay minerals of the Luzon volcanic province with an average of 87% (Liu Z.F. et al., 2009b). The Cenozoic volcanic rocks of the Central Range of Taiwan can also contribute to moderate amount of smectite due to their chemical weathering. Luzon consists of important Cretaceous to Quaternary volcanic deposits under the warm and humid EAM system. Such conditions are favorable to the production of large amounts of smectite by efficient bisialitization.

Kaolinite is produced in soils under strong hydrolysis conditions (Chamley, 1989). Kaolinite is found in monosialitic soils common to stable plains and steep slopes within a drainage basin with relatively good drainage conditions (Chamley, 1989). The kaolinite is composed of $Al_2Si_2O_5(OH)_4$. High proportion of kaolinite indicates strong hydrolysis conditions associated with warm and humid climate (Chamley, 1989). South China (<45%), is characterized by dominant kaolinite (Liu Z.F. et al., 2007b, 2016). The resulting intensive chemical weathering of the bedrocks overcomes the lithologic and tectonic controls. Inversely, Taiwan and Luzon region are characterized by little to no kaolinite. The lithological factor is dominant in Luzon's rock chemical weathering and the strong erosion of Taiwan rocks driven by the tectonic and steep basins prevent high kaolinite production (Liu Z.F. et al., 2009, Liu et al., 2010 2010).

Several studies used the isotopic composition of Nd and Sr to trace the sediment provenance in marine records (Grousset et al., 1988, Colin et al., 1999, 2006; Clift et al., 2002; Li et al., 2003; Boulay et al., 2005; Liu Z.F et al., 2005, 2016; Wei et al., 2012; Joussain et al., 2016). Nd and Sr isotopic compositions are contrasted between different regions surrounding the northern SCS (Liu Z.F. et al., 2016). We have reported in Table 1-1 the Sr and Nd isotopic composition of detrital materials derived from the main regions of the western and northeastern SCS region (Goldstein and Jacobsen, 1988; Li et al., 2003; Liu Z.F. et al., 2007c, 2016; Shao et al., 2009; Dou et al., 2016).

There is strong contrast in the Nd and Sr isotopic signatures of volcanic province of Luzon and of crustal rocks of the East Asian continent and Taiwan (Table 1-1). The Pearl River (-13.28 to -10.38; average = -11.79), and river of Taiwan (-13.26 to -11.19; average = 12.30) provide to the SCS sediments characterized by non-radiogenic isotopic signatures (very negative εNd values) (Li et al., 2003; Liu Z.F. et al., 2007d, 2016; Shao et al., 2009; Dou et al., 2016). On the contrary, the volcanic province of Luzon contributes sediments to SCS characterized by radiogenic isotopic signatures (with positive εNd values from 6.4 to

7.39; average = 6.96) (Goldstein and Jacobsen, 1988; Liu Z.F. et al., 2016). Such differences in the isotopic compositions result from the very contrasting lithology between young volcanic rocks (e.g. basalts) derived from the mantle and old crustal rocks from stable cratons (e.g. igneous and sedimentary rocks).

Table 1-1: $^{87}Sr/^{86}Sr$ and εN disotopic compositions from the provinces surrounding northern SCS (modified from Liu Z.F. et al., 2016):

Province	Rivers	$^{87}Sr/^{86}Sr$	± 2 σ	εNd	± 2 σ
Taiwan	Gaoping	0.718668	0.000011	-12.56	
		0.717834	0.000014	-12.5	
		0.718899	0.000029	-11.60	0.07
	Tsengwen	0.721323	0.000012	-12.24	0.09
		0.720955	0.000015	-13.26	
		0.720419	0.000013	-12.84	
	Erhjen	0.720608	0.000011	-12.63	0.09
	Zhuoshui	0.718828	0.000010	-11.83	0.07
		0.719782	0.000012	-12.7	
		0.719405	0.000016	-12.04	
		0.71861	0.000012	-12.21	
	Peinan	0.715471	0.000029	-11.19	0.07
Luzon	Pampanga	0.704391	0.000010	7.08	0.07
		0.070491	0.000050	7.10	
	Agno	0.704801	0.000011	7.02	0.08
		0.704350	0.000050	6.50	
	Arba	0.705020	0.000030	6.40	
	Vigan	0.704198	0.000029	7.39	0.08
	Cagayan	0.704608	0.000011	7.10	0.08
		0.705240	0.000040	6.90	
		0.704896	0.000029	7.19	0.09
Pearl river					
		0.733442	0.000003	-11.68	0.80
		0.742222	0.000005	-13.28	0.12
		0.735662	0.000006	-12.66	0.10
		0.735209	0.000003	-10.38	0.18
		0.727507	0.000002	-12.37	0.06
		0.730134	0.000003	-11.41	0.18
		0.737314	0.000005	-10.51	0.57
		0.728329	0.000002	-11.96	0.06

$^{87}Sr/^{86}Sr$ present very contrasted compositions between the main sedimentary sources. (Boulay et al., 2005; Liu Z.F. et al., 2005, 2016; Wei et al., 2012). Sediments from the volcanic province of Luzon have the lowest $^{87}Sr/^{86}Sr$ ratios (0.7042-0.7052) (Goldstein and

Jacobsen, 1988; Liu Z.F. et al., 2016). The Pearl River and South China have the highest $^{87}Sr/^{86}Sr$ ratios ranging from 0.7275 to 0.7422 (Liu Z.F. et al., 2007c). The sediments from rivers of Taiwan (0.7155-0.7213) have lower $^{87}Sr/^{86}Sr$ ratios than the Pearl River (Dou et al., 2016; Liu Z.F. et al., 2016). However, $^{87}Sr/^{86}Sr$ values can be also affected by alteration and grain size fractionation and have also been used to discuss chemical weathering (Derry and France-Lanord, 1996; Colin et al., 2006; Clift et al., 2014). Indeed, $^{87}Sr^{2+}$ ions are preferentially released during chemical weathering of Rb-rich minerals and fine grain size fractions tend to be enriched in ^{87}Sr (Clauer, 1979; Meyer et al., 2011).

1.2.5 Northern SCS Taiwan shelf sediments processes

The Taiwan shelf is very narrow and is incised by deep submarine canyons such as Gaoping Canyon and Penghu Canyon. Taiwan-sourced sediments are then rapidly transported to SCS deep basin mainly through turbidity currents on the slope and canyons (Milliman and Sivitsky, 1992; Liu J.P. et al., 2008). The hyperpycnal and hypopycnal flows resulting from Gaoping River discharge are composed of a significant amount of illite and chlorite (Liu Z.F. et al., 2008, 2016a; Nayak et al., 2021). Most of the hyperpycnal sediments are transported by turbidity currents in the Goaping Canyon.

This study gives important attention to the submarine canyon systems developed on Taiwan margin (Fig. 2.6) and particularly to Gaoping and Penghu Canyons. Many studies have focused on the Gaoping Canyon sedimentary processes (Milliman and Sivtsky, 1992; Chiang and Yu, 2006, 2011; Huh et al., 2009; Liu J.P. et al., 2008, Liu J.T. et al., 2009, 2016; Yu S.W. et al., 2017; Zhang et al., 2018; Chen et al., 2020). The canyon head is located at 1 km from the mouth of the Gaoping River and is directly connected to the river system (Liu J.P., et al., 2016). The Gaoping canyon is then a very active canyon system connecting the Gaoping River to the deep-sea trench system (Fig. 1-7). The Gaoping River is characterized by a relatively small and mountainous catchment with relatively reduced floodplain, delta and shelf. In such land-sea configurations, the Goaping Canyon is directly linked to the Gaoping River without any major storage of sediments on the shelf. Consequently, the Gaoping River discharges a large percentage of its sediment load directly into the sea because sediments can easily escape the narrow shelf and feed deep-basin during high and low stands of see level. Besides, the Gaoping canyon system is a short sediment transport system, suggesting that climate changes may have controlled the sedimentary inputs and the turbidite activity with minor impact of sea-level fluctuations.

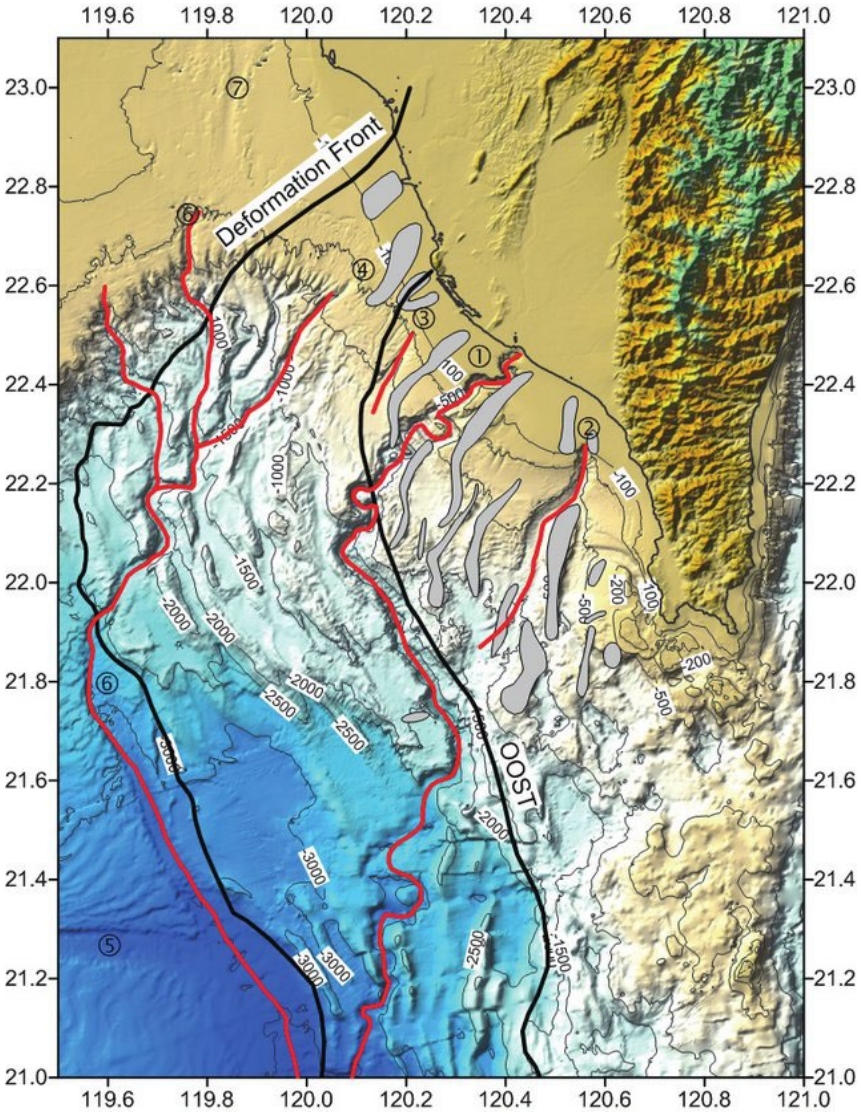

Figure 1-7. Map showing the location of the different submarine canyons and geomorphological units of South Taiwan slope (1: Gaoping Canyon; 2: Fanglio Submarine Canyon; Kaohsiung Submarine Canyon; Shousan Submarine Canyon; 5: Formosan Submarine Canyon; 6: Penghu Submarine Canyon; 7: Penghu Channel (from Su et al., 2018)

The river discharges 49Mt/yr of suspended sediments to the SCS including 80% through the submarine canyon (Dadson et al., 2003; Huh et al., 2009; Liu J.T., et al., 2009). Sediment deposits from the channel-levee system can be used to study the response of terrestrial surface erosion to climate change and reconstruct periodic floods (paleotyphoon) and/or the variability of monsoon rainfall, at longer time scales. The Gaoping Canyon is surrounded by a series of NE-SW submarine canyons parallel to the upper reach of the canyon (Kaohsiung and Fangliao submarine canyons) (Fig. 1-7). The canyon is 260 km with a depth which can reach 600 m below the slope bathymetry. The canyon has a U- to V-shaped topography with high

walls limiting the sediment overflow (Chiang et al., 2006, 2011). At more than 3000 m below sea level, the canyon merges with the Manilla Trench.

The Penghu Canyon presents different land-sea configuration. It is located at the junction of the Taiwan slope and South China Slope, and it connects the southeastern part of the Taiwan Strait through the deep-sea trench system. The Penghu Canyon is a 180 km long submarine canyon extending from the Taiwan Strait Shelf break to the Manilla Trench formed by the local collision (Yu and Chang, 2002; Yu and Hong, 2006). Unlike the Gaoping Canyon, Penghu Canyon is not connected to a river but near to the submarine Penghu Channel (Boggs, 1979, Liu et al. 1998). The channel is sometimes considered to be the remains of a paleo-Minchiang river draining the Taiwan Strait (Boggs, 1979; Dadson et al., 2005). However, the canyon and the channel do not appear to be connected and Huang and Yu (2003) considered this hypothesis unlikely. The Penghu Canyon mainstream has three tributaries including the Shousan Canyon which form a 80 km wide and 100 km long fan in the upper reach from the Taiwan Strait shelf break to a bathymetry of ~2000 m below the sea level (Chuang and Yu, 2002). In opposition, the lower reach is a 80 km long course that connects the upper reach and the Manilla Trench (Yu and Chang, 2002). The sedimentary dynamics of the canyon seem to result from the failure of slumps wall controlled by the tectonic forcings.

The response of sedimentary dynamics of Taiwan submarine canyons to the sea level rise, monsoon intensification and weakening, intense typhoon precipitation and hydrologic changes is still to be studied. The Gaoping submarine canyon sediment provenance is constrained by the connection of the canyon to the Gaoping River (Nayak et al., 2021). The alternation between the hemipelagic deposition and the typhoon and earthquakes-driven turbidity flows has been studied at different time scales from the scale of a typhoon, and from yearly time range to a climatic cycle (Gavey et al., 2017; Yu S.W. et al., 2017; Zhang et al., 2018). Nevertheless, in sedimentary records, the past relationship between the intensity and the frequency of typhoon activity and the climatic changes remains uncertain in the western Pacific region. The Penghu Canyon and levee's sedimentary dynamic is relatively unknown. Nayak et al., 2021 stated that sediments are derived from Taiwan and Luzon through the surface circulation. Within the canyon, geomorphology and seismic profiles are demonstrated that the sedimentation is driven by tectonic-triggered slumps (Yu and Chang, 2002). However, sedimentary records are not available to discuss the late Quaternary sedimentary dynamics. Thus, the sediment provenance, sedimentary processes (turbidites, hemipelagic deposition) and their response to the sea level variations (possible connection with a paleo-river versus

circulation dominated transport), hydrological (source changes) and climatic variations (terrigenous sediment flux) are still unknown. The study of the two canyons will give information on the similarity and differences of sedimentary dynamics and forcings of connected and not connected canyons of the Taiwan margin.

1.3 Climatic setting of northern South China Sea

1.3.1 East Asian monsoon system

The SCS climate is strongly influenced by the East Asian monsoon system. SCS region temperature varies mainly with latitude. In the subtropical northern SCS, the temperature varies widely from 10°C in winter to 20°C in summer with a clear seasonal variation. Inversely, the tropical SCS experiences warmer (27-28°C) and more stable (summer-winter gradient <5°C) temperatures. The main feature East Asian climate is the latitudinal atmospheric heat and moisture fast transport from low latitudes to poles (Webster, 1987, 1994, 1998). The East Asian Monsoon (EAM) consists of atmospheric exchanges between land and ocean and affects a region between the Indonesian Arc and the Siberian region. The EAM is characterized by a seasonal reversal of wind direction and a latitudinal shift of the Intertropical convergence zone (ITCZ). This phenomenon is controlled by the seasonal change in land-ocean heat gradient, which affects atmospheric circulation (Webster, 1987).

In summer, the solar radiation (insolation) received at low latitudes is high. The continental heating is more important than the oceanic heating. The ocean surface water loses part of the energy received from solar radiation due to evaporation and heat mixing in water column (Webster, 1987). This heat gradient associated with a heating of continent relative to ocean results in the development of a low pressure and warm air cell over the continent (Central China) and inversely a high pressure and low temperature over the ocean from May to September (Webster, 1987; Chu and Wang, 2003). The resulting atmospheric pressure gradient leads to a northeastward transport from high-pressure cell (ocean) to low-pressure cell (continent). The moisture transported by the NE winds to the continent rises due to the association of the pressure contrast with low-pressure cells and potential mountain belts (Webster et al., 1987). The resulting cooling of the moist air masses leads to heavy precipitation on the continents and the reliefs (Fig. 1-8). The East Asian Summer Monsoon (EASM) is characterized by the northward shift of ITCZ to 20-35°N over the SCS region (Wang B. et al., 2003, Wang P. 2003, Yi, 2011). The EASM (May-September) period represents the wet season of the northern SCS and is associated with 85 to 90% of the annual

rainfall precipitation of South China (1700-2000 mm), Taiwan (~2500 mm) and Luzon (1900-2100 mm) (Zhang et al., 1999; Dadson et al., 2003; Liu et al., 2007c, 2009).

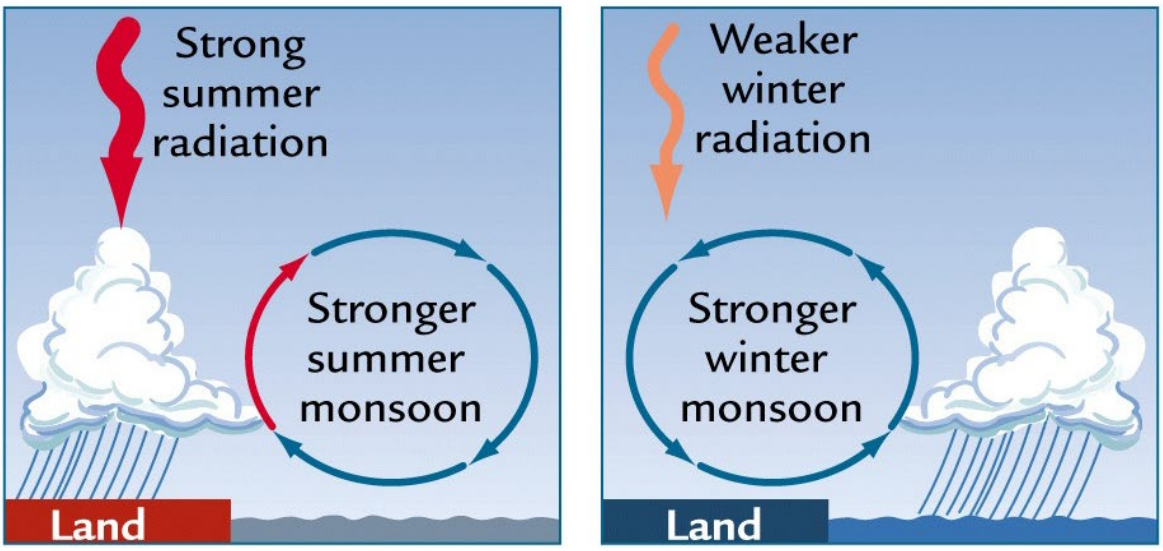

Figure 1-8. Schematic monsoon system process: seasonnal dichotomy (from Ruddiman, 2001)

Inversely, in winter from November to April, low latitudes receive weaker solar radiation. In the northern latitudes, snow cover amplifies the cooling effect and the temperature gradient between the continent and the ocean (Dickinson, 1983; Xiao and Duan, 2016). The continent cools faster than the ocean. The temperature gradient between continents and oceans is reversed compared to summer (Webster, 1987). High pressure cells are forming on the continent, such as the Siberian anticyclone (Sahsamanoglou et al, 1991) and in opposition low pressure cells form over the oceans (Fig. 1-8). The East Asian Winter Monsoon (EAWM) is characterized by strong and cold southwestward winds from continents to oceans (Webster, 1987). The ITCZ and precipitation front shift southward between 0 and 20°S over the Indonesian arc (Wang B. et al., 2003, Wang P. et al., 2003, Yi, 2011). Thus, the EAWM period is a dry season over the northern SCS and a wet season over the southern SCS with precipitations increase of around 20% (Liu and Dong, 2013).

1.3.2 Controls on East Asian Monsoon system

It has been demonstrated that the EAM system responds to global climate variations and major environmental and tectonic changes at different geological time scales (e.g. Sun and Wang, 2005; Shukla et al., 2014; Licht et al., 2016) (Fig 1-9).

On long time-scale, tectonic events affected the monsoon state (Liu and Dong, 2013). Since Cenozoic several major tectonic uplifts have occurred in Asia affecting the regional

climate regime (Liu and Dong, 2013). The uplifts of Iranian Plateau at the west and Mongolian Plateau at the north may have constrained the EAM (Liu and Yin, 2002; Tang et al., 2013). Another major tectonic event is the formation and uplift of Tibetan Plateau. The Tibetan Plateau uplift led to an increase of the temperature gradient in east and southeast Asia increasing the EAM system and the EASM precipitation (An et al, 2000; Liu and Yin, 2002; Guo et al., 2008; Liu and Dong, 2013). Long-term climatic events such as glaciations of Arctic and Antarctica have strongly affected the monsoon system. Several studies highlight the enhancement of EAM precipitation with the growth of polar icesheets (Ding et al., 1995; An, 2000; Yin et al., 2008; Ao et al, 2016).

Higher insolation over northern hemisphere strengthens the low-pressure cell over the east Asian continent increasing the intensity of EASM precipitations (Webster, 1987). During the interglacial intervals, the precession enhances solar insolation. This higher insolation increases the temperature gradient which favors the EASM over the EAWM. Inversely, in glacial times, EAWM is enhanced compared to the EASM (Clemens et al., 1996). The decrease of solar insolation weakens the importance of low-pressure atmospheric cells on the east Asia continent and temperature gradient between surface water and continent (Webster, 1987). Such a phenomenon results in a latitudinal shift of the ITZC over the different cycles, respectively southward in glacial times and northward in interglacial intervals (Wang et al., 2005). Currently, EAWM is strengthened compared to the EASM due to the decreasing trend of insolation since the early Holocene (Wang et al., 2001; Dykoski et al., 2005; Cheng et al., 2016).At different time scales such variations were observed both in marine and terrestrial sedimentological records (Wang et al., 2001; Tian et al, 2004; Dykoski et al., 2005; Yancheva et al., 2007; Cheng et al., 2016; Zhao et al., 2018) (Fig. 2.8). This shows the tight control of 19-23 ka and 40 ka periodicities of precession and obliquity on the east Asian monsoon system.

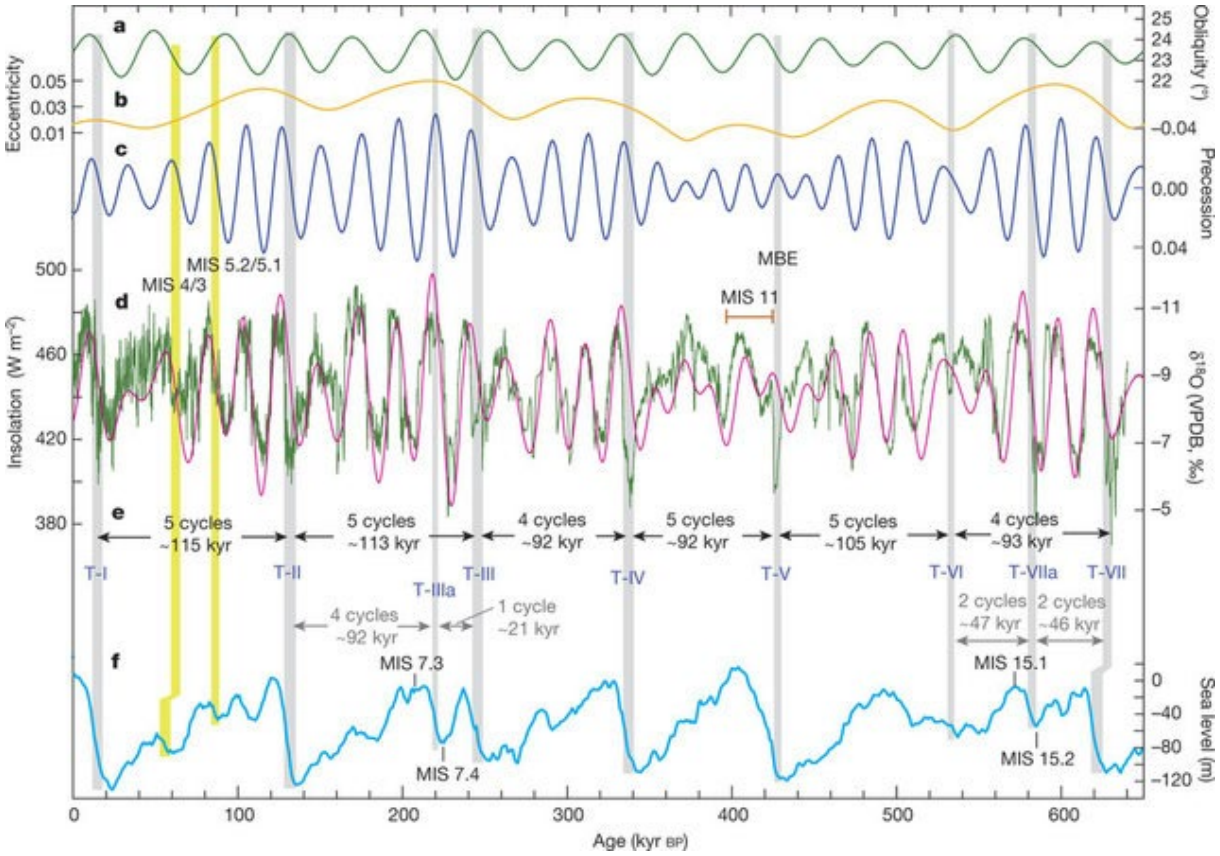

Figure 1-9. Temporal Asian monsoon variations (d: green curve) compared with orbital parameters such as obliquity, eccentricity and precession showing precession-obliquity driven insolation forcing on Asian monsoon (from Cheng et al., 2016).

1.3.3 Monsoon forcing on erosion and chemical weathering

The physical erosion is a process controlled by relief and the action of the climate, lithology, environment (e.g. vegetation cover) or humans (Wang et al., 2016; Ochoa et al., 2016).

The topographic factor is an important setting for erosion processes. Mountain slopes are more susceptible to experience stronger erosion than plains (Liu et al., 2000; Larsen and Montgomery, 2012). Tectonic processes have an important influence on erosion. Previous studies have shown that the erosion rate, river incision rate or landslide occurrence are enhanced by strong uplift rate or recurrent earthquake frequency (Ahnert, 1970, Dewey and Horsfield, 1970; Humphrey and Konrad, 2000; Dadson et al, 2003; Malamud et al., 2004; Larsen and Montgomery, 2012; Li Y. et al., 2014; Li G. et al., 2019). Land use and cover such as exposed soil, bushes and shrubs or agriculture tend to increase the efficiency of soil or rock erosion efficiency by rainfall and runoff in tropical mountainous region, while primary forests

tend to increase soil protection against erosion by the rainfall runoff (Descheemaeker et al., 2006; Mohammad and Adam, 2010; Arnaud et al., 2016; Vijith et al., 2018).

The climatic setting is one of the prevailing forcings of erosion. Tropical regions, except for high-altitude mountain regions, are not affected by the icesheet movements or freeze-thaw actions experienced in higher latitude regions (Sugden, 1978; Cowton et al., 2012; Deprez et al., 2020). Taiwan highest mountains show sporadic features of glacier presence during glacial periods (e.g. LGM) (Cui et al., 2002; Böse, 2004; Ono et al., 2005; Carcaillet et al., 2007). However, the heavy precipitation driven by monsoon system and typhoons in the tropical region is a major factor controlling the erosion (Mohamadi and Kavian, 2015; Meng et al., 2021; Zhao et al., 2021). The intense precipitation resulting from storms and monsoon leads to increased river incision of bedrocks and soils and higher occurrence of landslides (Page et al., 1994; Hsieh and Knuepfer, 2001, 2002; Clift et al., 2008; Colin et al., 2010; Montgomery et al., 2014; Saito et al., 2014; Joussain et al., 2017).

Thus, the small mountain rivers of Taiwan will incise, erode, and transport high sediment yields triggered by the high uplift, slope gradient and intense monsoon and typhoon precipitations (Hsieh and Knuepfer, 2001, 2002; Dadson et al., 2003). Despite moderate relief and stable tectonic context, the vegetal cover in South China and Pearl River basin regions (in present time: important cropland and grassland) (Zhang L., et al., 2016; Liao et al., 2020) and heavy monsoon precipitation make them very vulnerable to erosion. However, the vegetation cover may have been different prior to anthropic land use of soils. Inversely, Luzon is less sensitive to erosion due to its significant proportion of primary forest in the moderate elevation regions.

Chemical weathering is associated with the erosive action of water on rocks. The significant moisture over East Asia related to the EAM and the typhoons strongly affects the chemical weathering of rocks. Studies suggest an increase of chemical weathering related to higher humidity and warmer temperature (West et al. 2005; Goudie and Viles, 2012; Eppes et al., 2020). Thus, soils in Southeast Asia regions are sensitive to intense chemical weathering. Nevertheless, the chemical weathering depends on the complicated interactions of different feedbacks. Physical erosion or significant runoff associated with important precipitation could lead to higher chemical weathering enhanced by the breaking of rocks and induces greater alteration surfaces (Rasmusson and Carpenter, 1982; Allan et al., 1996; Gaillardet et al., 1999; Riebe et al., 2001; Lyons et al., 2005; Wan et al., 2012). However, when physical erosion is

too strong, soils tend to be removed and then the state of chemical weathering of soil material is reduced (Ferrier and Kirchner, 2008; Arnaud et al., 2012; Bajard et al., 2016, 2017a). In addition, chemical weathering also depends on the water exposure or sediment/rock residence time in water (Selvaraj and Chen, 2006). Sediments tend to be less affected by chemical weathering in systems with rapid transport, short length, or low storage in the river basin (Lyons et al., 2002). It is particularly the case for small mountain rivers (France-Lanord and Derry, 1997; Arnaud et al., 2012; Sun and Colin, 2014). The relationship between the climate cycles and the weathering is still unclear in the northern SCS and especially in south Taiwan. On the one hand, studies have shown enhanced sediments chemical weathering during the warm and humid periods such as Holocene (Chen et al., 2016; Miriyala et al., 2017; Sang et al., 2022). On the other hand, studies argued that the shortened residence time of sediments caused by the increased runoff and fastest transport from source-to-sink weakened the chemical weathering, particularly in small mountain river systems such as Taiwan (Dosseto et al., 2010; Bi et al., 2015; Dou et al., 2016; Zhao et al., 2017). Thus, the question of the chemical weathering variations through the climate changes in northern SCS still needs to be investigated.

1.3.4 Typhoons and El Niño Southern Oscillation

Typhoons (name for cyclones in the north Pacific basin) are the most intense tropical storm phenomena. They occur mostly (>95%) in tropical latitudes when the sea surface temperature exceeds 26°C and atmospheric conditions (large-scale vertical waves in easterly wind, cumulus convection with ascending warm and wet air and descending cold air) facilitate the development of clockwise circulation leading to a mature cyclone (Yanai, 1964; Emanuel, 2003; Dare and McBride, 2011; Tory & Dare, 2015). The typhoon intensity is largely related to the sea surface temperature and its track (Emanuel, 2003; Ulbrich et al., 2009)

Typhoon tracks in western Pacific region can have westward or poleward direction, which is controlled by the background atmospheric circulation (Walker circulation, monsoon winds) (Emanuel, 2003). The Pacific Walker circulation tends to suppress Coriolis force effects (poleward motion) and facilitate westward motion of typhoons (Emanuel, 2003; Chan, 2005). When Pacific Walker circulation is weaker and not balancing the Coriolis force and summer monsoon is stronger, the atmospheric circulation allows poleward motion where typhoon tracks curve around 25°N and 130°E (NE Taiwan, SW Japan) and shift northward (Emanuel, 2003; Chan, 2005; Zhang et al., 2013) (Fig. 1-10). Typhoons not dissipated in extratropical

latitudes tend to increase in intensity (Emanuel, 2003; Ulbrich et al., 2009). In most cases, typhoons dissipate quickly after hitting land (Emanuel, 2003).

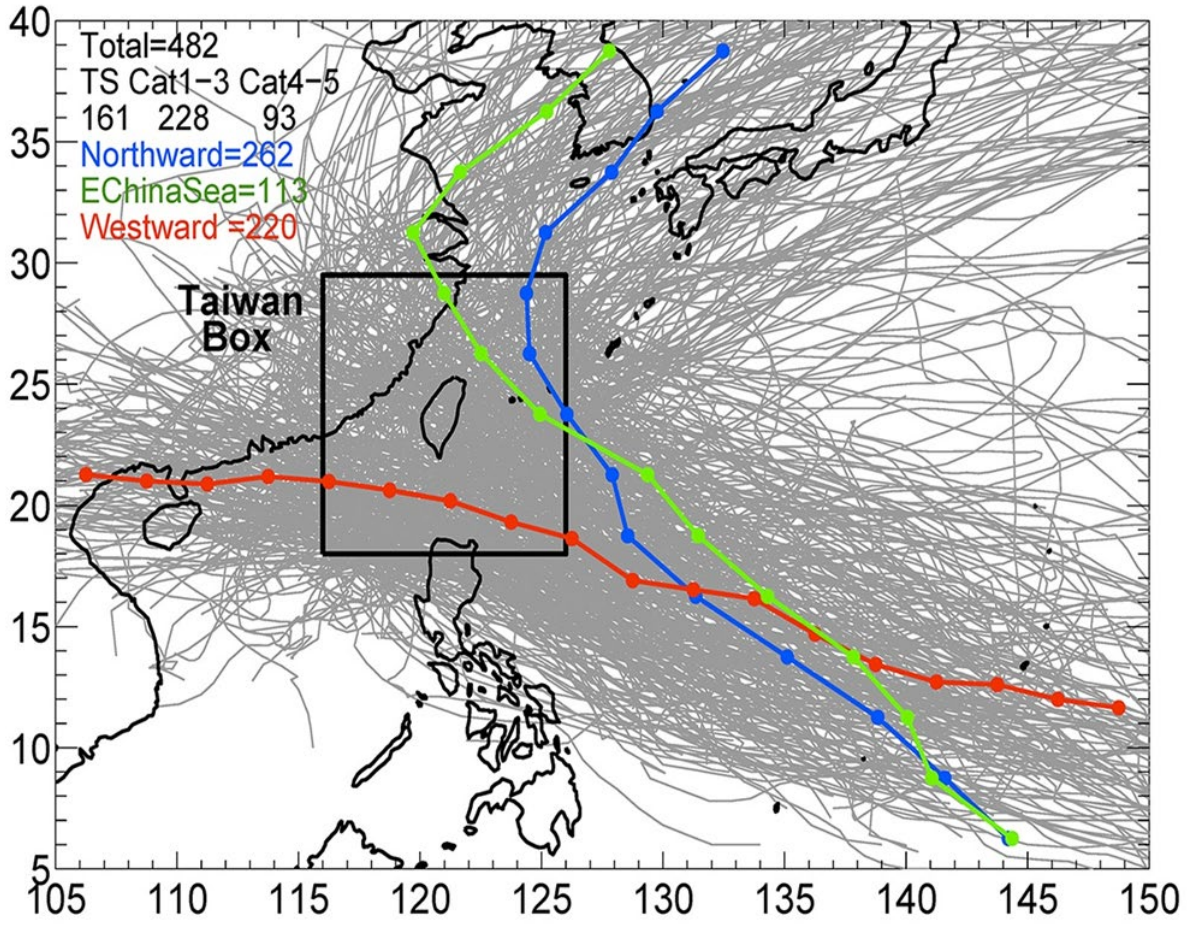

Figure 1-10. Tropical storms track 1950-2013 (Liang et al., 2017). The grey lines are showing the tracks of all the tropical storms. The red, green, and blue lines represent the average paths of westward, northwestward and northward tropical storms.

The northern SCS is particularly affected by tropical storm activity (Fig. 1-10). Taiwan experiences 3 to 4 typhoons (extreme tropical storms) per year (Wu and Kuo, 1999; Zhang et al., 2018). The summer and autumn seasons represent the typhoon season (Wu and Kuo, 1999; Chen and Chen, 2003; Su et al., 2012). Tropical storms such as typhoons are the sources of important and brutal rainfall precipitations. Over the last decades, major typhoons such as Herb (1996), Nari (2001) and Morakot (2009) have struck Taiwan. Typhoon Herb struck Taiwan and Ryukyu Islands and mainland China, from the 31st of July to the 1st of August 1999 and was one of the most intense and damaging tropical storms in recent decades (Wu and Kuo, 1999). The 320 km large typhoon struck Taiwan with winds of more than 200 km.h^{-1} and a total rainfall of 1994 mm (Lin and Jeng, 2000). Similarly, the typhoons Nari (16-

17th September 2001) and Morakot (7-10th August 2009) hit Taiwan with heavy rainfall, respectively more than 2000 mm (Yang and Huang, 2004) and 2600 mm in Taiwan (Chien and Kuo, 2011). The significant typhoon rainfall is often associated with important runoff leading to destructive processes such as landslide or floods on land resulting in damages and casualties (Shieh et al., 2010; Lo et al., 2014; Deng et al., 2016; Yang et al., 2018; Tsai e al., 2021, 2022), important river sediment discharge (Zhang et al., 2018) and gravity flows in marine domain resulting in infrastructure breakage (Su et al., 2012; Gavey et al., 2017).

El Niño Southern Oscillation (ENSO) is a prevailing feature of the climate variability and ocean-atmosphere exchange in tropical regions at short- and long-time scales and can strongly influence typhoon activity (Bjerknes, 1969; Neelin et al., 1998; Wang and Chan, 2002 Chan, 2007). It consists of an alternation of two opposite climatic conditions, La Niña and El Niño (Philander, 1990) driven by changes in sea surface temperatures (Bjerknes, 1969; Philander, 1980; Neelin et al., 1998). On an interannual time scale, the eastern equatorial Pacific Ocean surface warms leading to decrease of pressure, wind strength and the equatorial upwelling. These three responses to the initial warming are positive feedbacks that amplify the warming of eastern equatorial Pacific Ocean surface. These are the El Niño conditions. However, the waves associated with the warming lead to a lagged cooling of the equatorial subsurface waters later compensating for the surface warming, inducing a cooling of the equatorial surface waters. These are the La Niña conditions (Bjerknes, 1969; Philander, 1980; Neelin et al., 1998).

ENSO affects heat and moisture transport on the Pacific Ocean scale. The atmospheric circulation is influenced by the different ENSO conditions, which leads to the propagation of the effects of the ENSO fluctuations over the globe (Trenberth et al., 1998; Liu and Alexander, 2007). The El Niño and La Niña cause global disturbances of the natural climate with unusual droughts and floods (Ropelewski and Halpert, 1989; Trenberth et al., 1998; Mason and Goddard, 2001; Lenssen et al., 2020) (Fig. 1-11, 1-12). El Niño conditions are associated with wet autumn and winter seasons in Taiwan regions (Fig. 1-11). La Niña conditions are associated with drier climate in winter over northern SCS (Fig. 1-12).

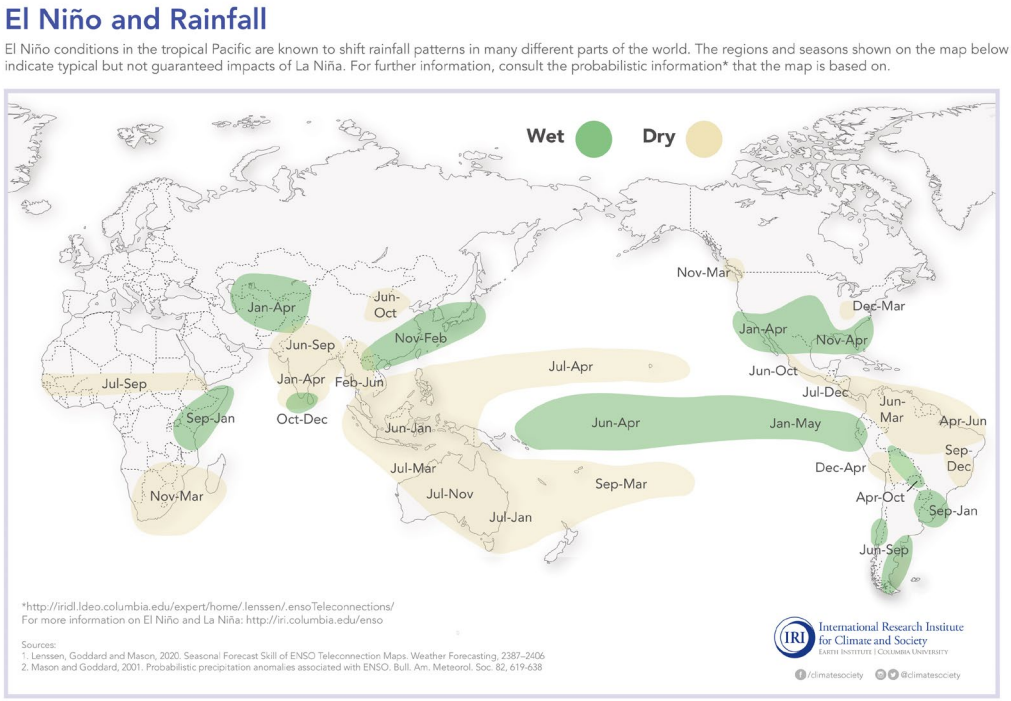

Figure 1-11. El Niño precipitation and drought patterns (from https://iri.columbia.edu/ enso/ modifed from Ropelewski and Halpert, 1989; Mason and Goddard, 2001)

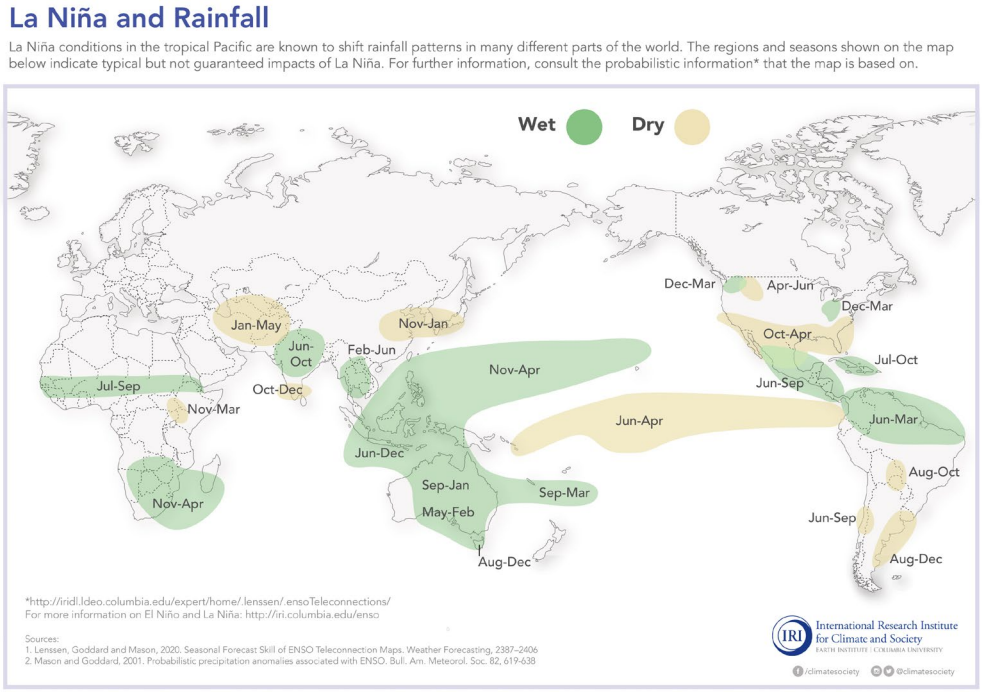

Figure 1-12. La Niña precipitation and drought patterns (from https://iri.columbia.edu/ enso/ modifed from Mason and Goddard, 2001 and Lenssen et al., 2020)

1.4 Hydrological setting of the northern SCS: Control of East Asian Monsoon

1.4.1 Hydrology of the SCS

The South China Sea surface circulation is mainly controlled by the seasonal reversal of the monsoon winds (Hu et al., 2000). In the northern SCS, the connections with the East China Sea, through the Taiwan Strait, and the Pacific Ocean, through the Luzon Strait, also influence the northern SCS surface current pattern (Hu et al., 2000).

In summer, the dominant northeastward monsoon winds induce a basin-scale anticyclonic surface circulation. A coastal current, the Guangdong coastal current (7) flows northward along east Asian continent from southern SCS to East China Sea through the Taiwan Strait (Fig. 1-13). The northern SCS surface circulation is strongly controlled by the weak Kuroshio intrusion (Caruso et al., 2006; Yuan et al., 2006). The warm water inflow through the Luzon Strait forms the SCS Branch of Kuroshio (2), a current flowing southwestward (Caruso et al., 2006). On the Taiwan and South China margins exist loop currents (1) and the SCS warm currents (6) which are northern detachments of the Kuroshio current (Hu et al., 2000; Caruso et al., 2006; Yuan et al., 2006). Loop currents are deriving from the SCS branch of Kuroshio (Li et al., 1998; Liu et al., 2013). The Kuroshio loop currents form when the strong winter monsoon winds deflect the SCS branch of Kuroshio westward (Farris and Wimbush, 1996; Li et al., 1998). The loop currents can generate shedding eddies that can propagate to the Taiwan Strait during strong winter monsoon and La Niña state of El Niño Southern Oscillation (ENSO) (Sun et al., 2020). The deep-water current entering the SCS through the Luzon Strait results in the SCS Contour Current circulation (Zhao et al., 2015; Liu Z.F. et al., 2016). The NW Luzon cyclonic gyre (3) and NW Luzon cyclonic eddies (4) are detachments of the Kuroshio current intrusion in NE SCS (Fang et al., 1998). The NW Luzon surface cyclonic circulation generates a northward NW Luzon coastal current (5) (Fang et al., 1998).

The Luzon Strait, with a depth of 2400 m is the only connection between the SCS and the western Pacific that allows intermediate and deep-water exchanges (Li and Qu 2006; Qu et al., 2006). A deep-water current inflows in the northern strait through the Bashi Channel and Taltung Canyon before entering the Luzon Through then turns westward (Lüdmann et al., 2005; Shao et al., 2007; Liu J. et al., 2010) and overflows in the northern SCS (1.5 Sv) (Zhao et al., 2014). A resulting cyclonic deep water current system exists in the SCS deep basin (Qu et al., 2004, 2006). A SCS contour current (8) (Qu et al., 2006) exists in the North SCS. It flows along the southern Taiwan margin and turns southwestward along the South China

margin (Qu et al., 2006; Zhao et al., 2014). In the south, the bottom current (9) flows southward with its path modified by the deep-sea mounts (Zhao et al., 2014). The SCS contour current then generates a deep cyclonic current circulation in the deeper central SCS basin along the South China continental margin (Qu et al., 2006; Wang et al., 2011). This inflow of water is accompanied by the eastward outflow of intermediate waters to the Pacific Ocean through the southern region of the strait (Yuan 2002; Tian et al., 2006; Gan et al., 2016; Zhu et al., 2019). The flow pattern in Luzon Strait is seasonally reversed (Yang et al., 2010; Xie et al., 2011; Zhu et al., 2019). At the SCS scale, the Pacific water inflow is compensated by the outflows occurring in Taiwan, Mindoro and Karimata Straits (Shaw and Chao, 1994; Dong et al., 2010).

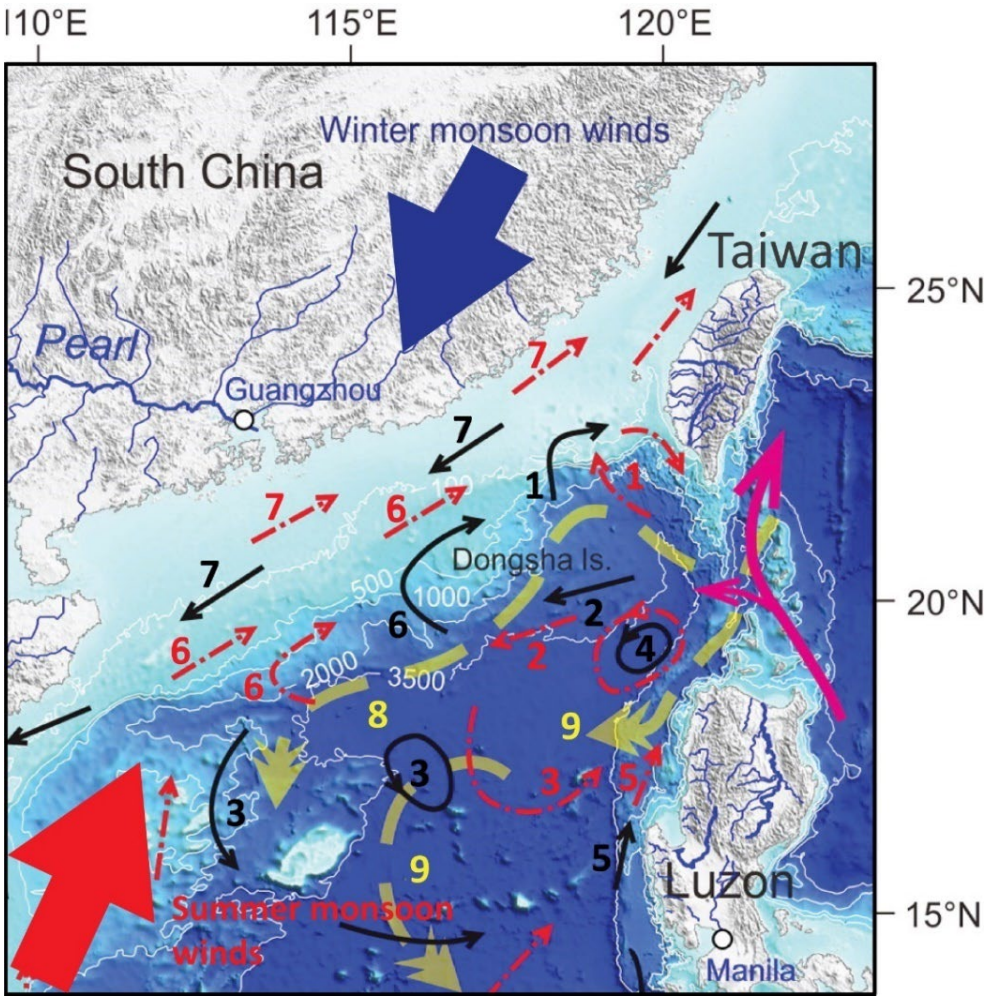

Figure 1-13. South China Sea oceanography: Sea surface current systems and monsoon winds, Pacific Ocean intrusion and deep-water circulation (Liu Z.F. et al., 2016)

The SCS circulation has been modified during the last Marine Isotopic Stages (MIS) by the climate, the sea-level fluctuations, and changes of land-sea configurations. During glacial

periods, sea level was lower than in present time. During the intervals of low-stand sea level, the huge (~390 million km²) shallow shelves (<100 m below sea level) were emerged (Wang et al., 1997) (2.13). Such a process results in the closure of the Taiwan Strait and the Karimata Strait and the hydrological exchanges with the East China Sea and the Java Sea (Fig. 2.13), water masses exchanges are limited in lowstand sea level.

Thus, Luzon Strait remained the only water passage to the Philippines Sea. Additionally, the Kuroshio pathway and intensity is modified by the climatic cooling (Wang and Wang, 1990). During Glacial periods (MIS2 and LGM), it has been shown that the Kuroshio current shifts eastward and is weakened suggesting that its intrusion into SCS is reduced (Ujiie et al., 1999, 2003; Kao et al., 2006 Zhang H. et al., 2016). The intrusion of the Kuroshio current through the Luzon Strait is significant during El Niño events (Shen et al., 2022). In this configuration, the monsoon winds are the dominant forcings of the surface circulation. The surface circulation consists mainly of the seasonal reversal of basin-wide anticyclonic (summer) and cyclonic (summer) gyres (1) (Fig. 1-14) with inflow of surface water through the northern Luzon Strait during the winter (Wang et al., 1995).

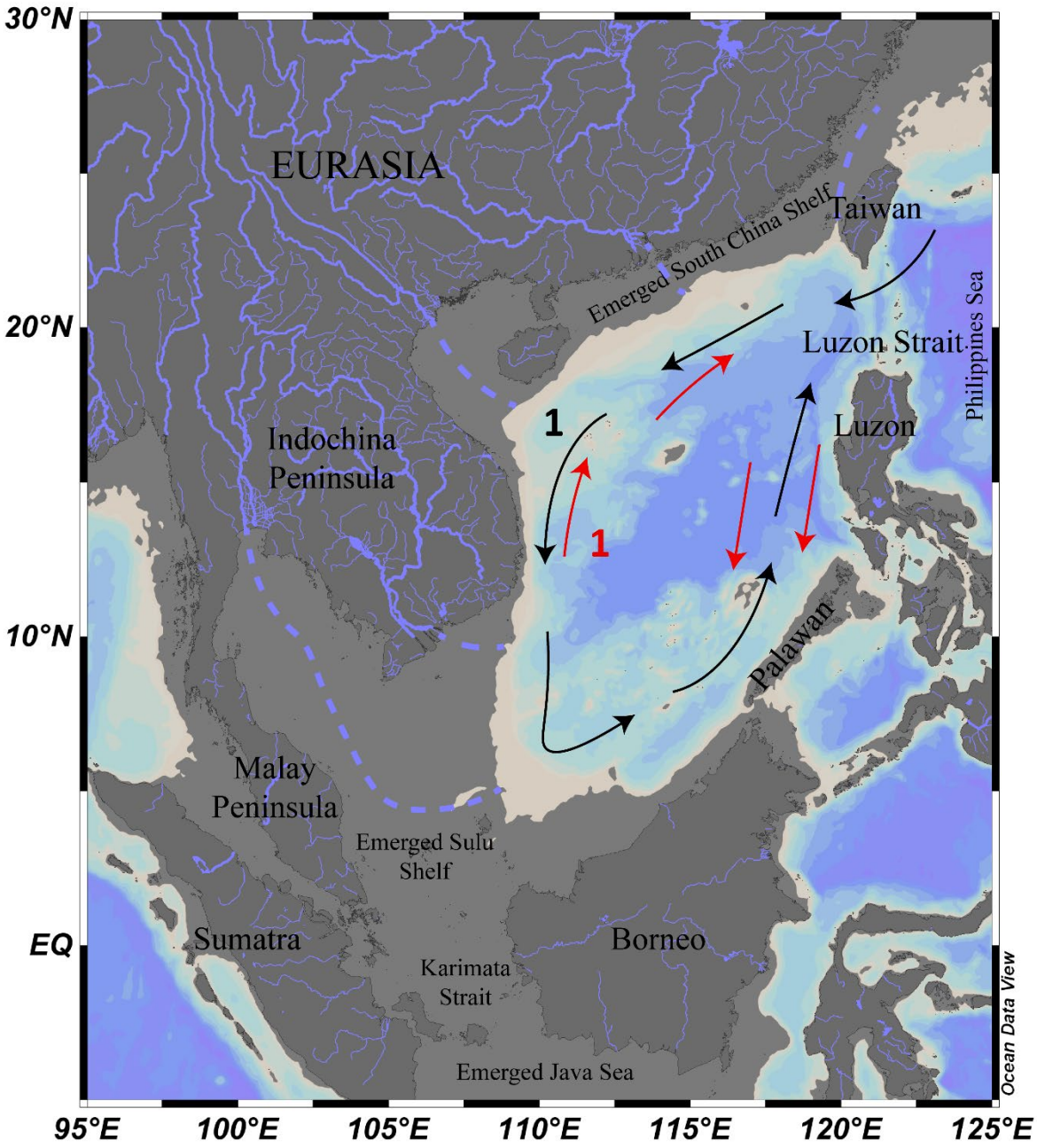

Figure 1-14. Paleogeography and simplified paleohydrology of the South China Sea during the Last Glacial Maximum. Dark grey color represents the present land masses configuration. The grey color represents the LGM land emerged according to the isobath of 100m modified from Liu Z.F. et al., 2016.

1.4.2 Present sediment transport and redistribution to the northern SCS

The northern SCS receives a significant amount of sediment from rivers draining the South China, Taiwan, and Luzon. The redistribution of the detrital material occurs following different processes due to the contrasting shelf morphologies and hydrological conditions.

The Pearl River discharges 107 Mt/yr of suspended kaolinite-rich sediments to the SCS through the South China Shelf and Slope. The long, wide, and well-developed South China Shelf is composed of about 50% of sediments derived from the Pearl River (Liu Z.F. et al., 2008). However, clay mineralogy of seafloor shows that the kaolinite is mainly limited to the coastal regions (Liu Z.F. et al., 2016). This results from the strong flocculation effect of kaolinite which causes the rapid sinking and deposition of the mineral near the river mouth (Xia et al., 2004). Most of the Pearl River sediments are distributed along the continental shelf and slope by the long-shore surface currents (Liu Z.F. et al., 2008). In general, the northern South China Slope is composed of about 30% of Pearl River-sourced sediments derived through the surface currents system. The Guangdong Coastal current transports the Pearl River-sourced sediments on the inner shelf, and South China Sea Warm Current transports the Taiwan-sourced sediments on the outer shelf (Jia et al., 2023). In summer, Pearl River's sediments are transported northward by the SCS Warm Current and Guangdong Coastal Current to the inner Taiwan Strait and the East China Sea. Inversely, in winter the reversed Guangdong Coastal Current transports southward the South China-sourced sediments. The reversed SCS Warm Current transport Taiwan-sourced sediments southward.

The redistribution of sediments from Luzon and Taiwan rivers is controlled by complex interactions between surface and deep current circulations (Liu Z.F. et al., 2008, 2016; Nayak et al., 2021). The sediments derived from Luzon are mainly dispersed in SCS by the westward surface circulation with a strong influence of the NW Luzon Coastal Current and the Kuroshio intrusion (Caruso et al., 2006; Wan et al., 2007; Liu Z.F. et al., 2008, 2016; Nayak et al., 2021). Thus, Luzon-sourced sediments can be transported and deposited on shelfs of Taiwan and South China. It has been shown that sediments derived from Luzon account for approximately 45% of the northern South China Slope (especially around Dongsha Islands Liu Z.F. et al., 2010a) and 20% of the northern South China Shelf sediments (Liu Z.F. et al., 2008).

A large amount of Taiwan-sourced sediments can be redistributed to deep basin by submarine canyons such as Gaoping Canyon and transported southward by the Bottom

Current (Shao et al., 2007, Liu Z.F. et al., 2010a) and on the South China Slope by the Contour Current induced by the North Pacific Deep Water intrusion (Lüdmann et al., 2005; Shao et al., 2007; Liu Z.F. et al., 2010a, 2016). In addition, Taiwan-sourced illite and chlorite are transported southwestward similarly to the Luzon sediments through the SCS Branch of Kuroshio (Liu Z.F. et al., 2010a, 2016; Nayak et al., 2021). Taiwan sediments contribute approximately to 30% of the northern South China Shelf and 23% of the northern South China Slope sediments (Liu Z.F. et al., 2010a).

1.4.3 Past fluvial sediments source-to-sink process in northern SCS

The source-to-sink processes affecting northern SCS are strongly influenced by the climatic and environmental conditions. Studies have shown that past climatic fluctuations and environmental changes have highly affected the sediment provenance and redistribution in the SCS at different time scales (Chen and Beaufort, 1998; Wang et al., 1999a, 1999b; Liu Z.F. et al., 2003, 2005, 2007a; 2010, 2016; Boulay et al., 2003, 2005, 2007, 2008; Clift et al., 2006, 2014; Wei et al., 2006; Hu et al., 2012; Huang T.H. et al., 2015, Huang et al., 2016; Li D. et al., 2014, 2017; Zhang et al., 2018).

The intensity of the SCS Contour Current appears to covary with the EASM intensity (Huang et al., 2011; Liu J. et al., 2016; Zhao et al., 2018). A strengthening of the Contour circulation has been recorded in the sediment drift located on the northern SCS Slope in the cold and drier intervals such as last glacial periods or Heinrich stadials. During these time intervals, the EASM was weakened (Sun et al., 2012; Wen et al., 2016; Zhang H. et al., 2016; Li N. et al., 2019). For example, during the Heinrich Event 1 (HS1), the formation of NPDW was enhanced (Basak et al., 2010; Okazaki et al., 2010) which increases the intrusion of deep Pacific water to SCS. The intense deep-sea circulation will enhance the redistribution of Taiwan-sourced sediments to the SCS slope and deep basin. When the SCS Contour Current intensity is weaker, as during strong EASM periods, the redistribution of Luzon-sourced sediment on the northern slope is enhanced compared to Taiwan-sourced sediment redistribution (Zhao et al., 2018).

The surface circulation of the northern SCS is strongly controlled by the climatic variations through the monsoon wind and Kuroshio intrusion. The monsoon forcing on the SCS surface circulation through the wind direction and seasonal reversal strongly controlled the redistribution of sediments in northern SCS in glacial and interglacial periods. In brief, during the interglacial periods, the northward direction of strong EASM winds driving the

northward flowing of the Guangdong Coastal Current is prone to enhance the transport of South China sediments northward on the South China shelf (Liu Z.F. et al., 2003, 2010a, 2010b, 2016; Boulay et al., 2005, 2007). Inversely, in glacial periods, the South China sediments are transported southward by the reversed Guangdong Coastal Current, and Luzon and Taiwan-sourced sediments transported by the surface Kuroshio intrusion are the dominant sediment deposited on northern SCS margins (Boulay et al., 2005, 2007; Liu Z.F. et al., 2010a, 2010b, 2016; Zhao et al., 2018; Nayak et al., 2021).

During low sea level stand and cold intervals, the Kuroshio Current intrusion intensity and pathway in SCS is strongly modified by the interaction of geographic setting and climatic conditions (ENSO, EAM, Pacific circulation; Sawada and Handa, 1998). The Kuroshio Current influence on the sedimentary dynamic was lower during the last glacial period when the EAWM was prevailing and El Niño-like conditions were weak (Liu J. et al., 2016; Zhang H. et al., 2016; Shen et al., 2022). With the weakened EAWM and enhanced El Niño-like conditions during the deglaciation, the Kuroshio Current intrusion was enhanced (Zhang H.et a., 2016; Shen et al., 2022) which favored the redistribution of sediments derived from Luzon and Taiwan. During the Holocene, the sea-level rise increased the influence of the Kuroshio Current in Taiwan and Luzon sediment redistribution and was combined with the prevailing El Niño-like conditions since middle-late Holocene (Liu J. et al., 2013, 2016; Zhang H. et al., 2016; Shen et al., 2022). However, the opening of the Taiwan Strait by the sea level rise and the formation of currents exchanging water with East China Sea affected the Kuroshio Current influence (Huang T.H., et al., 2015; Hsiung and Saito, 2017; Li et al., 2021). During spring El Niño events, the Kuroshio Current intrusion is strengthened and flows northward to the Taiwan Strait through the Penghu Canyon (Huang T.H., et al., 2015). Inversely, in winter the EAWM driven Taiwan Strait and Guangdong currents are reducing the Kuroshio influence and Taiwan and Luzon-derived sediments since middle Holocene (Huang T.H., et al., 2015; Hsiung and Saito, 2017; Li et al., 2021).

Chapter 2 Materials and methods

2.1 Study area

The Hydrosed campaign with the *R/V Marion Dufresne* in 2018 collected several Calypso cores on the south margin of Taiwan. In this study, we selected two cores, MD18-3569 and MD18-3574 located on the levee of the two main canyons, Penghu and Gaoping Canyons (Fig. 2-14). These two cores will bring new insight in the source to sink processes changes occurring in Taiwan during the late Quaternary.

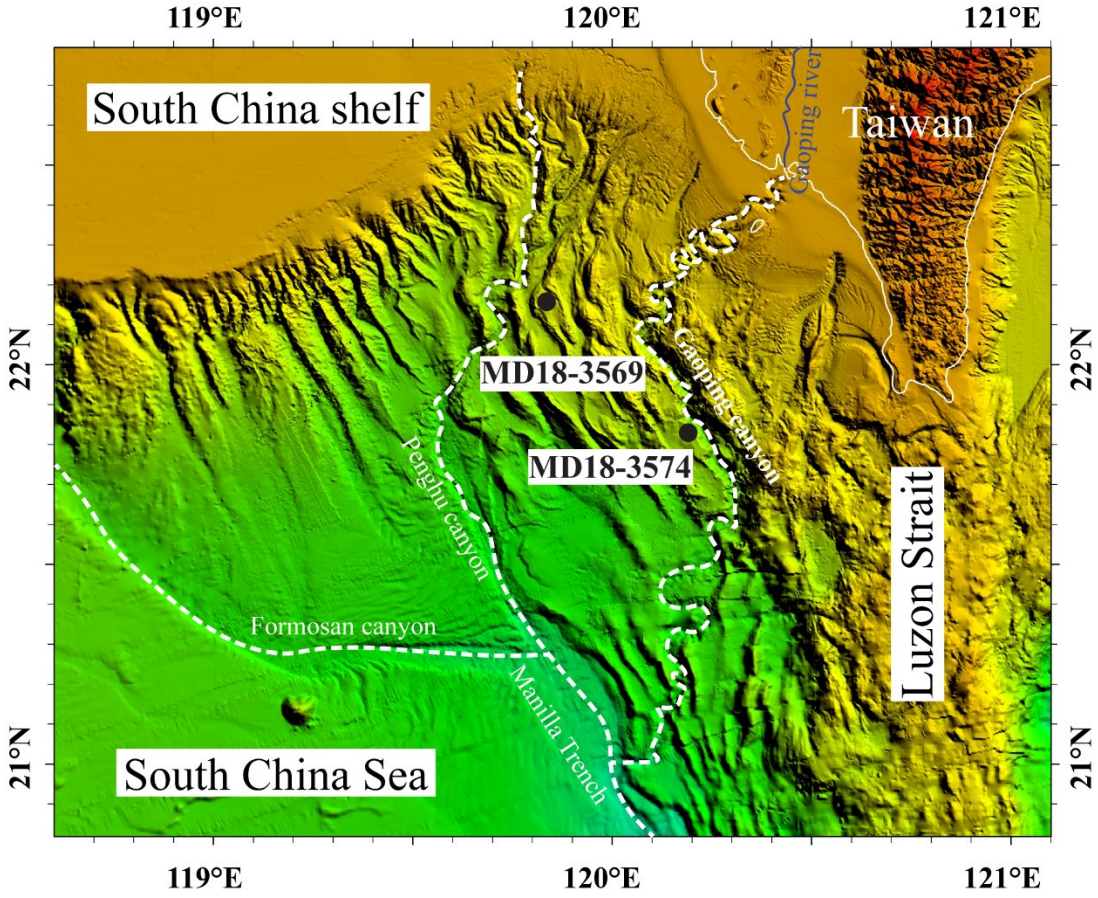

Figure 2-1. Bathymetric map of the northern SCS showing the locations of the cores MD18-3569 and MD18-3574 and the Manilla Trench system (Gaoping, Penghu and Formosan submarine canyons).

The different configurations of the two canyons allow us to study different processes and time-scales. The outcome of a study of the Gaoping Canyon will be the reconstruction of a turbidite record and the relationship between the turbidite, sediment transfer and climate

changes. While, the study of the Penghu Canyon can bring information on the impact of climate and environmental changes chemical weathering history of SW Taiwan, the possible connection of the canyon to rivers and the hydrodynamic changes related to sea level fluctuations.

Mineralogical, geochemical, sedimentological, and scanning methods will be applied to the two cores to study the sediment provenance, weathering and the dynamic of sediments redistribution from land to sea through submarine canyon and circulation (turbiditic current, surface, and deep-sea currents).

2.2 Studied cores and chronological framework

2.2.1 Core MD18-3569

The Calypso Core MD18-3569 was collected at the site HS8 (22°09.30'N; 119°49.24'E; water depth: 1315; 40.08 m long) on the eastern levee of the upper reach of the Penghu Canyon (Fig. 2.14). Core MD18-3569 is located at the southeastern bank of a meander of the Penghu Canyon at 600m of altitude above the canyon thalweg.

For this study, we have investigated the upper 15 m of this core. The upper 15 m are characterized by homogenous greenish gray hemipelagic sediments with no apparent visible turbidites covering 32 cal kyr BP (Fig. 2-2, Appendix 2-1, 2-2). Thus, the position of the core, 600 m of altitude above and far from the canyon thalweg, does not allow overspilling turbidity currents circulating on the Penghu Canyon to reaching this site. The sediments are mainly composted of clay and fine silt with presence of foraminifera from 15 to 8 m (Appendix 2-2). The absence of turbidites and their associated erosion surfaces indicates the Core MD18-3569 could provide a continuous record of the source-to-sink processes of SW Taiwan sediments and the influence of the surface circulation to the redistribution of sediments in northern SCS.

The age model of the upper 15 m of the Core MD18-3569 was established by using linear interpolation between the calibrated AMS ^{14}C dates obtained by Chen et al., 2021 on monospecific samples of *G.ruber* (>150 µm) (planktonic foraminifer). In addition, for this study, an additional ^{14}C date was obtained using *G.ruber* (>150 µm) at the Laboratoire des Sciences du Climat et de l'Environnement (LSCE, Gif-sur-Yvette). The record covers the last 31.4 kyrs, 31.348 cal kyr BP at 14.96 m and 0.703 cal kyr BP at 0.06 m) (Appendix 2-1).

The G.*ruber* $\delta^{18}O$ record of the upper 15 m was previously published by Chen et al., 2021. It displays glacial to Holocene variations with minimum values during the Holocene and maximum values during the glacial period (Chen et al., 2021) (Fig. 2-2). This record presents similar glacial-interglacial trends than LR04 benthic foraminifera $\delta^{18}O$ records and NGRIP H_2O $\delta^{18}O$ (Andersen et al., 2004; Lisiecki and Raymo, 2005). The average sedimentation rate of Core MD18-3569 is relatively high (54.7 cm/kyr). The sedimentation rate is low during LGM (between 34 and 39 cm/kyr) and increases during the deglaciation to 52 cm/kyr (Fig. 2-2). The sedimentation rate reaches the maximum value in the late Holocene after 4 cal kyr BP (73 cm/kyr) (Fig. 2-2). Thus, the analyses temporal resolution of the upper 15 m of core MD18-3569 is high (about 85 yrs). A sampling resolution of 5 cm from the upper 3 m is corresponding to a time resolution of ~62 yrs: 2.5 cm from 3 to 8 m corresponding to 76-100 yrs and 5 cm from 8 to 15 m corresponding to 93-144 yrs temporal resolution.

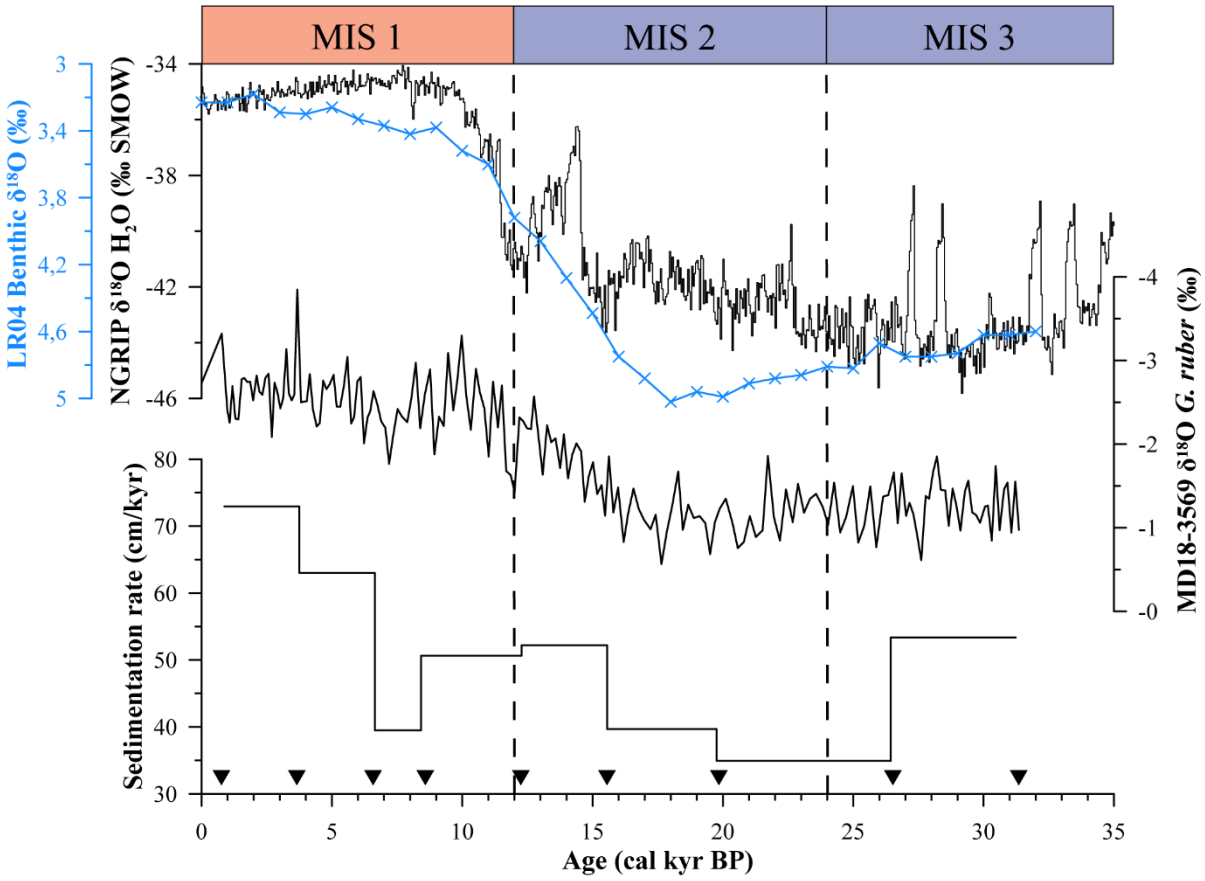

Figure 2-2 The age model of Core MD18-3569 was established based on accelerator mass spectrometry (AMS) 14C dates and oxygen isotope measurements of planktonic foraminifer *G. ruber* (Chen et al., 2021). Comparison with NGRIP and LR04 oxygen isotopic composition (Andersen et al., 2004; Lisiecki and Raymo, 2005)

A sampling resolution of 5 cm for the upper 3 m and 8 to 15 m and of 2.5 cm for the 3 to 8 m interval have been adopted. In total, 381 samples were collected to analyze the clay mineralogy, major elements, and laser grain-size. In addition, 33 samples were selected to measure the Nd and Sr isotopic compositions.

2.2.2 Core MD18-3574

The Core MD18-3574 was collected on the western levee of the Gaoping Canyon at the site HS14 (21°50.42'N 120°10.67'E; water depth: 1717 m). The coring site is located at 600m of altitude above the canyon thalweg (Fig. 2-1)

The core is 22.52 m long and characterized by dark greenish gray sediments showing numerous laminations with an alternance of light colored and dark colored millimetric levels (Appendix 2.3). The lithofacies of the Core MD18-3574 has been interpreted as the potential record of the turbidity currents activity occurring in the Gaoping Canyon. The laminations are more important in the interval from 8 to 22.52 m (Appendix 2-3).

Two scanning methods (XRF core scanning (1 mm to 1 cm resolution) and hyperspectral imaging (resolution of 150 µm), high resolution grain size of two sections (2mm resolution for 90 cm section) and the bulk mineralogy of 10 laminae have been processed to study the laminations and reconstruct the late Quaternary turbiditic activity of the Gaoping Canyon system.

Radiocarbon dating was undertaken at the UMS-ARTEMIS Facility (CNRS-CEA Saclay, France) using a Pelletron 3MV AMS on 8 mg of well-preserved calcareous test samples of planktonic foraminifera (plurispecific samples of *G. ruber*, *G. sacculifer, O. universa*) in the size fraction >150 µm (Appendix 2-4). The age model for the core was derived from the calibrated planktonic ages by applying a sea-surface reservoir ^{14}C correction of 400 yr and using Marine13 (Reimer et al., 2013) calibration curve in the CALIB 8.2 software (Stuiver and Reimer, 1993) (Fig. 2-3).

The ^{14}C dates range from 4.043 cal kyr BP at 22.47 m to 0.188 cal kyr BP at 0.55 m (Appendix 2-4). The age model of Core MD18-3569 has been established by using linear interpolation between eleven calibrated AMS ^{14}C dates processed with the Bacon package (Blaauw and Christen, 2011).

Regarding the small time-frame (4 kyrs), no stable oxygen isotopes were analyzed for Core MD18-3574. The average sedimentation rate of Core MD18-3574 is very high (5.6

mm/yr). This allows us to obtain a very high temporal resolution of analyses and turbiditic record during the late Holocene.

The mean sedimentation rate of Core MD18-3574 is very high (0.56 cm/yr), allowing us to obtain a high temporal resolution of analyses during the last 4 cal kyr BP (Fig 2-3). The sedimentation rate is very high in time intervals between 4.043 and 2.216 cal kyr BP (in average 0.68 cm/yr) and from 0.347 to 0.188 cal kyr BP to present time (0.79 cm/yr) (Fig. 2-3). The linear sedimentation rate displays a decreasing trend during the last 4 cal kyr BP (Fig. 2-3).

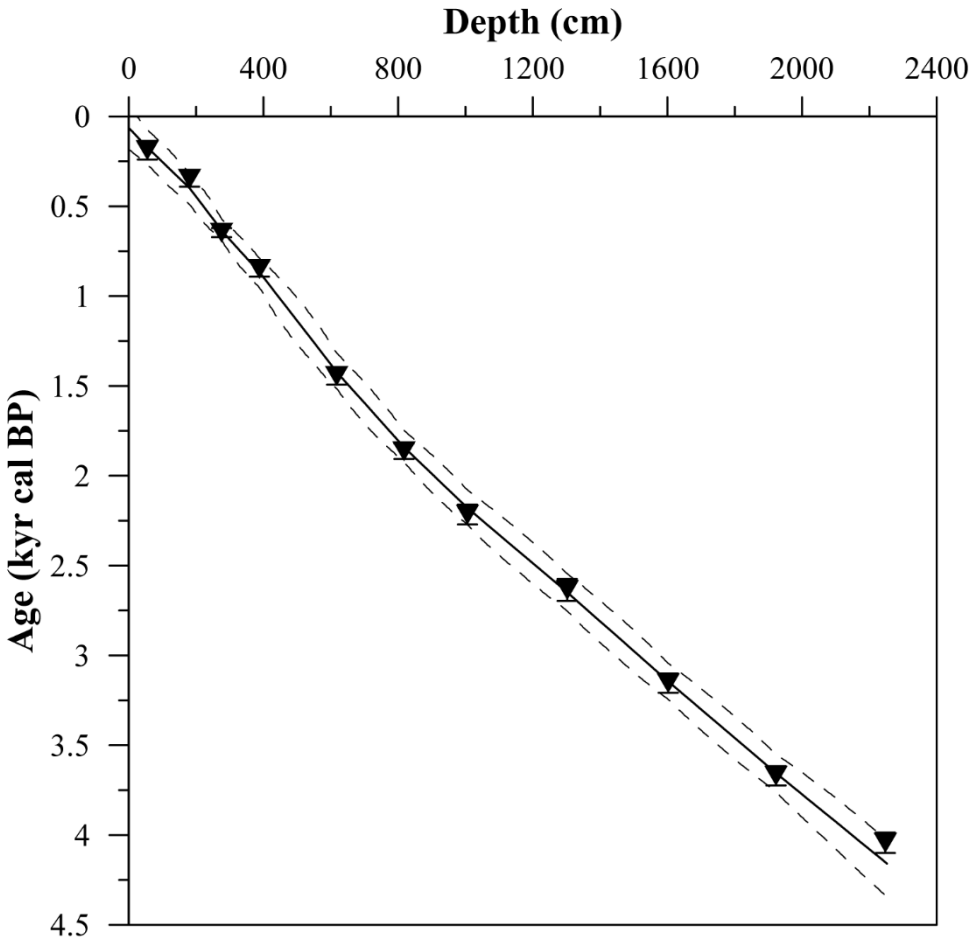

Figure 2-3. Chronological framework of the Core MD18-3574. The age model was established using 11 accelerator mass spectrometry (AMS) 14C dating of plurispecific plnktonic foraminifera G. ruber, G. sacculifer, O. universa, calibrated following (Stuiver and Reimer, 1993; Reimer et al., 2013).

2.3 Methods

2.3.1 Carbonate content

Calcium carbonate content ($CaCO_3$%) of the Core MD18-3569 was analyzed on 187 samples at the *State Key Laboratory of Marine Geology, Tongji University*, at a resolution of 5 cm in the upper 6 m, then 10 cm from 6 to 10 m and 20 cm in the lower 5 m of the record. $CaCO_3$% was analyzed using the gasometric techniques from Jones and Kaiteris (1983) with a precision higher than ±1%.

The analysis technique is based on the following reaction (1)

(1) $CaCO_3\% + 2\ HCl \rightarrow CO2 + H_2O + CaCl_2$

First, a standard curve of PCO_2 was established after the CO_2 pressure (pCO_2) (bar) resulting from the reaction of HCl and 0.01, 0.02, 0.03, 0.04, 0.05, 0.06, 0.07, 0.08, 0.09 ± 0.001g (and later a measurement of 0.09 ± 0.001g every 30 samples) in a vacuum receptacle with a CO_2 gauge (Fig. 2-4, Appendix 2-5). Analyses are then performed on 0.1g of sediment.

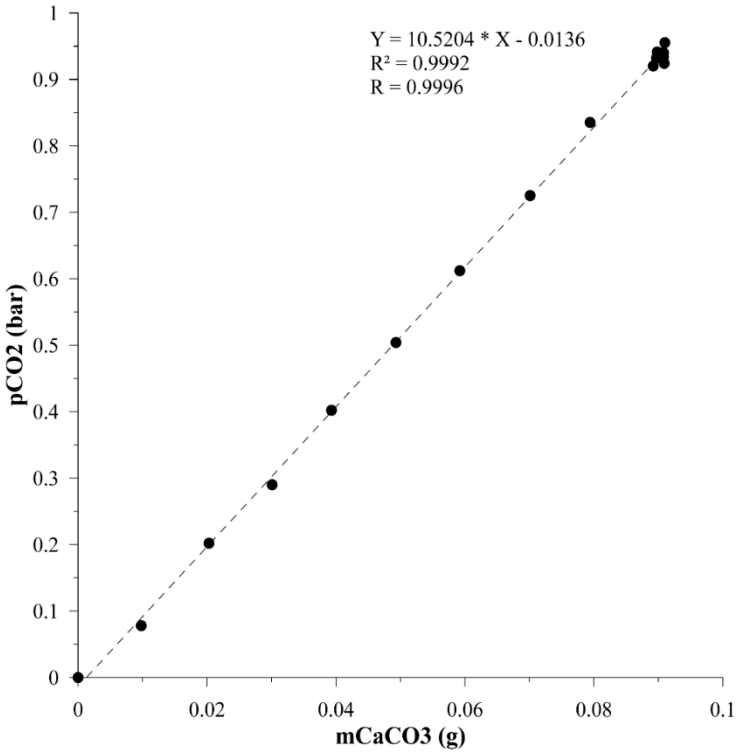

Figure 2-4. Standard calibration line of the pCO2 emitted by the dissolution of CaCO3 by HCl

2.3.2 Clay mineralogy

The clay mineralogy of Core MD18-3569 was analyzed with X-ray diffraction (XRD) on 381 samples at the *State Key Laboratory of Marine Geology, Tongji University*, in order to trace sediments provenance variation during the last 32 kyr following the procedure described by Liu et al. (2004) (Appendix 2-5).

Samples were first dehydrated in oven for 24h at 40°C in order to facilitate their dislocation in deionized water. Samples were put in suspension with deionized water and 10 ml of 0.5% hydrochloric acid (HCl) to dissolve the carbonates. The solution was stirred for 30 minutes with a magnetic agitator. The pH of the solution was then checked, if the pH was still acidic then the next step was continued. If pH was too basic, then HCl was added and the reaction ongoing until pH stays acid. After 10 minutes, the magnetic agitator was removed, and the solution container was filled with deionized water. Samples were then rinsed with deionized water several times until the water remained cloudy.

The organic matter was removed by adding 10 ml of 10% H_2O_2. The organic matter removal reaction occurred during 4 to 5 days. The solution was stirred gently every day until the absence of bubbles was noted. An additional 10% H_2O_2 was then added to verify that all the organic matter has been removed.

Then the water was changed similarly to the decarbonation for several days.

After stirring the solution and a wait of 1 h 35 minutes, the clay fraction (<2 μm) was collected using a syringe by extracting the upper 2 cm of the solution, following the Stokes' law ($v = \frac{2r^2 * \Delta d * g}{9\eta}$). The extracted clay fraction was stored in centrifuge tube and later centrifugated to remove excess water. Then, thin sections of oriented mounts were prepared. XRD measurements were performed with a a PANalytical X'Pert PRO diffractometer with a CuKα radiation and Ni filter, under a voltage of 45 kV and an intensity of 40 mA, an angle range from 3 to 29.9887 θ at a speed of 1°/min, and divergence silt of 0.38 mm, on air dried (1), saturated with ethylene glycol under vacuum for 24h (2) and heated at 490°C for 2h (3). Smectite is dilated by ethylene glycol allowing its identification. The samples were heated at 490°C in order to destabilize the structure of kaolinite without affecting the crystals of the other minerals (Roy, 1949; Grim, 1968).

The semi-quantitative estimation of the main four clay mineral groups was carried out on the ethylene glycol saturated samples diffractogram using MacDiff software by analyzing the

peak areas of the baseline for: smectite: 15–17 Å, including smectites and interstratified minerals (in the following discussion the term smectite refers to smectites and interstratified minerals); illite: 10 Å; and kaolinite/chlorite: 7 Å. The chlorite and kaolinite were distinguished using the 3.57/3.54 Å peak areas. The clay minerals contents were calculated with the following equations:

$$\Sigma = Sm1\,(15 - 17\ \text{Å}) + Ill1\,(10\ \text{Å}) + (Kaol1 + Chl2\,(7\ \text{Å}))$$

$$Smectite\% = \frac{Sm1}{\Sigma} * 100$$

$$Chlorite\% = \left(\frac{Chl4\,(3.57\ \text{Å})}{Chl4\,(3.57\ \text{Å}) + Kaol2(3.54\ \text{Å})} * \frac{Kaol1+Chl2}{\Sigma}\right) * 100$$

$$Kaolinite\% = \left(\frac{Kaol2}{Chl4 + Kaol2} * \frac{Kaol1+Chl2}{\Sigma}\right) * 100$$

$$Illite\% = \frac{Ill1}{\Sigma} * 100$$

The analyses were replicated leading to a relative error of ±5% (2σ).

Illite chemistry index was calculated using the 10 Å /5 Å peak areas. An illite chemistry index lower than 0.5 corresponds to illite produced under strong physical erosion like in Taiwan (Fe-Mg-rich), and higher than 0.5 correspond to illite produced under strong hydrolysis conditions (Al-rich) as in South China (Hu et al., 2014). The illite chemistry index was calculated as the ratio of the 5 Å and 10 Å illite peak areas (Esquevin, 1969). The illite chemistry index (Esquevin, 1969) has been used to estimate sediment weathering state (Liu Z.F. et al., 2007b, 2007c; Colin et al., 2010) and to constrain sedimentary sources (Gingele, 1996; Lamy et al., 1999; Ehrmann et al., 2007; Liu Z.F. et al., 2010). In general, low values of the illite chemistry indices correspond to Fe-Mg-rich illite, while high values correspond to Al-rich illite (Esquevin, 1969; Petschick et al., 1996; Liu Z.F. et al., 2012).

Illite crystallinity was calculated using the full-width at half-maximum value (FWHM) of the 10 Å illite peak. A low illite crystallinity indicates high crystallinity due to weak hydrolysis conditions corresponding to strong erosion such as Taiwan, while high illite crystallinity value indicates warm and humid climate with strong hydrolysis conditions such as in South China (Hu et al., 2014).

2.3.3 Bulk mineralogy

The bulk mineralogy analyses were performed on ten level samples of Core MD18-3574 (five dark and five light laminae) at the State Key Laboratory of Marine Geology, Tongji University, in order to distinguish the lithofacies mineralogy.

The samples were first dehydrated and later pre-grinded with an agate mortar. 0.5 to 1g of pre-grinded sediments were grinded finely (<1 μm) using a with agate balls and ethanol three times for 1 minute and 30 seconds.

The samples were dried and prepared in slides for the XRD analysis. The bulk mineralogy was then analyzed using a PANalytical X'Pert PRO diffractometer.

As the ethanol could have affected the smectite during the fine grinding process. The samples have been put in suspension in 1M CaCl2 to saturate the sample in calcium and reconstitute the peak of smectite (001) at 15 Å. Then, the samples were prepared in XRD slides again and the bulk mineralogy was analyzed a second time. Eventually the natural and calcium saturated samples were compared to reveal the presence or absence of smectite.

The samples' diffractometers have been treated using the open-source software Profex to identify the minerals.

2.3.4 Major elements concentrations analyses

The bulk elemental composition analysis was performed on 381 samples at the *State Key Laboratory of Marine Geology, Tongji University*.

First the samples were dehydrated in an oven at 40°C for 24h and grinded finely with an agate mortar.

The grinded samples were put in suspension with deionized water in centrifuge in order to wash the sea salt (Appendix 2-6). The solution was stirred firmly to put all the sediments in suspension then settled for 2h. The samples were then centrifuged, and the supernatant water was removed. This step was repeated three times to remove as much sea salt as possible. In result, the sodium value will be the terrigenous sodium.

Then, the samples were collected and dehydrated in an oven for 24h and grinded finely a second time with the agate mortar. Once dried, pressed pellet tablets were prepared for analysis. 3.5g of dried sediment was placed in a metallic cylinder contained in a larger metal container. Boric acid was added to the periphery of the cylinder and over the sediments to seal

the sample. The cylinder was removed, the container capped and placed under a hydraulic press machine to consolidate the pellet tablet.

In addition to the samples, three tablets of standards GDS-15, GSD-16 and GSR-6 were prepared. The standards were analyzed every 20 samples to control the analyses precision and are resulting in an average standard deviation of less than ±2%.

The sample tablets were analyzed using X-ray fluorescence (XRF) on a *PANalytical Axios spectrometer*. The major elements (SiO_2, Al_2O_3, Fe_2O_3, K_2O, CaO, MgO, Na_2O) are expressed as their oxides forms in percentage (%) as the absolute content of bulk samples.

In this study, since carbonates were not previously removed, the calcium oxide (CaO) have been calibrated with P and Na oxides molar content (Singh et al., 2005; Sang et al., 2018; Jiwarungrueangkul et al., 2019) to obtain calcium from the carbonate-free fraction (expressed as CaO*).

2.3.5 XRF core scanning

The relative geochemical composition of Core MD18-3574 was analyzed using XRF core scanning methods at two different resolutions.

Firstly, the relative geochemical composition was analyzed at the resolution of 1 mm using an Itrax XRF core scanner at the Second Institute of Oceanography, Ministry of Natural Resources of the People's Republic of China (Hangzhou) to constrain the relative geochemical composition variations at the scale of the lamina.

The sediment core surface was cleaned, flattened, and smoothed to avoid disturbances. The center of the sediment surface was covered with a Ultralene film (4 µm thick).

The Itrax XRF core scanner parameters were set to 60kV and 45 mA with an exposure time of 10 seconds.

The XRF core scanner results are relative geochemical compositions. The elemental composition is expressed in counts per second (cps).

Then, the Core MD18-3574 was scanned at the resolution of the centimeter at the State Key Laboratory of Marine Geology, Tongji University, using an Avaatech XRF core scanner in order to provide robust results for elements requiring longer exposition (e.g. Si, Al or Br). The sediment core was prepared similarly to the 1 mm resolution analyses. The Avvatech XRF core scanner parameters were set to 10 kV and 0.2 mA (covering Al to Fe), 30 kV and

0.8 mA (covering Co to Mo) and 50 kv and 0.2 mA (covering Tc to U) with an exposure time of 30 seconds.

2.3.6 Hyperspectral imaging

The hyperspectral imaging of Core MD18-3574 was processed at M2C laboratory, Université Rouen-Normandie, using two hyperspectral camera sensors covering the Visible and Near InfraRed (VNIR) and Short Wave-InfraRed (SWIR) spectral range, from 400 to 2500 nm.

The data were collected following the hyperspectral images acquisition protocols from Butz et al., (2015) and Jacq et al., (2020, 2022a).

First the sediment core surface was cleaned, smoothed, and flattened as much as possible to reveal the sedimentary structures masked by oxidation and eliminate sediment surface variations that could distort the signal.

The camera sensors were calibrated using calibration table, illumination unit and modifying the camera height to obtain relevant VNIR and SWIR images at high resolution (VNIR pixel size: 40-200 µm; SWIR pixel size: 150-500µm) (Fig. 2-5). The black (shutter closing, instrumental noise, 0% reflectance) and white (white spectra reference, 100% reflectance) spectra references were recorded to normalize sediments spectra in percentage of reflectance. The camera focus and parameters (integration time, frame rate) were set to optimize the recording to obtain a sharp and focused image.

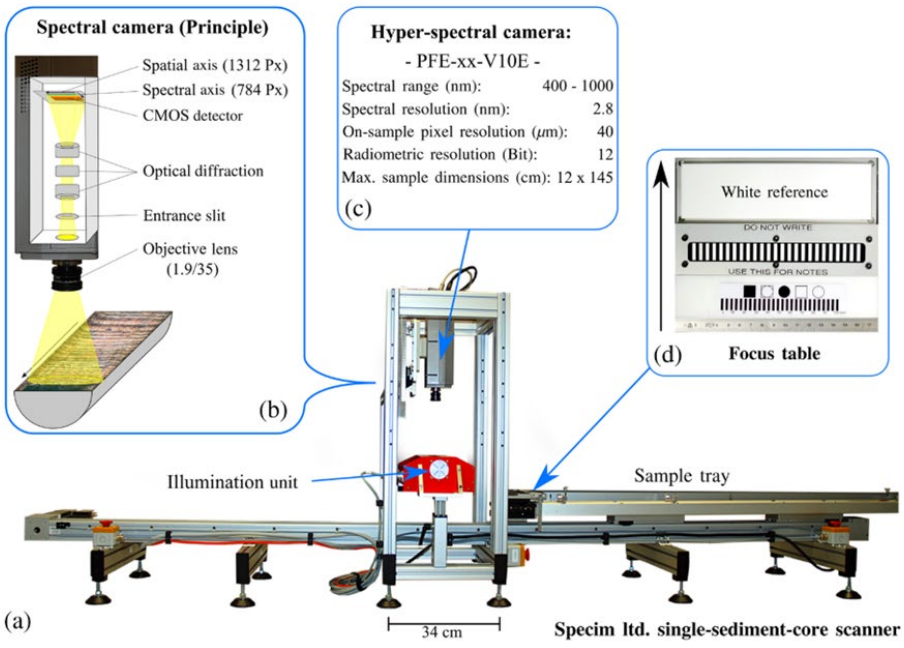

Figure 2-5. Analytic protocle and principles of hyperspectral imaging (Butz et al., 2015)

Once the camera was set, the reflectance spectra was recorded and detrended (black and white) to normalize the spectra from the baseline following Jacq et al., (2020, 2022a, 2022b).

The appendix 2-7 presents the different indices used in this study, their sensor, specific wavelength ranges and their significance (Viscarra Rossel and Behrens, 2010; Krupnik and Khan, 2019). All the indices were normalized using the Rmean (Appendix 2-7) of each camera sensor (Rmean VNIR and Rmean SWIR) to reduce the sediment matrix effect on the reflectance.

2.3.7 Laser grain size

The grain size analyses were conducted at the *State Key Laboratory of Marine Geology, Tongji University* using a *Beckman-Coulter LS230* with a particle size range of 0.02 to 2000 µm. The analyses were processed on bulk siliciclastic sediments (1) of 381 samples of Core MD18-3569 and bulk siliciclastic sediments (1) and carbonate free-sediments (2) 450 samples of Core MD18-3574 (Appendix 2-8).

(1) 0.5g of sediments were first dehydrated in an oven for 24h at 40°C to facilitate the dislocation of the samples. The samples were then put in suspension with ±20 ml of deionized water in 150 ml beakers. Organic matter was removed adding 5 ml of 10% H_2O_2. The sample was shaken gently for 4 to 5 days. Samples were then rinsed with deionized water three times.

(2) Similarly, to the bulk siliciclastic sediments, prior to the decarbonation the organic matter was removed. The sediments were decarbonated using 0.5% HCl. After the decarbonation, the HCl residues were then rinsed with deionized water three times.

The solution was then stirred, collected, and poured in the water container of the Beckman-Coulter LS230 to process the grain size analyses. The analyses consist of two acquisitions. The second acquisition is usually more stable than the first. So, the second acquisition was selected to represent the grain size of the sample.

2.3.8 Nd and Sr isotopic composition

Nd and Sr isotopic compositions were analyzed on 33 samples of the Core MD18-3569 on both clay fractions (<2 µm) and bulk siliciclastic sediments.

Clay fraction was extracted following the same analytical protocol as for the XRD clay mineralogical measurements. The bulk siliciclastic sediments were analyzed after decarbonation, with 20% acetic acid, and organic matter removal, with H_2O_2. After these two

steps, the samples were washed three times with Milli-Q water and centrifuged. The detailed separation protocol is reported in Appendix 2-9

Samples were first dissolved in HF-$HClO_4$ and HNO_3-HCl mixtures. Once the dissolution was completed, the solution was evaporated (Appendix 210).

A sequential ion chromatographic purification procedure was used to separate the Sr and the Nd.

First, the AG 50W-X8 resin was used to separate the Sr from REEs (Appendix 2-9-1). After preparing the resin, the samples were dissolved with 1.5 ml of 1 N HCl and introduced in the resin. The major and trace elements (at the exception of REEs) were eluted from the solution, first 35ml of 2N HCl before collecting Sr, then 27 ml of 2.5 N HNO_3. REEs were collected using 35 ml of 2.5N HNO_3.

The solutions containing the Sr and the REE were dried for the next steps The Sr fraction was purified in a 20 µl Sr-spec column (a polyethylene syringe with 4 mm Ø millex filter (Colin et al., 1999). The Sr sample was dissolved again using 400 µl of 4N HNO_3 and introduced in prepared Sr-spec resin for purification (Appendix 2-9-2). The resin was washed using 4N HNO_3 and Sr was eluted with Milli-Q water (Appendix 2-11).

The Nd was purified and collected from the REEs solution by using Ln-spec resin following the procedure described by Copard et al., (2010) (Appendix 2-12). The REEs solution was dissolved using 1 ml of 0.05 N HNO_3 and introduced in the Tru and Ln-Spec. The REEs were eluted, and the purified Nd was collected with 0.25 N HCl (Appendix 2-9-3).

Sr and Nd isotopic compositions were measured using a Thermo Scientific Multi-Collector Induced Coupled Plasma Mass Spectrometer (MC-ICP-MS *NEPTUNE^{Plus}*) hosted at the *Laboratoire des Sciences du Climat et de l'Environnement (LSCE)*, Gif-sur-Yvette (France). For the Sr and Nd isotope analyses. sample and standard concentrations were matched at 20 ppb. During the analytical sessions, every group of three samples was bracketed with analyses of appropriate Sr standard solution NIST SRM987 ($^{87}Sr/^{86}Sr \approx 0.710250 \pm 000016$) and Nd standard solution JNdi-1 ($^{143}Nd/^{144}Nd \approx 0.512115 \pm 0.000006$) (Lugmair et al., 1983; Tanaka et al., 2000). The Sr and Nd isotope ratios were corrected from mass bias according to the exponential law relative to $^{146}Nd/^{144}Nd = 0.7219$ and $^{86}Sr/^{84}Sr = 0.1194$. The analytical errors for each sample analysis were taken as the external reproducibility of the JNdi-1 or NIST SRM987 standards or unless the internal error

was larger. For convenience, Nd isotopic compositions are expressed as $\varepsilon_{Nd}(0) = [(^{143}Nd/^{144}Nd)_{sample}/(^{143}Nd/^{144}Nd)_{CHUR}-1]x10000$, with the present-day $(^{143}Nd/^{144}Nd)_{CHUR}$ of 0.512638 (Jacobsen & Wasserburg, 1980).

Chapter 3 Variations of sedimentation of the SW Taiwan margin since the last glacial maximum in link with climatic and environmental forcings

Abstract

Many scientific studies have been conducted over the past decades to constrain present and past source-to-sink processes and their controlling factors. In this context, the role of typhoon activity and monsoon rainfall on chemical weathering and soil erosion of the low latitude region is still not well established. Clay minerals and major elements, combined with Nd and Sr isotopic compositions of carbonate-free detrital bulk and clay-size (<2 μm) fractions, were analyzed on sediments from Core MD18-3569 located on the SW Taiwan margin in the northeastern South China Sea. The aim was to reconstruct the weathering history of small river basins of SW Taiwan and to establish the impact of East Asian summer monsoon (EASM) and typhoon rainfall as well as sea level changes on source to sink processes since the last glacial period. $^{87}Sr/^{86}Sr$ (0.7187 to 0.7213) and εNd values (from -11.6 to -10.9) combined with a predominance of illite (45-59%) and chlorite (27-39%) indicate that the river basins of SW Taiwan have remained the sole source of sediments to Core MD18-3569 over the past 32 kyr. Variations in clay mineral assemblages (smectite/(illite+chlorite) and kaolinite/(illite+chlorite)) and major elements (chemical index of alteration (CIA) and Al_2O_3/Na_2O) allow us to evaluate the intensity of past weathering in the river basins of SW Taiwan. We have thus demonstrated that long-term changes in the chemical weathering intensity record of SW Taiwan are mainly driven by changes in EASM rainfall. The time interval between 18 and 9 cal kyr BP is characterized by a progressive increase in the intensity of chemical weathering, which reached a maximum at the beginning of the Holocene (from 11 to 9 cal kyr BP). The degree of chemical weathering of sediments transferred to the South China Sea decreases during the middle and late Holocene in agreement with a weakening of the EASM, an increase in typhoon activity, and a change in the vegetation cover manifested by a drop in tree pollen and a higher proportion of herbs. All these processes induce soil destabilization, erosion, regressive pedogenesis, and transfer of detrital material that is less chemically weathered (lower CIA value and Al_2O_3/Na_2O ratio) due to a shorter residence time of minerals in the soils of SW Taiwan.

Key words: clay minerals, major elements, Nd and Sr isotopes, weathering, East Asian monsoon, SW Taiwan.

3.1 Introduction

Taiwan Island is characterized by one of the highest rates of tectonic uplift in the world (up to ~20 mm/yr, Ching et al., 2011) and is under the East Asian summer monsoon (EASM) and typhoon-driven precipitation regimes. This contributes to the transfer of large amounts of sediment directly to the East Asian marginal seas through several submarine canyons (e.g., the Gaoping and Penghu Canyons). EASM is a regional feature of the global monsoon system, which are controlled by precessional changes in solar insolation on global and long-term scales (Braconnot et al., 2008; An et al., 2015; Wang et al., 2017). The regional monsoons respond to regional forcings and have diverse behaviors at shorter timescales. Because of East Asia land-sea configuration (Tibetan Plateau, Indian and Pacific Oceans), the EASM is considered the strongest and largest monsoon system (An et al., 2015). Marine sediments collected on the East Asian margins, therefore, constitute an ideal archive for investigating the intensity of past chemical and physical weathering through time at a high temporal resolution and with respect to various local, regional and global forcings (e.g., climatic, anthropic).

During the late Quaternary, changes in EASM rainfall and typhoon frequency could have resulted in variations in the sediment budget delivered by a number of rivers to the northeastern South China Sea (SCS) from South China, Taiwan, and Luzon (Moy et al., 2002; Clift and Sun, 2006; Lei et al., 2015; Wang et al., 2015; Zhang Y et al., 2018; Zhao et al., 2018; Hu et al., 2020). On orbital timescales, paleoclimatic reconstructions suggest that temporal intervals characterized by a reinforcement of EASM rainfall are associated with an increase in soil alteration, runoff, and transfer of sediments from large Asian rivers to the ocean (Boulay et al., 2005; Xue et al., 2005; Colin et al., 2010; Liu Z.F. et al., 2016; Gebregiorgis et al., 2016). Such climatic variations are associated with changes in the sources and transportation of sediments delivered to the SCS (Liu Z.F. et al., 2016) and are recorded by variations in clay mineral assemblages and geochemistry of the sediments deposited in the SCS (e.g., Boulay et al., 2005; Colin et al., 2010; Liu Z.F. et al., 2016).

Previous studies of terrigenous fractions from cores collected in the SCS have indicated a strong link between sea-level variation, monsoon rainfall, and geochemical and mineralogical variations on different time scales, e.g., million-year (Boulay et al., 2007; Yu et al., 2016), orbital (Boulay et al., 2005; Colin et al., 2010; Liu et al., 2016), and millennial scales (Zhao et

al., 2018). All these results suggest that the supply of sediments by Asian rivers and the hydrology of the SCS were strongly reactive to past changes in monsoon rainfall and sea-level.

However, consensus has yet been reached regarding the relationship between precipitation and chemical weathering. Several previous studies have shown that enhanced silicate chemical weathering occurred in large river basins during warm, humid periods of the late Quaternary (Chen et al., 2016; Miriyala et al., 2017; Sang et al., 2022). In contrast, an intensification of monsoon rainfall has also been linked to a reduction in the residence time of sediments in river basins, like those of Taiwan, and thus to a weakening of chemical weathering (Dosseto et al., 2010; Bi et al., 2015; Dou et al., 2016; Zhao et al., 2017). In recent years, much attention has focused on chemical weathering and erosion of soils and rocks in tropical regions and their link to climatic and environmental changes or human activities; this is because understanding soils and "critical zones" are pressing issues for our societies (Brantley et al., 2007; Latour, 2014; Adhikari and Hartemink, 2016). Present-day changes have been studied with the development of monitoring observatories (Brantley et al., 2017; Gaillardet et al., 2018). Such results demonstrated that the paleo-soils of small mountain rivers, comparable to the SW Taiwan river system, are strongly controlled by climatic and tectonic changes (Arnaud et al., 2012; Sun and Colin, 2014; Bajard et al., 2016, 2017a, 2017b) and by human activities (Sabatier et al., 2014). The history of the state of pedogenesis in critical zones can be deduced from clay mineralogical, geochemical, and palynological variations in sedimentary records such as those from lakes or watersheds. The formation of soils during progressive pedogenesis results in the leaching of more mobile elements and influences the production of clay minerals. The vegetation of small river basins is also very sensitive to the level of soil maturity and pedogenesis; weathered soils are favorable for the installation of stable cover such as forests and trees (Sun and Colin, 2014; Bajard et al., 2016). Inversely, during regressive pedogenesis the erosion of soil leads to the production of illite (Sun and Colin, 2014), the transfer of mobile element-enriched sediments (Arnaud et al., 2012, Bajard et al., 2017a, 2017b), and the replacement of trees by herbs (Sun and Colin, 2014; Bajard et al., 2016).

Deep-sea sediments from the southwestern margin of Taiwan have great potential for reconstructing a continuous record of past weathering of SW Taiwan since the last glacial period. SW Taiwan has a particular land-sea configuration, with a narrow shelf and numerous submarine canyons, such as the Gaoping and Penghu Canyons, which facilitate the rapid

transport of sediments from Taiwan rivers to the deep-basin via turbidity currents (Milliman et al., 1992; Liu J.P. et al., 2008; Zhang et al., 2018). The Gaoping Canyon is connected to the Gaoping River mouth and sediments are transported directly by hyperpycnal and turbidity flows that are strongly dependent on typhoon events and, to a lesser extent, on earthquakes in the region (Liu J.T. et al., 2016; Zhang et al., 2018). At the present time, the Penghu Canyon is not directly connected to any river mouth but might have been connected, through the Penghu Channel, to SW Taiwan rivers during glacial low sea level intervals. Sediments transported by these canyons have been partially redistributed along the SW Taiwan margin by Pacific Deep Water (PDW) currents, which enter the SCS through the Luzon Strait (Fig. 3-1).

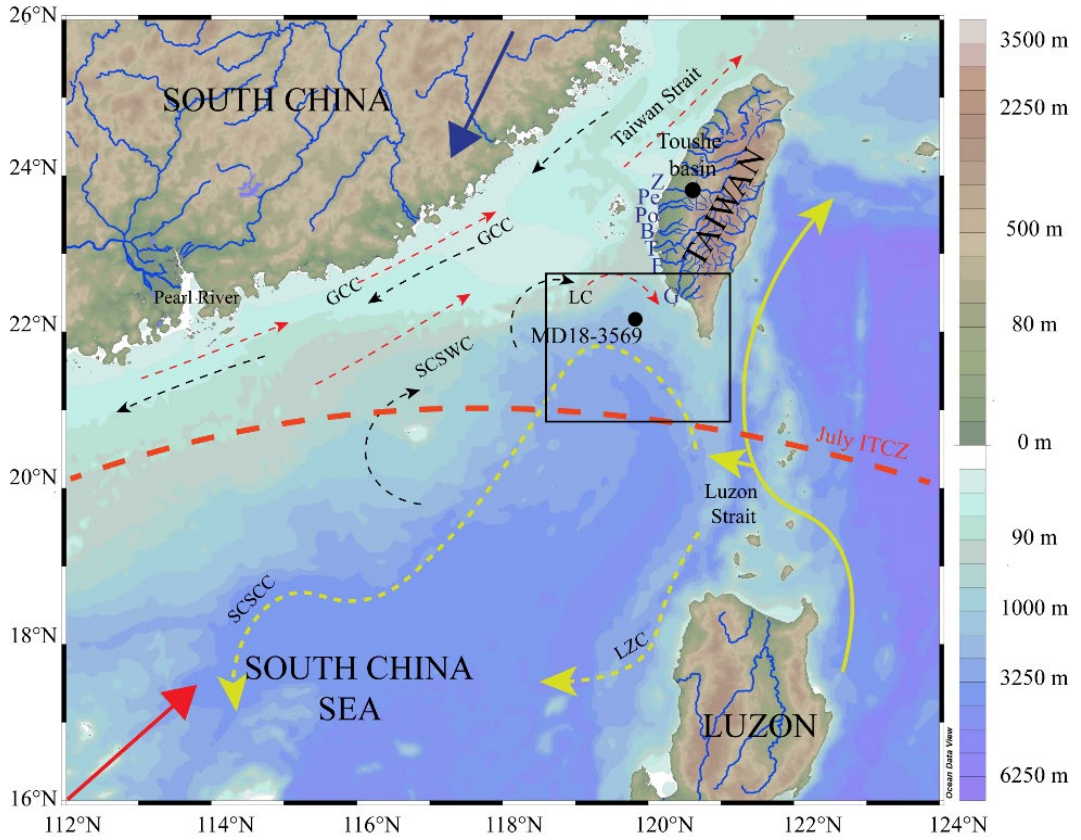

Figure 3-1. Bathymetric map of the northeastern SCS showing the location of Core MD18-3569. The location of the Toushe basin discussed in this study is also indicated. Main surface- and deep-current patterns (LZC: Luzon deep current; SCSCC: SCS contour current; SCSWC: SCS warm current; LC: Loop current; GCC: Guangdong coastal current) (Liu et al., 2016), southern limit of July intertropical convergence zone (ITCZ) and winter and summer monsoon wind directions are reported (Webster, 1994; Wang et al., 2003). The SW Taiwan

rivers are also reported (Z: Zhuoshui; Pe: Peikang; Po: Potzu; Ba: Bachang; T: Tsengwen; E: Ehrjen; G: Gaoping).

In this chapter, we conduct high-resolution analyses of clay mineral and major element concentrations, as well as Sr and Nd isotopic measurements, of a core located on the eastern bank of the Penghu Canyon; our aim is to reconstruct (i) temporal variations in sediment sources and transfer to the northeastern SCS and (ii) changes in the weathering degree of SW Taiwan and their potential links to climatic changes since the last glacial period.

3.2 Climatic and geological settings

3.2.1 East Asian monsoon and SCS hydrology

The East Asian monsoon is characterized by a seasonal reversal of wind direction and latitudinal shift of the intertropical convergence zone (ITCZ) associated with intense humidity over the northern SCS (Webster et al., 1994, 1998; Ruddiman, 2001) (Fig. 3-1). In summer, the ITCZ is located between 20 and 35°N, in the SCS region, and the EASM is responsible for 80% of the regional yearly precipitation. In contrast, in winter, the ITCZ shifts southwards to between 0 and 20°S (Wang et al., 2003). The precipitation rates are about 2500 mm/yr on Taiwan, 1700-2000 mm/yr in South China, and 1900-2100 mm/yr on Luzon (Dadson et al., 2003; Liu Z.F. et al., 2007, 2009). Taiwan rivers, the Pearl River, and Luzon rivers supply 176 Mt/yr, 102 Mt/yr, and 13 Mt/yr of detrital sediments to the northeastern SCS, respectively (Dadson et al., 2003; Liu et al., 2009; Zhang et al., 2012). The monsoon winds and the Kuroshio intrusion control the seasonal reversal of the surface ocean circulation pattern of the northeastern SCS (Hu et al., 2000).

The Luzon Strait, with a water depth of about 2400 m, is the only deep-sea channel connecting the SCS to the western Pacific Ocean (Li and Qu, 2006; Qu et al., 2006). At the surface, the intrusion of the Kuroshio Current into the northern SCS occurs through the Luzon Strait, from which it flows along the margin of Taiwan in the northern SCS (Caruso et al., 2006). During the winter, the dominant southwestward winds drive the formation of surface cyclonic gyres in the SCS and the coastal current flowing northwards on the South China shelf (Wu, 2014; Fang et al., 1998). During the summer, the dominant northeastward winds induce an anti-cyclonic surface gyre and a surface coastal current which flows northwards (Wu, 2014; Fang et al., 1998).

A vertical sandwich structure has been recognized in the Luzon Strait, where the inflow of surface and deep waters to the SCS is compensated by the outflow of intermediate water mass to the Pacific Ocean (Yuan, 2002; Tian et al., 2006; Gan et al., 2016; Zhu et al., 2019). Recent studies indicate that the exchange of intermediate water (from 500 to 1500 m) between the SCS and the Pacific Ocean is very complex with strong seasonal variability. During the summer, there is a westward inflow in the northern part of the strait and an eastward outflow in the southern part, while the flow pattern across the strait is reversed in winter (Yang et al., 2010; Xie et al., 2011; Zhu et al., 2019). After entering the SCS through the Luzon Strait, the deep-water current (2000–2500 m) turns northwestwards along the southern margin of Taiwan, and then turns southwestwards along the continental margin of South China (Qu et al., 2006; Wang et al., 2011) (Fig. 3-1). This deep-sea circulation corresponds to the SCS Contour Current system that contributes, like the Kuroshio Current at the sub-surface, to the redistribution of vast amounts of sediments along the southern margin of Taiwan (Zhao et al., 2015; Liu et al., 2016).

3.2.2 Sources of northeastern SCS sediments

The river basins of SW Taiwan, Luzon, and South China are the main sources of detrital sediments for the northeastern SCS (Dadson et al., 2003; Liu Z.F. et al., 2009; Milliman and Farnsworth, 2011; Zhang et al., 2012).

The coastal plain of SW Taiwan consists mainly of Pliocene to Holocene sedimentary formations. The eastern and central mountain ranges are characterized by Miocene and Pliocene sedimentary, metamorphic, and volcanic rocks. Due to a high degree of physical erosion induced by heavy monsoon rainfall and rapid uplift (up to ~20 mm/yr, Ching et al., 2011), the clay mineral assemblage of sediments delivered by the Taiwan rivers is characterized by dominant proportions of illite (average 56%) and chlorite (average 36%), with minor proportions of kaolinite and smectite (Liu Z.F. et al., 2010a).

South China is a cratonic region composed mainly of Paleozoic and Mesozoic sandstones, mudstones, and limestones with a significant presence of Mesozoic and Cenozoic granitic intrusive rocks. This region is characterized by intensive chemical weathering due to the relatively heavy monsoon precipitation and tectonic stability. Thus, the sediments transported to the northeastern SCS by the Pearl River are mainly composed of kaolinite (46%) and illite (35%), with a smaller proportion of chlorite (18%) and negligible amounts of smectite (1%). Illite from South China has undergone stronger chemical weathering than that

from Taiwan, and thus the illite chemistry index and crystallinity of sediments transported by the Pearl River are higher than those of sediments from Taiwan (Liu Z.F et al., 2008, 2010a).

In contrast, Luzon consists mainly of volcanic rocks, such as basalts and andesites. Under tropical climatic conditions and strong EASM precipitation, the clay mineral assemblage of the rivers draining this basaltic province differs significantly from sediments from Taiwan and South China with dominant smectite (87%) and low contents of illite (1%), chlorite (7%), and kaolinite (5%) (Liu Z.F. et al., 2009).

3.3 Material and methods

3.3.1 Material and age model

The Calypso Core MD18-3569 (22°09.30'N, 119°49.24'E; 40.08 m in length; 1320 m water depth) was collected in June 2018 on the eastern bank of the Penghu Canyon during the HYDROSED cruise aboard the R/V *Marion Dufresne* (Fig. 3-1). The lithology of Core MD18-3569 consists mainly of a greenish gray homogenous hemipelagic mud without any visible turbidites. For this study, the upper 15 m of Core MD18-3569 has been investigated with a sampling resolution of 5 cm for the upper 3 m and 8-15 m depth intervals and of 2.5 cm for the 3-8 m depth interval. A total of 381 samples were thus collected. They were used to analyze clay minerals and major elements, and among them, 33 samples were selected for Sr and Nd isotopic measurement of carbonate-free detrital bulk and clay-size (<2 μm) fractions.

The age model of the studied section of Core MD18-3569 was established using linear interpolation between eight calibrated AMS ^{14}C dates obtained from planktonic foraminifer *G. ruber* (250-355 μm) combined with oxygen isotope stratigraphy of planktonic foraminifer *G. ruber* (250-355 μm) (Chen et al., 2021) (Fig. 2-2). The *G. ruber* $\delta^{18}O$ record displays a glacial to Holocene $\delta^{18}O$ difference (considering maximum and minimum values) of ~3.1‰ (Chen et al., 2021) (Fig. 2-2). The mean sedimentation rate of Core MD18-3569 is high (54.7 cm/kyr) (Fig. 2-2). It increases from 34.9 to 52.0 cm/kyr during the last deglaciation and reaches the maximum value of 72.9 cm/kyr after 4 cal kyr BP. This permits us to obtain a high temporal resolution (about 85 yr) records of clay mineralogy and geochemistry during the past 32 kyr.

3.3.2 Clay mineralogical analysis

The clay mineral determination was obtained by X-ray diffraction (XRD) performed on a PANalytical X'Pert PRO diffractometer hosted at the *State Key Laboratory of Marine Geology* (Tongji University). The analytical procedure used has been described in detail by

Liu et al. (2004). In brief, after decarbonization (20% acetic acid) and removal of organic matter (H_2O_2), the clay fraction (<2 μm) was extracted following Stokes' Law. The XRD measurements were performed on oriented thin sections that had been successively air dried, saturated with ethylene glycol under vacuum for 24 hours, and heated at 490°C for 2 hours. Semi-quantitative estimates of the peak areas of the basal reflections for the main clay mineral groups (smectite: 15–17 Å; illite: 10 Å; and kaolinite/chlorite: 7 Å) were carried out on the ethylene glycol saturation diffractogram using MacDiff software. Kaolinite and chlorite were distinguished using the 3.57/3.54 Å peak areas. Illite chemistry was calculated using 10 Å/5 Å peak areas and illite crystallinity using the full-width at half-maximum (FMWH) value of the 10 Å peak. Replicate analysis of the sample produced results with a relative error margin of ±2% (2σ).

3.3.3 Major element analysis

Major elements (SiO_2, Al_2O_3, Fe_2O_3, K_2O, CaO, MgO, Na_2O) were analyzed using X-ray fluorescence (XRF) on a PANalytical Axios spectrometer at the *State Key Laboratory of Marine Geology* (Tongji University) on the same samples processed for the mineralogical analyses. Salt was removed after three centrifugations of a solution of deionized water and finely ground samples; supernatant water was removed between the centrifugations. After the salt removal, the samples were dried. Then, 3.5 g of finely ground samples were used to form pellet tablets with boric acid and a press machine. Samples were then analyzed by X-ray fluorescence in an X-ray spectrometer. GSD-15, GSD-16, and GSR-6 standards were used to control the analysis precision every 20 samples and showed an average standard deviation of less than ±2%. Major elements were expressed as their oxides (%) as absolute bulk content of samples.

3.3.4 Sr and Nd isotope analysis

Sr and Nd isotopic compositions were analyzed on the carbonate-free bulk and clay-size (<2 μm) siliciclastic fractions. The clay fraction was extracted following the same analytical procedure used for XRD measurements. The carbonate-free fractions were analyzed after decarbonation (20% acetic acid) and the removal of organic matter (H_2O_2). Samples were first dissolved in HF-$HClO_4$ and HNO_3-HCl mixtures. Sr and REEs were then separated using a Biorad column packed with AG50WX-8 200-400 mesh cationic exchange resin and using 2 N HCl and 2.5 N HNO_3, respectively. The Sr fraction was then purified on a 20-μl Sr-Spec column consisting of a polyethylene syringe with a 4 mm Ø millex filter (Colin et al., 1999).

Nd was purified from the REEs fraction using Ln-Spec resins and following the detailed analytical procedures described in Copard et al. (2010).

Sr and Nd isotopic compositions were measured using a Thermo Scientific Multi-Collector Induced Coupled Plasma Mass Spectrometer (MC-ICP-MS *NEPTUNE^{Plus}*) hosted at the *Laboratoire des Sciences du Climat et de l'Environnement (LSCE)*, Gif-sur-Yvette (France). For the Sr and Nd isotope analyses, sample and standard concentrations were matched at 20 ppb. During the analytical sessions, every group of three samples was bracketed with analyses of appropriate Sr standard solution NIST SRM987 ($^{87}Sr/^{86}Sr$ of 0.710245±0.000016) and Nd standard solution JNdi-1 ($^{143}Nd/^{144}Nd$ of 0.512115 ± 0.000006) (Lugmair et al., 1983; Tanaka et al., 2000). The Sr and Nd isotope ratios were corrected from mass bias according to the exponential law relative to $^{146}Nd/^{144}Nd = 0.7219$ and $^{86}Sr/^{88}Sr = 0.1194$. Nd isotopic compositions are expressed as $\varepsilon_{Nd}(0) = [(^{143}Nd/^{144}Nd)_{sample}/(^{143}Nd/^{144}Nd)_{CHUR}-1]\times10000$, with the present-day $(^{143}Nd/^{144}Nd)_{CHUR}$ of 0.512638 (Jacobsen and Wasserburg, 1980). The analytical errors for each sample analysis were taken as the external reproducibility of the JNdi-1 or NIST SRM987 standards unless the internal error was larger.

3.4 Results

3.4.1 Clay mineralogy

The clay mineral assemblage of Core MD18-3569 is dominated by illite (45-59%, average 52%) and chlorite (27-39, average 32%), along with a moderate proportion of smectite (4-22%, average 12%) and a minor proportion of kaolinite (2-8%, average 4%) (Fig. 3-2, Appendix 3-1). In general, variations in the proportions of illite and chlorite are similar, and they are inversely correlated to those of smectite and, to a lesser extent, to kaolinite distributions (Fig. 3-3).

Smectite content is low (average around 10-12%) during the late Holocene and in the time interval of 20-12 cal kyr BP, and slightly higher (average around 14%) during the early Holocene between 11 and 5 cal kyr BP. Similarly, kaolinite content is slightly higher (4%) during 11-5 cal kyr BP and lower (3%) during the late Holocene and last glacial periods. Illite and chlorite contents present inverse variations to smectite with high proportions during the late Holocene and last glacial period. Illite and chlorite contents are relatively lower during the early Holocene (11 and 5 cal kyr BP) (Fig. 3-2).

Illite crystallinity and illite chemistry index vary within narrow ranges of 0.132-0.206° Δ2θ (average 0.158° Δ2θ) and of 0.264-0.397 (average 0.324), respectively. Both mineralogical parameters do not display significant variations over the past 32 kyr.

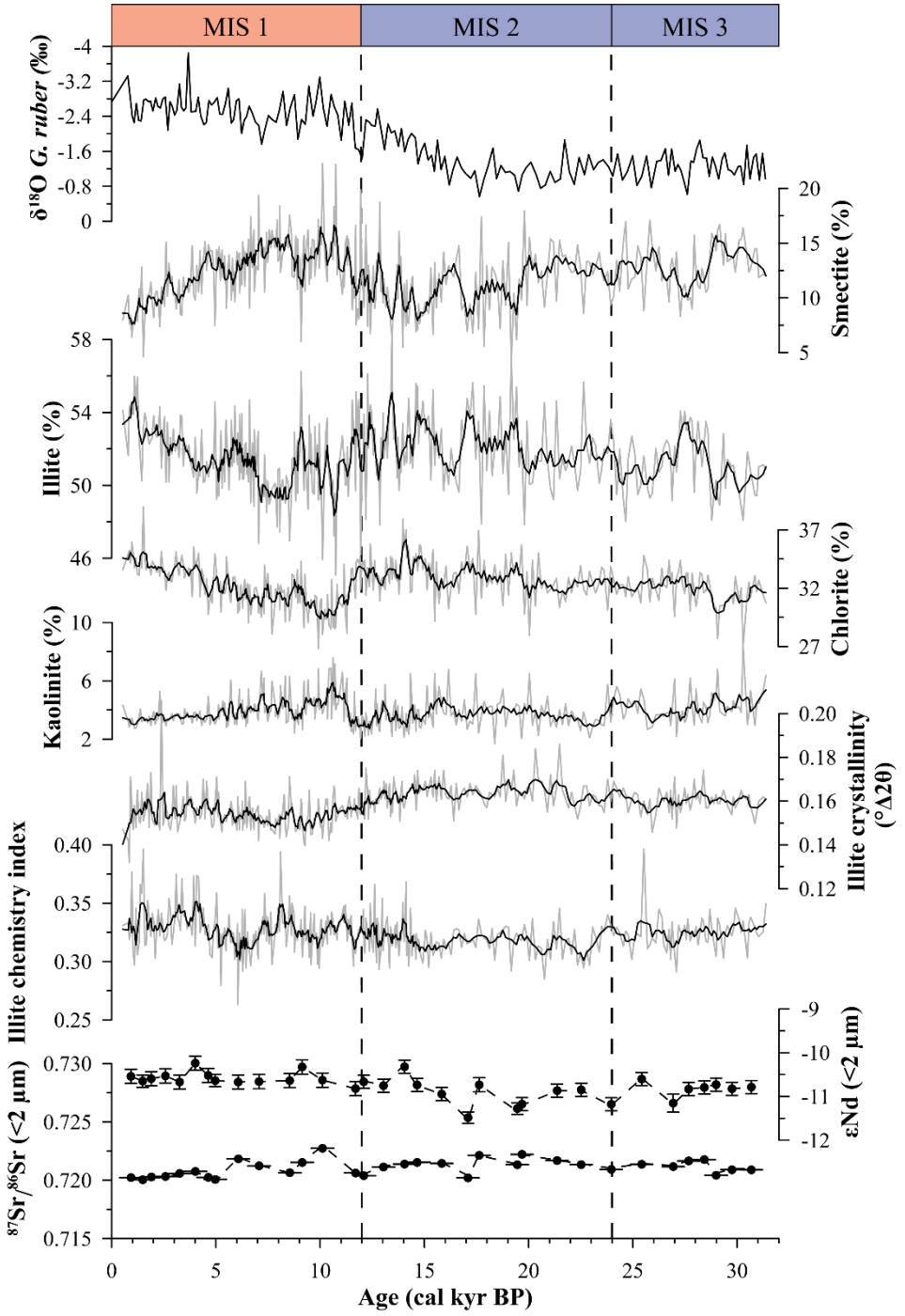

Figure 3-2. Temporal variations of clay mineral assemblage, illite crystallinity, illite chemistry index, clay fraction (<2 μm) Nd and Sr isotopic compositions, and G. ruber $\delta^{18}O$ of Core MD18-3569 during the last 32 kyr. *G. ruber* $\delta^{18}O$ from Chen et al. (2021).

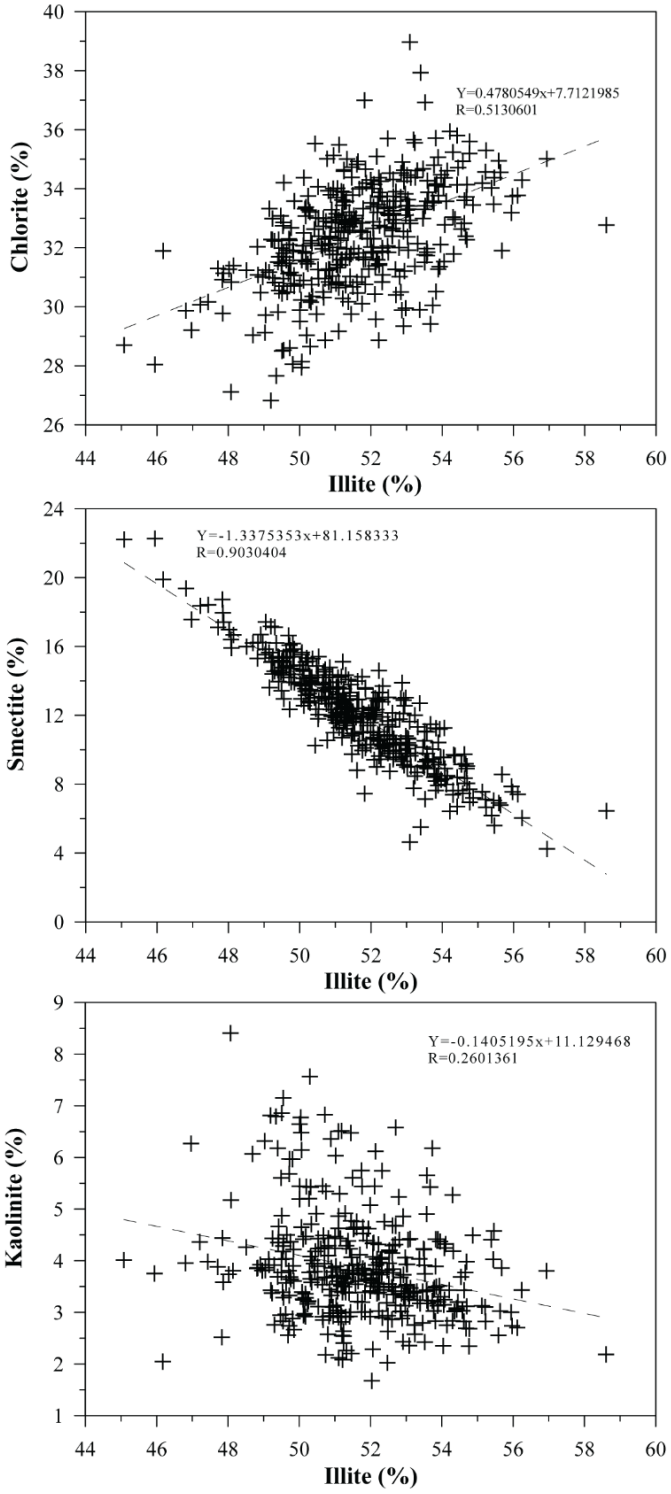

Figure 3-3. Correlation plots of clay mineral groups of Core MD18-3569. (A) Chlorite (%) versus illite (%). (B) Smectite (%) versus illite (%). (C) Kaolinite (%) versus illite (%).

3.4.2 Major elements

Major elements of Core MD18-3569 sediments mainly include SiO_2 (61.9-67.5%, average 65%), Al_2O_3 (13.9-16.6%, average 15%), and Fe_2O_3 (5.3-7.2%, average 6.2%) with lower concentrations of K_2O (2.8-3.4%, average 3%), MgO (1.9-2.4%, average 2.1%), Na_2O (1.1-1.3%, average 1.2%), and CaO (0.9-1.2%, average 1%) (Fig. 3-4). Al_2O_3, Fe_2O_3, K_2O, and MgO contents were relatively low and stable in the interval of 32-18 cal kyr BP and then increased progressively at 18 cal kyr BP to reach a maximum at 10 cal kyr BP. Thereafter, their concentrations decreased until ~7.8 cal kyr BP and then have increased slightly up to the present time. Long-term variations in SiO_2, Na_2O, and CaO concentrations are inversely correlated to those of Al_2O_3, Fe_2O_3, K_2O, and MgO. SiO_2, Na_2O, and CaO concentrations decreased during the time interval of 20-10 cal kyr BP and increased at ~7.8 cal kyr BP (Fig. 3-4).

3.4.3 Sr-Nd isotopic compositions

εNd values of bulk siliciclastic sediments display a narrow range from -11.63±0.15 to -10.96±0.13 (Fig. 3-4). εNd values of clay fraction also present a narrow range from -11.48±0.13 to -10.28±0.15 with slightly higher values than those obtained for the bulk siliciclastic sediments (Table 3-1) (Fig. 3-4). $^{87}Sr/^{86}Sr$ ratios of bulk siliciclastic sediments also display a narrow range, from 0.7187 to 0.7213, without any significant variation trends during the past 32 kyr apart from a peak at 17.1 cal kyr BP (0.7213) (Fig. 3-2). $^{87}Sr/^{86}Sr$ ratios obtained on the clay fraction present slightly higher values (from 0.7197 to 0.7230) from the MIS 3 to the early Holocene (with a maximum centered at 10 cal kyr BP) than the late Holocene, which is associated with a slight decrease of the $^{87}Sr/^{86}Sr$ ratio (Fig. 3-2).

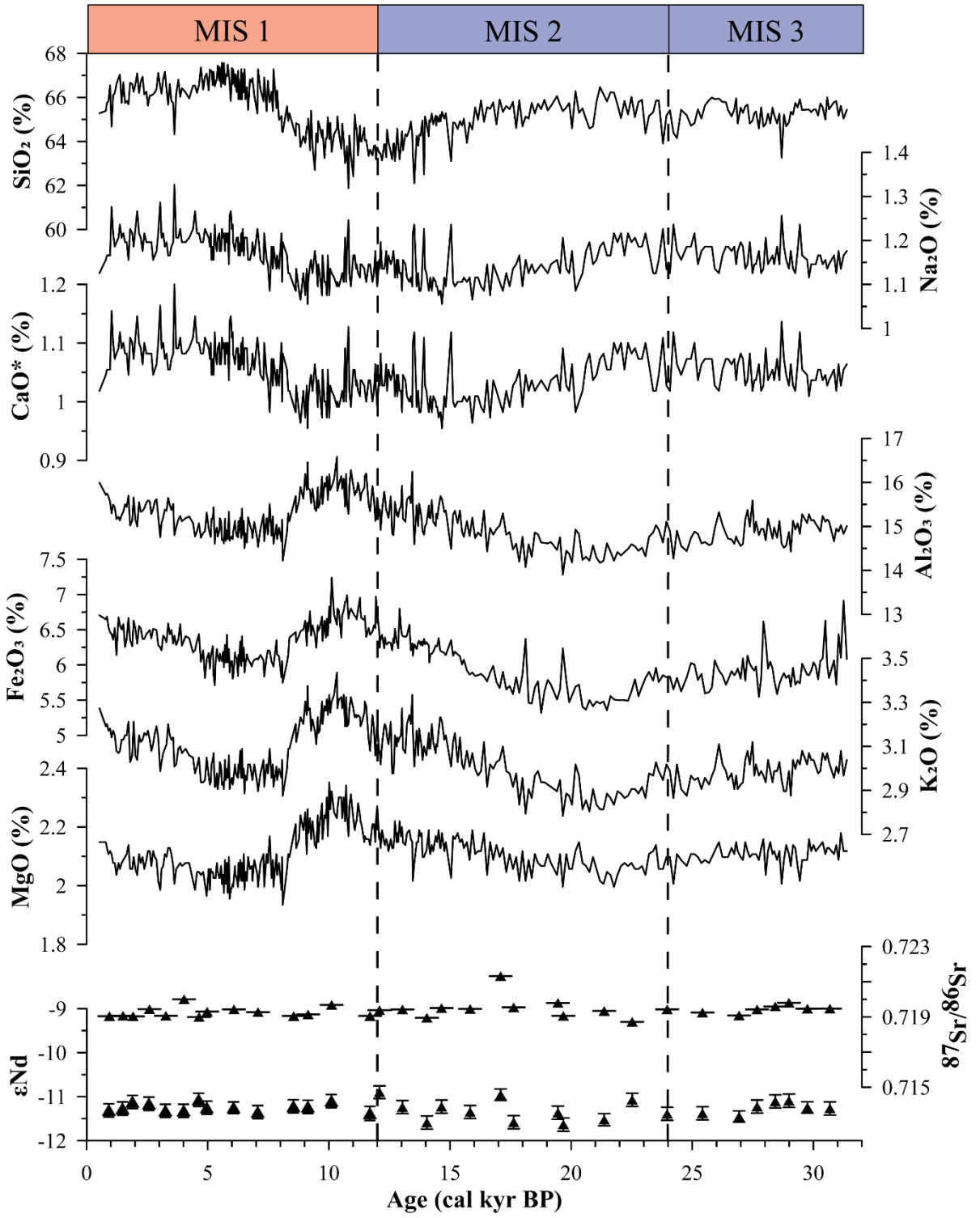

Figure 3-4. Temporal variations of major element contents (SiO_2, Na_2O, CaO, Al_2O_3, Fe_2O_3, K_2O and MgO) of Core MD18-3569 over the last 32 kyr. $^{87}Sr/^{86}Sr$ ratio and εNd value of the carbonate-free bulk fractions are also displayed.

Table 3-1. Sr and Nd isotopic compositions measured on the carbonate-free bulk and clay-size (<2 μm) siliciclastic fractions of sediments from Core MD18-3569.

Depth (cm)	Age (cal kyr BP)	$^{87}Sr/^{86}Sr$	± 2σ	$^{143}Nd/^{144}Nd$	± 2 σ	εNd	± 2 σ
Bulk siliciclastic							
20.5	0.92	0.71904	0.00001	0.512058	0.000008	-11.31	0.15
61.0	1.47	0.71906	0.00001	0.512060	0.000008	-11.27	0.15
91.0	1.89	0.71904	0.00001	0.512068	0.000008	-11.12	0.15
140.5	2.62	0.71944	0.00001	0.512066	0.000008	-11.16	0.15
190.5	3.31	0.71906	0.00001	0.512058	0.000008	-11.32	0.15
241.0	4.04	0.72000	0.00001	0.512058	0.000008	-11.32	0.15
280.5	4.65	0.71899	0.00001	0.512070	0.000008	-11.07	0.15
301.0	4.98	0.71930	0.00001	0.512061	0.000008	-11.25	0.15
370.5	6.13	0.71943	0.00001	0.512061	0.000007	-11.25	0.13
421.0	6.96	0.71927	0.00001	0.512056	0.000008	-11.35	0.15
481.0	8.22	0.71905	0.00001	0.512063	0.000008	-11.22	0.15
511.0	8.89	0.71914	0.00001	0.512062	0.000008	-11.23	0.15
560.5	9.97	0.71968	0.00001	0.512069	0.000008	-11.10	0.15
640.5	11.67	0.71905	0.00001	0.512055	0.000008	-11.38	0.16
661.0	12.09	0.71938	0.00001	0.512079	0.000007	-10.90	0.14
710.5	13.04	0.71942	0.00001	0.512062	0.000008	-11.24	0.15
760.5	14.05	0.71895	0.00001	0.512044	0.000008	-11.59	0.15
790.5	14.65	0.71950	0.00001	0.512062	0.000008	-11.23	0.15
850.5	15.83	0.71945	0.00001	0.512056	0.000008	-11.35	0.15
901.0	17.09	0.72132	0.00001	0.512076	0.000007	-10.96	0.13
920.5	17.63	0.71954	0.00001	0.512044	0.000008	-11.58	0.15
991.0	19.46	0.71979	0.00001	0.512055	0.000008	-11.37	0.15
1000.5	19.68	0.71906	0.00001	0.512042	0.000008	-11.63	0.15
1060.5	21.36	0.71933	0.00001	0.512047	0.000007	-11.52	0.14
1100.5	22.52	0.71872	0.00001	0.512070	0.000008	-11.07	0.15
1150.5	23.96	0.71943	0.00001	0.512054	0.000008	-11.39	0.15

1201.0	25.42	0.71925	0.00001	0.512055	0.000008	-11.38	0.15
1261.0	26.93	0.71908	0.00001	0.512051	0.000007	-11.45	0.13
1300.5	27.67	0.71942	0.00001	0.512063	0.000008	-11.23	0.15
1340.5	28.43	0.71959	0.00001	0.512069	0.000008	-11.11	0.15
1370.5	28.99	0.71980	0.00001	0.512069	0.000008	-11.09	0.15
1411.0	29.75	0.71947	0.00001	0.512062	0.000007	-11.25	0.13
1460.5	30.68	0.71947	0.00001	0.512060	0.000008	-11.27	0.15
Clay size fraction							
20.5	0.92	0.71995	0.00001	0.51210	0.000007	-10.56	0.15
61.0	1.47	0.71972	0.00001	0.512091	0.000008	-10.66	0.13
91.0	1.89	0.72001	0.00001	0.512094	0.000008	-10.61	0.15
140.5	2.62	0.72007	0.00001	0.512097	0.000008	-10.55	0.15
190.5	3.31	0.72039	0.00001	0.512090	0.000008	-10.68	0.15
241.0	4.04	0.72060	0.00001	0.512111	0.000008	-10.28	0.15
280.5	4.65	0.71997	0.00001	0.512198	0.000008	-10.54	0.15
301.0	4.98	0.71975	0.00001	0.512092	0.000007	-10.65	0.13
370.5	6.13	0.72193	0.00001	0.512091	0.000008	-10.68	0.15
421.0	6.96	0.72120	0.00001	0.512091	0.000008	-10.67	0.15
481.0	8.22	0.72047	0.00001	0.512092	0.000008	-10.65	0.15
511.0	8.89	0.72155	0.00001	0.512107	0.000008	-10.36	0.15
560.5	9.97	0.72305	0.00001	0.512093	0.000008	-10.64	0.15
640.5	11.67	0.72044	0.00001	0.512083	0.000008	-10.82	0.15
661.0	12.09	0.72039	0.00001	0.512091	0.000008	-10.66	0.15
710.5	13.04	0.72113	0.00001	0.512087	0.000008	-10.75	0.15
760.5	14.05	0.72138	0.00001	0.512109	0.000008	-10.32	0.15
790.5	14.65	0.72152	0.00001	0.512088	0.000008	-10.74	0.15
850.5	15.83	0.72144	0.00001	0.512077	0.000008	-10.94	0.15
901.0	17.09	0.72020	0.00001	0.512049	0.000007	-11.48	0.13
920.5	17.63	0.72213	0.00001	0.512088	0.000008	-10.73	0.16
991.0	19.46	0.72132	0.00001	0.512060	0.000007	-11.28	0.13
1000.5	19.68	0.72221	0.00001	0.512065	0.000008	-11.18	0.15

1060.5	21.36	0.72168	0.00001	0.512081	0.000008	-10.87	0.15
1100.5	22.52	0.72133	0.00001	0.512082	0.000008	-10.85	0.15
1150.5	23.96	0.72093	0.00001	0.512065	0.000008	-11.18	0.15
1201.0	25.42	0.72137	0.00001	0.512095	0.000008	-10.60	0.15
1261.0	26.93	0.72117	0.00001	0.512066	0.000011	-11.15	0.21
1300.5	27.67	0.72165	0.00001	0.512083	0.000008	-10.83	0.15
1340.5	28.43	0.72177	0.00001	0.512085	0.000008	-10.79	0.15
1370.5	28.99	0.72042	0.00001	0.512088	0.000008	-10.73	0.15
1411.0	29.75	0.72089	0.00001	0.512083	0.000008	-10.82	0.15
1460.5	30.68	0.72089	0.00001	0.512085	0.000008	-10.79	0.15

3.5 Discussions

3.5.1 Sources of sediments to the SW Taiwan margin

Several studies have shown that Sr and Nd isotopic compositions in deep-sea sediments of the northeastern SCS are particularly useful for determining the principal sources of sediments (Boulay et al., 2005; Liu Z.F et al., 2005; Wei et al., 2012). Compared to the original bedrock values, εNd values in sediments are usually not significantly influenced by erosion and transportation. In contrast, $^{87}Sr/^{86}Sr$ ratios can be modified significantly within different grain-size fractions because of sorting effects that occur during transport. Several previous studies have shown that the coarse fractions of sediments are characterized by different mineral compositions to the fine fraction. For example, it has been shown that the fine fraction mainly contains clay minerals and micas, which are often characterized by high $^{87}Sr/^{86}Sr$ ratios (Innocent et al., 2000; Colin et al., 2006; Meyer et al., 2011; Hu et al., 2012; Zhao et al., 2017). $^{87}Sr/^{86}Sr$ ratios can also be affected by chemical weathering of Rb-rich minerals such as micas (Colin et al., 2006). Therefore, Sr isotopes can be biased by sorting effects and caution must be considered when constraining sedimentary provenances. Since most previous results for the deep-sea sediments of the SCS and their sedimentary sources have been obtained on the decarbonated bulk sediment or <63 μm fraction, in figure 3-5 we have reported the εNd and $^{87}Sr/^{86}Sr$ ratios analyzed on the decarbonated bulk sediments from Core MD18-3569 together with Sr and Nd isotopic compositions of river sediments obtained on the <63 μm fraction.

The narrow ranges of εNd values and $^{87}Sr/^{86}Sr$ ratios of decarbonated bulk sediments (εNd from -11.63 to -10.89 and $^{87}Sr/^{86}Sr$ from 0.7187 to 0.7213) of Core MD18-3569 are similar to those of Taiwan river sediments (εNd from -11.2 to -12.2 and $^{87}Sr/^{86}Sr$ from 0.7176 to 0.7219) (Fig. 3-5). Such Sr and Nd isotopic compositions are in contrast with the εNd and $^{87}Sr/^{86}Sr$ ranges of Luzon river sediments (εNd from +6.4 to +7.4 and $^{87}Sr/^{86}Sr$ from 0.7044 to 0.7052) and Pearl River sediments (εNd from -1.4 to -10.5 and $^{87}Sr/^{86}Sr$ from 0.7275 to 0.7373) (Goldstein and Jacobsen, 1988, Dou et al., 2016, Liu Z.F. et al., 2016) (Fig. 3-5). More specifically, plots of the εNd and $^{87}Sr/^{86}Sr$ values of the decarbonated sediments of Core MD18-3569 closely overlie the ranges for SW Taiwan rivers (Zhuoshui, Tsengwen, Ehrjen, and Gaoping) (Fig. 3-5). However, variations in the Sr and Nd isotopic compositions of the decarbonated sediments are too small to allow a robust interpretation of changes in the provenance among SW Taiwan rivers since the last glacial period.

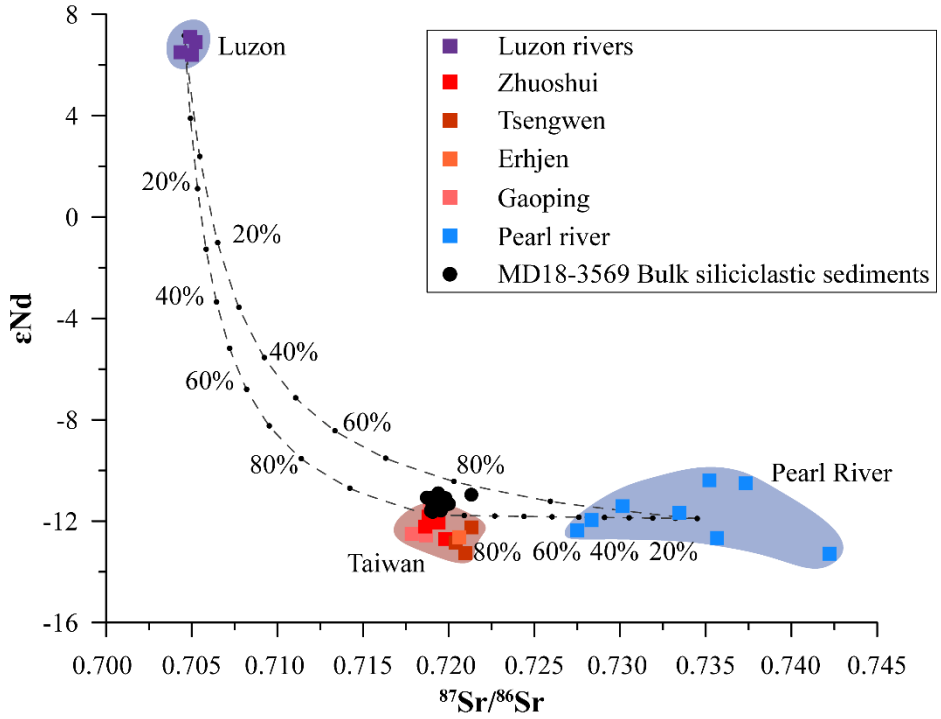

Figure 3-5. $^{87}Sr/^{86}Sr$ versus εNd diagram. $^{87}Sr/^{86}Sr$ ratios and εNd values obtained on the carbonate free-fractions of Core MD18-3569 (black dots, this study) are reported together with Sr and Nd isotopic compositions of Luzon rivers (purple squares) (Goldstein and Jacobsen, 1988; Liu Z.F. et al., 2016), Pearl River (blue squares) (Liu Z.F. et al., 2016), and SW Taiwan rivers (red squares) (Dou et al., 2016; Liu Z.F. et al., 2016).

This implies that the sediment provenance is a mixture of SW Taiwan rivers (Zuoshui: εNd=-12.2, $^{87}Sr/^{86}Sr$=0.7192; Tsengwen: εNd=-12.8, $^{87}Sr/^{86}Sr$=0.7209; Ehrjen: εNd=-12.6,

$^{87}Sr/^{86}Sr$=0.7206) (Fig. 3-5). Nevertheless, such ranges of Sr and Nd isotopic compositions indicate that the main sedimentary source remains as the SW Taiwan river basins and they exclude a significant contribution of sediments derived from the Luzon rivers as well as the Pearl River (Fig. 3-5). There are slightly higher εNd and $^{87}Sr/^{86}Sr$ ratios for the clay fraction compared to the decarbonated bulk sediments (Table 3-1) in agreement with previous results obtained in other study areas (Innocent et al., 2000; Meyer et al., 2011; Hu et al., 2012; Zhao et al., 2017). Nevertheless, the narrow ranges of εNd and $^{87}Sr/^{86}Sr$ ratios of the clay-size fraction (<2 μm) confirm that clay mineral sources have remained constant throughout the past 32 kyr (Fig. 3-6).

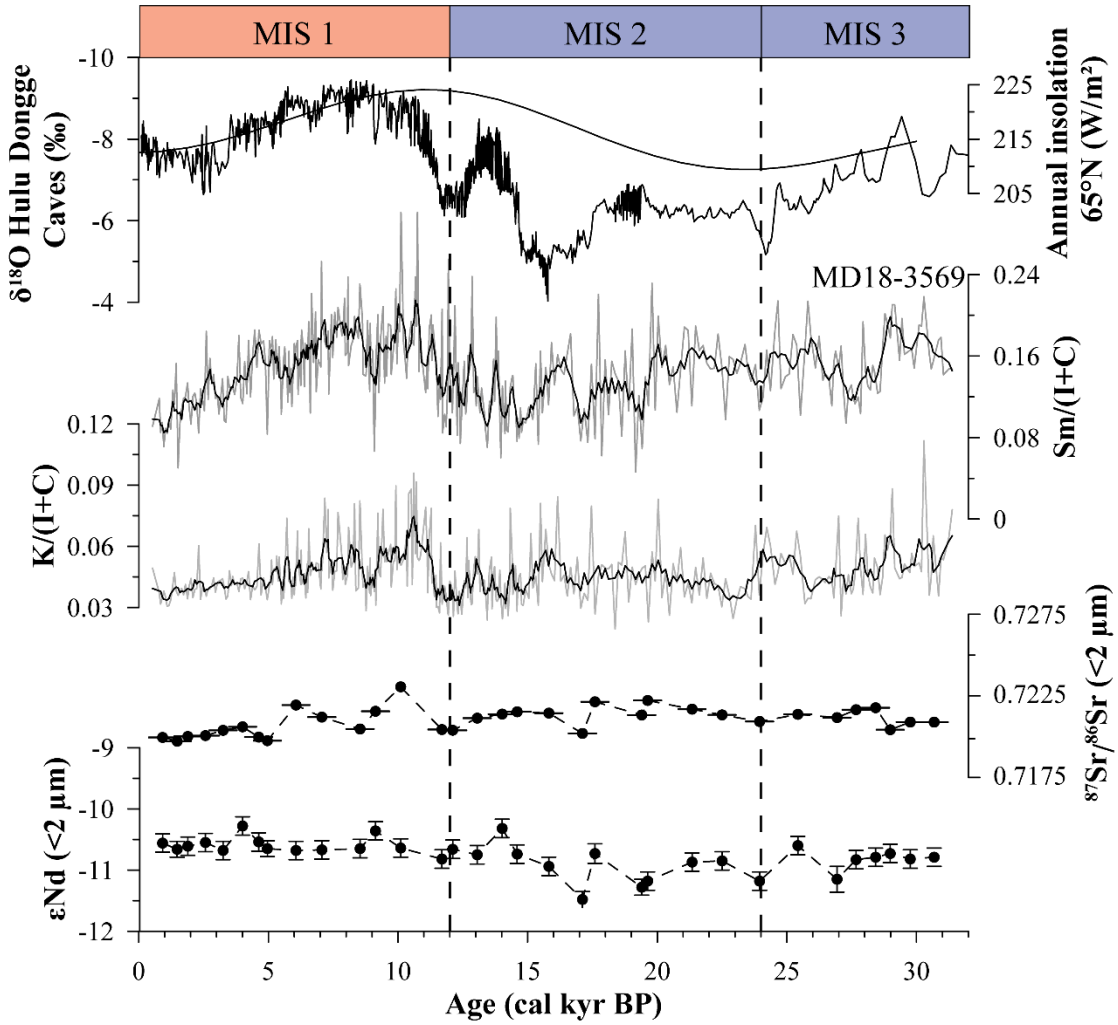

Figure 3-6. Temporal evolution of Sm/(I+C) and K/(I+C) mineralogical ratios and of $^{87}Sr/^{86}Sr$ ratio and εNd value obtained on the <2 μm siliciclastic fractions of Core MD18-3569. The insolation curve received by the earth at 65°N of latitude and the $\delta^{18}O$ record obtained on the Hulu and Dongge Cave speleothems (Wang et al., 2001; Dykoski et al., 2005) are reported for comparison.

Clay mineral assemblage has been used in previous studies to constrain sediment sources and transports to the oceanic margin of the northeastern SCS (Boulay et al., 2005; Liu Z.F. et al., 2010a, 2016; Zhao et al., 2018). Given the contrasted mineralogical signatures of the main sedimentary provinces (e.g., Liu Z.F. et al., 2016), it is possible to use the clay mineral assemblage of sediments from Core MD18-3569 to better constrain the sources of sediments on the eastern bank of the Penghu Canyon.

Clay mineralogical results for Core MD18-3569 are reported in a ternary diagram of (illite+chlorite)-kaolinite-smectite together with the mineralogical compositions of modern river sediments obtained using the same XRD analytical procedure (Liu Z.F. et al., 2016) (Fig. 3-7). The major proportions of illite (52%) and chlorite (32%) of Core MD18-3569 sediments are characteristic of assemblages related to illite and chlorite rich sediments from SW Taiwan rivers (56% illite and 36% chlorite) (Liu Z.F. et al., 2016) (Fig. 3-7). These results rule out the possibility that the Pearl River is the major source of clay to the studied site. First, the percentage of kaolinite is too low in the clay fraction of Core MD18-3569 (average 4%) to correspond to riverine sediment from South China (46%) and correspond instead to average kaolinite inputs from Taiwan rivers (4%) (Liu Z.F. et al. 2016) (Fig. 3-7).

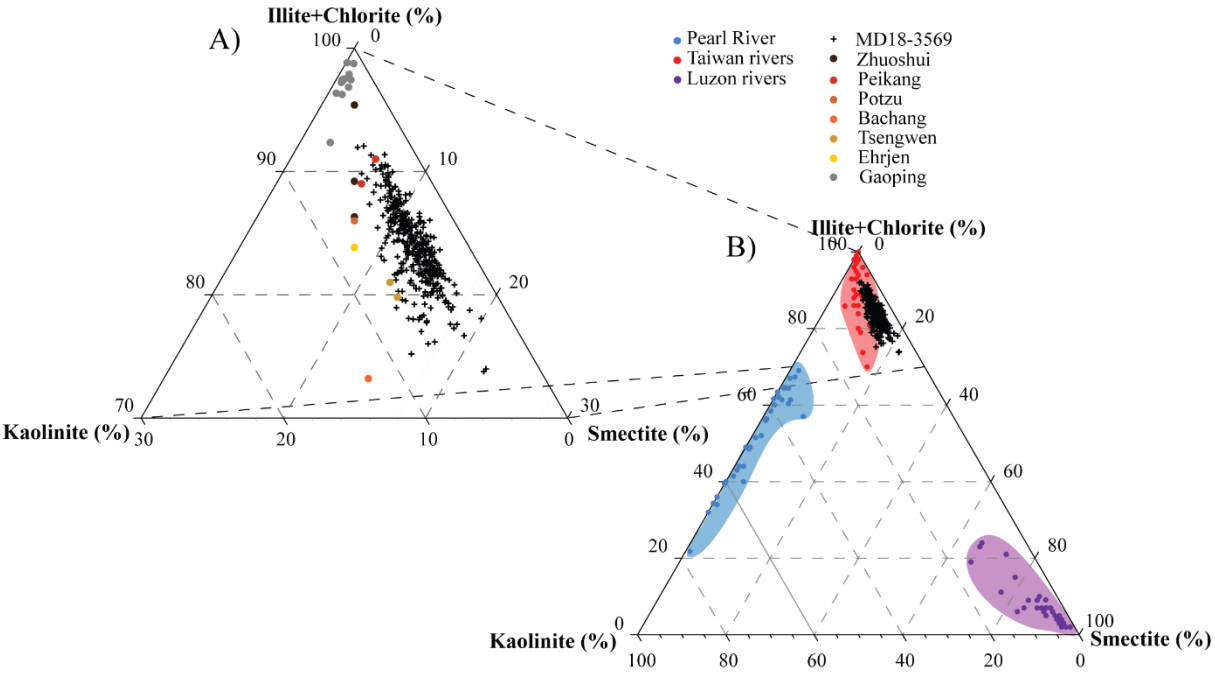

Figure 3-7. Ternary diagrams of major mineral groups of illite+chlorite, kaolinite, and smectite for Core MD18-3569 (A). Clay mineralogy compositions of surface sediments from Luzon rivers, Pearl River, and SW Taiwan rivers are included for comparison (Liu Z.F et al.,

2008, 2010a, 2016). Zoomed plots for surface sediments of Taiwan rivers and Core MD18-3569 (B).

This could be the result of the Guangdong Coastal Current (GCC) and the westward circulation induced by the Kuroshio intrusion (Caruso et al., 2006) that transport sediments from the Pearl River southwards, along the Chinese continental shelf and/or the flocculation effect of kaolinite causing the mineral to sink and deposit on the continual shelf close to the mouth of the Pearl River (Xia et al., 2004). In addition, the illite crystallinity and illite chemistry index (0.158°Δ2θ and 0.324, respectively) obtained on the clay-size fraction of Core MD18-3569 are too low to be consistent with the high chemical weathering experienced by sediments in South China (0.198° Δ2θ and 0.466, respectively) (Liu Z.F. et al., 2007b, 2007c) (Fig. 3-8). Thus, SW Taiwan is the main source of illite and kaolinite for the studied site, while the input of sediments from the Pearl River can be considered negligible. Such results are coherent with the Sr and Nd isotope results and the proximity of the study site to the southwestern coast of Taiwan and its river mouths.

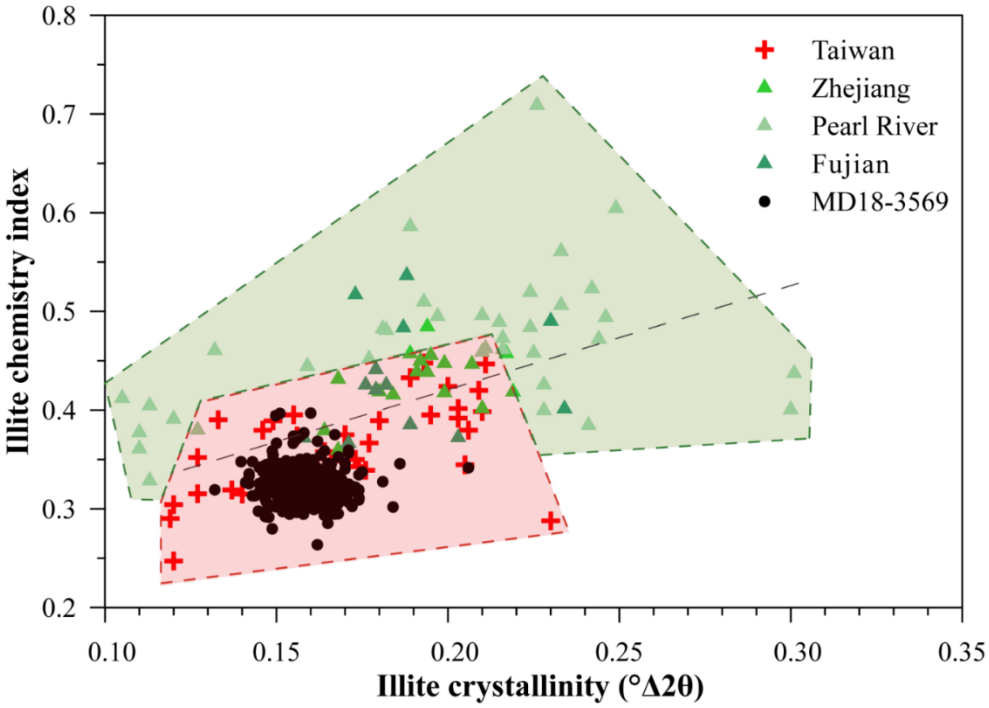

Figure 3-8. Illite crystallinity versus illite chemistry index of Core MD18-3569 (black dots) sediments compared to South China (green triangle) and Taiwan (red cross) river sediments (Liu Z.F. et al., 2010a, 2016).

However, the average smectite content (12%) of Core MD18-3569 is relatively high compared to the average of present-day inputs from SW Taiwan rivers to the SCS (4%) (Liu

Z.F. et al., 2016) (Fig. 3-7). Such results are coherent with one previous study that also indicates that smectite proportions are higher in sediments of the Penghu Canyon system than those in the Gaoping Canyon, a fact that can be attributed to different land-sea configurations (Nayak et al., 2021). In fact, at present the Penghu Canyon is not directly connected to a river mouth but may have been connected, via the Penghu Channel, to the SW Taiwan rivers during low sea level intervals. This is in contrast with the Gaoping Canyon which has always been connected to the Gaoping River mouth, at least since the last glacial period (Yu S.W. et al., 2017). Taking this into account, we cannot fully exclude the possibility that a small portion of the smectite from Core MD18-3569 derives from a potential additional source. Another important source of smectite to the northeastern SCS is the basaltic province of Luzon and the volcanic formations of western Taiwan (Liu Z.F. et al., 2009). However, higher proportions of smectite (or S/(I+C) ratio) are not systematically associated with more radiogenic εNd in the clay-size fraction. The $^{87}Sr/^{86}Sr$ ratios of the <2 μm fraction are even slightly higher during 10-6 cal kyr BP which contradicts the hypothesis of a greater volcanic contribution (Fig. 3-6). Consequently, we can assume that the smectite does not derive from the weathering of volcanic formations but rather from crustal rocks on the island of Taiwan (Fig. 3-6).

Several rivers located in western and southwestern Taiwan deliver moderate amounts of smectite to the SCS. These include Tsengwen (smectite content 15%) and Erhjen (smectite content 10%) rivers, which are close to the studied site, with sediment discharge of 9-16 Mt/yr and 21 Mt/yr, respectively, have some of the greatest sediment fluxes of all SW Taiwan rivers (Dadson et al., 2003). Figure 3.7 presents the clay mineral assemblages of the western and southwestern Taiwan rivers (Liu Z.F. et al. 2010a; 2016) in comparison to sediments from Core MD18-3569. It shows that most of the samples lie within the ranges of Tsengwen, Erhjen, and Bachang rivers, which are characterized by moderate smectite contents (8-17%), suggesting that these rivers are potentially the main sources of fine sediments to Core MD18-3569. A minor portion of samples are distributed within the range of rivers with low to negligible smectite contents such as Potzu (smectite content 7%), Peikang (smectite content 6%), and Zhuoshui (smectite content 5%) rivers, which are located further north in western Taiwan. This suggests that a small number of fine sediments could also have derived from these western Taiwan rivers during the glacial low sea level stand when the strait was emerged. In such the low sea level condition, these rivers might have been directly connected to the Penghu Canyon system (Lambeck et al., 2014; Spratt et Lisiecki., 2016).

To sum up, clay mineral assemblages combined with the Nd and Sr isotopic compositions confirm that the SW Taiwan rivers (mainly Tsengwen and Erhjen rivers) have been the principal sources of sediments to Core MD18-3569 since the last glacial period. There is also a possible minor contribution of clay materials derived from the rivers of western Taiwan (Zhuoshui, Bachang, Potzu, and Peikang rivers), which could have been transported to the SCS through the Taiwan Strait during the glacial low-sea level stand.

3.5.2 Variations in chemical weathering and physical erosion of SW Taiwan

Several forcings (such as climate, tectonics, and lithology) control the morphology of Taiwan. They impact on sediment discharge to the northeastern SCS via submarine canyons and this can be recorded in deep-sea cores. Taiwan has been characterized by rapid and irregular uplift over time since the late Miocene (Huang et al., 1997). Intervals of high uplift induce a steeper river slope, which leads to stronger physical erosion induced by the enhanced power of rivers to incise bedrocks (Bull, 1990; Hsieh et al., 2001; 2002). Taiwan is also affected by intense East Asian monsoon rainfalls and typhoon events (Wu et al., 1992; Hsieh et al., 2001; 2002). Such climatic conditions with heavy rains play a key role in the weathering and morphological changes of Taiwan river basins (Molnar, 2001; Hsieh et al., 2001; 2002). Moreover, enhanced hydrolysis conditions associated with rainfall conditions can induce rapid leaching of the most labile elements. This phenomenon is also enhanced by the breaking up of rocks by erosion, leading to greater surface alteration (Rasmusson and Carpenter, 1982). Thus, in a tectonically active region with marked climatic variability, weathering is triggered by the variation of the interactions between these forcings and their effects on erosion (Riebe et al., 2001).

Since SW Taiwan is the unique source of sediments to Core MD18-3569, the clay mineral assemblages and major element compositions of the core can be used to evaluate the state of chemical weathering of sediments transported to the study site (Wei et al., 2006; Hu et al., 2012; Clift et al., 2014; Huang et al., 2016; Liu Z.F. et al., 2016). Major elements are reported in Al_2O_3–(CaO+Na_2O)–K_2O (A–CN–K) ternary diagram to assess elemental leaching by chemical weathering (Fig. 3-9). Sample distributions in the A–CN–K diagram indicate that sediments experienced a moderate weathering in agreement with pronounced tectonic uplift of Taiwan which results in high rates of physical erosion. Such physical erosion conditions induce preferential leaching of Na and Ca, which is typical of Taiwan river sediments (Selvaraj and Chen, 2006; Liu Z.F. et al., 2016). Thus, Na is compared to an immobile element, Al, through the Al_2O_3/Na_2O ratio. Hence a pronounced state of chemical

weathering of sediments delivered to the study site from SW Taiwan will be associated with detrital material that is relatively depleted in Na and enriched in Al leading to an increase in the Al_2O_3/Na_2O ratio (Selvaraj and Chen, 2006) (Fig. 3-9).

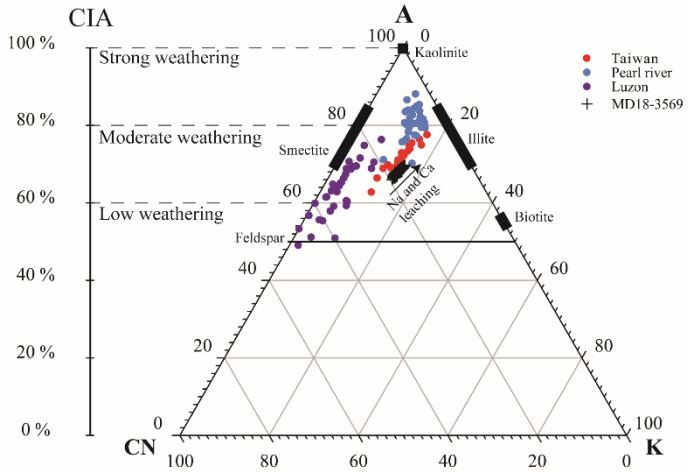

Figure 3-9. A–CN–K (Al_2O_3–($CaO+Na_2O$)–K_2O) ternary diagram plotting results obtained on Core MD18-3569 together with surface sediments from Luzon rivers (Liu et al., 2016), Pearl River (Liu et al., 2016), and SW Taiwan rivers (Liu et al., 2016) for comparison.

Smectite/(illite+chlorite) (Sm/I+C), kaolinite/(illite+chlorite) (K/I+C), chemical index of alteration (CIA = molar ratio of [$Al_2O_3/(Al_2O_3+Na_2O+K_2O+CaO^*) \times 100$]), Al_2O_3/SiO_2, and Al_2O_3/Na_2O are reported in Figure 3-10 as chemical weathering proxies. Smectite and, to a lesser extent, kaolinite contents display anti-covariations to illite and chlorite contents (Fig. 3-3). As smectite and kaolinite are of the result of chemical weathering of primary minerals and illite and chlorite result from strong physical erosion, we can use Sm/(I+C) and K/(I+C) as proxies to establish past changes in the relative intensity of chemical weathering and physical erosion within the rivers basins of SW Taiwan. We can thus hypothesize that higher Sm/(I+C) and K/(I+C) ratios would suggest enhanced chemical weathering and/or a decrease in the physical erosion of the sedimentary sources.

The CIA can also be used to evaluate the state of chemical alteration of sediments (Colin et al., 2006; Hu et al., 2012; Clift et al., 2014; Liu Z.F. et al., 2016). A CIA range of 80-100 indicates strong weathering, 80-60 indicates moderate weathering, 60-40 reflects low weathering, and values below 40 indicate no chemical weathering (Liu Z.F. et al., 2016). CIA values for Core MD18-3569 range from 66 to 70 with an average value of 68 (Fig. 3-10). These CIA values fall into the range of moderate chemical weathering values (80-60) and are in agreement with the A-CN-K ternary diagram (Fig. 3-9). Finally, concentrations of Si in

marine sediments are higher in the sand fraction (e.g., Quartz) than in the clay fraction, which is the product of grain-size sorting, where Al concentrations are high in the clay fraction, reflecting intense chemical weathering. Al_2O_3/SiO_2 variations can thus be attributed to changes in the relative proportion of clay and sand fractions and to siliciclastic discharge to the ocean linked to physical erosion versus chemical weathering on land (Clift et al., 2014). Clay minerals and bulk major elements were measured on different sediment fractions (<2 μm and bulk sediments). Clay minerals and the coarser minerals contained in bulk sediments respond differently to chemical weathering (e.g. quartz is considered to be more resistant to chemical weathering). Both proxies are resulting from slightly different chemical weathering degrees and processes and their variations can be slightly different.

The variations of CIA and Al_2O_3/Na_2O display slightly higher values during the MIS 3 than the Last Glacial Maximum (LGM) and an increasing trend from the LGM to the early Holocene. The minimum values of the CIA and Al_2O_3/Na_2O ratio occurred at 22 cal kyr BP during the LGM and during the middle-late Holocene (Fig. 3-10). Similar variations have been observed in the clay mineral assemblage with lower Sm/(I+C) and K/(I+C) ratios during the MIS2 compared to the MIS 3 and the early Holocene (between 11 and 5 cal kyr BP). Such variations indicate that chemical weathering was relatively enhanced during the MIS3 compared to the LGM (and MIS2) when more clays were produced as indicated by the higher Al_2O_3/SiO_2 (Hu et al., 2012; Clift et al., 2014; Liu Z.F. et al., 2016) (Fig. 3-10). The LGM is thus characterized by a relatively weakened state of chemical weathering (lower Sm/(I+C) and K/(I+C), Si and Na-rich sediments with lower CIA) (Hu et al., 2012; Clift et al., 2014; Liu Z.F. et al., 2016).

The continuous increase in proxies of weathering intensity (CIA, Al_2O_3/Na_2O, Sm/(I+C)) from the deglaciation to the beginning of the Holocene suggests a progressive enhancement of chemical weathering intensity during this period, with a maximum centered at 10 cal kyr BP. The early-middle Holocene transition is characterized by a decreasing of proxies of weathering intensity from 9.2 to 8.7 cal kyr BP; this trend is well marked in the CIA and the Al_2O_3/Na_2O ratio. The early to late Holocene is associated with a steady decrease of S/(I+C), K/(I+C), CIA, Al_2O_3/SiO_2, and Al_2O_3/Na_2O (Fig. 3-10). This indicates a decrease in the state of chemical weathering of detrital material transported from the SW Taiwan basins to the northeastern SCS.

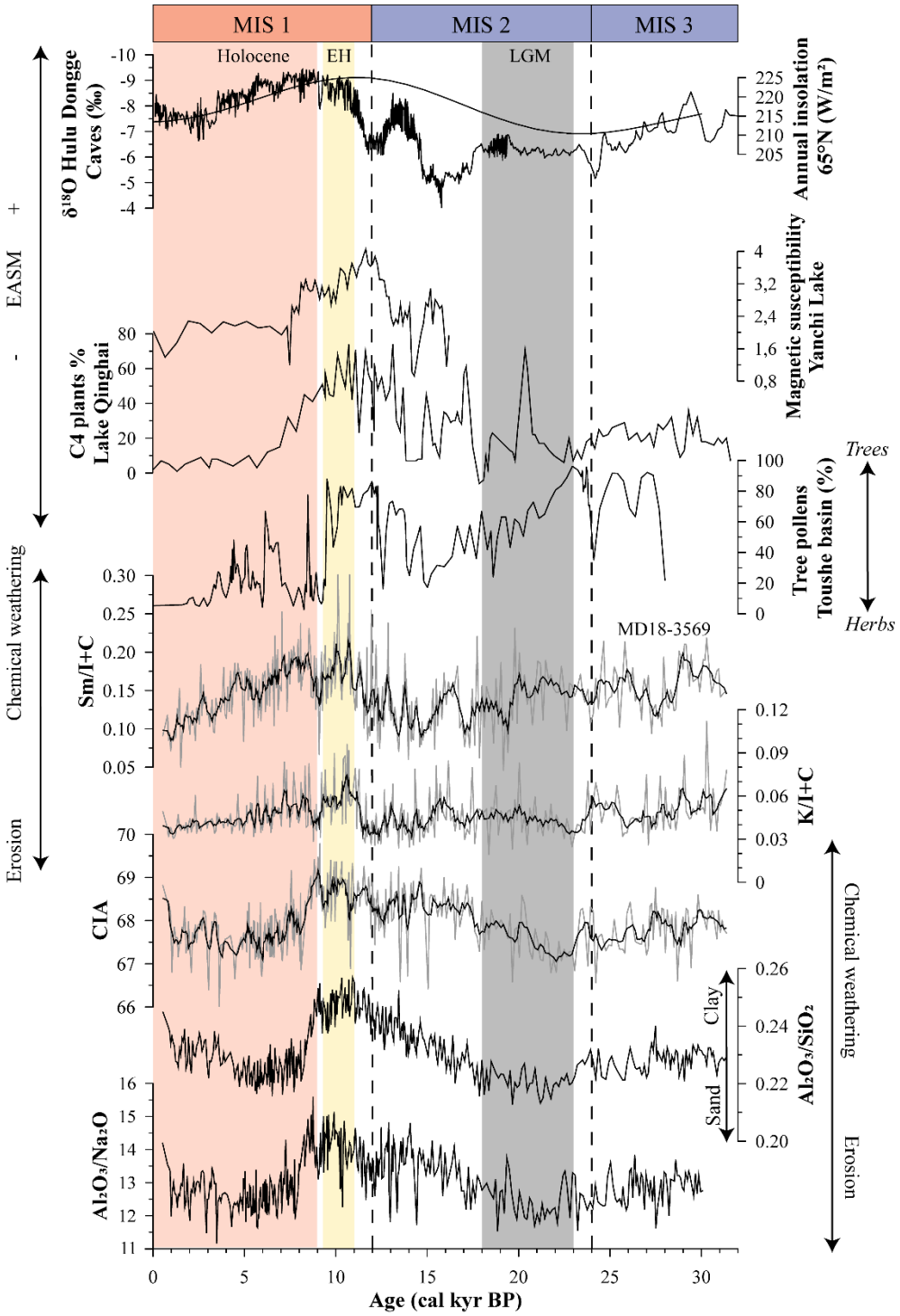

Figure 3-10. Temporal variations of erosional and weathering proxies of Core MD18-3569 for the past 32 kyr: clay mineralogical Sm/(I+C) and K/(I+C), major elemental CIA, Al_2O_3/SiO_2, and Al_2O_3/Na_2O, in comparison to climatic $\delta^{18}O$ variations of Hulu and Dongge Cave speleothems (Wang et al., 2001; Dykoski et al., 2005), the insolation curve received by the earth at 65°N of latitude (Berger 1978), magnetic susceptibility from Yanchi lake (Li et al., 2017), C4 plants proportion from Qinghai lake (central China) (Thomas et al., 2015)and pollen records from Toushe Basin (west Taiwan) (Sanchez Goñi et al., 2017).

3.5.4 Role of the East Asian monsoon and typhoon activity in variations of weathering in SW Taiwan

In Figure 3-10, chemical weathering proxy records of Core MD18-3569 are compared with $\delta^{18}O$ variations of Hulu and Dongge Cave speleothems (Wang et al., 2001; Dykoski et al., 2005) and Tibetan plateau lakes vegetation and magnetic susceptibility records (Qinghai and Yanchi lakes) (Li et al., 2013; Thomas et al., 2014). These $\delta^{18}O$ stalagmites have been used to reconstruct past rainfall in South China and the northeastern SCS region, 80% of which is generated by the EASM (Wang et al., 2001; Dykoski et al., 2005; Cheng et al., 2016). A negative shift of the $\delta^{18}O$ of the Hulu and Dongge Cave records corresponds to an increase in precipitation, while a period of more weakened EASM precipitation is characterized by a positive shift (Wang et al., 2001). Climate has important control on vegetation, e.g., C_4 plants are flourishing during summer season with warm and humid conditions. Liu et al. (2005) used C_4 plants proportions to reconstruct the moisture conditions. Magnetic susceptibility of sediments from north and central China is commonly used as a proxy of the summer monsoon variation, in wet time intervals, the enhanced chemical weathering and pedogenesis produce magnetic minerals increasing the magnetic susceptibility (An et al., 1991).

During the deglaciation and the early Holocene, clay mineralogical ratios (Sm/(I+C) and K/(I+C)) and elemental ratios (CIA, Al_2O_3/SiO_2, and Al_2O_3/Na_2O) increased, reaching a maximum at around 10 cal kyr BP. Thus, chemical weathering is increasing, and this can be correlated to a negative shift in the Hulu Dongge Cave $\delta^{18}O$ $\delta^{18}O$ and increase of magnetic susceptibility and C_4 plants proportions in Tibetan Plateau lakes resulting from intensified EASM rainfall (Fig. 3-10). The Holocene is characterized by a steady decrease of clay mineralogical ratios and leaching of mobile elements from 9 cal kyr BP to its minimum at the present time. This interval of reduced chemical weathering agrees with the progressive decrease in the EASM precipitation observed in the $\delta^{18}O$ record of the Hulu Dongge cave cave, Tibetan Plateau lakes (Fig. 3-10) and northern SCS (Contreras-Rosales et al., 2019). For Core MD18-3569, the state of chemical weathering of sediments recorded by Sm/(I+C) and K/(I+C) also displays a lower value interval, with minimum values occurring between 9.1 and 8.7 cal kyr BP (Fig. 3-10). This record is similar to the 9.2 kyr EASM collapse described by Zhang W et al. (2018) in a geochemical and pollen record from central China.

During the LGM, the clay mineral assemblage and major elements display less intensive chemical weathering than during the MIS3; this is in line with the shift to less negative $\delta^{18}O$ values resulting from weaker EASM precipitation. However, at a shorter time scale, rapid variations in the weathering proxies obtained on Core MD18-3569 (such as decreases of Sm/(I+C) centered at 17.5-16.8 cal kyr BP, 15.5-14.5 al kyr BP, 13.5-13 cal kyr BP, and 12.5-11.5 cal kyr BP, Fig. 3-10) are not associated with changes in monsoon rainfall as reconstructed from the Hulu Dongge cave $\delta^{18}O$ and Tibetan Plateau C4 plants and magnetic suceptibility records (Wang et al., 2001; Dykoski et al., 2005; Li et al., 2013; Thomas et al., 2014; Cheng et al., 2016). This could result from age models uncertainties or suggest that the chemical weathering record is sensitive to the long term EASM trends but less sensitive to short time and millennial scale changes with the exception of the major monsoon collapse at 9.2 cal kyr BP. Increased EASM precipitation slightly enhances the chemical weathering of sediments transferred from Taiwan to the northeastern SCS.

A pollen sequence from the Toushe Basin (west Taiwan) (Liew et al., 2006) is reported in Figure 3-10 and variations therein closely match those of the chemical weathering record obtained from Core MD18-3569 (Fig. 3-10). Long term changes in tree pollen are coeval with the those of the S/(I+C) mineralogical ratio. The proportion of herb pollen versus tree pollen increases during the MIS2, between 24 and 15 cal kyr BP, in agreement with colder and more arid conditions during this glacial time interval (Liew et al., 2006). Such variations in vegetation cover corroborate the LGM weakening of chemical weathering recorded by mineralogical (K/(I+C) and S/(I+C)) and geochemical (Al_2O_3/Na_2O, Al_2O_3/SiO_2, and CIA) ratios from Core MD18-3569 (Fig. 3-10). Similarly, during the deglaciation (from 15 and 9.6 cal kyr BP), contemporaneously with the increase of smectite and kaolinite production and leaching of Na and Ca (Fig. 3-10), warmer and subtropical forests were becoming established in the Toushe Basin, reflected in an increase in the proportion of tree pollen present (Liew et al., 2006). This implies a warming up of climatic conditions and a strengthening of EASM rainfall (Wang et al., 2001; Dykoski et al., 2005; Cheng et al., 2016). Such climatic conditions and vegetation cover led to progressive pedogenesis and chemical weathering of soil (Arnaud et al., 2012; Sun and Colin, 2014; Bajard et al., 2016, 2017a, 2017b). The short interval of weaker chemical weathering observed at about 9.2 cal kyr BP is also associated in the pollen sequence with a drastic change in the vegetation cover, with relatively fewer trees and a higher proportion of herbs; this change has been attributed to the monsoon rainfall collapse event (Liew et al., 2006; Zhang et al., 2018). The time interval covering the middle and late

Holocene is characterized by a decreasing trend in the proportion of trees pollen compared to herbs (Liew et al., 2006) indicating regressive pedogenesis (Arnaud et al., 2012; Sun and Colin, 2014; Bajard et al., 2016, 2017a, 2017b) synchronous with the weakening of chemical weathering recorded by core MD18-3569 sediments (Fig. 3-10). This interval is also marked by the weakening of the EASM (Wang et al., 2001; Dykoski et al., 2005; Cheng et al., 2016) which reduced chemical weathering. In addition, typhoons, which induce heavy precipitation events on the island of Taiwan, were shown to have been enhanced during the Holocene in the Pacific region (Wu, 1992; Moy et al., 2002; Chen et al., 2012; Zhou et al., 2019, 2021). Typhoon events induce intensive physical erosion of soils and rocks and rapid transport of sediment to the northeastern SCS through pronounced runoff (Liu J.P. et al., 2008; Xu et al., 2018a; Wang et al., 2020). However, typhoons frequency is considered to be associated with warm climate and intense summer monsoon and both induce rapid sediment transport, so clearly distinguishing typhoon and monsoon influence could be complicated (Clift, 2020). In present time, typhoons are triggering 70% of the turbidity currents on south Taiwan margin (Zhang Y., et al., 2018). A turbidites record from Gaoping submarine canyon (south Taiwan) indicates turbidite frequency, and by extension typhoon events frequency, is increased after 7 ka and not associated with the monsoon weakening (Yu S.W. et al., 2017). Such typhoon events, coupled with the weakened EASM during the Holocene, are favorable to soil destabilization and regressive pedogenesis as has been observed in terrestrial palynological records (Liew and al., 2006). This gives rise to a shorter residence time of minerals in the soils of the SW Taiwan river basins and a progressive erosion of soils which, in turn, results in the delivery to the ocean of deeper horizons of less chemically altered soil material. In such conditions, detrital material transported to the SW Taiwan margin will have undergone less chemical weathering (lower CIA value and Al_2O_3/Na_2O ratio) than during the early Holocene time interval.

The chemical weathering record obtained from Core MD18-3569 indicates that the EASM has similar forcings on chemical weathering in SW Taiwan small rivers sediments with the large east Asian river basins (Chen et al., 2016; Sang et al., 2022) in opposition with what has been reported previously (Zhao et al., 2017). Taiwan chemical weathering degree of soils is strongly affected by the changes of regional East Asian and Pacific moisture transport.

3.6 Conclusions

Clay mineral assemblages, major elements, and Nd-Sr isotopes of detrital sediments from Core MD18-3569 on the eastern bank of the Penghu Canyon in the northeastern SCS have been investigated to identify sediment provenance and reconstruct changes in the degree of weathering of the sediments from the SW Taiwan and their potential links to climatic change since the last glacial period.

The clay mineral assemblage - consisting mainly of illite (average 52%) and chlorite (average 32%), with a moderate proportion of smectite (average 12%) and small quantities of kaolinite (average 4%) - combined with Nd and Sr isotopes (average -11.27 for εNd and average 0.719 for $^{87}Sr/^{86}Sr$) indicates that SW Taiwan is the sole source of sediment to Core MD18-3569.

Variations in clay mineral assemblage (Sm/(I+C), K/(I+C)) and major elements (CIA, Al_2O_3/Na_2O) allow us to evaluate the intensity of weathering in the SW Taiwan river basins in the past. The CIA (average 68) and A-CN-K diagram indicate that sediments have experienced moderate weathering which allows us to use the Al_2O_3/Na_2O ratio to track the weathering state of sediments. We have demonstrated that long term changes in the intensity of chemical weathering in the drainage basins of SW Taiwan is mainly driven by changes in EASM rainfall and environmental changes (pedogenesis) over the past 32 kyr. The state of chemical weathering intensity of sediments transported to the SW Taiwan margin is modified by changes in vegetation cover. The time interval between 18 and 9 cal kyr BP is characterized by a progressive increase in the intensity of chemical weathering, which reaches a maximum at the beginning of the Holocene (from 11 to 9 cal kyr BP).

The state of chemical weathering of sediment transferred from SW Taiwan to the northeastern SCS decreases during the middle-late Holocene in agreement with a weakening of the EASM, a change in the vegetation cover (less tree pollen and a higher proportion of herbs) and an increase in typhoon activity. All these processes are favorable to soil destabilization, erosion, and regressive pedogenesis. In such conditions, detrital material transferred to the SW Taiwan margin will be less chemically weathered (lower CIA value and Al_2O_3/Na_2O ratio) due to minerals having a shorter residence time in the soils of SW Taiwan.

Chapter 4 Control of Sea-level on sedimentation of the Penghu Canyon bank during the last 32 kyr

Abstract

Submarine canyons are key conduits in sediment transport in marine environment, as they permit efficient and important sediment redistribution and accumulation in deep-sea basins. The responses of submarine canyon systems and sediment transport in Taiwan Strait to sea level changes are still unclear. A high-resolution grain size record covering the last 32 cal kyr BP obtained on Core MD18-3569, collected on the eastern levee of Penghu Canyon (south of Taiwan), was investigated to reconstruct the impact of the deglaciation sea level rise on the canyon sedimentary dynamic. Sediments deposited on the Penghu canyon levee are consisting of fine silt with an average mean grain size of 13.35 µm without any marks of turbiditic deposit. The grain size drops abruptly by 40% in 0.7 kyr from 10.7 to 10 cal kyr BP in a time interval corresponding to the Melt water pulse-1C. The rapid transgression completely reorganized the sediment transport, reducing the coarse grain end-member size directly supplied by rivers without changing sediment provenance. The rapid transition indicates a brutal land-sea reconfiguration which could suggest a disconnection of Penghu Canyon from rivers potentially draining the previously emerged Taiwan Strait. Prior to the MWP-1C, the grain size gradually decreased concurrently with the deglaciation triggered sea level rise. This demonstrates that the proximity of the deposit site to river mouths is a controlling factor of sediment redistribution in northern South China Sea. During highstand sea level periods, the sediments were finer with larger clay content and derived from the SW Taiwan rivers through the surface circulation. The variations of grain size could have resulted from the forcing of the East Asian monsoon system and El Niño Southern Oscillation on sediment supply or redistribution.

Key words: grain size, Penghu canyon, Taiwan, Taiwan Strait, sedimentology, sea level.

4.1 Introduction

Submarine canyons play an active role in terrigenous sediments and terrestrial organic matter and carbon redistribution to deep sea and marine sedimentation (Liu J.T. et al., 2009) Submarine canyons activity can be strongly affected by sea level fluctuations. Indeed, many canyons such as the Penghu submarine canyon have their head located far from the shoreline

at water depths that potentially emerged during low stand sea level intervals (Fig. 4-1). The configuration of the shelf (length, slopes, active margin) is the main factor controlling the canyon-head-shoreline connectivity response to sea-level fluctuation (Bernhardt and Schwanghart, 2021). Canyons located on narrow and steep shelves and active margins are more likely to stay connected to the shore despite sea-level rise (Bernhardt and Schwanghart, 2021). Such configuration coupled to the important discharge of Gaoping River explains why the Gaoping Canyon head remained connected to the river mouth. The Penghu Canyon direct connection to paleo river system remains controversial as the canyon head doesn't seem directly connected to the Penghu Channel on the Taiwan Strait (Huang and Yu, 2003). However, the Taiwan Strait could be considered as a relatively flat and large shelf explaining the canyon head didn't remain connected or close to the shoreline in present time high stand (Bernhardt and Schwanghart, 2021).

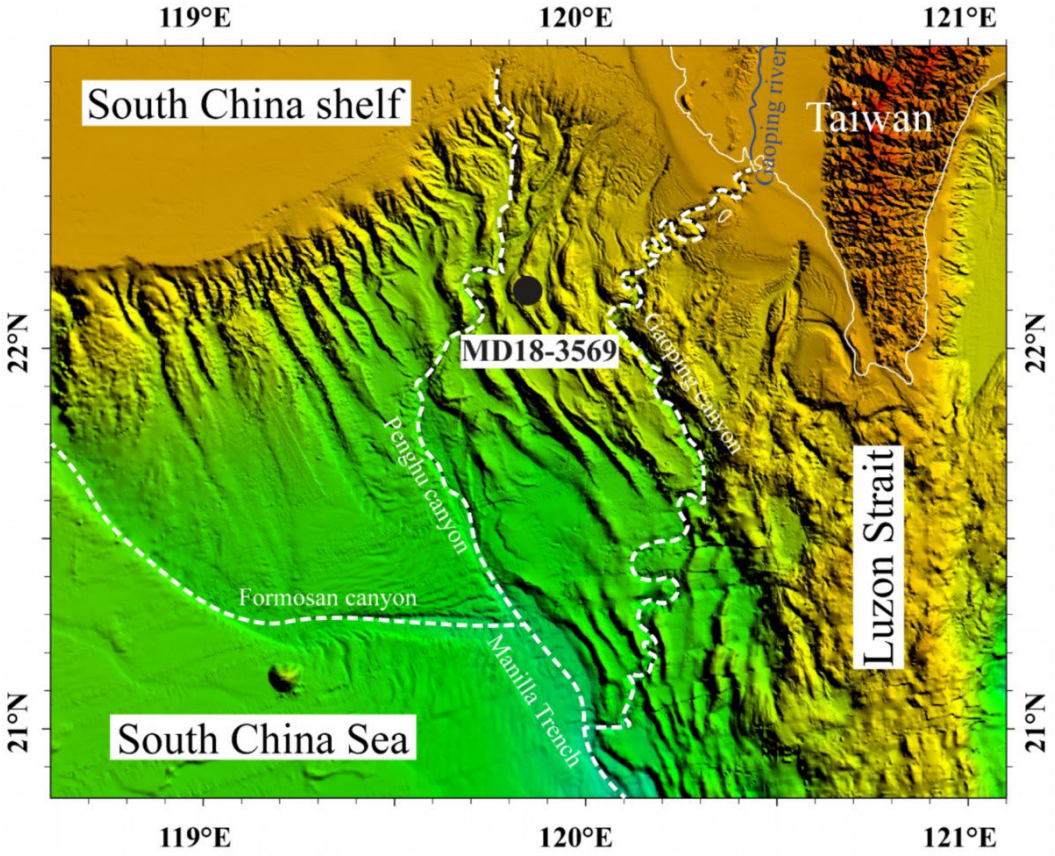

Figure 4-1. Bathymetric map of the margin of Taiwan in northeastern South China Sea displaying the location of Core MD18-3569. Manilla Trench system is also reported.

Many canyons not connected to shores at modern times have been studied on the different continents and present a substantial decrease of activity and sediment fining with sea level rises (Normark et al., 1983; Rasmussen, 1994; Druckman et al., 1995; Popescu et al.,

2004). Monterey Fan system, on the California continental margin, presents like the Manilla Trench system, active and connected (Monterey Canyon), and inactive and non-connected to shore (Ascension Canyon) canyons. The Monterey Canyon has an important turbiditic activity in recent time and high stand sea level. The Ascension Canyon, similarly, to Penghu Canyon, is thought to have been connected to the shore and direct sediment supply. It is indicated by the low stand turbiditic activity of the canyon and the high stand sediments fining and canyon inactivity (Hess and Normark, 1976; Normark et al., 1983; Paull et al., 2005, 2011; McGann, 2014). In general, in the northern South China Sea, during interglacial periods and high stand sea-level phases the terrigenous material transport is strongly affected from source-to-sink processes due to fluctuations in sea level and distance from river mouths to deposit sites (Boulay et al., 2003, 2007, 2008; Liu J., et al., 2016).

The Gaoping canyon sedimentary dynamic is characterized by high turbiditic activities (Yu S.W. et al., 2017; Zhang et al., 2018) typical of shore-connected submarine canyons. The sedimentary dynamic of the Penghu Canyon is unclear. Similarly to some non-connected canyons, Penghu Canyon could present turbiditic activity in present and past times (Kudrass et al., 1998; Zhong and Peng, 2021). The sediments deposited on the Penghu Canyon levees are sourced from the SW Taiwan rivers (Nayak et al., 2021). The sediment provenance didn't change with the last deglaciation induced sea-level rise (Fig 3-5, 3-7). Thus, the question of the potential direct connection between the Penghu Canyon head and a paleo river system is still debatable.

In this chapter, the high-resolution grain size record of Core MD18-3569, collected on the eastern levee of Penghu Canyon, has been investigated since the last glacial period. The aims are (1) to characterize potential Penghu Canyon turbiditic activity (2) to reconstruct the impacts of the glacial-interglacial sea level fluctuation on SW Taiwan sediment redistribution, (3) to identify a direct connection between the Penghu Canyon and south-west Taiwan rivers through the Taiwan Strait.

4.2 Climatic settings

Taiwan climate is controlled by the East Asian monsoon system and typhoons. The yearly rainfall rate of Taiwan is about 2500 mm/yr (Dadson et al., 2003). The East Asian monsoon system is characterized by a seasonal reversal of the direction of wind and a shift of intertropical convergence zone (ITCZ) latitude. The seasonal shift is associated with humidity migration over the East Asian region (Webster et al., 1994, 1998; Ruddiman, 2001).

The summer season represents most of the yearly rainfall in Taiwan when strong East Asian summer monsoon winds are coinciding with the early typhoon season (Wu and Kuo, 1999; Chen and Chen, 2003; Su et al., 2012). During the boreal summer, the ITCZ is located between 20 and 35°N and affects Taiwan region. During summer and autumn, from July to November, Taiwan is hit by 3 to 4 typhoons formed in western tropical Pacific and adjacent marginal seas (Liang et al., 2017; Zhang et al., 2018). In winter, the ITCZ is shifting southwards between 0 and 20°S, resulting in a relatively dry season over Taiwan (Wang P. et al., 2003).

The monsoon winds and the Kuroshio Current intrusion are controlling the northeastern SCS surface circulation (Hu et al., 2000). During the summer, the strong northeastward monsoon winds are generating an anti-cyclonic surface gyre in northern SCS and a surface current flowing northwards along the South China coast to the Taiwan Strait (Fang et al., 1998; Wu, 2014). In winter, the strong southwestwards monsoon winds are inducing the formation of a surface cyclonic gyre in northern SCS and the coastal current flows southwards on the South China Shelf from Taiwan Strait and East China Sea (Fang et al., 1998; Wu, 2014). The deep Luzon Strait, with a water depth of 2400m, is the only deep-sea direct connection between the SCS and the western Pacific Ocean (Li and Qu, 2006; Qu et al., 2006). Surface and deep waters are inflowing to the SCS through the Luzon Strait and compensated by an outflow of intermediate water to the western Pacific Ocean (Yuan, 2002; Tian et al., 2006; Gan et al., 2016; Zhu et al., 2019). During autumn and winter, the surface water mass flows along the Taiwan margin in northern SCS forming the SCS branch of Kuroshio (Caruso et al., 2006; Liu et al., 2013). In northern SCS, loop currents are deriving from the SCS branch of Kuroshio (Li et al., 1998; Liu et al., 2013). The Kuroshio loop currents are forming when the strong winter monsoon winds are deflecting the SCS branch of Kuroshio westward (Farris and Wimbush, 1996; Li et al., 1998). The loop currents can generate shedding eddies that can propagate to the Taiwan Strait during strong winter monsoon and La Niña state of El Niño Southern Oscillation (ENSO) (Sun et al., 2020). The deep-water current entering the SCS through the Luzon Strait results in the SCS Contour Current circulation (Zhao et al., 2014; Liu Z.F. et al., 2016).

4.3 Material and methods

4.3.1 Material

The Calypso core MD18-3569 (22°09.30'N - 119°49.24'E; 40.08 m in length; 1320 m water depth) was collected in June 2018 on the eastern bank of the Penghu Canyon during the HYDROSED cruise aboard the R/V *Marion Dufresne* (Fig. 4-1). Core MD18-3569 mainly consists of a greenish-gray homogenous hemipelagic mud without any visible laminations.

For this study, the upper 15 m of the core were investigated and sampled with a resolution of 5 cm for the upper 3 m and the depth interval from 8 to 15 m and 2.5 cm for the 3-8 m depth interval. A total of 381 samples were collected to perform grain size analyses. In addition, 185 sub-samples were selected with a resolution of 5 cm for the upper 6 m, 10 cm for the 6-10 m depth interval and 20 cm for the depth interval from 10 to 15 m to analyze the carbonate content.

The age model of the upper 15 m of Core MD18-3569 was established using linear interpolation between nine calibrated AMS ^{14}C dates obtained from monospecific samples of planktonic foraminifer *G. ruber* (>150 μm) (Chen et al., 2021). For this study, an additional ^{14}C date obtained from monospecific samples of planktonic foraminifer *G. ruber* (>150 μm) was analyzed at the *Laboratoire des Sciences du Climat et de l'Environnement (LSCE)*, Gif-sur-Yvette (France). The record covers the last 31.4 cal kyr BP with a mean sedimentation rate of 54.7 cm/kyr allowing us to obtain a high temporal resolution for the grain size analyses (~85 yrs). The linear sedimentation rate (LSR) is low during the last glacial maximum (LGM) (34.9 cm/kyr) and increases during the deglaciation and the Holocene peaking at 72.9 cm/kyr during the late Holocene.

4.3.2 Grain size analyses

Grain size analyses were processed on organic-free and decarbonated sediments at the State Key Laboratory of Marine Geology, Tongji University, using a Beckman-Coulter LS230 with a particle size range from 0.02 to 2000 μm.

Before the measurement of the bulk siliciclastic grain size distribution, the organic matter was removed using 5 ml of 10% H_2O_2, the solution was gently shaken for several days, and sediments were rinsed with deionized water. The 381 samples were then decarbonated using 10mL 0.5% hydrochloric acid (HCl) and HCL residues were rinsed. The sediments were

stirred and poured in the Beckman-Coulter LS230 to process the grain size analyses on two acquisitions. The second acquisition, more stable, was selected.

4.3.3 Carbonate content analysis

Carbonate content ($CaCO_3$%), clay minerals' X-Ray diffraction analyses were performed at the State Key Laboratory of Marine Geology (Tongji University) on 185 samples collected every 5 cm for the upper 6 m and every 10 to 20 cm from 10 to 15 m.

Carbonate content was analyzed using the gasometric techniques from Jones and Kaiteris (1983) with a precision higher than ±1%. After the establishment of a standard curve of PCO_2 emitted for different masses of $CaCO_3$%, the sample were dried and weighted. 100 mg of sample was put to react with the HCl, and the ridden PCO_2 was confronted with the standard curve to determine the mass of $CaCO_3$% in the bulk section.

4.4 Results

4.4.1 Grain size analyses and End-member (EM) modelling

Figure 4-2 presents the Core MD18-3569 temporal variations of grain size over the last 31.4 cal kyr BP. The average mean grain size is 13.35 µm, consisting of fine silt, vary with a small range from 8.35 to 20.31 µm. The sediments are mainly composed of silt (average: 75%; range: 84.80-91.40%) with minor clay (average: 24%; range: 7.33-14.95%) and scarce sand (average: 1%; range: 0-5.10%) (Fig. 4-2).

The grain size variation displays two major time intervals (Fig. 4-2). The Holocene is characterized by the finest sediments with an average mean grain size of 10.63 µm (Fig. 4-2). During the Holocene, the grain size distribution shows a relative increase of clay fraction (12.61%) proportion and decrease of sand fraction content (0.26%) (Fig. 4-2).

During glacial MIS2 and 3, the mean particle size is coarser (15.37 µm) driven by the increased proportion of silt (88.56%) sand (2.07%) and lower proportion of clay fraction (9.38%) (Fig. 4-2). The mean grain size peaks during the LGM with in a range of 15.48 to 20.10 µm from 23 to 18 cal kyr BP (Fig. 4-2). The two time intervals are separated by an abrupt decrease of the grain size from 10.7 to 10.0 cal kyr BP (Fig. 4-2). The transition is characterized by a drop of the 5 points average mean grain size from 15.19 to 9.10 corresponding to a decrease of 40% of the grain size (Fig. 4-2).

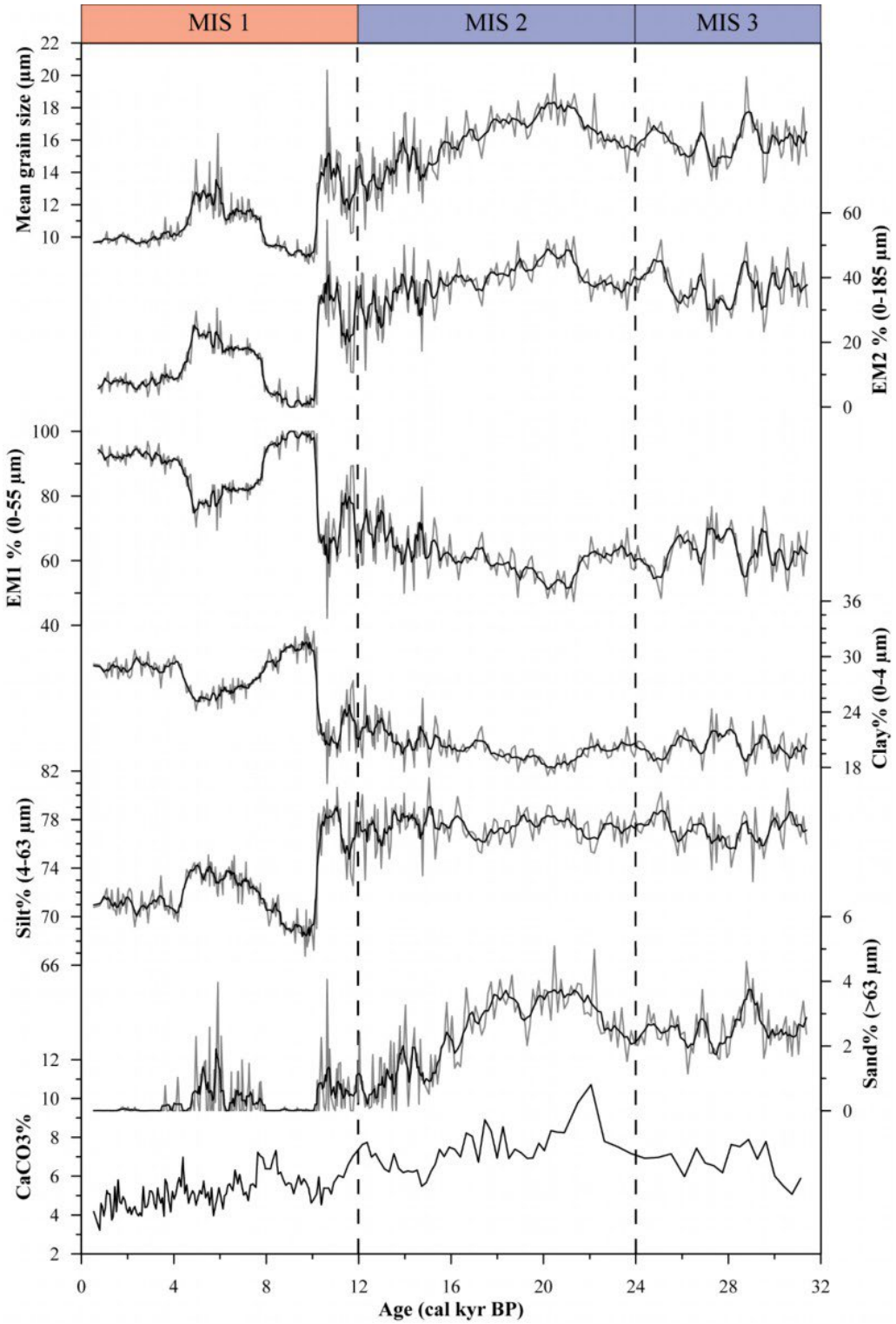

Figure 4-2. Past variations of Core MD18-3569 mean grain size, End-members 1 and 2, clay, silt and sand contents and carbonate contents during the last 32 cal kyr BP.

Additionally, the open-source software QGrain was used to proceed to a non-parametric grain size end-member (EM) modeling approach (Liu et al., 2021) (Fig. 4-3). For the last 31.4 cal kyr BP, a two EM model was selected. The EM1 has a grain size distribution ranging from

0 to 55 µm, containing clays and fine silts (6.46 µm) (Fig. 4-3). The EM2 contains coarser sediments (19.50 µm) ranging from 0 to 185 µm, consisting of medium to coarse silts and sands (Fig. 4-3). EM1 amounts for ~75% of total sediments, and EM2 accounts for ~25% (Fig. 4-2). The temporal variations of the EMs proportions are displaying anticorrelated variations. The proportion of EM2 covaries with the temporal variations of the mean grain size and EM1 proportion varies with the clay fraction proportion (Fig. 4-2). Both EMs are presenting two time intervals separated by the abrupt transition from 10.7 to 10.0 cal kyr BP. EM1 (EM2) proportion increases (decreases) from 60 to 100% (40 to 0%).

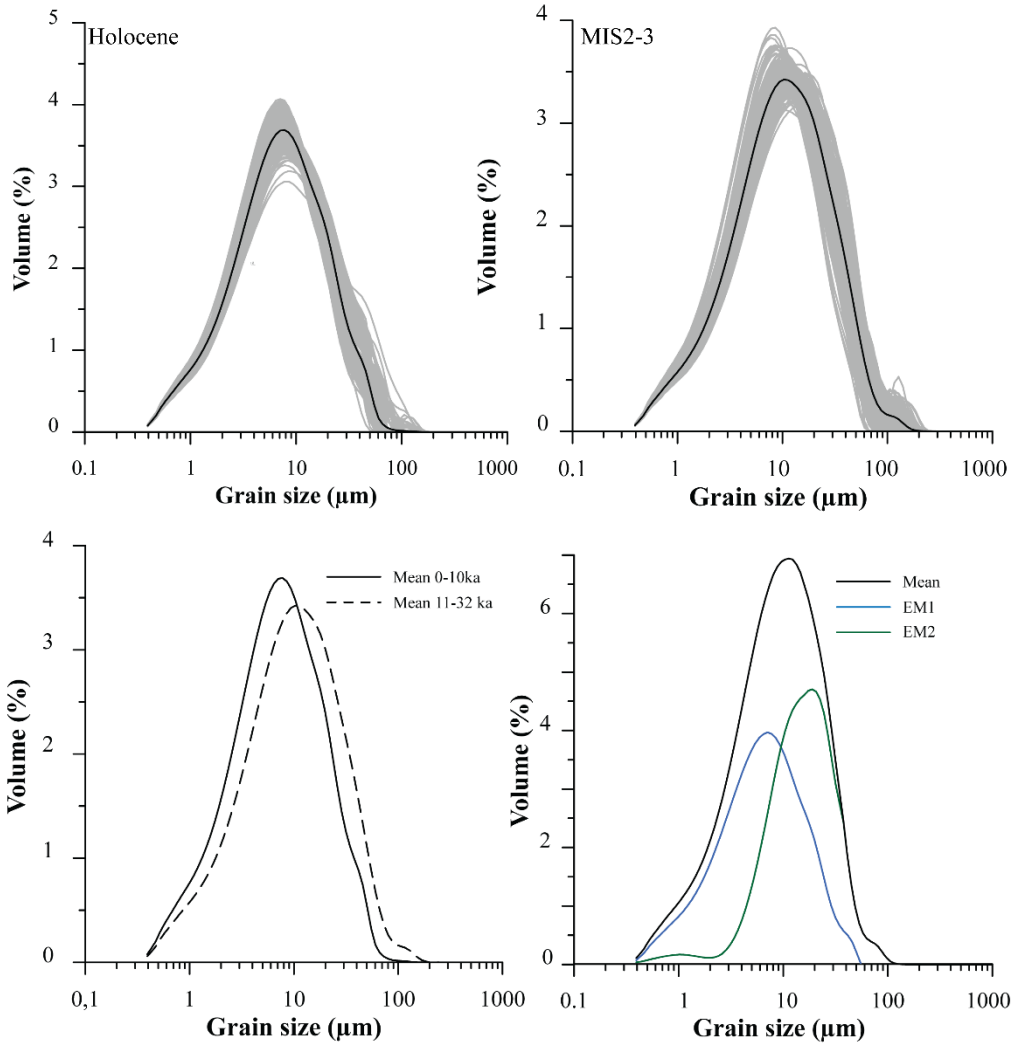

Figure 4-3. Grain size distribution of Core MD18-3569 sediments from 10 kyr to present, 32 to 11 kyr (gray curves are individual distribution, black curve represents the average distribution of each time interval). Comparison of the average size distribution of 0-10 kyr and 11-32 kyr time intervals. Size distribution of grain size End-members during the last 32 kyr obtained following Liu et al., 2021.

4.4.2 Carbonate content

The carbonate content of the upper 15 m of Core MD18-3569 is lower than 10% ranging from 3 to 10% (Fig. 4-2). Between 31.4 and 12 cal kyr BP, $CaCO_3$% display a slightly higher range from 5 to 10% with higher content during the LGM at 22 cal kyr BP (10.7%). Since the beginning of the Marine isotopic stage (MIS) 1, the $CaCO_3$% presents a steady decreasing trend from 10% to 3% in the late Holocene (Fig. 4-2).

The $CaCO_3$% of Core MD18-3569 is well correlated to the bulk sediments CaO% (Fig. 3-4). CaO% and $CaCO_3$% correlation (R) and determination (R^2) coefficient are close to 1 ($R=0.86$ and $R^2=0.74$) (Fig. 4-4). CaO% temporal resolution is higher than $CaCO_3$% as the carbonate content was measured on sub-samples of the 381 geochemical composition analyses. So, for the following discussions, the CaO% will be used as an indicator for the carbonate content.

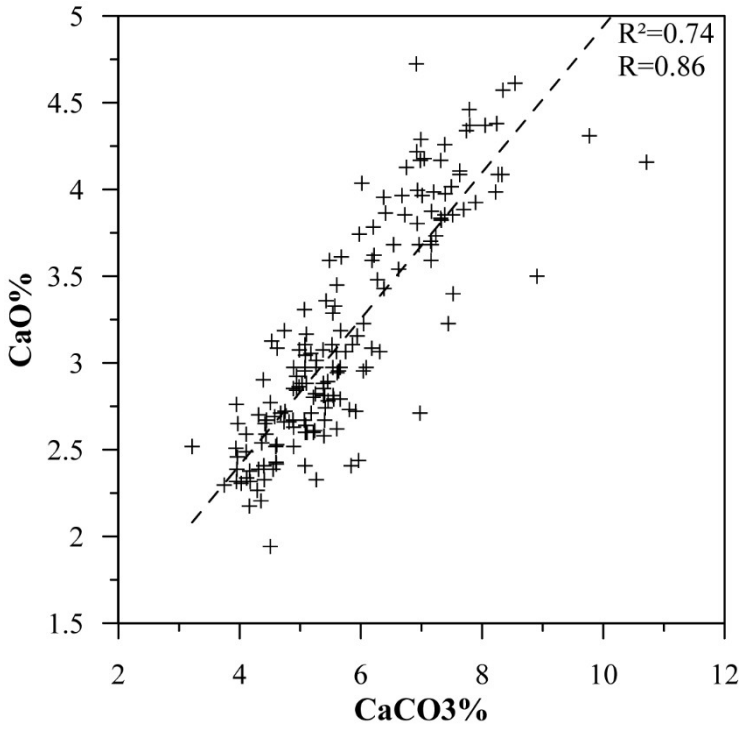

Figure 4-4. Correlation plot of carbonate content ($CaCO_3$%) versus CaO% of Core MD18-3569.

4.5 Discussion

4.5.1 Penghu canyon system sedimentary dynamic during sea level lowstand

Grain size variations and sea level variations display good co-variations in different marine sedimentary systems across the world (Normark, 1974; Normark et al., 1983; van Hengstum et al., 2011; Boulay et al., 2008; Yi et al., 2012; Switzer and Pile, 2015; Jiwarungrueangkul et al., 2019). Core MD18-3569 mean grain size of 13.35 µm is very fine compared to grain size measured in south-west Taiwan rivers (>100 µm) (Deng et al., 2019; Fang et al., 2022). This indicates that a major part of the sediments is not input directly, but potentially through surface circulation. For Core MD18-3569, EM1 (median 6.46 µm; 0-55 µm) corresponds to fine sediments derived from the source to the Penghu Canyon levee. Whereas EM2 (median 19.50 µm; 0-185 µm) corresponds to direct inputs from the closest rivers. EM1 accounts for ~75% of the sediment deposited on the Penghu Canyon levee. This is coherent with the hypothesis that a major part of the sediments derived from SW Taiwan rivers mouths through surface circulation.

Grain size record and EMs models of Core MD18-3569 display two major periods separated by an abrupt transition from 10.7 to 10.0 cal kyr BP (Fig. 4-2, Fig. 4-3). During this event, the mean grain size drops of around 40%, EM1 peaks to a proportion of 100% indicating that all sediments derived to the eastern canyon through the surface circulation which indicates an important modification of the sediment transport. The two EMs modeling approach has been applied to the two times intervals from 31.4 to 10.7 cal kyr BP and from 10 cal kyr BP to present time (Fig. 4-5) (Liu et al., 2021).

The EMs modeling applied to the two-time intervals shows that both EMs size distribution shifted to finer distribution and medians (Fig. 4.5). EM1 median grain size presents a minor shift from 7.52 µm (MIS2-3) to 6.26 µm (Holocene). However, EM2's median grain size is nearly divided by two, from 19.94 to 10.90 µm after the 10.7 cal kyr BP transition. This indicates that the direct terrigenous sediment transport is strongly impacted by this event.

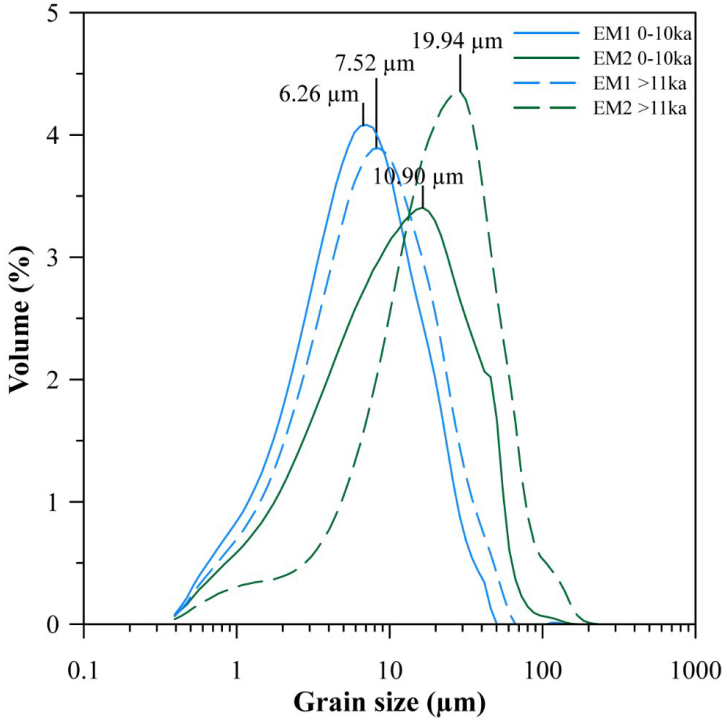

Figure 4-5. End-Member models grain size distribution of time intervals from 0 to 10 kyr (solid lines) and from 11 to 32 kyr (dashed lines) of Core MD18-3569 obtained with Qgrain (Liu et al., 2021). The median grain size of End-Members is also reported.

The time interval from 10.7 to 10 cal kyr BP corresponds to an important mangrove erosion episode on the Sunda Shelf associated with the Melt Water Pulse event 1C (MWP-1C) observed globally (Grant et al., 2012; Duan et al., 2023; Yu et al., 2023) (Fig. 4-6). The MWP-1C event locally led to rapid transgressions (e.g., ~20 m in East China Sea (Liu J.P. et al., 2004)).

Such abrupt transition could result from the disconnection of the Penghu Canyon from a potential sediment supply conduit (e.g., river or channel). It could also completely open the strait and stop the shelf remobilization. However, the provenance of the sediments deposited on the Penghu Canyon bank does not vary over the last 31.4 kyr (Fig. 4-6). During MIS2 and 3, the land-sea and environmental configurations were very different than Holocene and recent times. Coarse material was discharged to the Penghu Canyon by the rivers system developed on the emerged Taiwan Strait. With the rapid MWP-1C, the Penghu Canyon was cut from the close transport system and changes in the circulation could have occured. Then, the Penghu Canyon receives finer terrigenous sediments (40%) from the same rivers (southwest Taiwan) than before the MWP-1C. Coarse sediments are trapped in Taiwan Strait and fine sediments mostly derived from the river mouths similarly to others disconnected

submarine canyons (Hess and Normark, 1976; Normark et al., 1983; Paull et al., 2005, 2011; McGann, 2014).

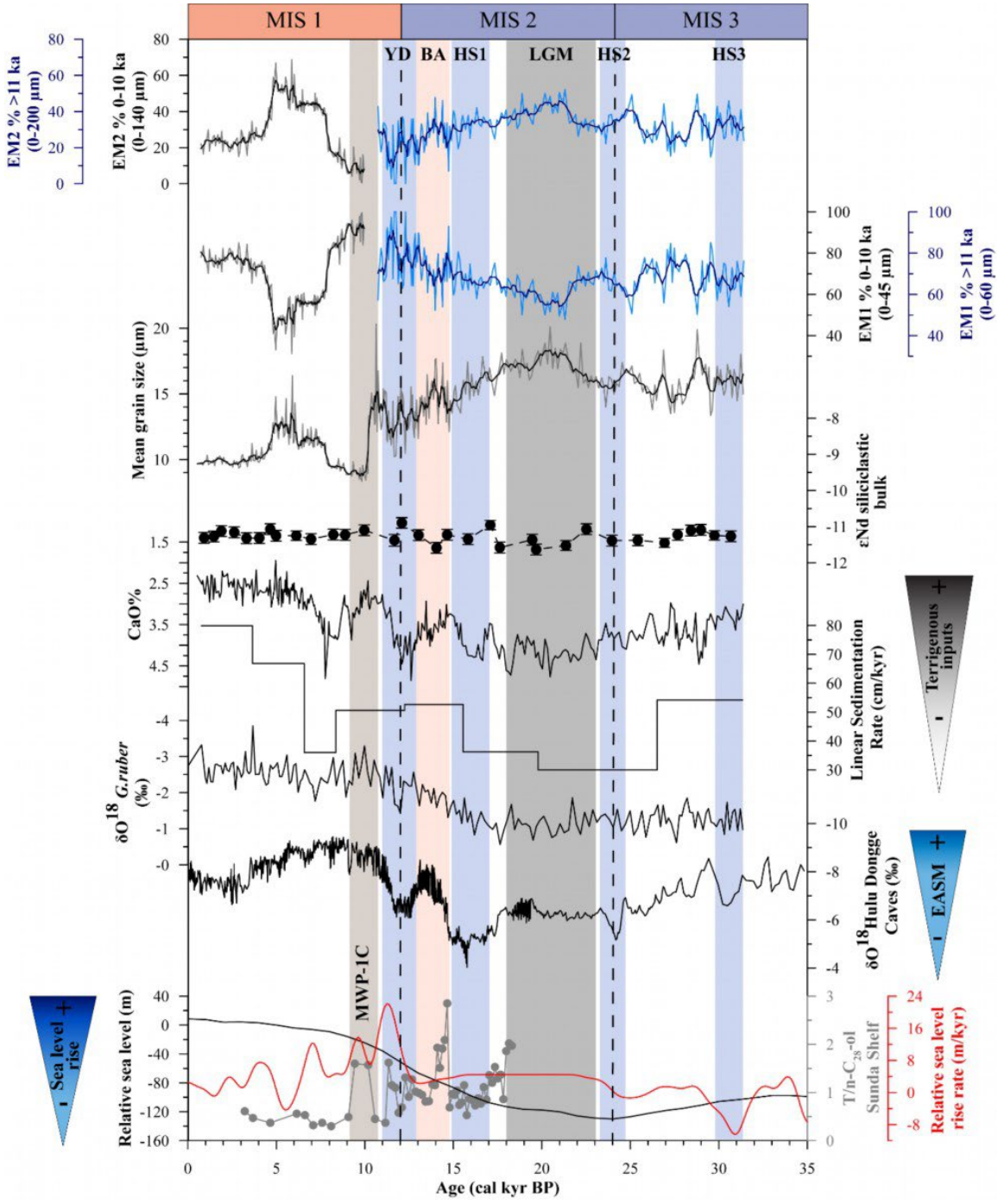

Figure 4-6. Temporal evolution of EMs, mean grain size, bulk siliciclastic εNd of the carbonate free fraction, CaO%, linear sedimentation rate and *G. ruber* $\delta^{18}O$ from Chen et al. (2021). The Hulu and Dongge Cave speleothems (Wang et al., 2001; Dykoski et al., 2005), relative sea level (Lisiecki and Raymo, 2005) and sea level rise rate (Grant et al., 2012; Yu et al., 2023) variations are reported.

Prior to the transition, the sedimentary dynamic was also affected by the gradual sea level rise since the LGM. The sediments are mainly composed of fine silts and clay without any turbidites. The mean grain size (15-20 µm), EM2 (~40%) (Fig. 4-2, 4-3) and sand content (~4%) (Fig. 4-2) are peaking between 23 and 18 cal kyr BP when the sea level is at the minimum (Lisiecki and Raymo, 2005; Lambeck et al., 2014; Spratt et Lisiecki., 2016) (Fig. 4-6). During the LGM, linear sedimentation rate of Core MD18-3569 is low (>40 cm/kyr) and carbonate content relatively high (Fig. 4-6), which indicates low dilution by terrigenous inputs in the northern SCS (Huang E. et al., 2015). So, the rivers sediment yield was low and coarse material was not enhanced by strong detrital material discharge. Moreover, during the MIS3 and early MIS2, climate is considered cold and dry (Wang et al., 2001; Dykoski et al., 2005; Cheng et al., 2016) (Fig. 4-6). In this time interval, SW Taiwan rivers, currently located at 80-100 km of the study site, were closer or directly connected to the Penghu Canyon. The increased vicinity of sediment sources enhanced coarser material transport to the study site (Boulay et al., 2003). From the LGM to 10.7 cal kyr BP, the mean grain size, EM2 and sand contents display a decreasing trend covarying with the gradual sea level rise (Lisiecki and Raymo, 2005; Lambeck et al., 2014; Spratt et Lisiecki, 2016) (Fig. 4-6).With the sea level rise and Taiwan Strait flooding, the distance between the river systems and the Penghu Canyon levee is increasing and sediments reaching the levee are fine (Boulay et al., 2003).

Grain size and terrigenous input records also show responses to shorter climatic events (Bolling Allerod (BA), Younger Dryas (YD)) during the deglaciation which is not the case during MIS3 and early MIS2 (Fig. 4-6). The BA is characterized by higher grain size (>15 µm), sand content (>2%) and sedimentation rate (>50 cm/kyr) and lower carbonate content, due to higher terrigenous inputs. This indicate more important and coarser detrital materials which are discharged to the SCS in link with higher precipitation (Wang et al., 2001; Dykoski et al., 2005; Huang E. et al., 2015; Cheng et al., 2016). Inversely, the YD is associated with lower precipitation, grain size and terrigenous inputs (Fig. 4-6). This indicates that less and finer detrital materials are redistributed to the SCS in association with the drier climate (Wang et al., 2001; Dykoski et al., 2005; Cheng et al., 2016). During the LGM and early deglaciation, the northern SCS shelves were exposed. River systems and vegetation cover were then largely extended on large emerged continental shelves and Taiwan Strait (Yu S. et al., 2017; Cheng et al., 2023). During the LGM, the climate was colder and drier and dense tropical to semi tropical grasslands and forests were installed on the Taiwan Strait (Liew et al., 1998; Sun et al., 2000; Ray and Adams, 2001). Several studies based on pollen records and

models have shown the presence of herbaceous plants and subtropical broad-leaved and conifers trees (Zhou et al., 2012; Dai et al., 2015a, 2015b; Zhang D. et al., 2016; Bandara et al., 2023). The vegetation cover on the emerged Taiwan Strait might have had an important impact on source-to-sink processes as important vegetation cover stabilizes the lands and enhance sedimentation (Ouyang et al., 2010; Vargas-Luna et al., 2015; Bhattacharjee et al., 2022). The thick vegetation cover of the time interval MIS3-LGM might have less sensitivity of soil to weathering by rapid climatic changes events like those induced by northern hemisphere cold Heinrich events. When sea level rose during the deglaciation, the shelves environmental configuration was reworked by the floodings and enhancing detrital records responses to Bølling-Allerød and Younger Dryas (Fig. 4-6). The low sediment yield associated to low precipitation and dense vegetation cover could also explain the absence of turbidite activity in Penghu submarine canyon during the time interval when the canyon was potentially connected to the rivers system.

4.5.2 Holocene high sea level sediment redistribution

After the MWP-1C, the land-sea configuration is disrupted, Taiwan Strait is completely immersed, and the closest rivers mouth (Erhjen and Tsengwen rivers) are located at ~40 km from the Penghu Canyon head. In such land-sea configuration, currents system might have impacted hydrodynamic conditions.

At 10.7 cal kyr BP, grain size becomes finer and clay fraction and EM1 proportions are more important reaching up 100% in agreement with a disconnection of the river system to the head of the Penghu Canyon (Fig. 4-1). The mean grain size drops below 10 µm, EM2 proportion and sand content are close to 0% and EM1 and EM2 median size are finer (Fig. 4-2) during the early and late Holocene. During the Holocene, the linear sedimentation rate is higher because of high terrigenous inputs due to the summer monsoon and typhoons rainfall (Fig. 4-6). However, the grain size is not constant and during the middle Holocene, a time interval from 8.1 to 4.4 cal kyr BP displays slightly coarser grain size (>11 µm) (Fig. 4-7). During this time interval, the sea level is stable, and the plateau of coarse grain size cannot be associated with closer river mouths (Fig. 4-7). Thus, the middle Holocene grain size variations might be resulting from changes in terrigenous inputs and/or hydrodynamic changes.

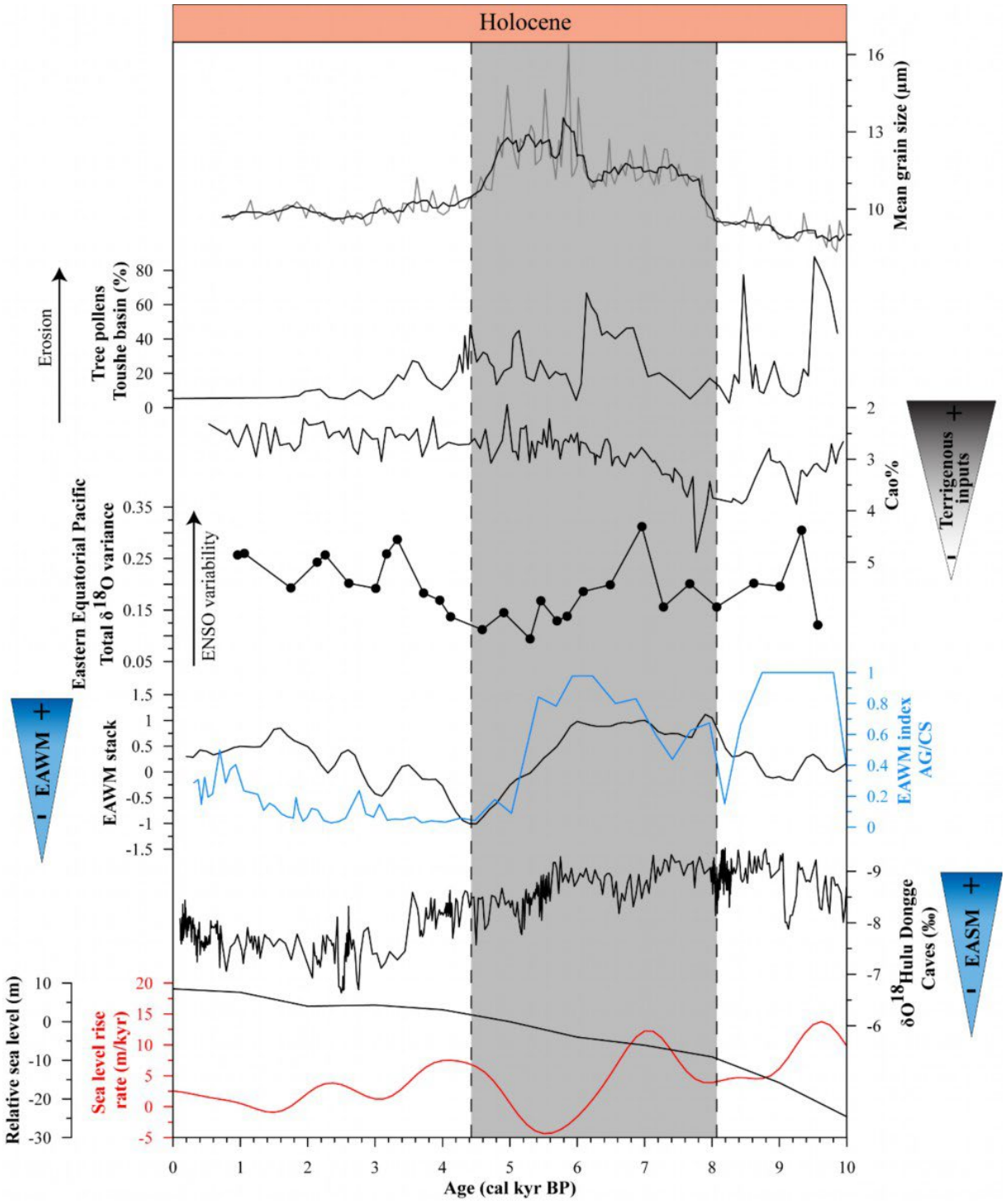

Figure 4-7. Holocene temporal evolution of mean grain size and Cao% of Core MD18-3569 in comparison to a pollen records from Toushe Basin (west Taiwan) (Sanchez Goñi et al., 2017), to climatic eastern equatorial Pacific Ocean $\delta^{18}O$ variance of *G. ruber* (Koutavas and Joanides, 2012), EAWM proxies (EAWM stack (Kaboth-Bahr et al., 2021), EAWM index (Wang et al., 2012), $\delta^{18}O$ variations of Hulu and Dongge Cave speleothems (Wang et al., 2001; Dykoski et al., 2005), and sea level variations (Lisiecki and Raymo, 2005; Grant et al., 2012).

During the middle Holocene, the carbonate content is low, indicating high terrigenous inputs (Fig. 4-7). Sediments derived from SW Taiwan rivers are highly affected by the high physical erosion associated to strong typhoon mild East Asian summer monsoon during the Holocene (Liew et al., 2006). In addition to the typhoon activity, the middle Holocene is characterized by strong East Asian winter monsoon from 8.5 to 4.5 cal kyr BP (Tian et al., 2010; Huang E., et al., 2011; Wang et al., 2012; Wu et al., 2019; Kaboth-Bahr et al., 2021; Cho et al., 2022). The EAWM is strengthening again after 4 cal kyr BP (Yancheva et al., 2007; Wang et al., 2012; Kaboth-Bahr et al., 2021) (Fig. 4-7). However, the amplitude of the variations of EAWM during late Holocene are still debated (Yancheva et al., 2007; Wang et al., 2012; Kaboth Bahr et al., 2021). At lower latitude ENSO and the higher proportion of El Niño period might modulate the EAWM variations (Koutavas and Joanides, 2012; Zhao et al., 2019; Cho et al., 2022). The middle Holocene is characterized by a lower ENSO activity (Lu et al., 2018) so the EAWM was not reduced during this interval. A pollen record from Toushe Basin displays a decrease of tree taxa compared to herbaceous plants after 8.5 kyr cal BP indicating an important episode of erosion (Liew et al., 2006, Sun and Colin, 2014). Thus, the strong erosion associated with high typhoon activity and enhanced EAWM could have resulted in coarser sediment discharge by the SW Taiwan rivers (Peizhen et al., 2001).

Grain size variations can also reflect hydrodynamic and current changes at different time scales (Gao et al., 1994; McCave et al., 1995b, 2017; Huang, et al., 2011; Liu J. et al., 2016). Sea surface hydrology of the northern South China Sea is controlled by the seasonal reversal of winds and Kuroshio Current intrusion through the Luzon Strait. This have been shown to modify sediment dynamic of the northern SCS (Liu J. et al., 2013; Wang et al., 2023). The loop currents are surface currents located in the northern South China Sea and deriving from the Kuroshio Current (Farris and Wimbush, 1996; Li et al., 1998). The Kuroshio loop current are forming when the strong winter monsoon winds are affecting Kuroshio intrusion (Farris and Wimbush, 1996). The Kuroshio loop current can produce shedding eddies during strong winter monsoon and La Niña periods. The eddies deriving from the loops can reach Taiwan Strait and have influence at an important vertical scale (<1000m) (Li et al., 1998; Sun et al., 2020). During the middle Holocene, the Kuroshio Current influence on the northern SCS was important in link with the stronger EAWM period and La Niña phase until 4.5 kyr (Jiang et al., 2006; Liu J. et al., 2013; Barr et al., 2019). The more important occurrence of the Kuroshio loop current could have also result in a more dynamic environment on the Taiwan margin and strait. The more energetic environment could also have impacted the sediment

redistribution and resulted in the increased grain size observed on the Penghu Canyon bank (Fig. 4-7) (McCave et al., 1995b). The Holocene grain size record of Core MD18-3574 could thus reflect the impact of the variation of monsoon system on sediment transfer from land to sea and redistribution by the surface currents.

4.6 Conclusion

In this chapter, the sediment grain size of the Core MD18-3569 collected on the eastern bank of Penghu Canyon (south Taiwan) has been investigated to reconstruct the impact of glacial-interglacial sea level fluctuations on sediment transfer to the deep-sea basin of the northern South China Sea.

The average grain size of sediments deposited on the eastern levee of the Penghu Canyon is 13.35 μm. The important difference between Penghu Canyon bank and Taiwan rivers sediment grain size and End-member modeling indicates that ~75% of sediments derive through surface circulation and ~25% sediments are transported by direct riverine inputs.

The grain size record displays a brutal transition from 10.7 to 10 cal kyr BP where the mean grain size drops by 40% in less than a millennial coinciding with a major transgression the MWP-1C. The transgression reconfigured the sediment redistribution strongly reducing the inputs of coarse EMs to nearly 0%. This characterized a potential disconnection of the Penghu Canyon from direct terrestrial sediment supply through the Taiwan Strait.

During the low sea level, the vicinity of the Penghu Canyon to SW Taiwan and emerged Taiwan Strait river systems enhanced the supply of coarse sediments. The deglaciation sea-level rise gradually reduced the proximity of the canyon to the surrounding rivers resulting in a steady decrease of terrestrial grain size deposited on the eastern Penghu Canyon bank.

Holocene grain size is finer than during the glacial period and characterizes sediments derived from SW Taiwan rivers by the surface circulation. In the high stand interval, climatic conditions such as winter monsoon could also have impacted the sediment supply and/or redistribution from the rivers to the sea.

Chapter 5 Late Holocene typhoon activities affecting Taiwan recorded by turbidity currents in Gaoping Canyon

Abstract

The reconstruction of paleo typhoon activity in East Asia, with associated climatic and environmental forcing mechanisms, are key to understand and predict evolution of typhoon frequency and intensity in the context of ongoing anthropic global warming. The Gaoping submarine canyon (south of Taiwan) transfers large amount of sediment to the deep basin of the South China Sea (SCS) mainly via typhoon-driven hyperpycnal flows. In this study, we have combined high resolution non-destructive analyses of Fe/Ca and Si/Al by XRF core scanning and darkness (Rmean) and clay fraction contents of sediments (Clay R2200) by hyperspectral imaging with punctual measurements of XRD bulk mineralogy and of laser grain size of fine laminate sediment (millimetric to centimetric) of Core MD18-3574. This core was collected on the western levee of the Gaoping submarine canyon. The main goal of this study is to establish the frequency and intensity of typhoon activity over the past 4500 yrs. The mean grain size ranges from 9 to 20.5 μm (average value of 13.4 μm) indicating that Core MD18-3574 sediments consist mainly of fine silt, presenting alternating fine-grained and coarse-grained laminations. Thick coarse-grained laminations display a fining-upward and asymmetric sorting of typical turbidite deposits. Principal component analyses (PCA) demonstrates that dark laminae are composed of coarser sediments with high Si/Al ratios, slightly higher contents of quartz and high contents of feldspar, higher Clay R2200 values (lower clay fraction contents) and lower Fe/Ca attributed to the deposition of sediment under hyperpycnal flow reaching the studied levee. Inversely, light laminae consist of fine sediments with low Si/Al, low proportions of muscovite and illite, low Clay R2200 (high (lower contents of clay fraction) and high Fe/Ca resulting from hemipelagic deposition. We have thus identified 2404 dark laminae attributed to hyperpycnal flow induced mainly by high-intensity typhoons affecting the Gaoping river basin. We have thus calculated, for the first time, a detail record of the frequency of typhoons which indicates a decrease in their frequency since 4.2 cal kyr BP in response to decreased sea surface temperature (SST) in the western subtropical Pacific Ocean and enhanced East Asian winter monsoon. The tropical storm intensity, deduced from the thickness of the turbidites, has increased since 2 cal kyr BP in La Niña-like periods indicating that the surge of super-typhoons hitting Taiwan could be triggered by El

Niño Southern Oscillation (ENSO) variability. We can thus infer that the tropical storm activity is controlled by SST of the western subtropical Pacific region, monsoon system and ENSO conditions. This study brings new insights in the prediction of the impact of ongoing climate change on storm activity in the western Pacific Ocean.

Key words: Taiwan, Gaoping submarine canyon, typhoon, ENSO, hyperpycnal flows.

5.1 Introduction

Around 80 tropical storms form each year at the tropical and subtropical latitudes of the Ocean (Emanuel, 2003). Tropical cyclones, called typhoons in the western North Pacific regions, are the most intense tropical storms, accounting for more than 50% of the yearly events (Emanuel, 2003; World Meteorological Organization). Tropical cyclones impact strongly on human societies and activities, costing about 43.9 billion US dollars every year in the United States and 28.7 billion yuans in China (Zhang et al., 2009; Smith, 2020). In the region of Taiwan, the rainfall associated with the 3-4 typhoons that occur per year leads to destructive processes on land, such as landslide, and floods which cause considerable damage and casualties (Shieh et al., 2010; Lo et al., 2014; Deng et al., 2016; Yang et al., 2018; Tsai et al., 2021, 2022). Strong typhoons like Morakot (2009) can produce rainfall and sediment loads sufficient to trigger deep-sea hyperpycnal flows and damage human submarine infrastructures like telecommunication cables to the south of Taiwan (Su et al., 2012; Gavey et al., 2017). The variations in the East Asian monsoon system linked with orbital forcing, and El Niño Southern Oscillation (ENSO) control the climate in Taiwan and western Pacific regions (Wang et al., 2001, 2005, 2014, 2015; Moy et al., 2002; Dykoski et al., 2005; Clift and Sun, 2006; Cheng et al., 2016; Yu et al., 2016; Zhang et al., 2018; Zhao et al., 2018; Hu et al., 2020). The interactions between the ENSO, monsoon, and sea surface temperature (SST) of the tropical Pacific Ocean determine the pattern of moisture distribution in the region (Elsner et Liu, 2003; Lin et al. 2008, Liu et al., 2017; Zhu et al., 2017).

The southern continental shelf of Taiwan is narrow and the head of the Gaoping submarine canyon is connected to the Gaoping River mouth (Liu J.T. et al., 2016) (Fig. 5-1). Because of this land-sea configuration, the transport of sediment in the Gaoping submarine canyon is mainly controlled by hyperpycnal flows deriving from floodwaters of the Gaoping River (Zhang et al., 2018). Hyperpycnal flows have an important erosional impact truncating the deposition sequences in the canyons (Mulder et al., 2003; Chiang and Yu, 2006). The overflow capacity of the hyperpycnal flows results in lower density and turbidity processes

reducing erosional processes on the levees of the Taiwan margin (Lehu et al., 2015). Data from a mooring system located on the canyon levee has shown that between 2013 and 2016 4 typhoon-driven hyperpycnal flows occurred per year (Zhang et al., 2018), accounting for 70% of the total sediments deposited on the levee (Zhang et al., 2018). During the monitoring time interval, about 70% of the turbidity currents observed on the levee were shown to have been triggered by high sediment river discharge induced by typhoon events (Zhang et al., 2018). The Gaoping submarine canyon rapidly transports sediment, via hyperpycnal flows, from the Gaoping River catchment to the deep basin of the South Chine Sea (SCS) (Milliman et al., 1992; Liu J.T. et al., 2009). Sediments deposits on the levee of the Gaoping submarine canyon, located on the Southern margin of Taiwan, are an ideal archive to reconstruct past changes in typhoon activity (Anschutz et al., 2002; Hess et al., 2005; Babonneau et al., 2013, Bonneau et al., 2014; Yu et al., 2017). The western levee of the Gaoping submarine canyon is located at about 600 m above the canyon thalweg. Thus, it should record major turbidity currents which overflow the canyon walls, and which are associated with major paleo typhoon river floods.

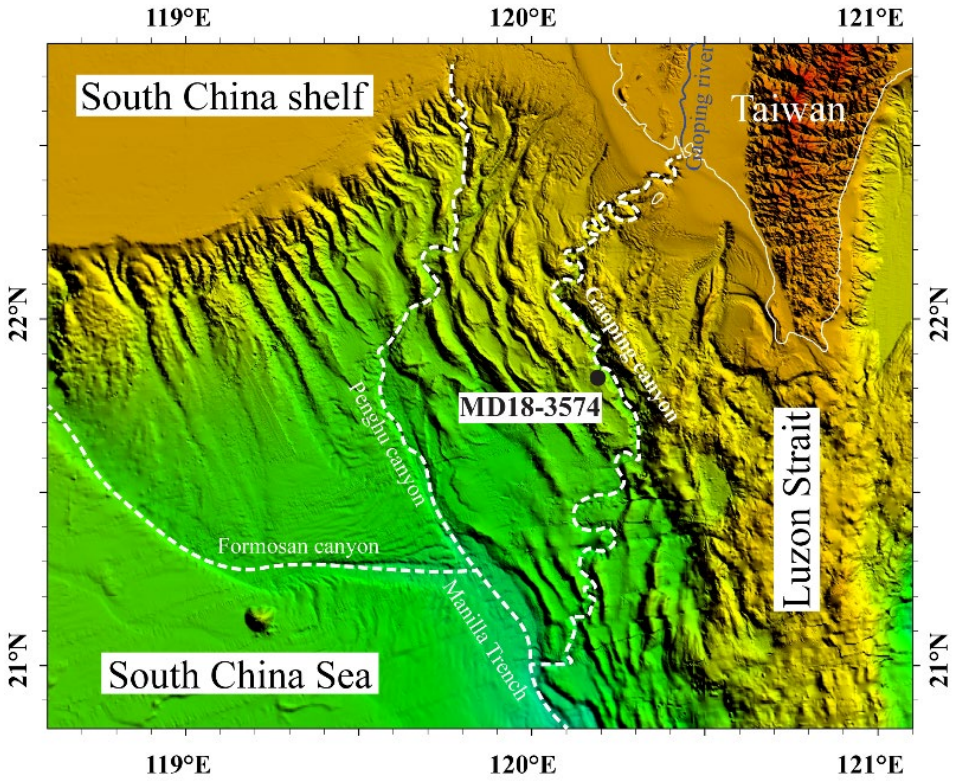

Figure 5-1. Bathymetric map of the northeastern SCS showing the location of Core MD18-3574.

The Gaoping River and the surrounding small rivers transport large volumes of fine sediments (fine silt and clay). At the river mouth, sediments are transported on the slope and the submarine canyon and settle by decantation on the southern margin of Taiwan (Stow and Tabrez, 1998; Stow and Smillie, 2020). During typhoons, the intense rainfall and runoff lead to high physical erosion and the sediment discharge of the Gaoping River to the South China Sea increases (Dadson et al., 2003; Xu et al., 2018b; Wang et al., 2020). In such conditions, the concentration of suspended-sediment in the river plume on the slope and canyon head can be high enough to generate nepheloid layers on the slope and turbulent hyperpycnal flows in the canyon (Milliman et al., 1992; Dadson et al., 2003; Mulder et al., 2003; Poppe et al., 2008; Liu J.T. et al., 2009, 2012, 2016; Liu Z.F. et al., 2010, 2016; Hsu et al., 2014; Zhang et al., 2018; Tian et al., 2022).

In recent decades, development in scanning methods, such as X-ray fluorescence (XRF) core scanning and hyperspectral imaging, has brought new insights in geosciences with non-destructive high-resolution analyses (1000 to few mm) spectra. XRF core scanning has been widely used to study, at high resolutions, relative geochemical compositions of records in lacustrine (Arnaud et al., 2016; Wang et al, 2019; Rapuc et al., 2020) and marine environments (Xie et al., 2014; Xu et al., 2018b; Yu et al., 2017; Hsiung et al., 2021; Bozyiğit et al., 2022). Attention has been given to highly dynamic environments around Taiwan to investigate turbiditic systems and floods linked with paleoclimatic changes at different time scales (Yu et al., 2017; Wang et al, 2019; Hsiung et al., 2021). Sediment cores have also been scanned using hyperspectral imaging in conjunction with XRF core scanning to reconstruct paleoclimatic and environmental changes in lacustrine and drainage basins (Butz et al., 2015; Jacq et al., 2020, 2022a; Sorrel et al., 2021). Hyperspectral imaging has also been used to determine occurrences of past floods in lacustrine and fluvial systems (Jacq et al., 2019, 2022b; Ghanbari et al., 2020; Rapuc et al., 2020). Whereas interest is growing in the use of hyperspectral imaging interest in the study of fine laminated sediments in continental environments, this analytical method is still rarely used in the context of marine sediments.

In this study, we have investigated high-resolution non-destructive hyperspectral imaging and XRF core scanning, combined with radiocarbon dating, XRD bulk mineralogy and high-resolution laser grain-size of laminated sediments from the Calypso Core MD18-3574. This core was collected on the western levee of the Gaoping submarine canyon in order (1) to constrain the sedimentary processes responsible for the deposition of the laminations and (2) to establish the frequency and intensity of typhoons affecting Taiwan over the past 4500 yrs.

The studied levee is located at an altitude of about 600 m above the thalweg of the Gaoping submarine canyon, close to the mooring system investigated by Zhang et al. (2018) who have identified several typhoon-driven hyperpycnal flows per year. The fine laminations that characterize the lithology of Core MD18-3574 thus have great potential to yield a continuous reconstruction of the turbidites resulting from typhoon-driven hyperpycnal flows and thus to establish the past intensity and frequency of typhoons that have affected southern Taiwan during the late Holocene.

5.2 Environmental setting

At the present time, the tropical climate of Taiwan is largely driven by the East Asian monsoon (EAM) system and typhoons (Webster, 1987; Wu and Kuo, 1999; Chen and Chen, 2003; Wang et al., 2003 Su et al., 2012; Liang et al., 2017; Zhang et al., 2018). In South Taiwan, the annual rainfall is about 2500 mm/yr and the summer season is characterized by 80% of the yearly rainfall (Chen and Chen, 2003; Dadson et al., 2003). The EAM is defined by a seasonal reversal of wind direction and a latitudinal shift of the intertropical convergence zone (ITCZ) and moisture transport over East Asia due to the inversion of land-ocean heat gradient (Webster et al., 1994, 1998; Ruddiman, 2001). During the summer, the ITCZ is located between 20 and 35°N leading to an important supply of moisture to the Taiwan region (Wang et al., 2003). In winter, the ITCZ shifts southwards, to between 0 and 20°S, resulting in a less humid winter season in the Taiwan region (Chen and Chen, 2003; Wang et al., 2003). Taiwan's rainfall regime is strongly affected by typhoon events. The typhoon season mainly spans from July to November and about 3 to 4 typhoons hit Taiwan yearly contributing up to 40% of Taiwan's total rainfall (Wu and Kuo, 1999; Su et al., 2012; Zhang et al., 2018). In modern times, typhoon mean rainfall intensity is about 20 mm/hour and the most extreme events can produce up to the average yearly total rainfall (e.g., Herbs ~1800 mm in 1996 and Morakot >3000 mm in 2009; (Wu and Kuo, 1999; Chien and Kuo, 2011; Su et al., 2012).

The Gaoping River, with a length of about 170 km, is one of the longest rivers in Taiwan (Liu J.P. et al., 2008; Liu J.T. et al., 2009). The river drains about 3260 km² (the largest draining basin in Taiwan), stretching from its source near Yu-shuan (Jade Mountain) in the Central Hsuehshan Range over 3000 m above sea level to its mouth in the northern SCS (Liu J.T. et al., 2009). The important runoff (2500 mm/yr) coupled with the steep topography of the Gaoping River basin result in a high erosion rate (3-6 mm/yr) and a sediment discharge to the SCS of 49 Mt/yr (Dadson et al., 2003; Liu J.T. et al., 2009). Some 80% of the sediments

supplied are delivered to the SCS by the canyon, and only about 20% of sediments are delivered to the Gaoping slope (Huh et al., 2009). Formed by the collision of the Philippines and China continental plates (Liu et al., 1997), the canyon is 260 km long and merges with the Manilla Trench. The depth of the canyon can reach 600 m and the relief varies from a V to a U profile, limiting the overflows (Chiang et al., 2006, 2011).

5.3 Material and Methods

5.3.1 Material

The Calypso Core MD18-3574 (21°50.42'N, 120°10.67'E; 22.52 m long; 1171 m water depth) was collected on the western levee of the Gaoping submarine canyon during the *HYDROSED cruise* on the *Marion Dufresne* in 2018 (Fig. 5-1). The sediment core is finely laminated with two different units, greenish light gray homogenous hemipelagic mud and fine pluri-millimetric heterogenous dark gray layers. For this study, all the cores were scanned for hyperspectral imaging and XRF core scanning at high resolutions. 450 samples were collected with a 2 mm depth resolution from selected core intervals of 13.65-13.85 m and 21.00-21.70 m for laser grain size analyses and 10 of these samples were also used for XRD bulk mineralogy analysis.

5.3.2 Chronological framework

Radiocarbon dating was undertaken at the UMS-ARTEMIS Facility (CNRS-CEA Saclay, France) using a Pelletron 3MV AMS on 8 mg of well-preserved calcareous test samples of planktonic foraminifera (plurispecific samples of *G. ruber*, *G. sacculifer, O. universa*) in the size fraction >150 µm (Table 5-1). The age model for the core was derived from the calibrated planktonic ages by applying a sea-surface reservoir ^{14}C correction of 400 yr and using Marine13 (Reimer et al., 2013) calibration curve in the CALIB 8.2 software (Stuiver and Reimer, 1993).

Table 5-1: Core MD18-3574 chronological framework, AMS ^{14}C dates obtained on plurispecific samples of *G. ruber, G. sacculifer*, *O. universa* and calibrated to calendar age using CALIB 7 and Marine13 curve (Stuiver and Reimer, 1993; Reimer et al., 2013).

Core	Section	Depth (cm)	Material	AMS ^{14}C ages (kyr BP)	Calendar age (cal kyr BP, 1σ)	error (± kyr)
MD17-3574	1	53.5-58.5	G. *ruber*, G. *sacculifer,* O. *universa*	0.540 ± 0.030	0.188	0.052
	2	178-183		0.705 ± 0.030	0.347	0.044
	2	275-280		1.080 ± 0.030	0.647	0.025
	3	385.5-390.5		1.300 ± 0.030	0.849	0.043
	5	615-620		1.895 ± 0.030	1.445	0.048
	6	815-820		2.260 ± 0.030	1.864	0.043
	7	1003.5-1008.5		2.535 ± 0.030	2.216	0.055
	9	1300-1305		2.850 ± 0.030	2.636	0.061
	11	1600-1605		3.310 ± 0.030	3.154	0.054
	13	1920-1925		3.750 ± 0.030	3.670	0.054
	16	2245-2250		4.035± 0.030	4.043	0.057

The ^{14}C dates range from 4.043 cal kyr BP at 22.47 m to 0.188 cal kyr BP at 0.55 m (Table 5-1). The age model of Core MD18-3569 has been established by using linear interpolation between eleven calibrated AMS ^{14}C dates processed with the Bacon package (Blaauw and Christen, 2011). The mean sedimentation rate of Core MD18-3574 is very high (0.56 cm/yr), permitting us to obtain a high temporal resolution of analyses spanning the last 4 cal kyr BP (Fig. 2-3). The sedimentation rate is very high in time intervals from 4.043 to 2.216 cal kyr BP (in average 0.68 cm/yr) and from 0.347 to 0.188 cal kyr BP to the present time (0.79 cm/yr) (Appendix 5-1). The linear sedimentation rate displays a decreasing trend during the last 4 cal kyr BP (Appendix 5-1).

5.3.3 Hyperspectral imaging

Hyperspectral imaging was processed at *M2C laboratory, Université Rouen-Normandie,* using two hyperspectral camera sensors covering the Visible and Near InfraRed (VNIR) and Short Wave-InfraRed (SWIR) spectral range of 400-2500 nm. The data collection followed hyperspectral image acquisition protocols from Butz et al. (2015) and Jacq et al. (2020, 2022). The sediment core surface was smoothed and flattened as much as possible to reveal sedimentary structures masked by oxidation and to eliminate sediment surface variations that might distort the signal. The calibration table, illumination unit and camera heights were adjusted to obtain relevant images for our study (VNIR pixel size: 40-200 µm; SWIR pixel size: 150-500 µm). Camera focus and parameters (integration time, frame rate) were optimized in order to get a sharp image. Black (shutter closing, instrumental noise, 0% reflectance) and white (white spectra reference, 100% reflectance) were recorded to normalize the spectra of the sediments in terms of percentage of reflectance. After pre-processing settings (exposition time calibrating noise), reflectance spectra information was captured and detrended to correct and normalize the spectra from a baseline following Jacq et al. (2020, 2021, 2022).

To consider the spectral variation of the sample, the Rmean indicator for average reflectance was used for both cameras (Rmean VNIR and Rmean SWIR) (Trachsel et al., 2010). VNIR and SWIR spectra show specific absorptions of certain compounds at specific wavelengths (Krupnik et al., 2019; Viscarra Rossel et al., 2010). To model them, a simple approach is to consider the reflectance value at this wavelength. It is also possible to use reflectance ratios or derivatives to correct for some effects (matrix, moisture, texture, other compounds). Thus, for the study of clays that absorb around 2200 nm (Madejová et al., 2017), the Clay R2200 index was created. Similarly, organic matter absorbs around 1650 nm (Viscarra Rossel et al., 2010) and the OM index R1650 was created to study it. To consider the effect of OH bonds induced by moisture as well as by clays or organic matter, the Moisture R1935 and Hydroxyl bonds R1450 indices have been created, as well as their R1935/R1450 ratio (Viscarra Rossel et al., 2010).

5.3.4 Relative geochemical composition analysis

XRF core scanning was processed on Core MD18-3574 at two different resolutions (1 mm and 1cm). The core surface was previously cleaned, flattened, and smoothed to prevent perturbations and its center covered with a Ultralene film (4 µm thick). The Core was then scanned firstly at a resolution of 1 mm using an Itrax XRF core scanner at the *Second Institute*

of Oceanography, Ministry of Natural Resources (Hangzhou, China) to obtain relative geochemical variations at the lamina scale. The Itrax XRF core scanner parameters were set for a 10 second exposure time at 60 kV and 45 mA. As some elements cannot be accurately analyzed under such conditions (e.g., Al, Si, Br), the core was also scanned at a resolution 1 cm at the *State Key Laboratory of Marine Geology, Tongji University* (Shanghai, China), using an Avaatech XRF core scanner set at a 30 second exposure time with 10 kV and 0.2 mA (covering Al to Fe), 30 kV and 0.8 mA (covering Co to Mo), and 50 kv and 0.2 mA (covering Tc to U). The XRF core scanner results are relative geochemical composition variations expressed in counts per second (cps).

5.3.5 Grain size analysis

Grain size of both bulk sediments (1) and carbonate free sediments (2) were processed using a Beckman-Coulter LS230 with a particle size ranging from 0.02 to 2000 µm. Prior to the measurement of bulk sediment grain size distributions (1), organic matter was removed using 5 mL of 10% H_2O_2. The solution was gently shaken for several days, and sediments were rinsed with deionized water. Organic matter was removed beforehand for the carbonate free sediments (2), then the sediments were decarbonated using 10 mL 0.5% hydrochloric acid (HCl). After the decarbonation, the HCl residues were washed three times using deionized water. The solution was introduced into the Beckman-Coulter LS230 to carry out the grain size analysis in two acquisitions; the second acquisition was usually more stable and was selected.

5.3.6 Bulk mineralogy analysis

Bulk mineralogy was determined on ten samples collected in laminae (five dark and five light laminar samples). 0.5 to 1 g of dried sediments were first pre-grinded before using a Retsch XRD-Mill McCrone with agate balls and ethanol for fine grinding (<1 µm). The bulk minerals were analyzed using X-ray diffraction (XRD) performed with a PANalytical X'Pert PRO diffractometer. As the fine grinding process with ethanol potentially may have affected the smectite, the samples were put in a 1M $CaCl_2$ to saturate the samples in calcium and to reconstitute the 001 smectite peak at 15 Å. A second analysis was performed and compared with the natural to reveal the presence or absence of smectite. Sample diffractometers results were treated using the open-source Profex software to identify the minerals.

5.4 Results

5.4.1 Relative geochemical composition and hyperspectral imaging

Relative geochemical compositions measured on Core MD18-3569 using the XRF core scanner at centimetric and millimetric resolutions are shown in figure 5-2. Fe, Ca, Ti, and K intensities display similar variations when analyzed at resolutions of both 1 mm and 1 cm (Appendix 5-2). However, for elements such as Al, Si, and Br the measurements have inconsistent results (Appendix 5-2). At a resolution of 1 mm, these elements were not detected from the background noise by the Itrax XRF core scanner due to the low exposure time of sediments to the X-ray used. At a resolution of 1 cm, the exposure time of sediments to X-ray is sufficient and the detection of Al, Si, and Br is no longer problematic. Thus, in what follows, Fe, Ca, Ti, and K are considered at a millimetric resolution, while Al, Si, and Br are discussed at a centimetric resolution (Fig. 5-2).

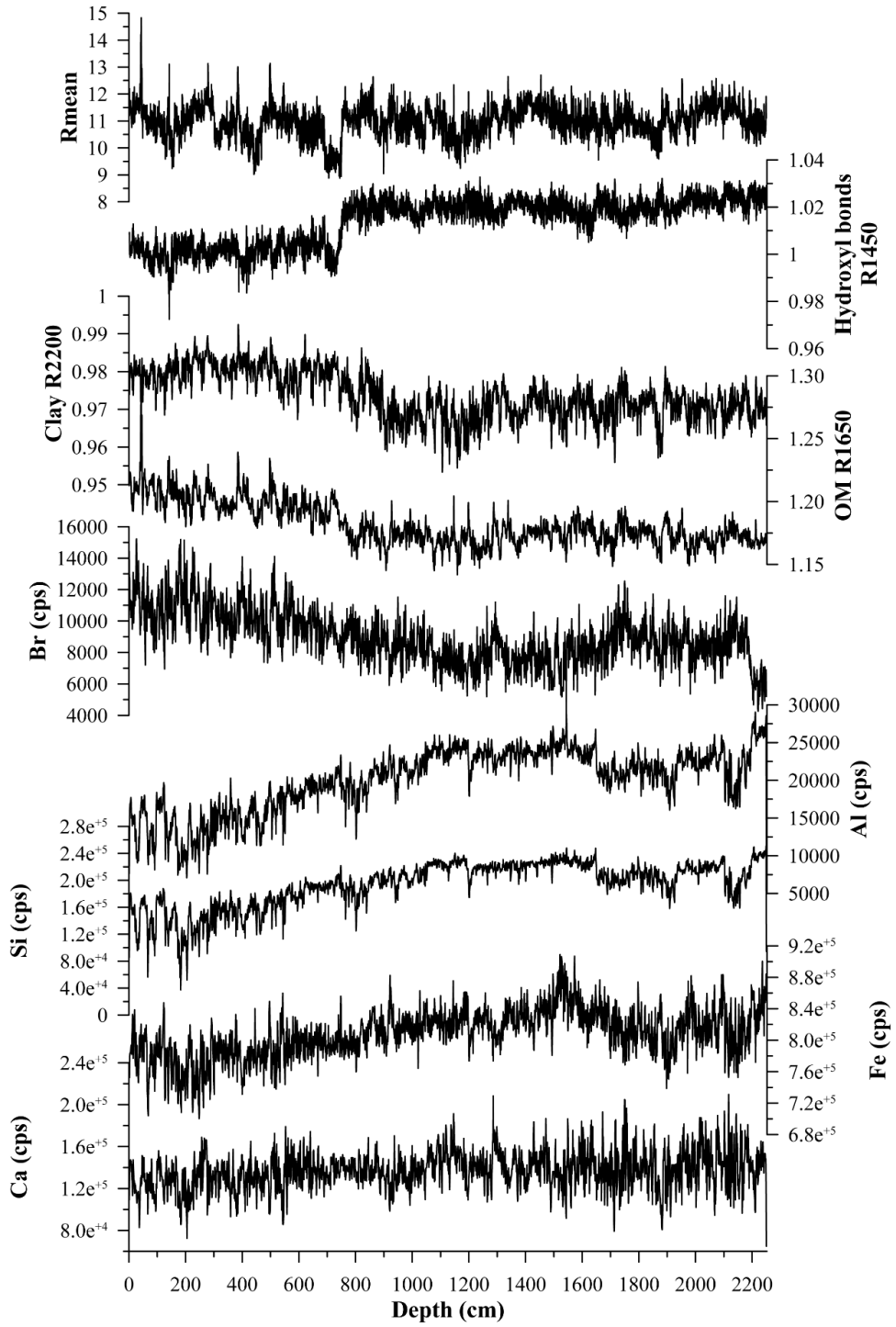

Figure 5-2. Core MD18-3574- variation in depth of relative geochemical composition (Ca, Br and terrigenous elements (Si, Al, Fe)) and hyperspectral imaging indices (Clay R2200 (clay fraction content), OM R1650 (organic matter content), Hydroxyl bonds R1450 (water content of sediments) and Rmean (sediment darkness))

For Core MD18-3569, Br and OM R1650 intensity remain relatively stable from 22.5 to 12.5 m and then increase upwards to the core top (Fig. 5-2). Terrigenous elements (Al, Si, Fe,

Ti and K) are characterized by similar long-term variations and present opposite variations with those of Clay R2200 and OM R1650. Their intensity is stable from 22.5 to 12.5 m and decreases continuously above 12.5 m (Fig. 5-2). The depth interval from 22.5 to 8 m is characterized by higher values of hydroxyl bonds R1450 than the upper 8 m. The shift at above 8 m observed in this index is also visible in the Rmean image with a very dark deposit. This double trend is also visible in the RGB image of the core, with a greyish color between 22.5 and 8 m and then a change to a more brownish color with specular reflection (white pixels) indicating a higher water content.

5.4.2 Laser grain-size analyses

Grain size variations for the depth interval 2100-2170 cm are reported in figure 5-3. Grain size variations for the depth interval 1365-1385 cm are reported in Appendix 5-3. The mean grain sizes of the two depth intervals (i.e. 2100-2170 cm and 1365-1385 cm) display variations ranging from 9.1 to 20.4 µm (average value of 13.4 µm) and from 10.5 to 17 (average value of 14.1 µm), respectively (Fig. 5-3). The sediments are mainly composed of silt (76% and 75%) with a moderate proportion of clay fraction (23% and 24%) and very little or no sand (1%) (Fig. 5-3). The grain size distribution indicates three main grain populations: a very fine silt and clay (8 µm), medium sized silt (20 µm) and coarse silt and fine sand (100 µm). Grain sizes processed on sediment with carbonates (1) and terrigenous sediments (2) display similar variations indicating that biogenic carbonates have no major effect on the grain size because the carbonate content is very low in the northern SCS during the Holocene (Huang et al., 2015).

We have selected the terrigenous sediment fractions 0-4mm, 4-63mm and >63mm for the following discussions. Sediments consist of an alternation of fine and coarser laminations, the thicknesses of which vary from about 2 to 25 mm. Fine sediment laminates (10 µm) are mainly composed of silt (75%), dominated by the fine silt population with a minor clay fraction (25%) and no sand. Coarse sediment laminates are mainly composed of silt (79%), with less clay fraction (19%) and a small proportion of sand (2%) (Fig. 5-3). The largest coarser levels display asymmetric sorting both in the mean grain size variations but also in the changes in the importance of grain size populations, with rapid grain size increase and steady decrease after the peak.

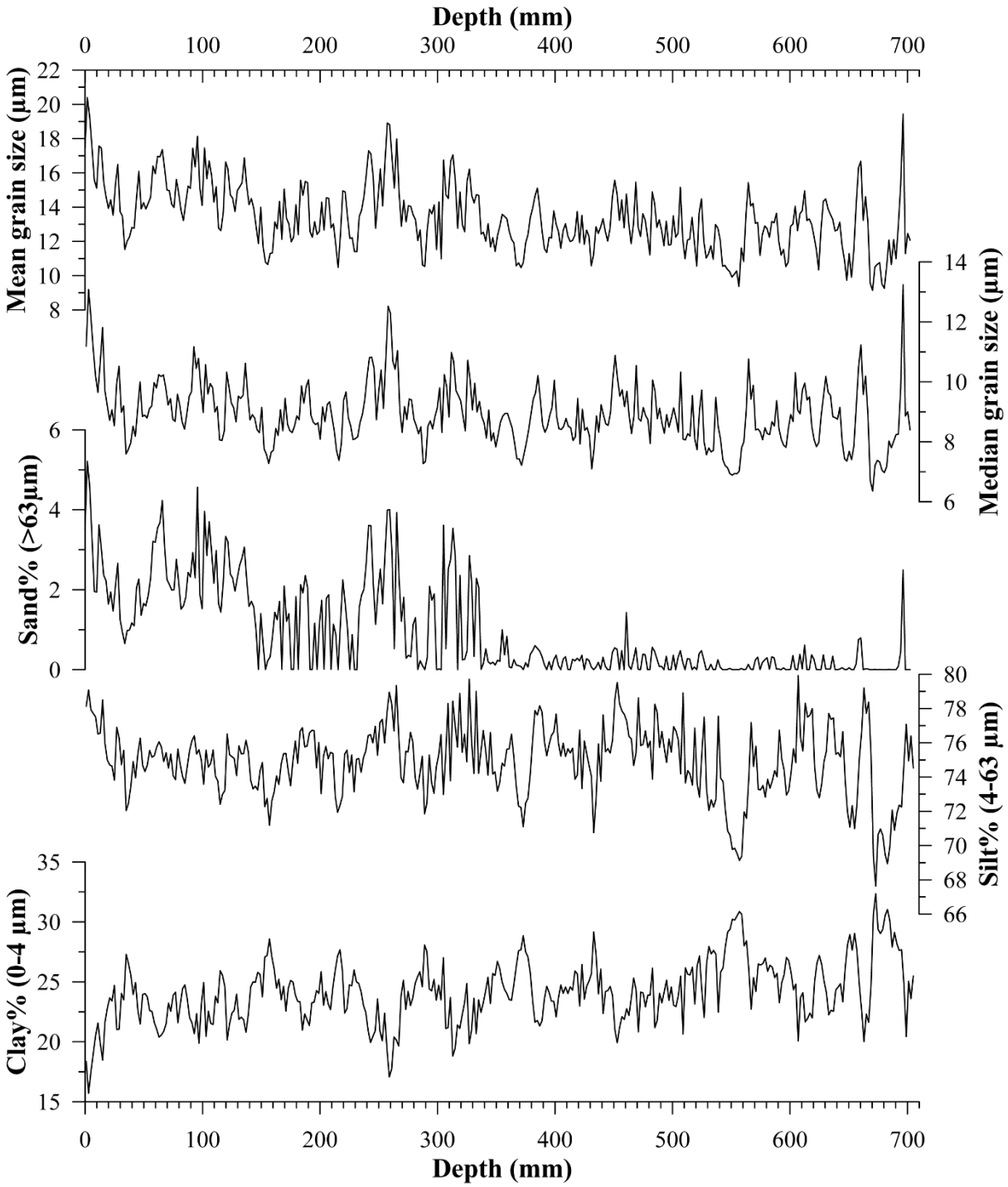

Figure 5-3. Depth variations of the mean and median grain size, and content of sand (>63 μm), silt (4-63 μm) and sand (0-4 μm) fractions of Core MD18-3574 section 15.

5.4.3 Bulk mineralogy

The bulk mineralogy of Core MD18-3574 mainly consists of abundant proportions of muscovite - illite (41-33%, mean value of 38%,) and quartz (40-32%, mean value of 36%), moderate proportions of chlorite (15-12%, mean value of 13%) and plagioclase (10-8%, mean value of 9%) and low proportions of calcite (3-2%, mean value of 2%) and microcline (3-2%, mean value of 2%) (Table 5-2). Darker and lighter laminae are associated with slightly different mineralogical compositions. Lighter laminae are composed of higher proportions of foliated minerals with 41% of muscovite and illite (mean value of 41%) and lower proportion of quartz (mean value of 34%), plagioclase (mean value of 8%) and calcite (mean value of 2%). Inversely, darker laminae consist of higher proportions of quartz (mean value of 38%), plagioclase (mean value of 10%) and calcite (mean value of 3%) and less important proportions of muscovite and illite (mean value of 35%).

Table 5-2: Bulk mineralogy of 10 laminae, 5 dark (turbidites) and 5 light (hemipelagic) laminae, of Core MD18-3574 section XV

Minerals		Quartz	Muscovite/illite	Chlorite	Plagiclase	Microcilne	Calcite
XV 374-382 mm	Dark lamina	38%	35%	13%	9%	3%	3%
XV 652-662 mm	Dark lamina	39%	34%	13%	10%	3%	2%
XV 234-248 mm	Dark lamina	40%	33%	13%	9%	3%	2%
XV 556-570 mm	Dark lamina	38%	36%	12%	9%	2%	2%
XV 248-264mm	Dark lamina	37%	35%	14%	10%	3%	2%
Average	**Dark laminae**	38%	35%	13%	10%	3%	2%
XV 362-370 mm	Light lamina	33%	41%	15%	8%	2%	2%
XV 640-650 mm	Light lamina	34%	41%	13%	8%	2%	2%
XV 664-688 mm	Light lamina	34%	41%	13%	8%	2%	2%
XV 540-556mm	Light lamina	34%	40%	13%	8%	2%	2%
XV 282-290 mm	Light lamina	35%	39%	13%	9%	2%	2%
Average	**Light laminae**	34%	41%	13%	8%	2%	2%

5.5 Discussions

5.5.1 Characteristics of laminae and their associated processes

Core MD18-3574 is highly laminated and composed of an alternation of light and dark laminae. The high resolution and non-destructive hyperspectral imaging and XRF core scanning were coupled with grain size analyses and XRD bulk mineralogy in order to constrain the processes responsible for the deposition of the light-dark coupled laminae.

Figure 5-4 presents for core MD18-3574, the mean grain size variations of the 2100-2170 cm depth interval compared to hyperspectral imaging proxies (clay contents from Clay R2200 and Rmean) and XRF relative geochemical Si/Al ratio obtained at a resolution of 1 cm and Fe/Ca ratio obtained at a resolution of 1cm. In general, the mean grain size closely covaries with the different proxies. Each increase in the mean grain size is associated with lower Rmean (darker sediments), higher Si/Al ratio, higher Clay R2200 (low clay-sized fraction contents) and lower Fe/Ca ratio (Fig. 5-4).

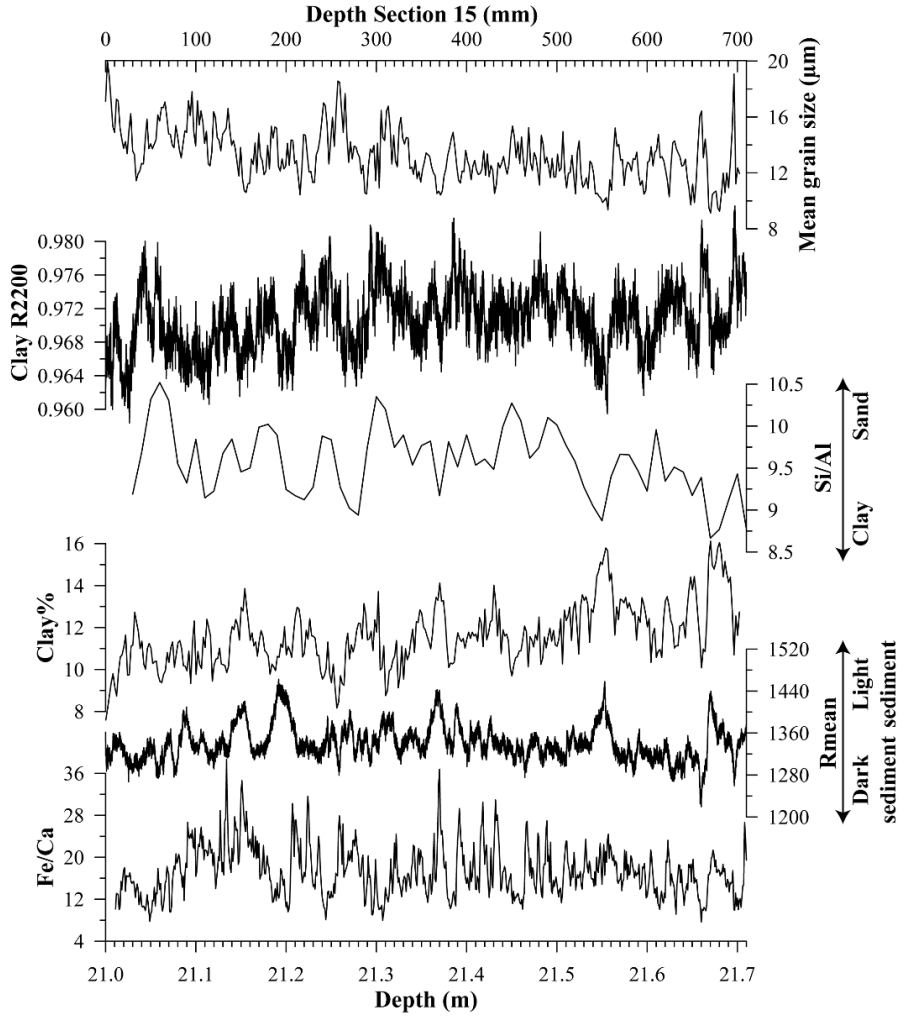

Figure 5-4. Core MD18-3574 section 15 depth variations of mean grain size, Clay R2200, Si/Al, clay fraction content (0-4 µm), Rmean (sediment color), Fe/Ca

Principal component analyses (PCA) have been conducted on all proxies analyzed at a resolution of 1-2mm in order to statistically constrain the light and dark laminae (Fig 5-5). Principal components (PC)1, 2 and 3 display two main end-members from all proxies (Fig. 5-5) PC1 indicates two populations, the coarser grain size populations are in the negative values of PC1 and inversely the positive values correspond to the finer grain size layers. The

comparison of PC1 with PC2 and PC3 (Fig. 5-5) demonstrates contrasts between the two end-members. The coarser grain size laminae (high mean and median grain size, high sand% and silt% and low clay%) have lower Rmean (darker sediments), high Clay R2200 (indicating low clay-sized fraction content) and low Fe/Ca, Ti/Ca and K/Ca ratios (Ca-rich sediments) (Fig. 5-5). On the contrary, the finer grain size laminae (low mean and median grain size, low sand% and silt% and high clay%) are associated with high Rmean (lighter sediments), low Clay R2200 (indicating high clay-sized fraction content) and high Fe/Ca, Ti/Ca and K/Ca ratios (Fig 5-5).

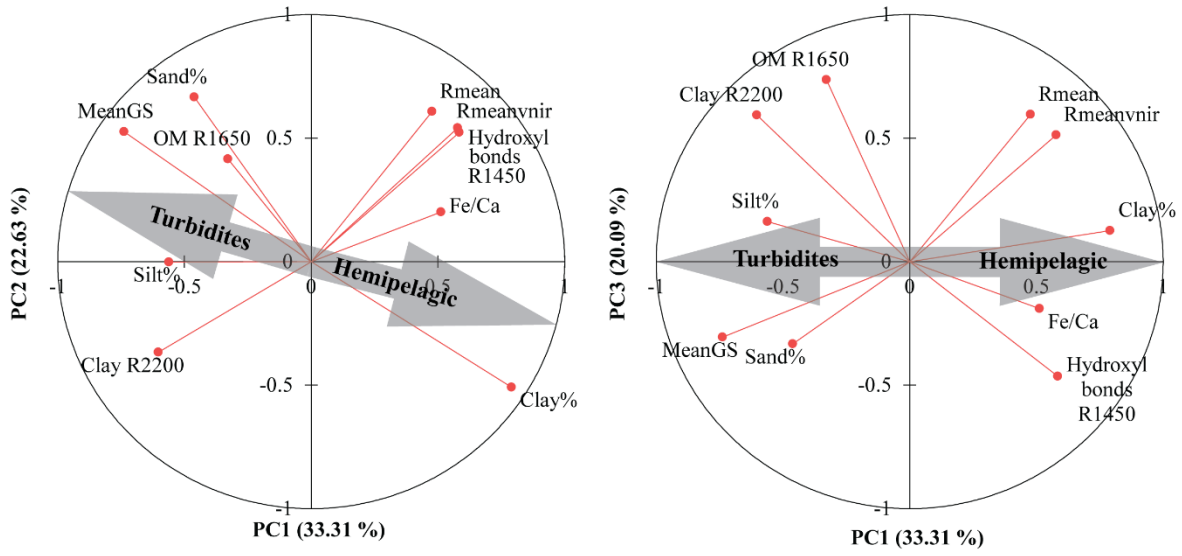

Figure 5-5. Core MD18-3574 section 15 principal component analyses (PCA) of grain size, hyperspectral indices, and relative geochemical composition PC1-PC2, PC1-PC3 showing the characterization of laminations.

Bulk mineralogy is also linked to the two end-members in close agreement with the relative geochemical composition obtained on light and dark laminae. Darker and coarser sediments have slightly higher proportions of quartz (38%), feldspars (11%) and calcite (3%) and lower proportions of micaceous minerals (34%) than lighter and finer sediments (33% Quartz; 10% feldspars, 2% calcite and 40% muscovite and illite) (Appendix 5-4-8) (Fig. 5-6). Quartz-, feldspar- and calcite-rich layers (Si, and Ca-rich) result in the high Si/Al values and low Ca ratios in opposition to the micaceous-rich layers (Si, Ca-poor and Al, Fe, K, Ti-rich) (Fig. 5-6).

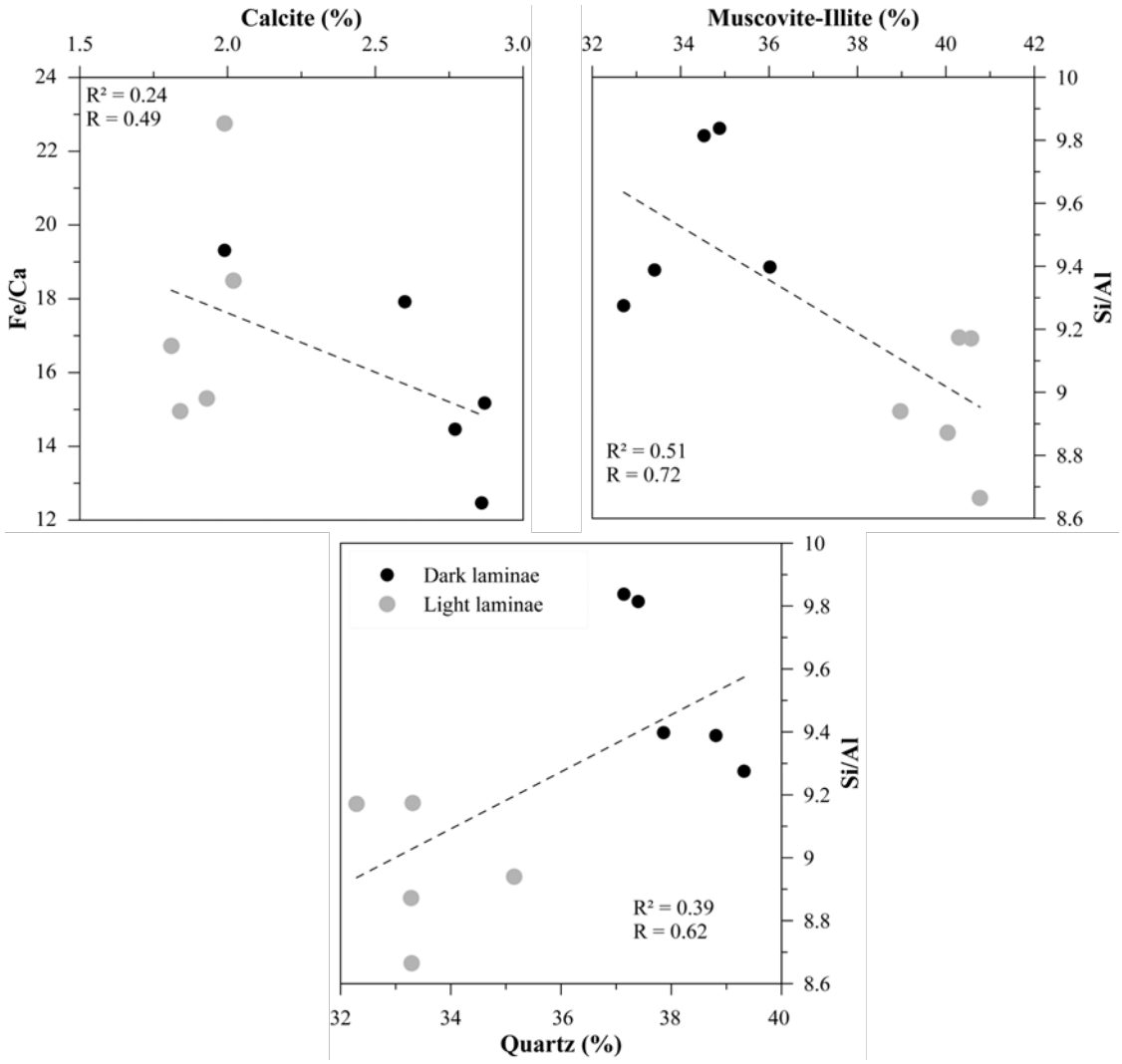

Figure 5-6. Correlation plots of mineral composition and relative geochemistry of Core MD18-3574 light and dark laminae: Calcite (%) vs Fe/Ca, muscovite-illite (%) vs Si/Al and quartz vs Si/Al.

Thus, dark and light laminae of Core MD18-3574 result from two different sedimentary processes. The coarse dark silty mud (medium size, coarse silt, and fine sand), rich in quartz, feldspar, and biogenic calcite (Hsiung et al., 2021), could be deposited from nepheloid layers or the overflow of the hyperpycnal flows within the canyon. The rapid grain size increase coupled with quartz and feldspar enrichment, lower Fe/Ca and the typical classical fining-upward fining characterizing the dark layers suggest that they result mainly from deposition by turbidity currents (Bouma, 1962; Stow and Shanmugam, 1980) (Fig. 5-7). However, the absence of visible erosion surfaces, the small thickness of the deposits and the low sand contents in sediments of Core MD18-3574 suggest relatively weak turbidity currents on the western levee of Gaoping submarine canyon. A similar sedimentary environment has already

been described in a previous study on the Eastern Taiwan slope (Lehu et al., 2015) (Fig. 5-4). Such results are in agreement with the position of the studied levee, which is ~600 m above the canyon thalweg. In such a configuration only the finest sediments of major turbidity currents flowing within the Gaoping submarine canyon reach the studied site. The light mud layers composed mainly of micaceous minerals with lower proportions of other minerals may result from sedimentation of fine hemipelagic sediments transported by the rivers of southern Taiwan (Liu J.T. et al., 2010, 2016; Nayak et al., 2021).

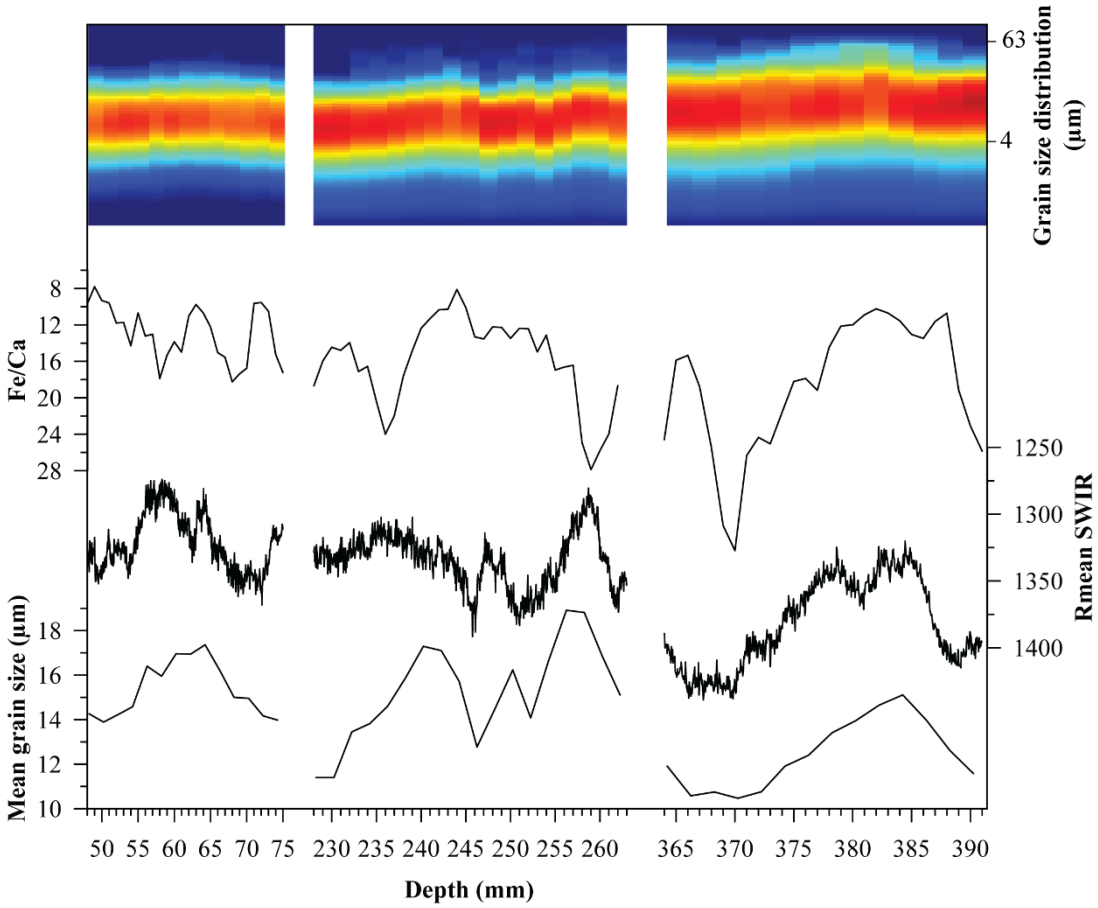

Figure 5-7. Depth variation of mean grain size, Rmean SWIR (sediment darkness, descending scale, Fe/Ca (descending scale) and grain size distribution of three turbiditic laminae of Core MD18-3574 section XV

5.5.2 Records of the frequency and intensity of typhoon activity for the last 4.2 cal kry BP

Since the coarser sediments of dark laminae can be attributed to hyperpycnal flows, mainly triggered by typhoon events affecting South Taiwan, we have used the Rmean SWIR index to identify the dark deposits and then establish past variations in the frequency of typhoon events. First, the deposits are detected through the identification of local maxima and

minima once the Rmean is enhanced by contrast-limited adaptive histogram equalization (CLAHE) to maximize the differences between the deposits (Zuiderveld, 1994) and smoothed (Savitzky and Golay, 1964). The local maxima and minima detection allows us to obtain the deposit count but does not provide more information. Core MD18-3574 is composed of 2404 laminations consisting of an alternation of millimetric to pluri-centimetric light and dark laminae. To obtain the thicknesses, it is necessary to identify the deposit boundaries and not their maxima or minima with Rmean (Fig. 5-8). A boundary is identified by finding the local maxima or minima of the unenhanced Rmean first derivative between the previously identified coordinates. The thickness is then obtained by measuring the space between two consecutive boundaries. To study the variation in the number of deposits and their thickness over a given period, a sum, and an average per time interval (100 years) are used.

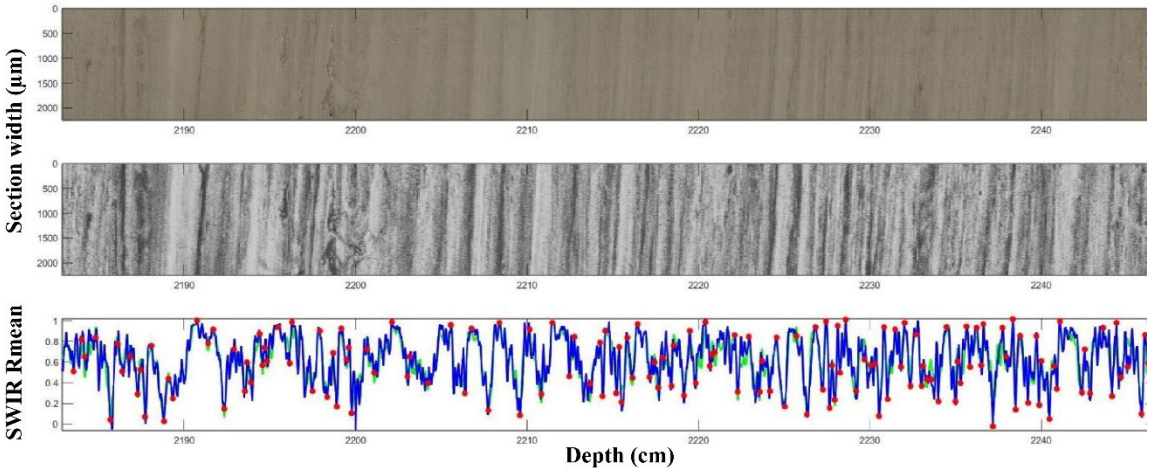

Figure 5-8. Hyperspectral imaging of Core MD18-3574 2180-2250: raw SWIR Rmean; corrected SWIR Rmean (contrasted and denoised) and corrected SWIR Rmean profils for the identification of turbiditic deposit (dark levels)

The frequency of typhoon activity affecting the Gaoping river basin (South Taiwan) displays a decreasing trend since the middle Holocene (Fig. 5-9a). Typhoon frequency peaked above 100 events per 100 years from 4 to 3.2 cal kyr BP before steadily decreasing to less than 20 typhoon events per 100 years at 1 cal kyr BP. An abrupt peak of typhoon frequency occurred after 0.3 cal kyr BP with nearly 60 recorded events per 100 years.

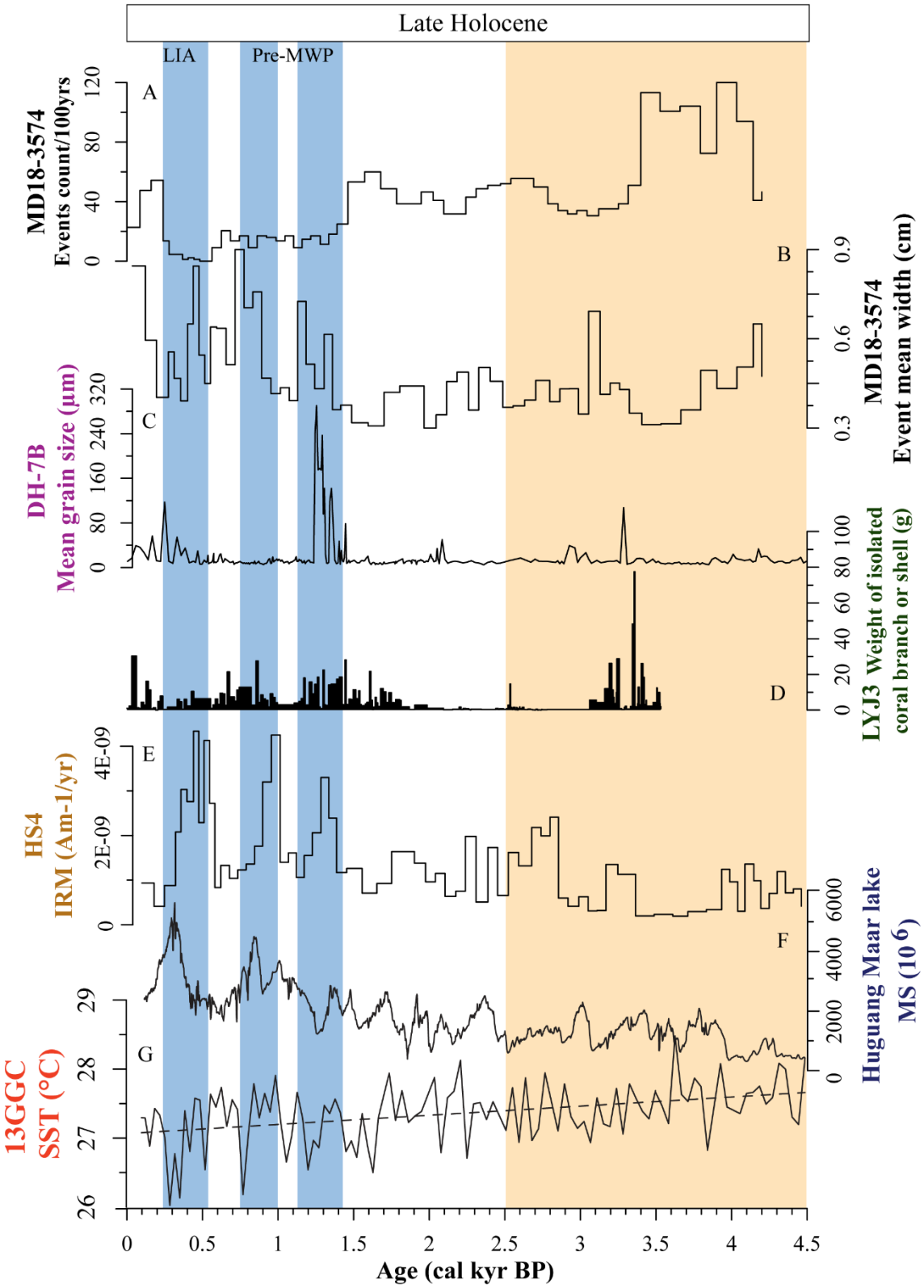

Figure 5-9. Temporal variations in typhoon frequency (event count) a) and intensity (event mean thicknesses) b) recorded by Core MD18-3574 in comparison to regional climatic records (typhoon activity (c) Chen et al., 2012, d) Yue et al., 2019, f) Zhu et al. 2017),

EAWM (Yancheva et al., 2007) e) and Pacific Ocean temperature (Lindsey et al., 2010) g) during late Quaternary.

The mean thickness of the laminae is relatively stable from 4.2 to 1.5 cal kyr BP with lamina thickness of between 0.3 and 0.7 cm (average values of 0.4 cm) (Fig. 5-9b). Inversely, from 1.5 cal kyr BP to the present time the mean thickness increased to 0.6 cm on average and displays greater variability of 0.3 to 1 cm. The thickness of hyperpycnal flow deposits depends on several forcings (e.g., sediment delivery, soil recovery state, land use) (e.g., Page et al., 1994; Gomez et al. 2012) but generally displays a close correlation with the total rainfall of a storm triggering hyperpycnal flow (Page et al., 1994). Thus, we can hypothesize that the thicknesses of the dark laminae represent the intensity of the typhoon rainfall responsible for triggering the hyperpycnal flows in the Gaoping submarine canyon (Page et al. 1994). The variation in the mean thicknesses of the laminae suggests that the intensity of typhoons was stable from 4 to 1.5 cal kyr BP and was more variable and stronger after 1.5 cal kyr BP.

After 1.5 cal kyr BP, the grain-size (Si/Al and clay-sized content from Clay R2200) and organic matter (Br and OM R1650) of Core MD18-3574 are higher than during the period of high typhoon frequency (Fig. 5-10). It indicates that periods of intense typhoon events enhance the sedimentation of detrital material and (terrestrial) organic-rich materials on the levee through intense hyperpycnal flows in the Gaoping submarine canyon. Inversely during time intervals characterized by high frequency but less intense typhoons, the redistribution of terrestrial organic matter on the levee through the canyon seems to be less efficient (Fig. 5-10).

The linear sedimentation rate (LSR) of core MD18-3574 displays a similar trend to the event and laminae frequency (Appendix 5-1). From 4 to 2.2 cal kyr BP, the LSR is extremely important, greater than 0.7 cm/year, but decreases steadily to 0.5 cm/yr between 2.5 and 1.4 cal kyr BP and 0.4 cm/yr between 1.3 and 0.35 kyr cal BP. From 0.35 to 0.18 cal kyr BP the LSR sharply increases to 0.79 cm/year. This correlation between LSR and the frequency of typhoon events indicates that the building of the canyon levee relies more on the frequency of hyperpycnal flows deposit than on the thickness of these deposits.

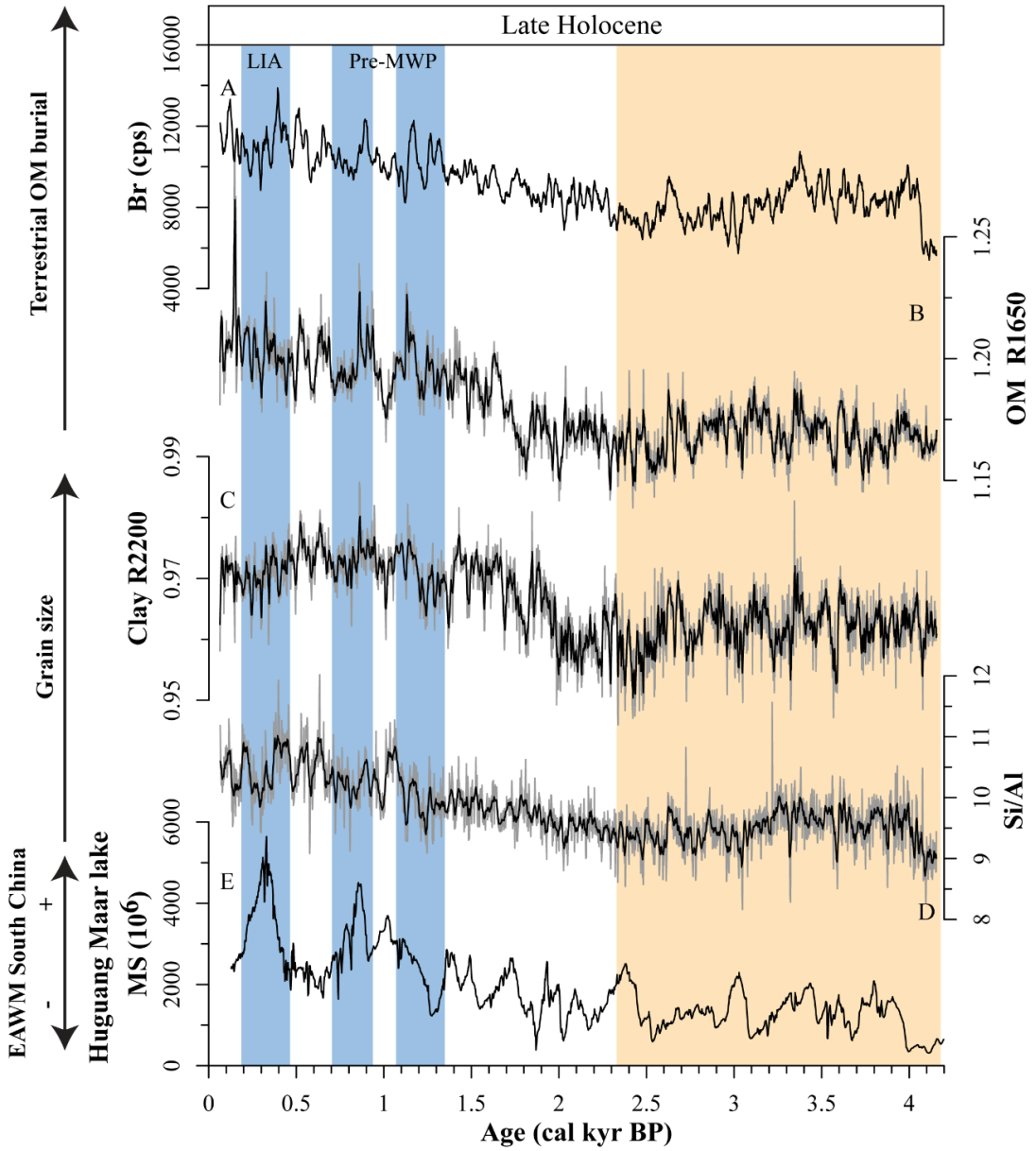

Figure 5-10: Temporal variations in grain size (d) Si/Al and c) Clay R2200) and organic matter proxies (a) Br and b) OM R1650) showing the control of EAWM intensity (Yancheva et al., 2007) e) on terrestrial organic matter burial and grain size in the Gaoping Canyon system during the late Holocene.

A record of turbidity frequency occurring within Gaoping Canyon (Core MD18-3565) is displaying totally different observed frequency in number (<20 events per 100 years) and in trend, with two frequent typhoon periods from 3. to 2.6 cal kyr BP and 1.4 to 0.6 cal kyr BP (Huang et al., 2023) (Fig 5-11).

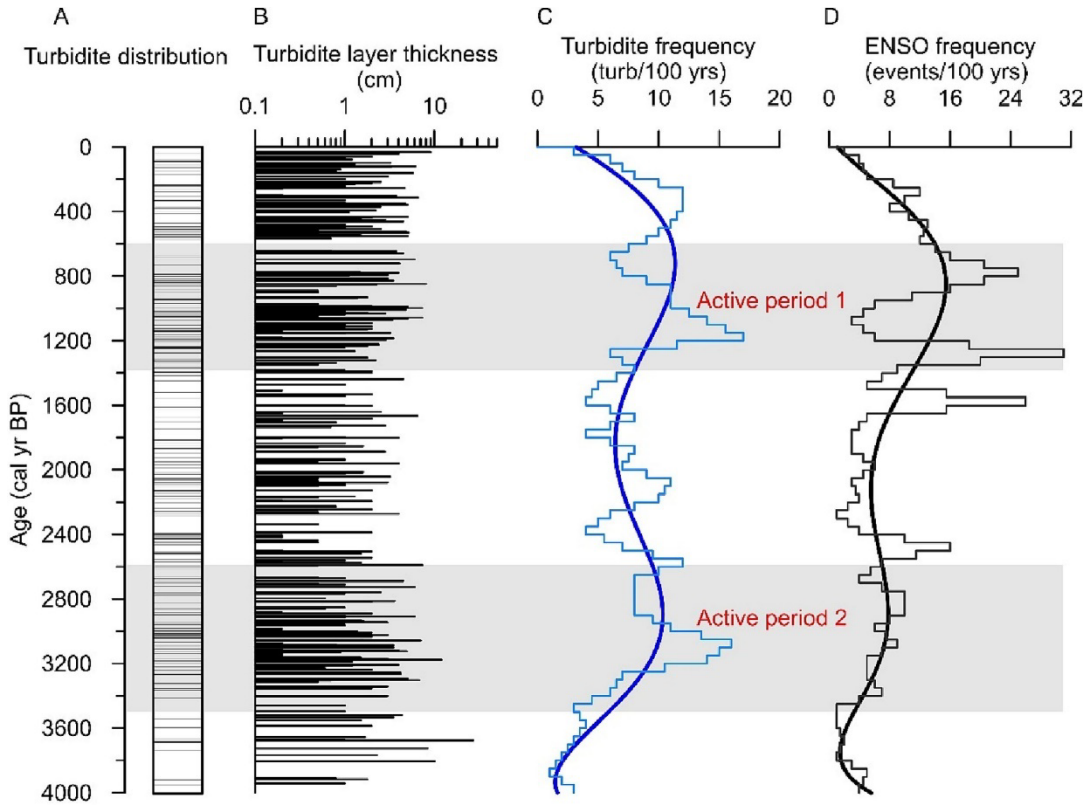

Figure 5-11. Frequency of turbidite occurrence at Core MD18–3565 over the past 4000 yr in the Gaoping Submarine Canyon (Huang et al., 2023)

The deposit thickness is larger than on the levee (up to 30 cm) and relatively stable in time. This indicates processes in the canyon and on its levee are different. Hyperpycnal flows on the levee, 600 m above the canyon thalweg, are low intensity overflow, with reduced erosion processes, of the fast and erosive hyperpycnal flows in the canyon. Core MD18-3574 records the most intense hyperpycnal flows events, not the total frequency. The core MD18-3565 site is located in a more distal environment, thus, less events might affect this region of the canyon. However, MD18-3565 turbidity layers are characterized by erosive surface, which suggests that the frequency records could be altered in the canyon. However, the two active periods identified could correspond to the period of high frequency (before 3.2 cal kyr BP) and of high and variable intensity (after 1.5 cal kyr BP) of typhoon record by Core MD18-3574 (Fig. 5-9a, 5-11). Studying a canyon system (levee, thalweg) response to turbidity current could be an important perspective to understand sediments transports by canyon systems.

5.5.3 Climatic implication of the evolution of the frequency and intensity of typhoon activity

Studies of tropical paleo-cyclones of the Holocene conducted in several other regions of East Asia (Fig. 5-12) allow us to compare our records obtained on the levee of Gaoping submarine canyon and to discuss a spatial distribution of typhoon activity.

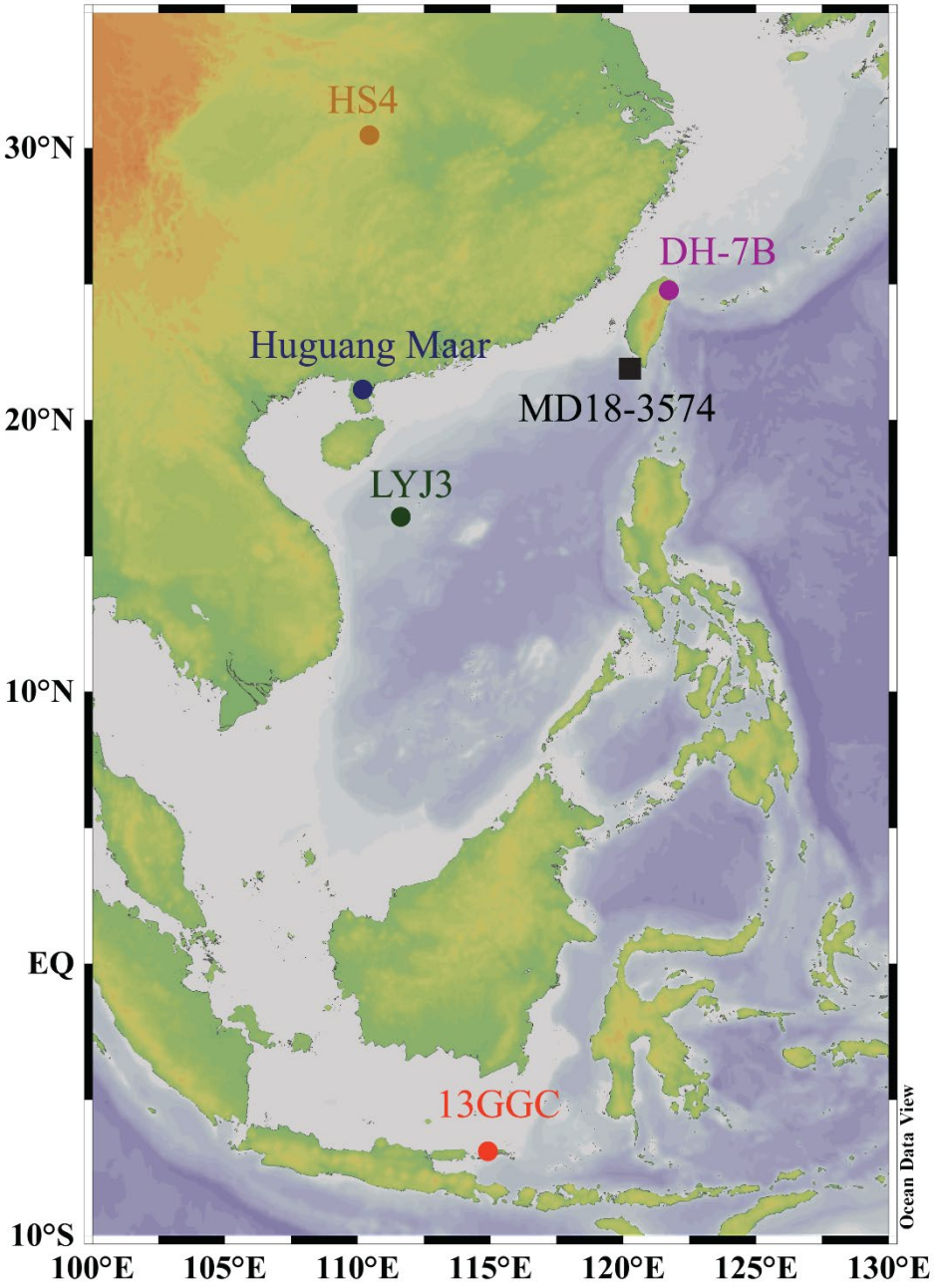

Figure 5-12. General East Asia map showing the location of the climatic records discussed in this study: Pacific Ocean warmpool temperature (13GGC (Lindsey et al., 2010)), tropical 3storm activity (HS4 (Zhu et al., 2017), Dahu Lake (Chen et al., 2012), Xisha Islands (Yue et al., 2019)) and East Asian Winter Monsoon (Huguang Marr Lake (Yancheva et al., 2007))

Studies of speleothems in Central China have revealed a strengthening of storm activity since the middle Holocene, and particularly during the late Holocene with peaks of activity at 1.3, 0.9 and 0.4 cal kyr BP (Fig. 5-9f) (Zhu et al., 2017). In addition, carbonate content decreases observed in several marine sediment cores of the northern SCS margin have been linked to increasing typhoon activity since the middle Holocene; these decreases are in carbonate content in marginal areas is mainly due an increase in the terrigenous material transported to the deep ocean by typhoon activities (Huang et al., 2015). It has also been shown that increased coral destruction on the Xisha Islands reefs (north SCS) can be linked to important typhoon activity during the time intervals 3.5-3.1 cal kyr BP and 1.8-0 cal kyr BP (Yue et al., 2019). Several peaks in the detailed curve of coral destruction g (Fig. 5-9d) match well with our curve of typhoon intensity (Fig. 5-9b). In north-eastern Taiwan, grain size variations in a lacustrine sediment core have been associated with two periods of super-typhoon activity from 1.45 to 1.25 cal kyr BP and from 0.4 to 0.15 cal kyr BP (Fig. 5-9c) (Chen et al., 2012). These two super-typhoon periods also closely match with periods of increased typhoon activity affecting the Gaoping river basin (time intervals of 1.4-1.1 and 0.5-0.3 cal kyr BP; Fig. 5-9b). Thus, a regional pattern emerges in which more important typhoon activity occurs around 3.5-3 cal kyr BP and after 2-1.5 cal kyr BP with time interval associated to more intense typhoons (Fig. 5-9).

During recent decades, many studies based on speleothems and marine sediment archives have reconstructed the ENSO variability of the Holocene and its link with the SST in western tropical Pacific and a decrease in insolation (Moy et al., 2002; Riedinger et al., 2002; Peltier, 2004; Rein et al., 2005; Conroy et al., 2008; Joos et Spahni, 2008; Chiang et al., 2009; Koutavas et Joanides, 2012; Cobb et al., 2013; Liu et al., 2014; Zhang et al., 2014; Peltier et al., 2015; Emile-Geay et al., 2016; Yu et al., 2016; Thompson et al., 2017; Zhu et al., 2017; Lu et al., 2018). These studies have shown a strengthening of ENSO activity in the late Holocene in comparison to the middle Holocene. Such changes may have strongly impacted typhoon activity over southern Taiwan.

Despite the increased ENSO variability and stronger El Niño and La Niña-like conditions since 3 cal kyr BP (Koutavas et Joanides, 2012; Thompson et al., 2017), typhoon frequency over south Taiwan decreases (Fig. 5-9a). It has also been shown that SST continuously decreased in the western Pacific, with more negative temperature anomalies, since the middle Holocene (Stott et al., 2004; Linsley et al., 2010; Dang et al., 2020). Such variations in the SST pattern in the western Pacific are also associated with an enhancement

of the EAWM (Yancheva et al., 2007) and a reinforcement of La Niña-like conditions (Lin et al., 2008) (Fig 5-9e,5-9g). Such changes may have affected local typhoon activity in Southern Taiwan. Indeed, the decreased western tropical Pacific SST and enhanced EAWM inhibit the formation and/or weaken the intensity of locally formed typhoons (Dong et al., 2021) as conditions are more likely to be close to the threshold SST (26-27°C) for typhoon genesis (Dare and McBride, 2011; Tory and Dare, 2015).

In our record of typhoon activity affecting south Taiwan (Gaoping river basin), the time interval after 3 cal kyr BP is associated with a decrease in the frequency of typhoons (Fig. 5-9a). Such results are in agreement with other records for the northern SCS such as paleo-typhoon events reconstructed from tropical corals in Xisha Island reefs which also indicate a decrease in typhoon activity after 3 cal kyr BP (Yue et al., 2019) (Fig. 5-9d). The tropical western Pacific region is thus globally drier (Barr et al., 2019), as indicated by the decreased typhoon frequency. However, from 4 to 1.5 cal kyr BP, our new record of typhoon intensity (deduced from the thicknesses of turbidite deposits) is stable and does not indicate a decrease in typhoon intensity in this time interval. The intensity of many typhoons may have decreased below a potential intensity threshold below which the concentration of suspended sediment is not sufficient to generate hyperpycnal flow in the Gaoping submarine canyon (Mulder et al., 2003) and thus will not be recorded on the studied levee of the Gaoping submarine canyon. This may also amplify the apparent decrease in typhoon frequency within the record established from Core MD18-3574 (Fig. 5-9a).

The time interval from 1.5 to 0.3 cal kyr BP is marked by a decrease in the frequency of typhoons recorded on the Gaoping Canyon levee. However, this time interval is also associated with an intensification of typhoon activity affecting southern Taiwan, particularly with more intense typhoons during the time intervals 1.4-1.1 cal kyr BP, 1.0-0.8 cal kyr BP and 0.5-0.2 cal kyr BP (Fig. 5-9b). These time intervals are also characterized by an intensification of typhoon activity on Xisha Island (Yue et al., 2019), in Central China (Zhu et al., 2017) and in north-eastern Taiwan, with two periods of super-typhoon surges (Chen et al., 2012) (Fig. 5-9c, d,f). The northern SCS is also affected by an enhancement of the EAWM at 1.4-1.1 cal kyr BP, at 1.0-0.8 cal kyr BP and at 0.5-0.2 cal kyr BP coeval with colder periods in the northern hemisphere (such as the Little Ice Age from 0.6 to 0.2 cal kyr BP, LIA) and dominant La Niña-like conditions (Yancheva et al., 2007) (Fig. 5-9e). These colder periods are interrupted by an interval of warmer climate from 1.1 to 1.0 cal kyr BP and from 0.8 to 0.5 cal kyr BP (Medieval Warm Period, MWP) in the northern Hemisphere, weakened EAWM

and prevailing El Niño-like conditions (Yancheva et al., 2007; Dong et al., 2021), in which the intensity of typhoons to the south of Taiwan (Fig. 5-9b) and in Central China is weakened (Fig. 5-9f; Zhu et al., 2017). After the LIA period (around 0.3 cal kyr BP), the global climate becomes warmer and the typhoon frequency in Southern Taiwan increases significantly (Fig. 5-9a).

In La Niña-like conditions, the Pacific warm pool shrinks, and the typhoon genesis region is mainly located in the warm Central Pacific Ocean. In addition, the pacific Walker circulation (Barr et al., 2019) and EAWM winds (Yancheva et al., 2007) are strengthened. Such oceanic and atmospheric configurations affect typhoon tracks which are intensified and shift westward to Taiwan and Central China (Chen et al., 2012; Zhu et al., 2017; Yue et al., 2019; Wang et al., 2021). Before 3 cal kyr BP and after 0.3 cal kyr BP, the warmer climate (dominant El Niño-like conditions) and weakened EAWM (Yancheva et al., 2007) led to more low-moderate intensity typhoons that formed in the SCS and Taiwan region (et al., 2004). Nevertheless, the weakened Pacific Walker circulation, the northeastward East Asian summer monsoon winds and the Coriolis force shifted northward the track of strong typhoons formed in the Equatorial Pacific (Emanuel, 2003; Woodruff et al., 2009; Chen et al., 2012; Wang et al., 2021).

Overall, our study shows a decoupling of Taiwan typhoon frequency and intensity strongly controlled by the interactions of the EAM system, ENSO and SST of the western tropical Pacific and the northern SCS. Such results provide us with new insights to predict the future evolution of regional typhoon activity linked to the forecasted climate changes (Tan et al., 2019). The warming and stronger El Niño-like conditions predicted by CMIP5 models suggest that there could be a rise in typhoon frequency in Taiwan coupled with reduced regional super-typhoon activity. This agrees with the long-term record of typhoons over Taiwan from 1950 to 2013 (Liang et al., 2017). It has been observed that the frequency of typhoons over Taiwan for 63 years increased but the frequency of strong typhoons (category 4 and 5) decreased (Liang et al., 2017). In contrast, Japan and the Korean peninsulas could experience an important surge of strong typhoons due to the warmer climate and changes in typhoon tracks. This agrees with the northward shift of typhoon track observed from 1950 to 2013 (Liang et al., 2017).

5.6 Conclusions

High-resolution non-destructive hyperspectral imaging and XRF core scanning, combined with high resolution laser grain-size, bulk mineralogy and radiocarbon dating have been investigated on laminated sediments of Core MD18-3574 which was collected on the western levee of the Gaoping submarine canyon. Our aims were (1) to constrain the sedimentary processes inducing laminae deposits and (2) to establish the frequency and intensity of typhoon activity affecting southern Taiwan over the past 4.5 cal kyr BP. We conclude that:

(1) Core MD18-3574 consists of an alternation of dark laminae composed of coarse sediments enriched in quartz, feldspars, and calcite and of light laminae composed of fine sediments enriched in micas and depleted in quartz, feldspars and calcite. Dark laminae display a typical upward grain size decrease implying a sedimentation resulting from hyperpycnal flows in the Gaoping submarine canyon triggered by typhoons. Light laminae are the facies of hemipelagic sedimentation. A total of 2400 dark laminae, mostly associated with typhoon events, have been identified for the last 4.2 cal kyr BP.

(2) Typhoon frequency and intensity recorded on the Gaoping Canyon levee are decoupled. Since the middle Holocene the recorded frequency of typhoon activity shows a decrease from more than 1 event recorded per year on average for the period between 4 and 3.5 cal kyr BP to less than 0.2 event per year after 1.5 cal kyr BP. Typhoon intensity remained stable from 4 to 1.5 cal kyr BP. After 1.5 cal kyr BP, the typhoon intensity has become more variable and increased during three-time intervals, i.e. 1.4-1.1 cal kyr BP, 1.0-0.8 cal kyr BP and 0.5-0.2 cal kyr BP.

(3) The decrease in typhoon frequency since the middle Holocene is driven by the interaction between the cooling of western Pacific SST and the enhancing of EAWM. Such conditions reduce the local typhoon genesis and/or intensity of typhoons. Cold events of the late Holocene are associated with super typhoons formed in central Pacific and surging in Taiwan region because their tracks are affected by the la Niña-like conditions, and the stronger Pacific Walker Circulation and EAWM winds. This study of the frequency and intensity of storms provides us new perspectives on the forecasting of storm activity around Taiwan in the context of ongoing climate change and global warming.

Chapter 6 General conclusion

6.1 Climatic forcing and sea level fluctuations controls on the sedimentary dynamic of a non-connected canyon since last glacial period: the Penghu Canyon

6.1.1 Eastern Penghu Canyon bank sediments provenance

A first study has permitted us to identify the provenance of the sediments and potential sources changes over the record. The contrasted geological contexts of the northern South China Sea land masses allow mineralogical (clay minerals assemblage) and geochemical (Nd-Sr isotopes) investigations to determine the main sedimentary sources of sediments from the southern margin of Taiwan.

X-ray diffraction was performed on the terrigenous clay-sized fraction (<2 μm) to determine the sediment provenance and potential mixing between Taiwan rivers, Luzon rivers and Pearl River. The clay minerals assemblage of Core MD18-3569 is dominated by illite, ranging from 45 to 59% average of 52%), and chlorite, 27-39% (average of 32%), moderate smectite content ranging from 4 to 22% (average of 12%) and scarce proportion of kaolinite, ranging from 2 to 8% (average of 4%). Proportions of illite and chlorite display similar variations which are inversely correlated to those of smectite. The major proportions of illite (52%) and chlorite (32%) are characteristic of the clay minerals assemblages associated with sediments transported by Taiwan rivers (illite: 56%; chlorite: 36%). In turn, moderate smectite content (12%) is higher than Taiwan rivers (4%) could suggest a source mixing with Luzon-sediments (87%) (Liu et al., 2016). However, SW Taiwan rivers like Erhjen and Tsengwen can also transport moderate proportion of smectite (~15%) (Liu et al., 2016). The low proportion of kaolinite and the value of illite crystallinity (0.158°Δ2θ) and chemistry index (0.324) are too low compared to the sediments transported by the Pearl River which consists of 64% of kaolinite with illite crystallinity value of 0.198° Δ2θ and illite chemistry index value of 0.466 (Liu et al., 2010).

The isotopic composition of Sr and Nd of the decarbonated bulk sediments and clay fractions (<2 μm) were measured to better constrain the sediment provenance and determine potential additional contribution of detrital material from the volcanic province of Luzon where the clay size-fraction is rich in smectite. The $^{87}Sr/^{86}Sr$ and εNd of the decarbonated bulk sediments display narrow ranges from 0.7187 to 0.7213 and -11.63 to -10.89, respectively. Such narrow ranges are characteristic of sediments from Taiwan rivers ranges

($^{87}Sr/^{86}Sr$: 0.7176 to 0.7219 and εNd: -11.2 to -12.2) and are not consistent with inputs from Luzon rivers ($^{87}Sr/^{86}Sr$: 0.7044 to 0.7052; εNd: +6.4 to +7.4) and Pearl River ($^{87}Sr/^{86}Sr$: 0.7275 to 0.7373; εNd: -1.4 to -10.5). In addition, variations of εNd obtained on the clay fraction are not correlated with the smectite proportions of the sediments, which indicates that the smectite cannot derive from Luzon river basins. We can then conclude that sediments from the eastern bank of the Penghu Canyon results from the mixing of rivers of the SW Taiwan (mainly Erhjen and Tsengwen rivers). The sedimentary sources seem to be constant and do not present any major changes due to sea level variations associated with the opening or closure of the Taiwan Strait.

6.1.2 Chemical weathering history of SW Taiwan sediments

The sources of the sediments deposited on the eastern bank of the Penghu Canyon has been determined as the rivers of the SW Taiwan which remains the sole source during the last 32 ka according to Nd-Sr isotopic composition results. Thus, clay minerals can be used to determine the chemical weathering state of the sediments, in addition to major elements composition.

Major elements composition of sediments from Core MD18-3569 mainly consists of SiO_2 (65%), Al_2O_3 (15%), and Fe_2O_3 (6.2%) and low concentrations of K_2O (3%), MgO (2.1%), Na_2O (1.2%), and CaO (1%). Al_2O_3, Fe_2O_3, K_2O, and MgO covary together. They present low contents during the LGM and Holocene and peaks during the deglaciation. proportions of SiO_2, Na_2O, and CaO are inversely correlated to those of Al_2O_3, Fe_2O_3, K_2O, and MgO. They display decreasing trend during the deglaciation and higher content during the Holocene. Ternary diagram A–CN–K (Al_2O_3–(CaO+Na_2O)–K_2O) Chemical Index of Alteration (CIA=68) (CIA = molar ratio of [Al_2O_3/(Al_2O_3+Na_2O+K_2O+CaO*) ×100]), indicate that sediments experienced a moderate chemical weathering and a preferential leaching of Na and Ca, which is typical of Taiwan moderate weathering.

CIA, Al_2O_3/SiO_2, Al_2O_3/Na_2O, smectite/(illite+chlorite) and kaolinite/(illite+chlorite) have been used to reconstruct the chemical weathering state of Core MD18-3569 sediments. Kaolinite, smectite, and leaching of mobile elements (high Al_2O_3/Na_2O and CIA) are the product of chemical weathering. Conversely, illite, chlorite, coarse sediments (low Al_2O_3/SiO_2)) and the presence of mobile elements (low Al_2O_3/Na_2O and CIA) indicate a lower relative chemical weathering and are likely to be the product of a more intense relative erosion. CIA, Al_2O_3/SiO_2, Al_2O_3/Na_2O, smectite/(illite+chlorite) and kaolinite/(illite+chlorite)

variations are relatively low. Nevertheless, they display low value during the LGM, which indicates that the chemical weathering was relatively low. The time interval of the deglaciation is marked by an increase in all the chemical weathering ratios with maximum values during the early Holocene. These peaks indicate a relative increase of the chemical weathering during the deglaciation until the early Holocene. The Holocene is characterized by a gradual relative decrease in chemical weathering proxy since the 9 cal kyr BP. Such chemical weathering record is coherent with existing paleo East Asian summer monsoon records and pollen records of a lake from west Taiwan (Liew et al., 2006).

During time interval of high summer monsoon precipitations (deglaciation, early Holocene), sediments lake from the SW Taiwan lacustrine (dominant trees pollens indicating progressive pedogenesis of soils) and marine terrigenous sediments (smectite, kaolinite, leaching of Ca, Na, clay contents) from the northern SCS indicate a relative increase of chemical weathering intensity. During drier interval (LGM, Holocene weakening of monsoon precipitation), lacustrine (dominant herbs pollens indicating regressive pedogenesis of soils) and marine terrigenous sediment exhibit a decrease in relative chemical weathering and a more important physical erosion. This trend is enhanced during the Holocene by the strong typhoon activity strengthening soils erosion of the SW Taiwan. We can conclude that, the strengthening of East Asian summer monsoon precipitations triggers a relative increase of the SW Taiwan soils chemical weathering in the draining basins of SW Taiwan small mountainous rivers.

6.1.3 Hydrodynamic conditions and sediments transport and redistribution from SW Taiwan rivers to the northern SCS

The glacial-interglacial sea level changes have no major impact on the sediment provenance of the eastern Penghu Canyon levee. However, it necessarily affects the hydrodynamic conditions and the redistribution of sediments (e.g., opening of the Taiwan Strait and of surface currents flowing in the Strait) or vicinity change of the river mouths to the study site (Boulay et al. 2003). Grain size analyses are suitable proxy to establish hydrodynamic conditions of our studies site. They were used in many paleo hydrological studies in the northern SCS (Boulay et al., 2003; Huang et al., 2011; Clift et al., 2014).

Grain size analyses were realized on the decarbonated bulk sediments of Core MD18-3569 at a high time-resolution (~85 years). The average mean grain size of Core MD18-3569 sediments is ~13 μm (8-20 μm) and mainly consist of fine silt (~75%) and clays (~24%) and low to no sand (~1%). Grain size results do not show any indication of turbidite on the

sediment bank of the Penghu Canyon. Such fine grain size also differs from grain size measured on sediments transported by Taiwan rivers (>100 μm). End-member modeling was applied to the grain size distributions and highlights a quasi-unimodal distribution. Two end members were identified: EM1 with a grain size distribution from 0 to 55 μm, consisting mainly of clay and fine silts with a median grain size of ~6.5 μm and EM2 ranging from 0 to 185 μm, consisting of medium to coarse silts and fine sands with a median grain size of ~19.5 μm. The EM1 could correspond to fine sediments derived from rivers through the surface circulation while the EM2 can be interpreted as coarse sediments input resulting from more direct processes (Penghu Canyon). EM1 amounts for ~75% of sediments since 32 ka, while EM2 amounts for less than 25%. This indicates that the majority of the sediments deposited on the eastern bank of Penghu Canyon are transported by surface and intermediate circulation from the SW Taiwan rivers basins. About 25% of the detrital fraction of the sediment could have been discharged by direct inputs from river mouth through the Penghu Canyon.

The grain size highlights two main time intervals:

(1) From 32 to 10.7 cal ka BP: the mean grain size is relatively coarse (~15.5 μm) with higher content in silt (~78%) and sand (<2 %). Total EM2 displays higher proportions (~40%) and can reach about 50% of the total sediments. The EM modeling was applied on 32-10.7 and 10-0 ka. For sediments of the time interval 32-10.7 ka, the two end members EM1 and EM2 have median grain size of ~7.5 and 20 μm respectively.

(2) Since 10 ka: the mean grain size dropped of 40% in 0.7 ka from 15.2 to 9.1 μm with an increase in clay proportions (25-30%) and decreases of silt (78-74%) and sand (0-2%) content. The proportions of EM also change strongly, EM2 content decreases to less than 20% and EM1 represents 80 to 100% of the sediments deposited. In addition, the separate EM modeling displays a strong decrease of EM2 median grain size in this interval (~11 μm) while EM1 median grain size is relatively stable (6.3 μm).

The two time intervals 32-10.7 cal kyr BP and 10-0 cal kyr BP are separated by a transition from 10.7 to 10 cal kyr BP. This transition is contemporaneous to a rapid global transgression (of ~20 m) identified as the Melt Water Pulse 1C (Grant et al., 2012). This abrupt sea-level rise has significantly changed the land-sea configuration and then sediment transport dynamic from land to the southern margin of Taiwan. These two-time intervals characterize two different sedimentary dynamics in different land-sea configuration affecting the redistribution with modifying the provenance of sediments. The time interval (1) is mostly characterized by

a lowstand sea-level period during the LGM and termination of the last glacial period. In this context, the sea level resulted 100-120 m lower than at modern time. Thus, the Taiwan Strait was closed, and the coastline was located near to the head of the submarine of the Penghu Canyon and to our studied site. This configuration enabled the canyon to receive sediments directly from the rivers potentially draining the emerged strait and fluvial networks like the Erhjen River. This would result in coarser sediments, higher silt and sand content, and higher proportion of direct inputs (EM2). The grain size gradually decreased during the deglaciation due to the sea level rise before the MWP-1C linked with the gradual decrease of rivers proximity to the canyon head. However, the sedimentary dynamic was significantly reworked after the MWP-1C (Fig. 6-1).

During the Holocene, the sea level reached values comparable to present time and opened the Taiwan Strait. The proximity of the river mouth of Erhjen strongly decreases and the potential connection of the canyon to rivers was cut. This determined the deposition of finer sediments on the studied site and the increase of the importance of derived inputs to nearly 100% (EM1). During periodw of sea level highstand, the surface current circulation is an important forcing of the sedimentary dynamic. The middle Holocene is characterized by coarser grain size. This time interval of coarser grain size is concurrent with a stronger winter monsoon period. The East Asian winter monsoon could have impacted the hydrodynamic conditions by enhancing and strengthening the loop current induced by the Kuroshio Current intrusion and its shredded eddies and/or enhanced the inputs of coarser material by rivers to the northern South China Sea.

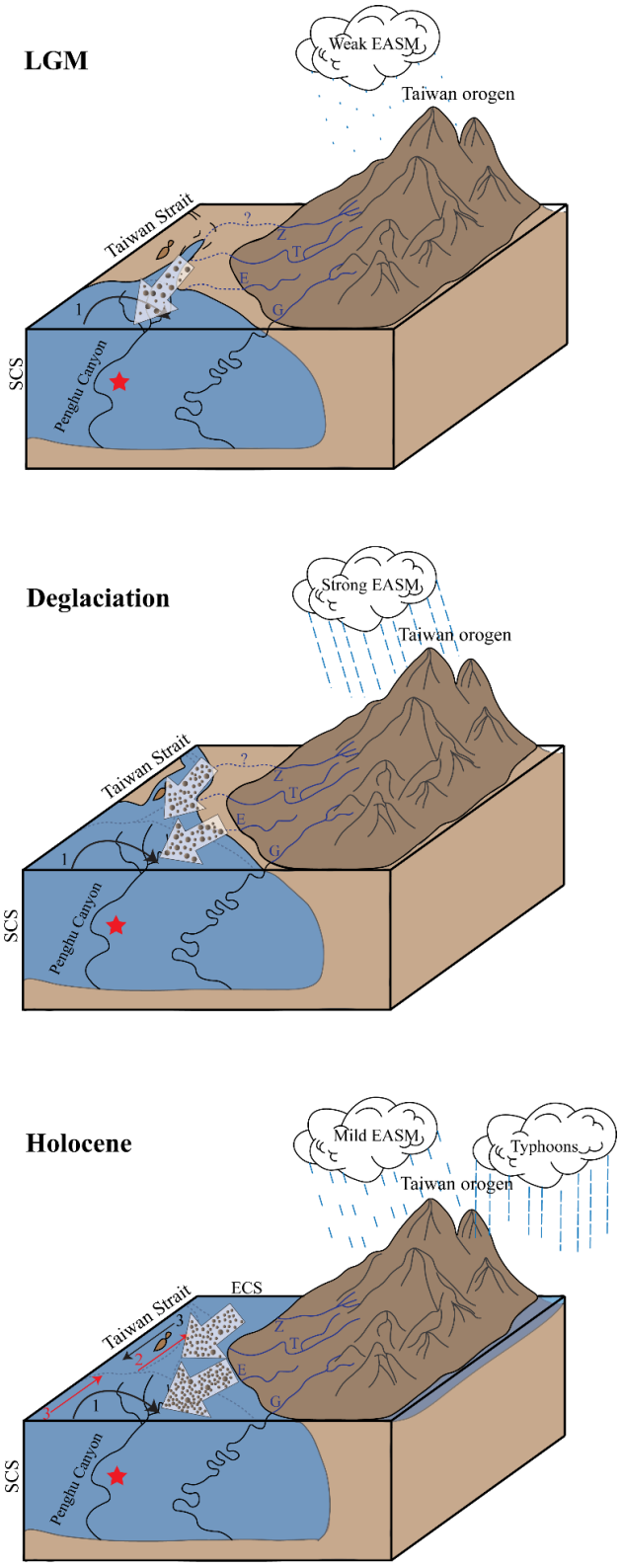

Figure 6-1: Schematic representation of the sedimentary dynamic of the eastern Penghu Canyon during the LGM, deglaciation and Holocene as established in this study.

6.2 Paleo-typhoons activity reconstructed from Turbidites sequence deposit of the Gaoping Canyon levee and its link with climate changes during the last 4.5 kyr.

The head of the Gaoping submarine canyon is connected to the Gaoping River leading to fast sediment transport from the river to the deep-sea basin. The Gaoping Canyon is an efficient conduit for terrestrial sediments, in particular through turbidity currents resulting from the important sediment discharge triggered by typhoons and floods of the Gaoping River. Mooring systems on the levee of the canyon has shown that every year 3 to 4 typhoons trigger about 70% of the turbiditic activity of the Gaoping Canyon.

The core MD18-3574 was collected on the western levee of the Gaoping Canyon, 600 m above the canyon thalweg in order to obtain an archive of the intense typhoon-triggered turbiditic activity and preserving it from erosion by turbidity currents. The age model of the Core MD18-3574 was established by using 11 radiocarbon dating. The Core MD18-3574 is highly laminated with pluri-millimetric dark levels and covers the late Holocene, (last 4 kyr), with a high sedimentation rate (mean sedimentation rate of 500 $cm.kyr^{-1}$).

The laminations were investigated by coupling two non-destructive and high-resolution methods, hyperspectral imaging and XRF core scanning. In addition, laser grain size of sediments from two depth intervals of core MD18-3574 was measured at high resolution of 2 mm and XRD the bulk mineralogy of 10 samples from laminae were investigated to constrain the sedimentary processes responsible for the deposition of the laminations. Hyperspectral imaging allowed us to obtain at the resolution of 150 µm raw information about sediment color (Rmean Short-wave-infrared), grain size (Clay R2200) or organic matter contents (OM R1650) and XRF core scanning gives information on the relative geochemistry of the sediments. The sediments of the two-core section analyzed have a mean grain size ranging from 9 to 20 µm consisting mainly of silt (~75%) and clay (~24%) with low sand (1%). The sediments consist of an alternance of light and fine-grained and dark and coarse-grained levels. We have demonstrated that thick coarse-grained laminations (about 2 to 25 mm) display a fining-upward and asymmetric sorting of typical turbidite deposits. Bulk mineralogy is also slightly contrasted. We have shown that dark levels are coarse sediments rich in quartz, feldspar, calcite and organic matter with high Si/Al, Br and low Fe/Ca values and high Clay R2200 (low clay-sized fraction proportion) and OM R1650 (organic matter content) values. The dark levels are deposited on the levee by the low intensity overflow of turbidity currents occurring in the canyon. Inversely, light laminations are characterized by fine sediments enriched in muscovite, illite and muscovite with low Si/Al, Br, low Clay R2200 (high clay-

sized fraction proportion) and OM R1650 (organic matter content) values and high Fe/Ca values. Such laminations have been associated to hemipelagic sedimentation between turbidity currents. The Rmean SWIR index was used to detect the dark deposits at high resolution.A total of 2400 dark laminae, mostly associated with typhoon events, have been identified for the last 4.2 cal kyr BP. We have then estimated the typhoon frequency (number of dark laminiation per 100 yrs) and intensity (thickness of the dark laminations) recorded on the Gaoping Canyon levee. The frequency record of typhoon events displays a decreasing trend (and controlling the sedimentation rate) ranging from 100 events per 100 years from 4 to 3.2 cal kyr BP and 60 events per 100 years at 300 years to less than 20 events per 100 years after 0.18 cal kyr BP. The thickness of dark laminations ranges from ~0.3 cm to ~1 cm.

The decreasing frequency of typhoon-triggered turbidity deposits after 3 ka co-vary with the cooling of the tropical western Pacific and marginal seas sea surface temperatures (SST), resulting in a shrinking of the Pacific warm pool. This reduces the potential of typhoon genesis in the western Pacific region. From 4 to 1.5 cal kyr BP, the thickness of the deposit, associated with the typhoon intensity, is stable and relatively low (~0.4 cm). However, after 1.5 cal kyr BP the thickness of the deposit shows more variability and in average thicker deposits (~0.6 cm) indicating more variability and intensity of typhoons. The turbidity deposit record of Core MD18-3574 is consistent with many storm and typhoon records previously obtained in Eastern Asia (Central China, northern South China Sea, north-east Taiwan). All the records indicate higher typhoon intensity in time intervals from ~1.5-1.2 ka, 1.0-0.8 ka and 0.5-0.2 ka.

The decrease in typhoon frequency during the late Holocene is driven by the interactions between the cooling of the western tropical Pacific region SST and the strengthening of East Asian winter monsoon. This results in the reduction of the local typhoon genesis and/or the intensity of the typhoons. After 1.5 ka, cold periods are associated with strong typhoon (formed in Central Pacific) surge in Taiwan region and Central China). Their tracks are controlled by the La Niña-like conditions, the stronger Pacific Walker Circulation and East Asian winter monsoon winds.

6.3 Synthesis

Our study focused on the southern margin of Taiwan and particularly on sediments from the bank of the Penghu and Gaoping submarine canyons. Their very contrasted configurations

allowed us to frame the impacts of climatic and environmental changes on various source to sink processes.

The Gaoping Canyon is connected to the Gaoping River which directly discharges sediments to the canyon, resulting in an important turbiditic activity. The head of the Penghu Canyon is not connected to any rivers at present time. Our study allowed us to identify a mixing of SW Taiwan rivers (e.g. Erhjen, Tsengwen rivers) sediment mostly derived through surface circulation (>75%) as the source of sediments on the eastern Penghu Canyon levee. The sediment provenance is not affected by sea-level fluctuations. However, sea level fluctuations strongly affected the hydrodynamic conditions by decreasing the vicinity between our study site to river mouths and potentially disconnecting the Penghu Canyon of direct sediment inputs from SW Taiwan rivers extending to Taiwan Strait during the Melt Water Pulse-1C.

East Asia climate is largely dominated by the monsoon system and typhoons. Due to their configurations, both canyons have different but complementary responses to climate variations. The monsoon system strongly affects the sedimentary dynamic in south Taiwan. The important summer monsoon precipitations enhance the chemical weathering and pedogenesis of south Taiwan in humid periods such as the deglaciation and early Holocene. The chemical weathering is reduced when the summer monsoon precipitations over Taiwan are weakened, during the LGM and since the early Holocene. During the Holocene, the soils of south Taiwan are strongly eroded by the intense typhoon activity as recorded by the high typhoon-triggered turbidity current activity observed on the Gaoping Canyon levee. The climate cooling since middle Holocene optimum induced a weakening of summer monsoon precipitation and typhoon frequency in south Taiwan region. However, the typhoon frequency decrease was associated with an increase of intensity of typhoons precipitation in south Taiwan during late Holocene induced by the strengthening of winter monsoon and La Niña states of El Niño Southern Oscillation.

6.4 Perspectives

This research work brought new insights in the understanding of the sedimentary processes and dynamics on the northern SCS margin of Taiwan since the last glacial period. However, further investigations could be performed to explore more in detail the sedimentary processes in the south of Taiwan.

Core MD18-3569 collected on the eastern levee of the Penghu Canyon was only studied on the top 15m covering 32 ka. However, the core has a total length of ~40m. Considering that the sedimentation rate during the last glacial maximum ranges from 35 to 50 cm/kyr, the bottom of the core could cover further than 100 ka (MIS 5). Thus, the sedimentary dynamic of the Penghu Canyon and SW Taiwan could be explored in great details during a complete glacial-interglacial cycle.

The hyperspectral imaging performed on the Core MD18-3574 brings high resolution (150 μm) raw information on organic matter transfer and burial in a submarine canyon. With a very precise age model and the high sedimentation rate (5mm/yr), it would be possible to study in detail the seasonality of the processes and controls (climate) organic matter cycle on northern SCS margin canyons. In addition, hyperspectral imaging offers various indices that were not fully understood which could bring divers advances in the understanding of Gaoping Canyon dynamics.

The approach coupling hyperspectral imaging and XRF core scanning to the laminated core MD18-3574 appears to be adapted to this sedimentary environment and could bring new perspective in marine core routine studies. More hyperspectral investigations on different marine cores (e.g Penghu Canyon levee cores, marine drilling cores, …) would be important for the development of hyperspectral imaging insight and limits in marine geology research.

The future changes of typhoon activity, associated with the ongoing anthropic global climatic changes, deduced from the past typhoon activity history recorded by Gaoping Canyon, could be investigated using climate models.

References

Adhikari, K., & Hartemink, A.E., (2016), Linking soils to ecosystem services—A global review. *Geoderma 262*, 101-111. https://doi.org/10.1016/j.geoderma.2015.08.009

Ahnert, F., (1970), Functional relationships between denudation, relief, and uplift in large, mid-latitude drainage basins. *American Journal of Science*, *268*(3), 243-263.

Allan, R., Lindesay, J., & Parker, D., (1996), El Niño southern oscillation & climatic variability. *CSIRO publishing*

Allen, S.E., & Durrieu de Madron, X. (2009). A review of the role of submarine canyons in deep-ocean exchange with the shelf. Ocean *Science, 5*(4), 607-620.

An, Z., Kukla, G. J., Porter, S. C., & Xiao, J. (1991). Magnetic susceptibility evidence of monsoon variation on the Loess Plateau of central China during the last 130,000 years. *Quaternary Research. 36*(1), 29-36. https://doi.org/10.1016/0033-5894(91)90015-W

An, Z., (2000), The history and variability of the East Asian paleomonsoon climate. *Quaternary Science Reviews*, *19*(1-5), 171-187.

An, Z., Wu, G., Li, J., Sun, Y., Liu, Y., Zhou, W., Cai, Y., Duan, A., Li, L., Mao, J., Cheng, H., Shi, Z., Tan, L., Yan, H., Ao, H., Chang, H., & Feng, J. (2015). Global monsoon dynamics and climate change. *Annual Review of Earth and Planetary Sciences, 43*, 29-77 https://doi.org/10.1146/annurev-earth-060313-054623

Andersen, K.K., Azuma N., Barnola J.M., Bigler M., Biscaye P., Caillon N., Chappellaz J., 2004. High-resolution record of Northern Hemisphere climate extending into the last interglacial period. Nature 431 (7005), 147-51. https://doi.org/10.1038/nature02805

Anschutz, P., Jorissen, F. J., Chaillou, G., Abu-Zied, R., & Fontanier, C. (2002). Recent turbidite deposition in the eastern Atlantic: early diagenesis and biotic recovery. *Journal of Marine Research*, *60*(6), 835-854.

Ao, H., Roberts, A.P., Dekkers, M.J., Liu, X., Rohling, E.J., Shi, Z., An, Z., & Zhao, X., (2016), Late Miocene–Pliocene Asian monsoon intensification linked to Antarctic ice-sheet growth. *Earth and Planetary Science Letters*, *444*, 75-87.

Arnaud, F., Révillon, S., Debret, M., Revel, M., Chapron, E., Jacob, J., Giguet-Covex, C., Poulenard, J., & Magny, M., (2012), Lake Bourget regional erosion patterns

reconstruction reveals Holocene NW European Alps soil evolution and paleohydrology. *Quat. Sci. Rev*. 51, 81–92. https://doi.org/10.1016/j.quascirev.2012.07.025.

Arnaud, F., Poulenard, J., Giguet-Covex, Ch., Wilhelm, B., Revillon, S., Jenny, J.-P., Revel, M., Enters, D., Bajard, M., Fouinat, L., Doyen, E., Simonneau, A., Pignol, C., Chapron, E., Vanniere, B., & Sabatier, P., (2016), Erosion under climate and human pressures: an alpine lake sediment perspective. *Quat. Sci. Rev*. 152, 1–18.

Babonneau, N., Delacourt, C., Cancouët, R., Sisavath, E., Bachèlery, P., Mazuel, A., Jorry, S.J., Deschamps, A., Ammann, J., & Villeneuve, N. (2013). Direct sediment transfer from land to deep-sea: Insights into shallow multibeam bathymetry at La Réunion Island. *Marine Geology*, *346*, 47-57.

Bajard, M., Sabatier, P., David, F., Develle, A.-L., Reyss, J.-L., Fanget, B., Malet, E., Arnaud, D., Augustin, L., Crouzet, C., Poulenard, J., & Arnaud, F., (2016), Erosion record in Lake La Thuile sediments (Prealps, France): Evidence of montane landscape dynamics throughout the Holocene. *The Holocene* 26, 350–364. https://doi.org/10.1177/0959683615609750

Bajard, M., Poulenard, J., Sabatier, P., Develle, A.-L., Giguet-Covex, C., Jacob, J., Crouzet, C., David, F., Pignol, C., & Arnaud, F., (2017a), Progressive and regressive soil evolution phases in the Anthropocene. *CATENA 150*, 39–52. https://doi.org/10.1016/j.catena.2016.11.001.

Bajard, M., Poulenard, J., Sabatier, P., Etienne, D., Ficetola, F., Chen, W., Gielly, L., Taberlet, P., Develle, A.-L., Rey, P.-J., Moulin, B., de Beaulieu, J.-L., & Arnaud, F., 2017b. Long-term changes in alpine pedogenetic processes : Effect of millennial agro-pastoralism activities (French-Italian Alps). *Geoderma* 306, 217–236. https://doi.org/10.1016/j.geoderma.2017.07.005

Bandara, G., Luo, C., Chen, C., Xiang, R., Herath, D. B., Yang, Z., & Thilakanayaka, V., (2023), Sedimental pollen records in the northern South China Sea and their paleoenvironmental significance. *Journal of Asian Earth Sciences*, *241*, 105457.

Barr, C., Tibby, J., Leng, M. J., Tyler, J. J., Henderson, A. C. G., Overpeck, J. T., Simpson, G.L., Cole, J.E., Phipps, S.J., Marshall, J.C., McGregor, B., Hua, Q., & McRobie, F. H., (2019), Holocene El Niño–southern Oscillation variability reflected in subtropical Australian precipitation. *Scientific Reports*, *9*(1), 1627.

Basak, C., Martin, E.E., Horikawa, K., & Marchitto, T.M., (2010), Southern Ocean source of 14C-depleted carbon in the North Pacific Ocean during the last deglaciation. *Nature Geoscience*, *3*(11), 770-773.

Berger, A., (1978), Long-term variations of daily insolation and Quaternary climatic changes. *J. Atmos. Sci. 35(*12), 2362-2367. https://doi.org/10.1175/1520-0469(1978)035<2362:LTVODI>2.0.CO;2

Bernhardt, A., & Schwanghart, W., (2021), Where and why do submarine canyons remain connected to the shore during sea-level rise? Insights from global topographic analysis and Bayesian regression. *Geophysical Research Letters*, *48*(10), e2020GL092234

Bhattacharjee, S., Bookhagen, B., & Sinha, R., (2022), Sediment-transport rates from decadal to millennial timescales across the Indo-Gangetic Plain: Impacts of tectonics, climatic processes, and vegetation cover. *Earth-Science Reviews*, 104165.

Bi, L., Yang, S., Li, C., Guo, Y., Wang, Q., Liu, J.T., & Yin, P, (2015), Geochemistry of river-borne clays entering the E ast C hina S ea indicates two contrasting types of weathering and sediment transport processes. *Geochemistry, Geophysics, Geosystems*, *16*(9), 3034-3052.

Bjerknes, J., (1969), Atmospheric teleconnections from the equatorial pacific 1. *Mon. Weather Rev.*, 97, 163–172.

Blaauw, M., Christen, A., (2011), Flexible paleoclimate age-depth models using an autoregressive gamma process. *Bayesian Analysis* 6, 457–474.

Boggs, S., (1979), Sediment properties and water characteristics of the Taiwan shelf and slope. *Acta Oceanogr. Taiwan.*, *10*, 10-49.

Bonneau, L., Jorry, S. J., Toucanne, S., Silva Jacinto, R., & Emmanuel, L. (2014). Millennial-scale response of a western Mediterranean river to late Quaternary climate changes: a view from the deep sea. *The Journal of Geology*, *122*(6), 687-703.

Böse, M., (2004)., Traces of glaciation in the high mountains of Taiwan. In *Developments in Quaternary Sciences* (Vol. 2, pp. 347-352)

Boulay, S., Colin, C., Trentesaux, A., Pluquet, F., Bertaux, J., Blamart, D., Buehring, C., & Wang, P. (2003), Mineralogy and sedimentology of Pleistocene sediment in the South China Sea (ODP Site 1144). In *Proceedings of the ocean drilling program, scientific results* (Vol. 184, No. 211, pp. 1-21).

Boulay, S., Colin, C., Trentesaux, A., Frank, N., & Liu, Z., (2005), Sediment sources and East Asian monsoon intensity over the last 450 ky. Mineralogical and geochemical investigations on South China Sea sediments. *Palaeogeography, Palaeoclimatology, Palaeoecology*, *228*(3-4), 260-277.

Boulay, S., Colin, C., Trentesaux, A., Clain, S., Liu, Z., & Lauer-Leredde, C., (2007), Sedimentary responses to the Pleistocene climatic variations recorded in the South China Sea. *Quaternary Research*, *68*(1), 162-172.

Boulay, S., Colin, C., & Trentesaux, A., (2008), Traceurs sédimentaires des variations du niveau marin et de la mousson sud-est asiatique depuis 450 ka en mer de Chine du Sud. *Comptes Rendus Geoscience*, *340*(6), 367-378.

Bouma, A.H., (1962), Sedimentology of Some Flysch Deposits: A Graphic Approach to Facies Interpretation. *Elsevier, Amsterdam vol. 168*

Bozyiğit, C., Eriş, K.K., Sicre, M.A., Çağatay, M.N., Uçarkuş, G., Klein, V., & Gasperini, L., (2022), Middle-late Holocene climate and hydrologic changes in the Gulf of Saros (NE Aegean Sea). *Marine Geology*, *443*, 106688.

Brantley, S.L., Goldhaber, M.B., & Ragnarsdottir, K.V., (2007), Crossing disciplines and scales to understand the critical zone. *Elements 3(5),* 307-314. https://doi.org/10.2113/gselements.3.5.307

Brantley, S.L., McDowell, W.H., Dietrich, W E., White, T.S., Kumar, P., Anderson, S.P., Chorover, J., Lohse, K.A., Bales, R.C., Richter, D.D., Grant, & G., Gaillardet, J., (2017), Designing a network of critical zone observatories to explore the living skin of the terrestrial Earth. *Earth Surf. Dyn. 5(4),* 841-860. https://doi.org/10.5194/esurf-5-841-2017

Bull, W.B., (1990), Stream-terrace genesis: implications for soil development. *Geomorphology 3*(3-4), 351-367. https://doi.org/10.1016/0169-555X(90)90011-E

Butz, C., Grosjean, M., Fischer, D., Wunderle, S., Tylmann, W., & Rein, B., (2015), Hyperspectral imaging spectroscopy: a promising method for the biogeochemical analysis of lake sediments. *Journal of Applied Remote Sensing*, *9*(1), 096031-096031.

Canals, M., Puig, P., de Madron, X.D., Heussner, S., Palanques, A., & Fabres, J. (2006). Flushing submarine canyons. *Nature, 444* (7117), 354-357.

Carcaillet, J., Siame, L. L., Chu, H. T., Bourlès, D. L., Lu, W. C., Angelier, J., & Dussouillez, P., (2007)., First cosmic ray exposure dating (in situ produced 10Be) of the late Pleistocene and Holocene glaciation in the Nanhutashan Mountains (Taiwan). *Terra Nova*, *19*(5), 331-336.

Caruso, M., Gawarkiewicz, G., & Beardsley R. (2006), Interannual variability of the Kuroshio intrusion in the South China Sea. *Journal of Oceanography* 62: 559-75. https://doi.org/10.1007/s10872-006-0076-0.

Chamley, H., (1989), Clay Sedimentology. *Springer, New York* (623 pp.).

Chan, J. C. (2005). The physics of tropical cyclone motion. *Annu. Rev. Fluid Mech.*, 37, 99-128.

Chan, J. C. L., (2007), Interannual variations of intense typhoon activity. *Tellus* 59, 455–460.

Chen, C.S., & Chen, Y.L. (2003). The rainfall characteristics of Taiwan. *Monthly Weather Review*, *131*(7), 1323-1341.

Chen, H.F., Wen, S.Y., Song, S.R., Yang, T.N., Lee, T.Q., Lin, S.F., Hsu, S.C., Wei, K.Y., Chang, P.Y., & Yu, P.S., (2012), Strengthening of paleo-typhoon and autumn rainfall in Taiwan corresponding to the Southern Oscillation at late Holocene. *Journal of Quaternary Science*, *27*(9), 964-972.

Chen, H., Xie, X., Mao, K., He, Y., Su, M., & Zhang, W., (2020), Depositional Characteristics and Formation Mechanisms of Deep-Water Canyon Systems along the Northern South China Sea Margin. *J. Earth Sci. 31*, 808–819 https://doi.org/10.1007/s12583-020-1284-z

Chen, Y., Wang, Y., Dang, H., & Jian, Z., (2021), Hydroclimatic changes in the northeastern South China Sea since the Last Glacial Maximum. *Quaternary Sciences* 41 (4): 1031-1043. doi: 10.11928/j.issn.1001-7410.2021.04.13.

Chen, Z., Ding, Z., Yang, S., Zhang, C., & Wang, X., (2016), Increased precipitation and weathering across the Paleocene-Eocene Thermal Maximum in central China. *Geochemistry, Geophysics, Geosystems*, *17*(6), 2286-2297.

Chen, M.T., & Beaufort, L., (1998), Exploring Quaternary Variability of the East Asia Monsoon, Kuroshio Current, and Western Pacific Warm Pool Systems: High-Resolution Investigations of Paleoceanography from the IMAGESIII (MD106)-IPHIS Cruis. *Terrestrial, Atmospheric and Oceanic Sciences*, *9*(1), 129-142.

Cheng, H., Edwards, R.L., Sinha, A., Spötl, C., Yi, L., Chen, S., Kelly, M., Kathayat, G., Wang, X., Li, X., Kong, X., Wang, Y., Ning, Y., & Zhang, H. (2016), The Asian monsoon over the past 640,000 years and ice age terminations. *Nature*, *534*(7609), 640-646.

Cheng, Z., Wu, J., Luo, C., Liu, Z., Huang, E., Zhao, H., Dai, L, & Weng, C., (2023), Coexistence of savanna and rainforest on the ice-age Sunda Shelf revealed by pollen records from southern South China Sea. *Quaternary Science Reviews*, *301*, 107947.

Ching, K.-E., Hsieh, M.-L., Johnson, K.M., Chen, K.-H., Rau, R.-J., & Yang, M., (2011), Modern vertical deformation rates and mountain building in Taiwan from precise leveling and continuous GPS observations, 2000–2008. *J. Geophys. Res.* 116. https://doi.org/10.1029/2011JB008242

Chiang, C.S., & Yu, H.S., (2006), Morphotectonics and incision of the Kaoping submarine canyon, SW Taiwan orogenic wedge. *Geomorphology*, *80*(3-4), 199-213.

Chiang, C., & Yu, H., (2011), Sedimentary erosive processes and sediment dispersal in Kaoping submarine canyon. *Science China Earth Sciences*, *54*(2), 259-271.

Chiang, J.C.H., Fang, Y., & Chang, P., (2009), Pacific climate change and ENSO activity in the mid-Holocene. *Journal of Climate*, *22*(4), 923-939.

Chien, F.C., & Kuo, H.C. (2011), On the extreme rainfall of Typhoon Morakot (2009). *Journal of Geophysical Research: Atmospheres*, *116*(D5).

Cho, A., Lim, J., Kim, Y., & San Ahn, U., (2022), Variability of East Asian winter monsoon during Middle–Late Holocene: A study based on a crater lake on Jeju Island, South Korea. *Palaeogeography, Palaeoclimatology, Palaeoecology*, *603*, 111193.

Chu, P.C., & Wang, G., (2003), Seasonal variability of thermohaline front in the central South China Sea. J. Oceanogr. 59, 65–78.

Chuang, C.Y., & Yu, H.S., (2002), Morphology and canyon forming processes of upper reach of the Penghu submarine canyon off southwestern Taiwan. *Terrestrial Atmospheric and Oceanic Sciences*, *13*(1), 91-108.

Clauer, N., (1979), Relationship between the isotopic composition of strontium in newly formed continental clay minerals and their source material, *Chem. Geol.*, 27, 115 – 124.

Clemens S.C., Murray D.W., & Prell W.L. (1996), Nonstationary phase of the Plio-Pleistocene Asian monsoon. *Science* 274, 943-948.

Clift, P., Lee, J. I., Clark, M. K., & Blusztajn, J., (2002), Erosional response of South China to arc rifting and monsoonal strengthening; a record from the South China Sea. *Marine Geology*, *184*(3-4), 207-226.

Clift, P.D., Sun, Z., (2006), The sedimentary and tectonic evolution of the Yinggehai–Song Hong basin and the southern Hainan margin, South China Sea: Implications for Tibetan uplift and monsoon intensification. *J. Geophys. Res.: Solid Earth 111*(B6). https://doi.org/10.1029/2005JB004048

Clift, P.D., Giosan, L., Blusztajn, J., Campbell, I.H., Allen, C., Pringle, M., Tabrez, A.R;, Danish, M., Rabbani, M.M., Alizai, A., Carter, A., & Lückge, A., (2008), Holocene erosion of the Lesser Himalaya triggered by intensified summer monsoon. *Geology*, *36*(1), 79-82.

Clift, P.D., Wan, S., & Blusztajn, J., (2014), Reconstructing chemical weathering, physical erosion and monsoon intensity since 25 Ma in the northern South China Sea: a review of competing proxies. *Earth-Science Reviews*, *130*, 86-102.

Clift, P. D. (2020). Asian monsoon dynamics and sediment transport in SE Asia. *Journal of Asian Earth Sciences. 195*, 104352. https://doi.org/10.1016/j.jseaes.2020.104352

Cobb, K.M., Westphal, N., Sayani, H.R., Watson, J.T., Di Lorenzo, E., Cheng, H., Edwards, R., & Charles, C.D., (2013), Highly variable El Niño–southern oscillation throughout the Holocene. *Science*, *339*(6115), 67-70.

Colin, C., Turpin, L., Bertaux, J., Desprairies, A., & Kissel, C., (1999), Erosional history of the Himalayan and Burman ranges during the last two glacial–interglacial cycles. *Earth and Planetary Science Letters*, *171*(4), 647-660.

Colin, C., Turpin, L., Blamart, D., Frank, N., Kissel, C., & Duchamp, S., (2006), Evolution of weathering patterns in the Indo-Burman Ranges over the last 280 kyr: Effects of sediment provenance on 87Sr/86Sr ratios tracer. *Geochemistry, Geophysics, Geosystems*, *7*(3).

Colin, C., Siani, G., Sicre, M. A., & Liu, Z., (2010), Impact of the East Asian monsoon rainfall changes on the erosion of the Mekong River basin over the past 25,000 yr. *Marine Geology*, *271*(1-2), 84-92.

Conroy, J.L., Overpeck, J.T., Cole, J.E., Shanahan, T.M., & Steinitz-Kannan, M., (2008), Holocene changes in eastern tropical Pacific climate inferred from a Galápagos lake sediment record. *Quaternary Science Reviews*, *27*(11-12), 1166-1180.

Contreras-Rosales, L.A., Jennerjahn, T., Steinke, S., Mohtadi, M., & Schefuß, E., (2019), Holocene changes in biome size and tropical cyclone activity around the Northern South China Sea. *Quaternary Science Reviews*, *215*, 45-63.

Copard, K., Colin, C., Douville, E., Freiwald, A., Gudmundsson, G., De Mol, B., & Frank, N., (2010), Nd isotopes in deep-sea corals in the North-eastern Atlantic. *Quat. Sci. Rev*. 29, 2499–2508. https://doi.org/10.1016/j.quascirev.2010.05.025.

Cowton, T., Nienow, P., Bartholomew, I., Sole, A., & Mair, D., (2012), Rapid erosion beneath the Greenland ice sheet. *Geology*, *40*(4), 343-346.

Cui, Z., Yang, C., Liu, G., Zhang, W., Wang, S., & Sung, Q., (2002), The Quaternary glaciation of Shesan Mountain in Taiwan and glacial classification in monsoon areas. *Quaternary International*, *97*, 147-153.

Dadson, S.J., Hovius, N., Chen, H., Dade, W.B., Hsieh, M.L., Willett, S.D, & Hu, J.C., (2003), Links between Erosion, Runoff Variability and Seismicity in the Taiwan Orogen. *Nature* 426 (6967): 648-51. https://doi.org/10.1038/nature02150.

Dadson, S., Hovius, N., Pegg, S., Dade, W.B., Horng, M.J., & Chen, H., (2005), Hyperpycnal river flows from an active mountain belt. *Journal of Geophysical Research: Earth Surface*, *110*(F4).

Dai, L., & Weng, C., (2015a), Marine palynological record for tropical climate variations since the late last glacial maximum in the northern South China Sea. *Deep Sea Research Part II: Topical Studies in Oceanography*, *122*, 153-162.

Dai, L., Weng, C., & Mao, L., (2015b), Patterns of vegetation and climate change in the northern South China Sea during the last glaciation inferred from marine palynological records. *Palaeogeography, Palaeoclimatology, Palaeoecology*, *440*, 249-258.

Dang, H., Jian, Z., Wang, Y., Mohtadi, M., Rosenthal, Y., Ye, L., Bassinot, F., & Kuhnt, W., (2020), Pacific warm pool subsurface heat sequestration modulated Walker circulation and ENSO activity during the Holocene. *Science Advances*, *6*(42), eabc0402.

Dare, R.A., & McBride, J.L., (2011), The threshold sea surface temperature condition for tropical cyclogenesis. *Journal of climate*, *24*(17), 4570-4576.

Deng, K., Yang, S., Bi, L., Chang, Y.P., Su, N., Frings, P., & Xie, X., (2019), Small dynamic mountainous rivers in Taiwan exhibit large sedimentary geochemical and provenance heterogeneity over multi-spatial scales, *Earth and Planetary Science Letters, 505*, 96-109.

Deng, Y.C., Tsai, F., & Hwang, J.H., (2016), Landslide characteristics in the area of Xiaolin Village during Morakot typhoon. *Arabian Journal of Geosciences*, *9*, 1-16.

Deprez, M., De Kock, T., De Schutter, G., & Cnudde, V., (2020), A review on freeze-thaw action and weathering of rocks. *Earth-Science Reviews*, *203*, 103143.

Derry, L.A., & France-Lanord, C., (1996), Neogene Himalayan weathering history and river87Sr86Sr: impact on the marine Sr record. *Earth and Planetary Science Letters*, *142*(1-2), 59-74.

Descheemaeker, K., Nyssen, J., Poesen, J., Raes, D., Haile, M., Muys, B., & Deckers, S., (2006), Runoff on slopes with restoring vegetation: a case study from the Tigray highlands, Ethiopia. *Journal of hydrology*, *331*(1-2), 219-241.

Dewey, J.F., & Horsfield, B. (1970), Plate tectonics, orogeny and continental growth. *Nature*, *225*(5232), 521-525.

Dickinson, R.E., (1983), Land surface processes and climate—Surface albedos and energy balance. *Adv. Geophys*. 25, 305–353.

Ding, Z., Liu, T., Rutter, N.W., Yu, Z., Guo, Z., & Zhu, R., (1995), Ice-volume forcing of East Asian winter monsoon variations in the past 800,000 years. *Quaternary Research*, *44*(2), 149-159.

Dong, D., Zhou, W., Yang, Y., & Du, Y. (2010), On outflow passages in the South China Sea. *Advances in Atmospheric sciences*, *27*, 60-68.

Dong, J., Li, A., Lu, Z., Liu, X., Wan, S., Yan, H., Yu, Z., Feng, X., & Shi, X., (2021), Millennial-scale interaction between the East Asian winter monsoon and El Niño-related tropical Pacific precipitation in the Holocene. *Palaeogeography, Palaeoclimatology, Palaeoecology*, *573*, 110442.

Dosseto, A., Hesse, P.P., Maher, K., Fryirs, K., & Turner, S, (2010), Climatic and vegetation control on sediment dynamics during the last glacial cycle. *Geology*, *38*(5), 395-398.

Dou, Y., Yang, S., Shi, X., Clift, P.D., Liu, S., Liu, J., & Zhao, Y., (2016), Provenance weathering and erosion records in southern Okinawa Trough sediments since 28 ka: geochemical and Sr–Nd–Pb isotopic evidences. *Chem. Geol*. 425, 93–109. https://doi.org/10.1016/j.chemgeo.2016.01.029.

Druckman, Y., Buchbinder, B., Martinotti, G. M., Tov, R. S., & Aharon, P., (1995), The buried Afiq Canyon (eastern Mediterranean, Israel): a case study of a Tertiary submarine canyon exposed in Late Messinian times. *Marine Geology*, *123*(3-4), 167-185.

Duan, B., Li, T., Wang, L., & Xiong, Z., (2023), Holocene sea level change and paleoenvironmental evolution off the Shandong Peninsula: Evidence of benthic foraminifera assemblages from core LHSD-1 in a subaqueous clinoform. *Journal of Sea Research*, 102338.

Durkee, E.F., Selmer L.P., (1961), Geology of Northern Luzon, Philippines. *AAPG Bulletin* 45 (2): 137–168. doi: https://doi.org/10.1306/0BDA632F-16BD-11D7-8645000102C1865D

Dykoski, C., Edwards, R., Cheng, H., Yuan, D., Cai, Y., Zhang, M., Lin, Y., Qing, J., An, Z., & Revenaugh, J., (2005), A High-Resolution, Absolute-Dated Holocene and Deglacial Asian Monsoon Record from Dongge Cave, China. *Earth and Planetary Science Letters* 233 (1-2): 71-86. https://doi.org/10.1016/j.epsl.2005.01.036.

Elsner, J.B., & Liu, K.B., (2003), Examining the ENSO-typhoon hypothesis. *Climate Research*, *25*(1), 43-54.

Emanuel, K., (2003), Tropical cyclones. *Annual review of earth and planetary sciences*, *31*(1), 75-104.

Emile-Geay, J., Cobb, K.M., Carré, M., Braconnot, P., Leloup, J., Zhou, Y., Harrison, s., Corrège, T., McGregor, H., & Tudhope, A., (2016), Links between tropical Pacific seasonal, interannual and orbital variability during the Holocene. *Nature Geoscience*, *9*(2), 168-173.

Eppes, M. C., Magi, B., Scheff, J., Warren, K., Ching, S., & Feng, T., (2020), Warmer, wetter climates accelerate mechanical weathering in field data, independent of stress-loading. *Geophysical Research Letters*, 47, 2020GL089062. https://doi.org/10.1029/2020GL089062

Ehrmann, W., Schmiedl, G., Hamann, Y., Kuhnt, T., Hemleben, C., &Siebel, W., (2007), Clay minerals in late glacial and Holocene sediments of the northern and southern Aegean Sea, *Palaeogeography, Palaeoclimatology, Palaeoecology 249*, 36–57

Esquevin, J., (1969,) Influence de la composition chimique des illites sur leur cristallinité: *Bull. Centre de Recherches de Pau (Soc. National des Pétroles d'Aquitaine) 3*, 147–153.

Fang, G., Fang, W., Fang, Y., & Wang, K., (1998), A survey of studies on the South China Sea upper ocean circulation. *Acta Oceanographica Taiwanica* 37: 1-16.

Fang, T.H., Huang, Z.T., &Chang, F.W., (2022), The geochemical and environmental characteristics of trace metals in surface sediments of the river estuarine mouths around the Taiwan Island and the Taiwan Strait, *Marine Pollution Bulletin, 182*.

Farris, A., & Wimbush, M. (1996). Wind-induced Kuroshio intrusion into the South China Sea. *Journal of Oceanography*, *52*, 771-784.

Ferrier, K L., & Kirchner, J.W., (2008), Effects of physical erosion on chemical denudation rates: A numerical modeling study of soil-mantled hillslopes. *Earth and Planetary Science Letters*, *272*(3-4), 591-599.

France-Lanord, C., & Derry, L.A., (1997), Organic carbon burial forcing of the carbon cycle from Himalayan erosion. *Nature*, *390*(6655), 65-67.

Gaillardet, J., Dupré, B., Louvat, P., & Allegre, C.J., (1999), Global silicate weathering and CO2 consumption rates deduced from the chemistry of large rivers. *Chemical geology*, *159*(1-4), 3-30.

Gaillardet, J., Braud, I., Hankard, F., Anquetin, S., Bour, O., Dorfliger, N., de Dreuzy, J.R., Galle, S., Galy, C., Gogo, S., Gourcy, L., Habets, F., Laggoun, F., Longuevergne, L., Le Borgne, T., Naaim-Bouvet, F., Nord, G., Simonneaux, V., Six, D., Tallec, T., Valentin, C., Abril, G., Allemand, P., Arènes, A., Arfib, B., Arnaud, L., Arnaud, N., Arnaud, P., Audry, S., Comte, V.B., Batiot, C., Battais, A., Bellot, H., Bernard, E., Bertrand, C., Bessière, H., Binet, S., Bodin, J., Bodin, X., Boithias, L., Bouchez, J., Boudevillain, B., Moussa, I.B., Branger, F., Braun, J.J., Brunet, P., Caceres, B., Calmels, D., Cappelaere, B., Celle-Jeanton, H., Chabaux, F., Chalikakis, K., Champollion, C., Copard, Y., Cotel, C., Davy, P., Deline, P., Delrieu, G., Demarty, J., Dessert, C., Dumont, M., Emblanch, C., Ezzahar, J., Estèves, M., Favier, V., Faucheux, M., Filizola, N., Flammarion, P., Floury, P., Fovet, O., Fournier, M., Francez, A.J., Gandois, L., Gascuel, C., Gayer, E., Genthon, C., Gérard, M.F., Gilbert, D., Gouttevin, I., Grippa, M., Gruau, G., Jardani, A., Jeanneau, L., Join, J.L., Jourde, H., Karbou, F., Labat, D., Lagadeuc, Y., Lajeunesse, E., Lastennet, R., Lavado, W., Lawin, E., Lebel, T., Le Bouteiller, C., Legout, C., Lejeune, Y., Le Meur, E., Le Moigne, N., Lions, J., Lucas, A., Malet, J.P., Marais-Sicre, C., Maréchal, J.C., Marlin, C., Martin, P., Martins, J., Martinez, J.M., Massei, N., Mauclerc, A., Mazzilli, N., Molénat, J., Moreira-Turcq, P., Mougin, E., Morin, S., Ngoupayou,

J.N., Panthou, G., Peugeot, C., Picard, G., Pierret, M.C., Porel, G., Probst, A., Probst, J.L., Rabatel, A., Raclot, D., Ravanel, L., Rejiba, F., René, P., Ribolzi, O., Riotte, J., Rivière, A., Robain, H., Ruiz, L., Sanchez-Perez, J.M., Santini, W., Sauvage, S., Schoeneich, P., Seidel, J.L., Sekhar, M., Sengtaheuanghoung, O., Silvera, N., Steinmann, M., Soruco, A., Tallec, G., Thibert, E., Lao, D.V., Vincent, C., Viville, D., Wagnon, P., & Zitouna, R., (2018), OZCAR: The French network of critical zone observatories. *Vadose Zone J. 17*(1), 1-24. https://doi.org/10.2136/vzj2018.04.0067

Gan, J., Liu, Z., & Hui, C., (2016), A three-layer alternating spinning circulation in the South China Sea. *J. Phys. Oceanogr.* 46, 2309–2315. https://doi.org/10.1175/JPO-D-16-

Gao, S., Collins, M. B., Lanckneus, J., De Moor, G., & Van Lancker, V., (1994), Grain size trends associated with net sediment transport patterns: An example from the Belgian continental shelf. *Marine Geology*, *121*(3-4), 171-185.

Gavey, R., Carter, L., Liu, J.T., Talling, P.J., Hsu, R., Pope, E., & Evans, G., (2017), Frequent sediment density flows during 2006 to 2015, triggered by competing seismic and weather events: Observations from subsea cable breaks off southern Taiwan. *Marine Geology*, *384*, 147-158.

Gebregiorgis, D., Hathorne, E.C., Sijinkumar, A.V., Nath, B.N., Nürnberg, D., & Frank, M., (2016), South Asian summer monsoon variability during the last~ 54 kyrs inferred from surface water salinity and river runoff proxies. *Quat. Sci. Rev. 138*, 6-15. https://doi.org/10.1016/j.quascirev.2016.02.012

Ghanbari, H., Jacques, O., Adaïmé, M.É., Gregory-Eaves, I., & Antoniades, D., (2020), Remote sensing of lake sediment core particle size using hyperspectral image analysis. *Remote Sensing*, *12*(23), 3850.

Gingele F.X. (1996), Holocene climatic optimum in Southwest Africa—evidence from marine *Palaeogeogr. Palaeoclimatol. Palaeoecol. 122,* 77-87

Goldstein, S.J., & Jacobsen, S.B., (1988), Nd and Sr isotopic systematics of river water suspended material: implications for crustal evolution. *Earth and Planetary Science Letters*, *87*(3), 249-265.

Gomez, B., Carter, L., Orpin, A.R., Cobb, K.M., Page, M.J., Trustrum, N.A., & Palmer, A.S. (2012). ENSO/SAM interactions during the middle and late Holocene. *The Holocene*, *22*(1), 23-30.

Goudie, A. S., and Viles, H. A., (2012), Weathering and the Global Carbon Cycle: Geomorphological Perspectives. *Earth-Science Rev.* 113, 59–71. doi:10.1016/j.earscirev.2012.03.005

Grant, K.M., Rohling, E.J., Bar-Matthews, M., Ayalon, A., Medina-Elizalde, M., Ramsey, C.B., Satow, C., & Roberts, A.P., (2012), Rapid coupling between ice volume and polar temperature over the past 150,000 years. *Nature*, *491*(7426), 744-747.

Grim, R.E., (1968), Clay Mineralogy. *McGraw-Hill, Inc., New York*, 596 p

Grousset, F. E., Biscaye, P. E., Zindler, A., Prospero, J., & Chester, R., (1988), Neodymium isotopes as tracers in marine sediments and aerosols: North Atlantic. *Earth and Planetary Science Letters*, *87*(4), 367-378.

Guo, Z.T., Sun, B., Zhang, Z.S., Peng, S.Z., Xiao, G.Q., Ge, J.Y., Hao, Q.Z., Qiao, Y.S., Liang, M.Y., Liu, J.F., Yin, Q.Z., & Wei, J. J. (2008), A major reorganization of Asian climate regime by the Early Miocene. *Climate of the past Discussions,* 4(3), 535-584.

Hall, R., (2002), Cenozoic geological and plate tectonic evolution of SE Asia and the SW Pacific: computer-based reconstructions, model and animations. *J. Asian Earth Sci*. 20, 353–431.

Hall, R., (2013), Contraction and extension in northern Borneo driven by subduction rollback, *Journal of Asian Earth Sciences*, 76, p. 399–411.

Hess, G. R., & Normark, W. R., (1976), Holocene sedimentation history of the major fan valleys of Monterey Fan. *Marine Geology*, *22*(4), 233-251.

Hess, S., Jorissen, F. J., Venet, V., & Abu-Zied, R. (2005). Benthic foraminiferal recovery after recent turbidite deposition in Cap Breton Canyon, Bay of Biscay. *Journal of Foraminiferal Research*, *35*(2), 114-129.

Ho, C.H., Baik, J.J., Kim, J.H., Gong, D.Y., & Sui, C.H., (2004), Interdecadal changes in summertime typhoon tracks. *Journal of Climate*, *17*(9), 1767-1776.

Hsieh, A. I., Dashtgard, S. E., Wang, P.-L., Horng, C.-S., Su, C.-C., Lin, A. T., Vaucher, R., & Löwemark, L. (2022), Multi-proxy evidence for rapidly shifting sediment sources to the Taiwan Western Foreland Basin at the Miocene–Pliocene transition. *Basin Research*, 00, 1– 17. https://doi.org/10.1111/bre.12741

Hsieh, M.L., & Knuepfer, P.L.K., (2001), Middle–Late Holocene River Terraces in the Erhjen River Basin, Southwestern Taiwan—Implications of River Response to Climate Change and Active Tectonic Uplift. *Geomorphology* 38. 337–372

Hsieh, M.-L., & Knuepfer, P.L.K., (2002), Synchroneity and morphology of Holocene river terraces in the southern Western Foothills, Taiwan: A guide to interpreting and correlating erosional river terraces across growing anticlines, *in Byrne, T.B., and Liu, C.-S., eds., Geology and Geophysics of an Arc-Continent Collision, Taiwan: Boulder, Colorado, Geological Society of America Special Paper* 358, p. 55–74.

Hsiung, K.H., & Saito, S., (2017),Sediment trapping in deltas of small mountainous rivers of southwestern Taiwan and its influence on East China Sea sedimentation, *Quaternary International, 455,* 30-44.

Hsiung, K.H., Kanamatsu, T., Ikehara, K., Usami, K., Horng, C.S., Ohkouchi, N., Ogawa, N.O., Saito, S., & Murayama, M., (2021), X-ray fluorescence core scanning, magnetic signatures, and organic geochemistry analyses of Ryukyu Trench sediments: turbidites and hemipelagites. *Progress in Earth and Planetary Science*, *8*, 1-17.

Hsu, R.T., Liu, J.T., Su, C.C., Kao, S.J., Chen, S.N., Kuo, F H., & Huang, J.C., (2014), On the links between a river's hyperpycnal plume and marine benthic nepheloid layer in the wake of a typhoon. *Progress in Oceanography*, *127*, 62-73.

Hu, B., Li, J., Cui, R., Wei, H., Zhao, J., Li, G., Fang, X., Ding, X., Zou, L., & Bai, F., (2014), Clay mineralogy of the riverine sediments of Hainan Island, South China Sea: Implications for weathering and provenance, *Journal of Asian Earth Sciences 96,* 84-92

Hu, D., Böning, P., Köhler, C. M., Hillier, S., Pressling, N., Wan, S., Brumsack, H.J., Clift, P.D., (2012), Deep sea records of the continental weathering and erosion response to East Asian monsoon intensification since 14 ka in the South China Sea. *Chem. Geol.* 326, 1-18. https://doi.org/10.1016/j.chemgeo.2012.07.024

Hu, J., Kawamura, H., Hong, H., & Qi, Y., (2000), A Review on the Currents in the South China Sea: Seasonal Circulation, South China Sea Warm Current and Kuroshio Intrusion. *Journal of Oceanography* 56 (6): 607-24. https://doi.org/10.1023/A:1011117531252.

Hu, S., Zeng, Z., Fang, X., Yin, X., Chen, Z., Li, X., Zhu, B., & Qi, H., (2020), Increasing terrigenous sediment supply from Taiwan to the southern Okinawa Trough over the last

3000 years evidenced by SrNd isotopes and geochemistry. *Sediment. Geol. 406*, 105725. https://doi.org/10.1016/j.sedgeo.2020.105725

Huang, C.Y., Chang, C.P., Wu, W.Y., Tsao, S., & Yeh, Y.H., (1997), Evolution of the plate boundary and origin of the Lichi mélange in the arc-continent collision terrane of Taiwan. Earth *Planet. Sci. Lett.*

Huang, E., Tian, J., & Steinke, S., (2011), Millennial-scale dynamics of the winter cold tongue in the southern South China Sea over the past 26 ka and the East Asian winter monsoon. *Quaternary Research*, *75*(1), 196-204

Huang, E., Tian, J., Qiao, P., Wan, S., Xie, X., & Yang, W., (2015), Early interglacial carbonate-dilution events in the South China Sea: Implications for strengthened typhoon activities over subtropical East Asia. *Quaternary Science Reviews*, *125*, 61-77.

Huang, H., Liu, Z.F., Zhao, Y., Fernandez, A.R., Colin, C., Lin, A.T.S., (2023), Clay mineral assemblages of late Holocene turbidites in the Gaoping Submarine Canyon of the northeastern South China Sea and their responses to typhoon activities. *Palaeogeography, Palaeoclimatology, Palaeoecology 624,* 111650

Huang, J., Li, A., & Wan, S., (2011), Sensitive grain-size records of Holocene East Asian summer monsoon in sediments of northern South China Sea slope. *Quaternary Research*, *75*(3), 734-744.

Huang, J., Wan, S., Xiong, Z., Zhao, D., Liu, X., Li, A., & Li, T., (2016), Geochemical records of Taiwan-sourced sediments in the South China Sea linked to Holocene climate changes. *Palaeogeography, Palaeoclimatology, Palaeoecology*, *441*, 871-881.

Huang, T.H., Chen, C.T.A., Zhang, W.Z., & Zhuang, X.F., (2015), Varying intensity of Kuroshio intrusion into Southeast Taiwan Strait during ENSO events. *Continental Shelf Research*, *103*, 79-87.

Huang, Z.Y., & Yu, H.S., (2003), Morphology and geologic implications of Penghu Channel off southwest Taiwan. *Terrestrial Atmospheric and Oceanic Sciences*, *14*(4), 469-486.

Huh, C.A., Lin, H.L., Lin, S., & Huang, Y.W., (2009), Modern accumulation rates and a budget of sediment off the Gaoping (Kaoping) River, SW Taiwan: a tidal and flood dominated depositional environment around a submarine canyon. *Journal of Marine Systems*, *76*(4), 405-416.

Humphrey, N.F., & Konrad, S.K., (2000), River incision or diversion in response to bedrock uplift. *Geology*, *28*(1), 43-46.

Innocent, C., Fagel, N., Hillaire-Marcel, C., (2000), Sm–Nd isotope systematics in deep-sea sediments: clay-size versus coarser fractions. *Mar. Geol. 168(1-4)*, 79-87. https://doi.org/10.1016/S0025-3227(00)00052-9

Jacobsen, S.B., & Wasserburg, G.J., (1980), Sm–Nd isotopic evolution of chondrites. *Earth and Planetary Science Letters* 50, 139 – 155.

Jacq, K., Giguet-Covex, C., Sabatier, P., Perrette, Y., Fanget, B., Coquin, D., Debret, M., & Arnaud, F. (2019). High-resolution grain size distribution of sediment core with hyperspectral imaging. *Sedimentary Geology*, *393*, 105536.

Jacq, K., Martinez-Lamas, R., Van Exem, A., & Debret, M., (2020), Hyperspectral core-logger image acquisition.

Jacq, K., Debret, M., Fanget, B., Coquin, D., Sabatier, P., Pignol, C., Arnaud, F., & Perrette, Y., (2022a), Theoretical Principles and Perspectives of Hyperspectral Imaging Applied to Sediment Core Analysis. *Quaternary*, *5*(2), 28.

Jacq, K., Rapuc, W., Benoit, A., Coquin, D., Fanget, B., Perrette, Y., Sabatier, P., Wilhelm, B., Debret, M., & Arnaud, F., (2022b), Sedimentary structure discrimination with hyperspectral imaging in sediment cores. *Science of the Total Environment*, *817*, 152018.

Jia, J., Wang, C., Su, M., Yan, W., Zeng, L., & Cui, H. (2023). Provenance and dispersal patterns of sediments on the continental shelf of northern South China Sea: Evidence from detrital zircon geochronology. *Marine Geology*, 107013.

Jiang, H., Björck, S., Ran, L., Huang, Y., & Li, J., (2006), Impact of the Kuroshio Current on the South China Sea based on a 115 000 year diatom record. *Journal of Quaternary Science: Published for the Quaternary Research Association*, *21*(4), 377-385.

Jiwarungrueangkul, T., Liu, Z., Stattegger, K., & Sang, P.N., (2019), Reconstructing chemical weathering intensity in the Mekong River basin since the Last Glacial Maximum. *Paleoceanography and Paleoclimatology*, *34*(11), 1710-1725.

Jones, G.A., & Kaiteris, P., (1983), A vacuum-gasometric technique for rapid and precise analysis of calcium carbonate in sediments and soils: Research-method paper. *Journal of Sedimentary Research*, *53*(2).

Joos, F., & Spahni, R., (2008), Rates of change in natural and anthropogenic radiative forcing over the past 20,000 years. *Proceedings of the National Academy of Sciences*, *105*(5), 1425-1430.

Joussain, R., Colin, C., Liu, Z., Meynadier, L., Fournier, L., Fauquembergue, K., Zaragosi, S., Schmidt, F., Rojas, V., & Bassinot, F., (2016), Climatic control of sediment transport from the Himalayas to the proximal NE Bengal Fan during the last glacial-interglacial cycle. *Quaternary Science Reviews*, *148*, 1-16.

Joussain, R., Liu, Z., Colin, C., Duchamp-Alphonse, S., Yu, Z., Moreno, E., Fournier, L., Zaragosi, S., Dapoigny, A., Meynadier, L., & Bassinot, F., (2017), Link between Indian monsoon rainfall and physical erosion in the Himalayan system during the Holocene. *Geochemistry, Geophysics, Geosystems*, *18*(9), 3452-3469.

Kaboth-Bahr, S., Bahr, A., Zeeden, C., Yamoah, K.A., Lone, M.A., Chuang, C.K., Löwemark, L., & Wei, K.Y., (2021), A tale of shifting relations: East Asian summer and winter monsoon variability during the Holocene. *Scientific Reports*, *11*(1), 1-10.

Kao, S.J., Roberts, A. P., Hsu, S.C., Chang, YP., Lyons, W. B., & Chen, MT., (2006), Monsoon forcing, hydrodynamics of the Kuroshio Current, and tectonic effects on sedimentary carbon and sulfur cycling in the Okinawa Trough since 90 ka. *Geophysical Research Letters*, *33*(5).

Katili, John A., (1975), Volcanism and plate tectonics in the Indonesian island arcs. *Tectonophysics* 26 (3–4), 165–188. https://doi.org/10.1016/0040-1951(75)90088-8.

Koutavas, A., & Joanides, S., (2012), El Niño–Southern oscillation extrema in the holocene and last glacial maximum. *Paleoceanography*, *27*(4).

Krupnik, D., & Khan, S., (2019), Close-range, ground-based hyperspectral imaging for mining applications at various scales: Review and case studies. *Earth-science reviews*, *198*, 102952.

Kudrass, H.R., Michels, K.H., Wiedicke, M., & Suckow, A., (1998) Cyclones and tides as feeders of a submarine canyon off Bangladesh. *Geology*, *26*(8), 715-718.

Lambeck, K., Rouby, H., Purcell, A., Sun, Y., & Sambridge, M., (2014), Sea level and global ice volumes from the Last Glacial Maximum to the Holocene. *PNAS. 111*(43), 15296-15303. https://doi.org/10.1073/pnas.1411762111

Lamy S., Ruas A., Demazeu Y., Jackson M,. Mackaness W., & Weibel R., (1999), The Application of Agents in Automated Map Generalisation, *CD-Rom Proceedings 19th Int. Cartographic Coneference, Ottawa*

Larsen, I.J., & Montgomery, D.R., (2012), Landslide erosion coupled to tectonics and river incision. *Nature Geoscience*, *5*(7), 468-473.

Latour, B., (2014), Some advantages of the notion of "Critical Zone" for geopolitics. *Procedia Earth Planet. Sci. 10*, 3-6. https://doi.org/10.1016/j.proeps.2014.08.002

Lehu, R., Lallemand, S., Hsu, S.K., Babonneau, N., Ratzov, G., Lin, A.T., & Dezileau, L., (2015), Deep-sea sedimentation offshore eastern Taiwan: facies and processes characterization. *Marine Geology*, *369*, 1-18.

Lei, C., Ren, J., Sternai, P., Fox, M., Willett, S., Xie, X., Clift, P.D., Liao, J., & Wang, Z., (2015), Structure and sediment budget of Yinggehai–Song Hong basin, South China Sea: Implications for Cenozoic tectonics and river basin reorganization in Southeast *Asia. Tectonophysics 655,* 177-190. https://doi.org/10.1016/j.tecto.2015.05.024

Lenssen, N.J., Goddard, L., & Mason, S., (2020), Seasonal forecast skill of ENSO teleconnection maps. *Weather and Forecasting*, *35*(6), 2387-2406.

Lester, R., McIntosh, K., Van Avendonk, H.J.A., Lavier, L., Liu, C.-S., & Wang, T.-K., (2013), Crustal accretion in the Manila Trench accretionary wedge at the transition from subduction to mountain-building in Taiwan. *Earth Planet. Sci. Lett.* 375, 430–440. https://doi.org/10.1016/j.epsl.2013.06.007.

Li, D., Zhao, M., & Chen, M.T, (2014), East Asian winter monsoon controlling phytoplankton productivity and community structure changes in the southeastern South China Sea over the last 185 kyr. *Palaeogeography, Palaeoclimatology, Palaeoecology*, *414*, 233-242.

Li, D., Zhao, M., & Tian, J., (2017), Low-high latitude interaction forcing on the evolution of the 400 kyr cycle in East Asian winter monsoon records during the last 2.8 Myr. *Quaternary Science Reviews*, *172*, 72-82.

Li, G., West, A.J., & Qiu, H., (2019), Competing effects of mountain uplift and landslide erosion over earthquake cycles. *Journal of Geophysical Research: Solid Earth*, *124*(5), 5101-5133.

Li, L., Nowlin Jr, W. D., & Jilan, S. (1998). Anticyclonic rings from the Kuroshio in the South China Sea. *Deep Sea Research Part I: Oceanographic Research Papers*, *45*(9), 1469-1482

Li, L., & Qu, T., (2006), Thermohaline circulation in the deep South China Sea basin inferred from oxygen distributions, *J. Geophys. Res*.,111,C05017, doi:10.1029/2005JC003164

Li, N., Yang, X., Peng, J., Zhou, Q., & Su, Z., (2019), Deep-water bottom current evolution in the northern South China Sea during the last 150 kyr: Evidence from sortable-silt grain size and sedimentary magnetic fabric. *Journal of Asian Earth Sciences*, *171*, 78-87.

Li, X. H., Wei, G., Shao, L., Liu, Y., Liang, X., Jian, Z., Sun, M., & Wang, P., (2003), Geochemical and Nd isotopic variations in sediments of the South China Sea: a response to Cenozoic tectonism in SE Asia. *Earth and Planetary Science Letters*, *211*(3-4), 207-220.

Li, Y., Wang, N. A., Li, Z., Zhou, X., & Zhang, C. (2013). Climatic and environmental change in Yanchi Lake, Northwest China since the Late Glacial: A comprehensive analysis of lake sediments. *Journal of Geographical Sciences. 23*, 932-946. https://doi.org/10.1007/s11442-013-1053-3

Li, Y., Zhou, R., Zhao, G., Li, H., Su, D., Ding, H., Yan, Z., Yan, Y., Yun, K., & Ma, C. (2014), Tectonic uplift and landslides triggered by the Wenchuan earthquake and constraints on orogenic growth: a case study from Hongchun Gully, Longmen Mountains, Sichuan, China. *Quaternary international*, *349*, 142-152.

Li, Y., Wang, N., Li, Z., Zhou, X., & Zhang, C. (2017): NOAA/WDS Paleoclimatology - Yanchi Lake, Northwest China 16,000 Year Geochemical Data. *NOAA National Centers for Environmental Information*. [dataset] https://doi.org/10.25921/rsdz-5b03.

Li, Z., Pospelova, V., Liu, L., Francois, R., Wu, Y., Mertens, K. N., Saiton Y., Zhou, R., Song, B., & Xie, X. (2021), High-resolution reconstructions of Holocene sea-surface conditions from dinoflagellate cyst assemblages in the northern South China Sea. *Marine Geology*, *438*, 106528.

Liang, A., Oey, L., Huang, S., & Chou, S. (2017). Long-term trends of typhoon-induced rainfall over Taiwan: In situ evidence of poleward shift of typhoons in western North Pacific in recent decades. *Journal of Geophysical Research: Atmospheres*, *122*(5), 2750-2765.

Liao, W., Liu, X., Xu, X., Chen, G., Liang, X., Zhang, H., & Li, X., (2020), Projections of land use changes under the plant functional type classification in different SSP-RCP scenarios in China. *Science Bulletin*, *65*(22), 1935-1947.

Licht, A., Dupont-Nivet, G., Pullen, A., Kapp, P., Abels, H.A., Lai, Z., Guo, Z., Abell, J., & Giesler, D. (2016), Resilience of the Asian atmospheric circulation shown by Paleogene dust provenance. *Nature Communications*, 7(1), 12390.

Liew, P.M., Kuo, C.M., Huang, S.Y., & Tseng, M.H., (1998), Vegetation change and terrestrial carbon storage in eastern Asia during the Last Glacial Maximum as indicated by a new pollen record from central Taiwan. *Global and Planetary Change*, *16*, 85-94.

Liew, P.M., Huang, S.Y., & Kuo, C.M., (2006), Pollen stratigraphy, vegetation and environment of the last glacial and Holocene—a record from Toushe Basin, central Taiwan. *Quat. Int. 147*(1), 16-33. https://doi.org/10.1016/j.quaint.2005.09.003

Lin, M.L., & Jeng, F.S. (2000), Characteristics of hazards induced by extremely heavy rainfall in Central Taiwan—Typhoon Herb. *Engineering Geology*, *58*(2), 191-207.

Lin, I.I., Wu, C.C., Pun, I.F., & Ko, D.S., (2008), Upper-ocean thermal structure and the western North Pacific category 5 typhoons. Part I: Ocean features and the category 5 typhoons' intensification. *Monthly Weather Review*, *136*(9), 3288-3306.

Linsley, B.K., Rosenthal, Y., & Oppo, D.W., (2010), Holocene evolution of the Indonesian throughflow and the western Pacific warm pool. *Nature Geoscience*, *3*(8), 578-583.

Lisiecki, L.E., Raymo, M.E., 2005. A Pliocene-Pleistocene stack of 57 globally distributed benthic δ18O records. Paleoceanography, 20(1). https://doi.org/10.1029/2004PA001071

Liu, B.Y., Nearing, M.A., Shi, P.J., & Jia, Z.W. (2000), Slope length effects on soil loss for steep slopes. *Soil Science Society of America Journal*, *64*(5), 1759-1763.

Liu, C.S., Liu, S.Y., Lallemand, S.E., Lundberg, N., & Reed, D.L., (1998), Digital elevation model offshore Taiwan and its tectonic implications. *Terrestrial, Atmospheric and Oceanic Sciences*, *9*(4), 705-738.

Liu, F., Chen, H., Cai, H., Luo, X., Ou, S., & Yang, Q., (2017), Impacts of ENSO on multi-scale variations in sediment discharge from the Pearl River to the South China Sea. *Geomorphology*, *293*, 24-36.

Liu, J., Chen, M., Chen, Z., & Yan, W., (2010), Clay mineral distribution in surface sediments of the South China Sea and its significance for in sediment sources and transport. *Chinese Journal of Oceanology and Limnology*, *28*(2), 407-415.

Liu, J., Li, T., Xiang, R., Chen, M., Yan, W., Chen, Z., & Liu, F. (2013). Influence of the Kuroshio Current intrusion on Holocene environmental transformation in the South China Sea. *The Holocene*, *23*(6), 850-859.

Liu, J., Xiang, R., Kao, S. J., Fu, S., & Zhou, L., (2016), Sedimentary responses to sea-level rise and Kuroshio Current intrusion since the Last Glacial Maximum: Grain size and clay mineral evidence from the northern South China Sea slope. *Palaeogeography, Palaeoclimatology, Palaeoecology*, *450*, 111-121.

Liu, J. P., Milliman, J. D., Gao, S., & Cheng, P., (2004), Holocene development of the Yellow River's subaqueous delta, North Yellow Sea. *Marine geology*, *209*(1-4), 45-67.

Liu, J.P., Liu, C.S., Xu, K.H., Milliman, J.D., Chiu, J.K., Kao, S.J., & Lin, S.W., (2008), Flux and Fate of Small Mountainous Rivers Derived Sediments into the Taiwan Strait. *Marine Geology* 256 (1-4): 65-76. https://doi.org/10.1016/j.margeo.2008.09.007.

Liu, J.T., Hung, J.J., Lin, H.L., Huh, C.A., Lee, C.L., Hsu, R.T., Huang, Y.W., & Chu, J.C., (2009), From suspended particles to strata: The fate of terrestrial substances in the Gaoping (Kaoping) submarine canyon. *Journal of Marine Systems*, *76*(4), 417-432.

Liu, J.T., Wang, Y.H., Lee, I.H., & Hsu, R.T., (2010), Quantifying tidal signatures of the benthic nepheloid layer in Gaoping Submarine Canyon in Southern Taiwan. *Marine Geology*, *271*(1-2), 119-130.

Liu, J.T., Wang, Y.H., Yang, R.J., Hsu, R.T., Kao, S.J., Lin, H.L., & Kuo, F.H., (2012), Cyclone-induced hyperpycnal turbidity currents in a submarine canyon. *Journal of Geophysical Research: Oceans*, *117*(C4).

Liu, J.T., Hsu, R.T., Hung, J.J., Chang, Y.P., Wang, Y.H., Rendle-Bühring, R.H., Lee, CL., Huh, CA., & Yang, R.J. (2016). From the highest to the deepest: The Gaoping River–Gaoping Submarine Canyon dispersal system. *Earth-Science Reviews, 153*, 274-300.

Liu, W., Huang, Y., An, Z., Clemens, S. C., Li, L., Prell, W. L., & Ning, Y. (2005). Summer monsoon intensity controls C4/C3 plant abundance during the last 35 ka in the Chinese Loess Plateau: carbon isotope evidence from bulk organic matter and individual leaf waxes. *Palaeogeography, Palaeoclimatology, Palaeoecology. 220*(3-4), 243-254. https://doi.org/10.1016/j.palaeo.2005.01.001

Liu, X., & Yin, Z.Y., (2002), Sensitivity of East Asian monsoon climate to the uplift of the Tibetan Plateau. *Palaeogeography, Palaeoclimatology, Palaeoecology*, 183(3-4), 223-245.

Liu, X., & Dong, B., (2013), Influence of the Tibetan Plateau uplift on the Asian monsoon-arid environment evolution. *Chin. Sci. Bull.* 58, 4277–4291. https://doi.org/10.1007/s11434-013-5987-8

Liu, Y., Liu, X., & Sun, Y., (2021), QGrain: An open-source and easy-to-use software for the comprehensive analysis of grain size distributions. *Sedimentary Geology*, *423*, 105980.

Liu, Z., & Alexander, M., (2007), Atmospheric bridge, oceanic tunnel, and global climatic teleconnections. *Reviews of Geophysics*, 45(2).

Liu, Z., Lu, Z., Wen, X., Otto-Bliesner, B.L., Timmermann, A., & Cobb, K.M., (2014), Evolution and forcing mechanisms of El Niño over the past 21,000 years. *Nature*, *515*(7528), 550-553.

Liu, Z.F., Colin, C., Trentesaux, A., Blamart, D., Bassinot, F., Siani, G., Sicre, M.A., (2004). Erosional history of the eastern Tibetan Plateau since 190 kyr ago: clay mineralogical and geochemical investigations from the southwestern South China Sea. Mar. Geol. 209(1-4), 1-18. https://doi.org/10.1016/j.margeo.2004.06.004

Liu, Z.F., Colin, C., Trentesaux, A., Siani, G., Frank, N., Blamart, D., & Farid, S., (2005), Late Quaternary climatic control on erosion and weathering in the eastern Tibetan Plateau and the Mekong Basin. *Quaternary Research*, *63*(3), 316-328.

Liu, Z.F., Zhao, Y., Li, J., & Colin, C., (2007a)., Late Quaternary clay minerals off Middle Vietnam in the western South China Sea: Implications for source analysis and East Asian monsoon evolution. *Science in China Series D: Earth Sciences*, *50*(11), 1674-1684.

Liu, Z.F., Colin, C., Huang, W., Chen, Z., Trentesaux, A., & Chen, J., (2007b), Clay minerals in surface sediments of the Pearl River drainage basin and their contribution to the South China Sea. *Chinese Science Bulletin*, *52*(8), 1101-1111.

Liu, Z.F., Colin, C., Huang, W., Le, K. P., Tong, S., Chen, Z., & Trentesaux, A., (2007c), Climatic and tectonic controls on weathering in south China and Indochina Peninsula: Clay mineralogical and geochemical investigations from the Pearl, Red, and Mekong drainage basins. *Geochemistry, Geophysics, Geosystems*, *8*(5).

Liu, Z.F., Tuo, S., Colin, C., Liu, J. T., Huang, C. Y., Selvaraj, K., Chen, C.T.A., Zhao, Y., Siringan, F.P., Boulay, S., & Chen, Z., (2008), Detrital fine-grained sediment contribution from Taiwan to the northern South China Sea and its relation to regional ocean circulation. *Marine Geology*, *255*(3-4), 149-155.

Liu, Z.F., Zhao, Y., Colin, C., Siringan, F.P & Wu, Q., (2009), Chemical Weathering in Luzon, Philippines from Clay Mineralogy and Major-Element Geochemistry of River

Sediments. *Applied Geochemistry* 24 (11): 2195-2205. https://doi.org/10.1016/j.apgeochem.2009.09.025.

Liu, Z.F., Colin, C., Li, X., Zhao, Y., Tuo, S., Chen, Z., Siringan, F.P., Liu, J.T., Huang, C.Y., You, C.F., & Huang, K.F., (2010a), Clay mineral distribution in surface sediments of the northeastern South China Sea and surrounding fluvial drainage basins: Source and transport. *Marine Geology*, *277*(1-4), 48-60.

Liu, Z.F., Li, X., Colin, C., & Ge, H., (2010b), A high-resolution clay mineralogical record in the northern South China Sea since the Last Glacial Maximum, and its time series provenance analysis. *Chinese Science Bulletin*, *55*, 4058-4068.

Liu, Z.F. , Wang, H., Hantoro, W.S., Sathiamurthy, E., Colin, C., Zhao, Y.L., & Li, J.R., (2012), Climatic and tectonic controls on chemical weathering in tropical Southeast Asia (Malay Peninsula, Borneo, and Sumatra). Chem. Geol. 291, 1–12.

Liu, Z.F., Zhao, Y.L., Colin, C., Stattegger, K., Wiesner, M.G., Huh, C.A., Zhang, Y.W., Li, X.J., Sompongchaiyakul, P., You, C.F., Huang, C.Y., Liu, J.T., Siringan, F.P., Le, K.P., Sathiamurthy, E., Hantoro, W.S., Liu, J.G., Tuo, S.T., Zhao, S.H., Zhou, S.W., He, Z.D., Wang, Y.C., Bunsomboonsakul, S., Li, Y.L., (2016), Source-to-sink transport processes of fluvial sediments in the South China Sea. *Earth Sci. Rev*. 153, 238–273.

Lo, C.M., Lee, C.F., Chou, H.T., & Lin, M.L., (2014), Landslide at Su-Hua highway 115.9 k triggered by typhoon Megi in Taiwan. *Landslides*, *11*, 293-304.

Lu, Z., Liu, Z., Zhu, J., & Cobb, K.M., (2018), A review of paleo El Niño-southern oscillation. *Atmosphere*, *9*(4), 130.

Lüdmann, T., Wong, H.K., & Berglar, K. (2005), Upward flow of North Pacific Deep Water in the northern South China Sea as deduced from the occurrence of drift sediments. *Geophysical Research Letters*, *32*(5).

Lugmair, G. W., Shimamura, T., Lewis, R. S., & Anders, E., (1983), Samarium-146 in the Early Solar System: Evidence from Neodymium in the Allende Meteorite. *Science*, 222 (4627). 1015-1018. doi:10.1126/science.222.4627.1015.

Lyons, W.B., Nezat, C.A., Carey, A.E., & Hicks, D.M., (2002), Organic carbon fluxes to the ocean from high-standing islands. *Geology*, *30*(5), 443-446.

Lyons, W.B., Carey, A.E., Hicks, DM., & Nezat, C.A., (2005), Chemical weathering in high-sediment-yielding watersheds, New Zealand. *Journal of Geophysical Research: Earth Surface*, *110*(F1).

Madejová, J., Gates, W. P., & Petit, S., (2017), IR spectra of clay minerals. In *Developments in clay science* (Vol. 8, pp. 107-149). Elsevier.

Malamud, B.D., Turcotte, D.L., Guzzetti, F., & Reichenbach, P., (2004)., Landslides, earthquakes, and erosion. *Earth and Planetary Science Letters*, *229*(1-2), 45-59.

Mason, S.J., & Goddard, L., (2001), Probabilistic precipitation anomalies associated with EN SO. *Bulletin of the American Meteorological Society*, *82*(4), 619-638.

Masson, D.G., Huvenne, V.A.I., De Stigter, H.C., Wolff, G.A., Kiriakoulakis, K., Arzola, R.G., & Blackbird, S. (2010). Efficient burial of carbon in a submarine canyon. *Geology, 38*(9), 831-834.

McCave, I.N., Manighetti, B., Robinson, S.G., (1995a), Sortable silt and fine sediment size/ composition slicing: parameters for palaeocurrent speed and palaeoceanography. *Paleoceanography* 10, 593–610.

McCave, I.N., Manighetti, B., & Beveridge, N.A.S., (1995b), Circulation in the glacial North Atlantic inferred from grain-size measurements. *Nature*, *374*(6518), 149-152.

McCave, I.N., Thornalley, D.J.R., & Hall, I.R., (2017), Relation of sortable silt grain-size to deep-sea current speeds: Calibration of the 'Mud Current Meter'. *Deep Sea Research Part I: Oceanographic Research Papers*, *127*, 1-12.

McGann, M., (2014), Delivery of terrigenous material to submarine fans: Biological evidence of local, staged, and full-canyon sediment transport down the Ascension-Monterey Canyon system. *Geosphere*, *10*(6), 1061-1075.

McKinley, J. M., Worden, RH., & Ruffell, A.H., (1999), Smectite in sandstones: a review of the controls on occurrence and behaviour during diagenesis. *Clay mineral cements in sandstones*, 109-128.

Meng, X., Zhu, Y., Yin, M., & Liu, D., (2021), The impact of land use and rainfall patterns on the soil loss of the hillslope. *Scientific Reports*, *11*(1), 16341.

Meyer, I., Davies, G.R., Stuut, J.B.W., (2011), Grain size control on Sr-Nd isotope provenance studies and impact on paleoclimate reconstructions: An example from deep-sea sediments offshore NW Africa. *Geochem. Geophys. Geosyst.* 12(3).

Milliman, J.D., & Syvitski, J.P.M., (1992), Geomorphic/tectonic control of sediment discharge to the ocean: The importance of small mountainous rivers. *J. Geol.* 100, 525–544. https://doi.org/10.1086/629606.

Milliman, J.D., & Farnsworth, K.L., Albertin, C.S., (1999), Flux and fate of fluvial sediments leaving large islands in the East Indies. *J. Sea Res.* 41, 97–107.

Milliman, J.D., & Farnsworth, K.L., (2011), River Discharge to the Coastal Ocean: A Global Synthesis. *Cambridge University Press, Cambridge*, 384 pp.

Miriyala, P., Sukumaran, N.P., Nath, B.N., Ramamurty, P.B., Sijinkumar, A.V., Vijayagopal, B., Ramaswamy, V., & Sebastian, T., (2017), Increased chemical weathering during the deglacial to mid-Holocene summer monsoon intensification. *Scientific Reports*, *7*(1), 1-11.

Mohamadi, M.A., & Kavian, A., (2015), Effects of rainfall patterns on runoff and soil erosion in field plots. *International soil and water conservation research*, *3*(4), 273-281.

Mohammad, A.G., & Adam, M.A., (2010), The impact of vegetative cover type on runoff and soil erosion under different land uses. *Catena*, *81*(2), 97-103.

Molnar, P., (2001), Climate change, flooding in arid environments, and erosion rates. *Geology 29*(12), 1071-1074. https://doi.org/10.1130/0091-7613(2001)029<1071:CCFIAE>2.0.CO;2

Montgomery, D.R., Huang, M.Y.F., & Huang, A.Y.L., (2014), Regional soil erosion in response to land use and increased typhoon frequency and intensity, Taiwan. *Quaternary research*, *81*(1), 15-20.

Moy, C.M., Seltzer, G.O., Rodbell, D.T., & Anderson, D.M., (2002), Variability of El Niño/Southern Oscillation activity at millennial timescales during the Holocene epoch. *Nature 420*(6912), 162-165. https://doi.org/10.1038/nature01194

Mulder, T., Syvitski, J.P., Migeon, S., Faugères, J.C., & Savoye, B., (2003), Marine hyperpycnal flows: initiation, behavior and related deposits. A review. *Marine and Petroleum Geology*, *20*(6-8), 861-882.

Nayak, K., Lin, A.T., Huang, K.-F., Liu, Z., Babonneau, N., Ratzov, G., Pillutla, R.K., Das, P., Hsu, S.-K., (2021), Clay-mineral distribution in recent deep-sea sediments around Taiwan: Implications for sediment dispersal processes. *Tectonophysics* 814, 228974.

Neelin, J.D., Battisti, D.S., Hirst, A.C., Jin, F.F., Wakata, Y., Yamagata, T., & Zebiak, S.E. (1998), ENSO theory. *J. Geophys. Res. Oceans*, 103, 14261–14290.

Normark, W.R., (1974), Submarine canyons and fan valleys: factors affecting growth patterns of deep-sea fans.

Normark, W.R., Gutmacher, C.E., Chase, T.E., & Wilde, P., (1983), Monterey Fan: Growth pattern control by basin morphology and changing sea levels. *Geo-Marine Letters*, *3*, 93-99.

Ochoa, P.A.A., Fries, A., Mejía, D., Burneo, J.I., Ruíz-Sinoga, J.D., & Cerdà, A., (2016), Effects of climate, land cover and topography on soil erosion risk in a semiarid basin of the Andes. *Catena*, *140*, 31-42.

Okazaki, Y., Timmermann, A., Menviel, L., Harada, N., Abe-Ouchi, A., Chikamoto, M.O., Mouchet, A., & Asahi, H. (2010), Deepwater formation in the North Pacific during the last glacial termination. *Science*, *329*(5988), 200-204.

Ono, Y., Aoki, T., Hasegawa, H., & Dali, L., (2005)., Mountain glaciation in Japan and Taiwan at the global Last Glacial Maximum. *Quaternary international*, *138*, 79-92.

Ouyang, W., Hao, F., Skidmore, A.K., & Toxopeus, A.G., (2010), Soil erosion and sediment yield and their relationships with vegetation cover in upper stream of the Yellow River. *Science of the Total Environment*, *409*(2), 396-403.

Page, M.J., Trustrum, N.A., & DeRose, R.C., (1994), A high resolution record of storm-induced erosion from lake sediments, New Zealand. *Journal of paleolimnology*, *11*, 333-348.

Paull, C. K., Mitts, P., Ussler III, W., Keaten, R., & Greene, H. G., (2005), Trail of sand in upper Monterey Canyon: offshore California. *Geological Society of America Bulletin*, *117*(9-10), 1134-1145.

Paull, C. K., Caress, D. W., Ussler, W., Lundsten, E., & Meiner-Johnson, M., (2011), High-resolution bathymetry of the axial channels within Monterey and Soquel submarine canyons, offshore central California. *Geosphere*, *7*(5), 1077-1101.

Peizhen, Z., Molnar, P., & Downs, W.R., (2001), Increased sedimentation rates and grain sizes 2–4 Myr ago due to the influence of climate change on erosion rates. *Nature*, *410*(6831), 891-897.

Peltier, W.R., (2004), Global glacial isostasy and the surface of the ice-age Earth: the ICE-5G (VM2) model and GRACE. *Annu. Rev. Earth Planet. Sci.*, *32*, 111-149.

Peltier, W.R., Argus, D.F., & Drummond, R., (2015), Space geodesy constrains ice age terminal deglaciation: The global ICE-6G_C (VM5a) model. *Journal of Geophysical Research: Solid Earth*, *120*(1), 450-487.

Petschick, R., Kuhn, G., Gingele, F., 1996. Clay mineral distribution in surface sediments of the South Atlantic: sources, transport, and relation to oceanography. *Mar. Geol. 130*, 203–229.

Philander, S.G.H., (1985), El Niño and La Niña. *Journal of Atmospheric Sciences*, *42*(23), 2652-2662.

Popescu, I., Lericolais, G., Panin, N., Normand, A., Dinu, C., & Le Drezen, E., (2004), The Danube submarine canyon (Black Sea): morphology and sedimentary processes. *Marine Geology*, *206*(1-4), 249-265.

Poppe, L.J., McMullen, K.Y., Williams, S.J., Crocker, J.M., & Doran, E.F., (2008), Estuarine sediment transport by gravity-driven movement of the nepheloid layer, Long Island Sound. *Geo-Marine Letters*, *28*, 245-254.

Qu, T., Kim, Y.Y., Yaremchuk, M., Tozuka, T., Ishida, A., & Yamagata, T. (2004), Can Luzon Strait transport play a role in conveying the impact of ENSO to the South China Sea?. *Journal of Climate*, *17*(18), 3644-3657.

Qu, T., Girton, J.B., & Whitehead, J. A., (2006), Deepwater Overflow through Luzon Strait. *Journal of Geophysical Research* 111 (C1): C01002. https://doi.org/10.1029/2005JC003139.

Rapuc, W., Jacq, K., Develle, A. L., Sabatier, P., Fanget, B., Perrette, Y., Coquin, D., Debret, M., Wilhelm, B., & Arnaud, F., (2020), XRF and hyperspectral analyses as an automatic way to detect flood events in sediment cores. *Sedimentary Geology*, *409*, 105776.

Rasmussen, E. S., (1994), The relationship between submarine canyon fill and sea-level change: an example from Middle Miocene offshore Gabon, West Africa. *Sedimentary Geology*, *90*(1-2), 61-75.

Rasmusson, E.M., & Carpenter, T.H., (1982), Variations in tropical sea surface temperature and surface wind fields associated with the Southern Oscillation/El Niño. *Monthly Weather Review*, *110*(5), 354-384.

Ray, N., & Adams, J., (2001), A GIS-based vegetation map of the world at the last glacial maximum (25,000-15,000 BP). *Internet archaeology*, *11*.

Reimer, P.J., Edouard Bard, B., Alex Bayliss, B., Warren Beck, B.J., Paul Blackwell, B.G., Christopher Bronk Ramsey, B., (2013), Intcal13 and Marine13 radiocarbon age calibration curves 0–50,000 years cal BP. *Radiocarbon 55*, 1869–1887.

Rein, B., Lückge, A., Reinhardt, L., Sirocko, F., Wolf, A., & Dullo, W.C., (2005), El Niño variability off Peru during the last 20,000 years. *Paleoceanography*, *20*(4).

Riebe, C.S., Kirchner, J.W., Granger, DE., & Finkel, R.C., (2001), Strong tectonic and weak climatic control of long-term chemical weathering rates. *Geology*, *29*(6), 511-514.

Riedinger, M.A., Steinitz-Kannan, M., Last, W.M., & Brenner, M., (2002), A~ 6100 14 C yr record of El Niño activity from the Galápagos Islands. *Journal of Paleolimnology*, *27*, 1-7.

Ropelewski, C.F., & Halpert, M.S., (1989), Precipitation patterns associated with the high index phase of the Southern Oscillation. *Journal of climate*, 268-284.

Roy, R., (1949), Decomposition and resynthesis of the micas. *J Am Ceram Soc,* 32: 202–210.

Ruddiman, W. (2001), Earth's Climate: Past and Future. In W. H. Freeman and Company.

Sabatier, P., Poulenard, J., Fanget, B., Reyss, J.L., Develle, A L., Wilhelm, B., Ployon, E., Pignol, C., Naffrechoux, E., Dorioz, J.-M., Montuelle, B., & Arnaud, F., (2014), Long-term relationships among pesticide applications, mobility, and soil erosion in a vineyard watershed. *PNAS 111*(44), 15647-15652. https://doi.org/10.1073/pnas.1411512111

Sahsamanoglou, H.S., Makrogiannis, T.J., & Kallimopoulos, P.P., (1991), Some aspects of the basic characteristics of the Siberian anticyclone. *International Journal of Climatology*, 11(8), 827-839.

Saito, H., Korup, O., Uchida, T., Hayashi, S., & Oguchi, T., (2014), Rainfall conditions, typhoon frequency, and contemporary landslide erosion in Japan. *Geology*, *42*(11), 999-1002.

Sanchez Goñi, M.F., Desprat, S, Daniau, AAL., Liew, P.M., Huang, S.Y., & Kuo, C.M., (2017), CLAM age model and pollen profile of sediment core Toushe_Basin. *PANGAE.* https://doi.org/10.1594/PANGAEA.872916

Sang, P.N., Liu, Z., Zhao, Y., Zhao, X., Pha, P.D., & Van Long, H., (2018), Chemical weathering in central Vietnam from clay mineralogy and major-element geochemistry of sedimentary rocks and river sediments. *Heliyon*, *4*(7), e00710.

Sang, P.N., Liu, Z., & Colin, C., (2022), Chemical Weathering of the Mekong River Basin With Implication for East Asian Monsoon Evolution During the Late Quaternary: Marine Sediment Records in the Southern South China Sea. *Frontiers in Earth Science*, 1027.

Sawada, K., & Handa, N., (1998), Variability of the path of the Kuroshio ocean current over the past 25,000 years. *Nature*, *392*(6676), 592-595.

Selvaraj, K., & Chen, C.T.A., (2006), Moderate chemical weathering of subtropical Taiwan: constraints from solid-phase geochemistry of sediments and sedimentary rocks. *The Journal of Geology*, *114*(1), 101-116.

Shao, L., Li, X., Geng, J., Pang, X., Lei, Y., Qiao, P., Wang, L., & Wang, H. (2007), Deep water bottom current deposition in the northern South China Sea. *Science in China Series D: Earth Sciences*, *50*(7), 1060-1066.

Shao, L., Qiao, P., Pang, X., Wei, G., Li, Q., Miao, W., & Li, A., (2009), Nd isotopic variations and its implications in the recent sediments from the northern South China Sea. *Chinese Science Bulletin*, *54*(2), 311-317.

Shaw, P.T., & Chao, S.Y. (1994), Surface circulation in the South China sea. *Deep Sea Research Part I: Oceanographic Research Papers*, *41*(11-12), 1663-1683.

Shen, X., Hu, B., Yan, H., Dodson, J., Zhao, J., Li, J., Ding, X., Li, Q., Wang, X., & Xu, F., (2022), Reconstruction of Kuroshio intrusion into the south China sea over the last 40 kyr. *Quaternary Science Reviews*, *290*, 107622.

Shieh, C.L., Wang, C.M., Chen, Y.S., Tsai, Y. ., & Tseng, W.H., (2010), An overview of disasters resulted from Typhoon Morakot in Taiwan. *Journal of Disaster Research*, *5*(3), 236-244.

Shukla, A., Mehrotra, R.C., Spicer, R.A., Spicer, T.E., & Kumar, M., (2014), Cool equatorial terrestrial temperatures and the South Asian monsoon in the Early Eocene: evidence from the Gurha Mine, Rajasthan, India. *Palaeogeography, Palaeoclimatology, Palaeoecology*, 412, 187-198.

Singh, M., Sharma, M., & Tobschall, H.J. (2005), Weathering of the Ganga alluvial plain, northern India: implications from fluvial geochemistry of the Gomati River. *Applied Geochemistry*, *20*(1), 1-21.

Smith, A., (2020), 2010–2019: A landmark decade of US. billion-dollar weather and climate disasters. *National Oceanic and Atmospheric Administration*.

Sorrel, P., Jacq, K., Van Exem, A., Escarguel, G., Dietre, B., Debret, M., McGowan, S., Ducept, J., Gauthier, E., & Oberhänsli, H., (2021), Evidence for centennial-scale Mid-Holocene episodes of hypolimnetic anoxia in a high-altitude lake system from central Tian Shan (Kyrgyzstan), *Quaternary Science Reviews, 252*, 106748

Spratt, R.M., & Lisiecki, L.E., (2016), A Late Pleistocene Sea level stack. *Clim. Past 12*(4), 1079-1092. https://doi.org/10.5194/cp-12-1079-2016

Savitzky, A., & Golay, M.J., (1964), Smoothing and differentiation of data by simplified least squares procedures. *Analytical chemistry*, *36*(8), 1627-1639.

Stott, L., Cannariato, K., Thunell, R., Haug, G.H., Koutavas, A., & Lund, S., (2004), Decline of surface temperature and salinity in the western tropical Pacific Ocean in the Holocene epoch. *Nature*, *431*(7004), 56-59.

Stow, D.A., & Shanmugam, G., (1980), Sequence of structures in fine-grained turbidites: comparison of recent deep-sea and ancient flysch sediments. *Sedimentary Geology*, *25*(1-2), 23-42.

Stow, D.A., & Tabrez, A.R., (1998), Hemipelagites: processes, facies and model. *Geological Society, London, Special Publications*, *129*(1), 317-337

Stow, D.A., & Smillie, Z., (2020), Distinguishing between deep-water sediment facies: Turbidites, contourites and hemipelagites. *Geosciences*, *10*(2), 68.

Stuiver, M., Reimer, P.J., (1993), Extended ^{14}C data base and revised CALIB 3.0 ^{14}C age calibration program. *Radiocarbon* 35, 215–230.

Su, C.C., Tseng, J.Y., Hsu, H.H., Chiang, C.S., Yu, H.S., Lin, S., & Liu, J.T., (2012), Records of submarine natural hazards off SW Taiwan. *Geological Society, London, Special Publications*, *361*(1), 41-60.

Su, C.C., Hsu, ST, Hsu, H.H., Lin, J.Y., & Dong, J.J., (2018), Sedimentological characteristics and seafloor failure offshore SW Taiwan. *Terrestrial, Atmospheric and Oceanic Sciences* 29, 65-76.

Sugden, D.E., (1978), Glacial erosion by the Laurentide ice sheet. *Journal of Glaciology*, *20*(83), 367-391.

Sun, Q., & Colin, C., (2014), Paleoclimate and Paleoenvironment of Gonghe Basin, Qinghai-Tibet Plateau, During the Last deglacial: Weathering, Erosion and Vegetation Cover Affect Clay Mineral Formation. *Acta Geologica Sinica*. Vol. 88 No. 2pp. 801-840

Sun, X., Li, X., Luo, Y., & Chen, X., (2000), The vegetation and climate at the last glaciation on the emerged continental shelf of the South China Sea. *Palaeogeography, palaeoclimatology, palaeoecology*, *160*(3-4), 301-316.

Sun, X., & Wang, P., (2005), How old is the Asian monsoon system?—Palaeobotanical records from China. *Palaeogeography, Palaeoclimatology, Palaeoecology*, 222(3-4), 181-222.

Sun, Y., Clemens, S. C., Morrill, C., Lin, X., Wang, X., & An, Z., (2012), Influence of Atlantic meridional overturning circulation on the East Asian winter monsoon. *Nature Geoscience*, *5*(1), 46-49.

Sun, Z., Zhang, Z., Qiu, B., Zhang, X., Zhou, C., Huang, X., Zhao, W., & Tian, J. (2020). Three-dimensional structure and interannual variability of the Kuroshio Loop Current in the northeastern South China Sea. *Journal of Physical Oceanography*, *50*(9), 2437-2455

Switzer, A. D., & Pile, J., (2015), Grain size analysis. *Handbook of sea-level research*, 331-346.

Tan, K., Huang, P., Liu, F., Murakami, H., & Hsu, P.C, (2019), Simulated ENSO's impact on tropical cyclone genesis over the western North Pacific in CMIP5 models and its changes under global warming. *International Journal of Climatology*, *39*(8), 3668-3678.

Tanaka, T., Togashi, S., Kamioka, H., Amakawa, H., Kagami, H., Hamamoto, T., Yuhara, M., Orihashi, Y., Yoneda, S., Shimizu, H., Kunimaru, T., Takahashi, K., Yanagi, T., Nakano, T., Fujimaki, H., Shinjo, R., Asahara, Y., Tanimizu, M., Dragusanu, C., (2000), JNdi-1: a neodymium isotopic reference in consistency with LaJolla neodymium. *Chem. Geol.* 168(3-4), 279-281. https://doi.org/10.1016/S0009-2541(00)00198-4

Tang, H., Micheels, A., Eronen, J.T., Ahrens, B., & Fortelius, M., (2013), Asynchronous responses of East Asian and Indian summer monsoons to mountain uplift shown by regional climate modelling experiments. *Climate Dynamics*, *40*, 1531-1549.

Thomas, E. K., Huang, Y., Morrill, C., Zhao, J., Wegener, P., Clemens, S. C., Colman S. M., & Gao, L. (2014). Abundant C4 plants on the Tibetan Plateau during the Lateglacial and early Holocene. *Quaternary Science Reviews. 87*, 24-33. https://doi.org/10.1016/j.quascirev.2013.12.014

Thomas, E.-K., Huang, Y., Clemens, S. C., Colman, S. M., Morrill, C., Wegener, P., & Zhao, J. (2015). NOAA/WDS Paleoclimatology - Lake Qinghai, China 32,000 Year Leaf Wax Hydrogen Isotope Data. *NOAA National Centers for Environmental Information*. [dataset]

Thompson, D.M., Conroy, J.L., Collins, A., Hlohowskyj, S.R., Overpeck, J.T., Riedinger-Whitmore, M., Cole, JE., Bush, M.B., Whitney, H., Corley, T.L., & Kannan, M.S., (2017), Tropical Pacific climate variability over the last 6000 years as recorded in Bainbridge Crater Lake, Galápagos. *Paleoceanography*, *32*(8), 903-922.

Tian, J., Wang, P., & Cheng, X. (2004), Development of the East Asian monsoon and Northern Hemisphere glaciation: oxygen isotope records from the South China Sea. *Quaternary Science Reviews,* 23(18-19), 2007-2016.

Tian, J., Yang, Q., Liang, X., Xie, L., Hu, D., Wang, F., & Qu, T., (2006), Observation of Luzon Strait transport, *Geophys. Res. Lett*.,33,L19607, doi:10.1029/2006GL026272.

Tian, J., Huang, E., & Pak, D.K., (2010), East Asian winter monsoon variability over the last glacial cycle: Insights from a latitudinal sea-surface temperature gradient across the South China Sea. *Palaeogeography, Palaeoclimatology, Palaeoecology*, *292*(1-2), 319-324.

Tory, K.J., & Dare, R.A., (2015), Sea surface temperature thresholds for tropical cyclone formation. *Journal of Climate*, *28*(20), 8171-8183.

Trachsel, M., Grosjean, M., Schnyder, D., Kamenik, C., & Rein, B., (2010), Scanning reflectance spectroscopy (380–730 nm): a novel method for quantitative high-resolution climate reconstructions from minerogenic lake sediments. *Journal of Paleolimnology*, *44*, 979-994.

Trenberth, K.E., Branstator, G.W., Karoly, D., Kumar, A., Lau, N.C., & Ropelewski, C., (1998), Progress during TOGA in understanding and modeling global teleconnections associated with tropical sea surface temperatures. *Journal of Geophysical Research: Oceans*, *103*(C7), 14291-14324.

Tsai, C.H., Shyu, J.B.H, Chung, S.L., Ramos, N.T., Lee, H.Y., (2019), Detrital zircon record from major rivers of Luzon Island: implications for Cenozoic continental growth in SE Asia. *Journal of the Geological Society*. 176 (4): 727–735. doi: https://doi.org/10.1144/jgs2019-003

Tsai, Y.J., Syu, F.T., Shieh, C.L., Chung, C.R., Lin, S.S., & Yin, H.Y., (2021), Framework of Emergency Response System for Potential Large-Scale Landslide in Taiwan. *Water*, *13*(5), 712.

Tsai, T.T., Tsai, Y.J., Shieh, C.L., & Wang, J.H.C., (2022). Triggering Rainfall of Large-Scale Landslides in Taiwan: Statistical Analysis of Satellite Imagery for Early Warning Systems. *Water*, *14*(21), 3358.

Ujiié, H., & Ujiié, Y., (1999), Late Quaternary course changes of the Kuroshio Current in the Ryukyu Arc region, northwestern Pacific Ocean. *Marine Micropaleontology*, *37*(1), 23-40.

Ulbrich, U., Leckebusch, G.C., & Pinto, J.G., (2009), Extra-tropical cyclones in the present and future climate: a review. *Theor Appl Climatol 96,* 117–131 https://doi.org/10.1007/s00704-008-0083-8

van Hengstum, P.J., Scott, D.B., Gröcke, D.R., & Charette, M.A., (2011), Sea level controls sedimentation and environments in coastal caves and sinkholes. *Marine Geology*, *286*(1-4), 35-50.

Vargas-Luna, A., Crosato, A., & Uijttewaal, W.S., (2015), Effects of vegetation on flow and sediment transport: comparative analyses and validation of predicting models. *Earth Surface Processes and Landforms*, *40*(2), 157-176.

Viscarra Rossel, R.A., & Behrens, T., (2010). Using data mining to model and interpret soil diffuse reflectance spectra. *Geoderma*, *158*(1-2), 46-54.

Vijith, H., Hurmain, A., & Dodge-Wan, D. (2018), Impacts of land use changes and land cover alteration on soil erosion rates and vulnerability of tropical mountain ranges in Borneo. *Remote Sensing Applications: Society and Environment*, *12*, 57-69.

Wan, S., Li, A., Clift, P.D., & Stuut, J.B.W., (2007), Development of the East Asian monsoon: mineralogical and sedimentologic records in the northern South China Sea since 20 Ma. *Palaeogeography, Palaeoclimatology, Palaeoecology*, *254*(3-4), 561-582.

Wan, S., Clift, P.D., Li, A., Yu, Z., Li, T., & Hu, D., (2012), Tectonic and climatic controls on long-term silicate weathering in Asia since 5 Ma. *Geophysical Research Letters*, *39*(15).

Wang, B. & Chan, J. C. L., (2002), How strong ENSO events affect tropical storm activity over the western North Pacific. *J. Climate* ***13****,* 1517–1536

Wang, B., Clemens, S.C., & Liu, P., (2003), Contrasting the Indian and East Asian monsoons: implications on geological timescales. Mar. Geol. 201, 5–21.

Wang, G.H., Xie, S.P., Qu, T.D., Huang, R.X., (2011), Deep South China Sea circulation. Geophys. Res. Lett. 38, L05601. http://dx.doi.org/10.1029/2010GL046626.

Wang, L., & Wang, P., (1990), Late Quaternary paleoceanography of the South China Sea : glacialinterglacial contrasts in an enclosed basin. *Paleoceanography* 5(1): 77-90.

Wang, L., Sarnthein, M., Erlenkeuser, H., Grimalt, J., Grootes, P., Heilig, S., Ivanova, E., Kienast, M., Pelejero, C., & Pflaumann, U. (1999a), East Asian monsoon climate during the Late Pleistocene: high-resolution sediment records from the South China Sea. *Marine Geology*, *156*(1-4), 245-284.

Wang, L., Li, J., Lu, H., Gu, Z., Rioual, P., Hao, Q., Mackay, A.W., Jiang, W., Cai, B., Xu, B;, Han, J., & Chu, G., (2012), The East Asian winter monsoon over the last 15,000 years: its links to high-latitudes and tropical climate systems and complex correlation to the summer monsoon. *Quaternary Science Reviews*, *32*, 131-142.

Wang, L.C., Behling, H., Lee, T.Q., Li, H.C., Huh, C.A., Shiau, L.J., & Chang, Y.P., (2014), Late Holocene environmental reconstructions and their implications on flood events, typhoon, and agricultural activities in NE Taiwan. *Climate of the Past*, *10*(5), 1857-1869.

Wang, L.C., Behling, H., Kao, S.J., Li, H.C., Selvaraj, K., Hsieh, M.L., & Chang, Y.P., (2015), Late Holocene environment of subalpine northeastern Taiwan from pollen and diatom analysis of lake sediments. *J. Asian Earth Sci. 114*, 447-456. https://doi.org/10.1016/j.jseaes.2015.03.037

Wang, L.C., Tang, Z.W., Chen, H.F., Li, H.C., Shiau, L.J., Huang, J.J.S., Wei, K.Y., Chuang, C.K., & Chou, Y.M., (2019), Late Holocene vegetation, climate, and natural disturbance records from an alpine pond in central Taiwan. *Quaternary International*, *528*, 63-72.

Wang, L.C., Chou, Y.M., Chen, H.F., Chang, Y.P., Chiang, H.W., Yang, T.N., Shiau, L.J., & Chen, Y.G., (2021), Paleolimnological evidence for lacustrine environmental evolution and paleo-typhoon records during the late Holocene in eastern Taiwan. *Journal of Paleolimnology*, 1-17.

Wang, M., Shao, Y., Jiang, Q. O., Xiao, L., Yan, H., Gao, X., Wang, L., & Liu, P., (2020), Impacts of climate change and human activity on the runoff changes in the Guishui River Basin. *Land 9(9)*, 291. https://doi.org/10.3390/land9090291

Wang, P., Wang, L., Bian, Y., & Jian, Z., (1995), Late Quaternary paleoceanography of the South China Sea: surface circulation and carbonate cycles. *Marine Geology*, *127*(1-4), 145-165.

Wang, P., Bradshaw, M., Ganzei, S.S., Tsukawaki, S., Hassan, K.B., Hantoro, W.S., Poobrasert, S., Burner, R., Zhao, Q., & Kagami, H., (1997). West Pacific marginal seas during last glacial maximum: amplification of environmental signals and its impact on monsoon climate. In *Marine Geology and Palaeoceanography* (pp. 65-85). CRC Press.

Wang, P, (1999b), Response of Western Pacific marginal seas to glacial cycles: paleoceanographic and sedimentological features. *Marine geology*, *156*(1-4), 5-39.

Wang, P., Jian, Z., Zhao, Q., Li, Q., Wang, R., Liu, Z., Wu, G., Shao, L., Wang, J., Huang, B., Fang, D., Tian, J., Li, J., Li, X., Wei, G., Sun, X., Luo, Y., Su, X., Mao, S., & Chen, M., (2003), Evolution of the South China Sea and monsoon history revealed in deep sea records, *Chinese Sci. Bull.*, 48, 2549–2561.

Wang, P., Wang, B., Cheng, H., Fasullo, J., Guo, Z., Kiefer, T., & Liu, Z. (2017). The global monsoon across time scales: Mechanisms and outstanding issues. *Earth-Science Reviews. 174*, 84-121. https://doi.org/10.1016/j.earscirev.2017.07.006

Wang, X., Zhao, X., Zhang, Z., Yi, L., Zuo, L., Wen, Q., Liu, F., Xu, J., Hu, S., & Liu, B., (2016), Assessment of soil erosion change and its relationships with land use/cover change in China from the end of the 1980s to 2010. *Catena*, *137*, 256-268.

Wang, X., Zhong, Y., Clift, P. D., Feng, Y., Wilson, D. J., Kaboth-Bahr, S.,Bahr, A., Gong, X., Zhao, D., Chen, Z., Zhang, Y., Tian, Y., Liu, Y., Liu, X., Liu, J., Xia, W., Yang, H., Cao, W., & Liu, Q., (2023), Interactions between depositional regime and climate proxies in the northern South China Sea since the Last Glacial Maximum. *Paleoceanography and Paleoclimatology*,

Wang, Y., Fan, W., Zhang, G., & Zhang, Y., (2013), Phanerozoic tectonics of the South China Block: Key observations and controversies. *Gondwana Research*. 23 (4): 1273–1305.

Wang, Y.J., Cheng, H., Edwards, R.L., An, Z.S., Wu, J.Y., Shen, C.C., & Dorale, J.A., (2001), A high-resolution absolute dated Late Pleistocene monsoon record from Hulu Cave, *China. Science* 294(5550):2345–8

Wang, Y.J., Cheng, H., Edwards, R.L., He, Y., Kong, X., An, Z.S., Wu, J.Y., Kelly, M.J., Dykoski, C.A., & Li, X., (2005), The Holocene Asian monsoon: links to solar changes and North Atlantic climate. *Science* 308, 854–857

Webster, P. J. (1987), The elementary monsoon. *John Wiley & Sons Eds, New York*: 3-32.

Webster, P.J., (1994), The role of hydrological processes in ocean – atmosphere interactions. *Rev. Geophys*. 32, 427–476.

Webster, P.J., Magana, V.O., Palmer, T.N., Shukla, J., Tomas, R.A., Yanagi, M., & Yasunari, T., (1998), Monsoons: process, predictability and the prospects for prediction. Journal of Geophysical Research 103 (C7), 14451–14510.

Wei, G., Li, X. H., Liu, Y., Shao, L., & Liang, X., (2006), Geochemical record of chemical weathering and monsoon climate change since the early Miocene in the South China Sea. *Paleoceanography*, *21*(4).

Wei, G., Liu, Y., Ma, J., Xie, L., Chen, J., Deng, W., & Tang, S., (2012), Nd, Sr isotopes and elemental geochemistry of surface sediments from the South China Sea: implications for provenance tracing. *Marine Geology*, *319*, 21-34.

Wen, X., Liu, Z., Wang, S., Cheng, J., & Zhu, J., (2016), Correlation and anti-correlation of the East Asian summer and winter monsoons during the last 21,000 years. *Nature Communications*, *7*(1), 11999.

West, A.J., Galy, A., & Bickle, M., (2005), Tectonic and climatic controls on silicate weathering. *Earth and Planetary Science Letters*, *235*(1-2), 211-228.

Woodruff, J.D., Donnelly, J.P., & Okusu, A., (2009), Exploring typhoon variability over the mid-to-late Holocene: evidence of extreme coastal flooding from Kamikoshiki, Japan. *Quaternary Science Reviews*, *28*(17-18), 1774-1785.

Wu, C. C., & Kuo, Y. H. (1999). Typhoons affecting Taiwan: Current understanding and future challenges. *Bulletin of the American Meteorological Society*, *80*(1), 67-80.

Wu, J., Liu, Q., Cui, QY., Xu, D. K., Wang, L., Shen, C.M., Chu, G.Q., & Liu, J.Q., (2019), Shrinkage of East Asia Winter Monsoon associated with increased ENSO events since the mid-Holocene. *Journal of Geophysical Research: Atmospheres*, *124*(7), 3839-3848.

Wu, M.C., (1992), On the monitoring and prediction of the summer drought in Taiwan area (I): Meteorological conditions in the abundant and deficit rainfall years. *Atmos Sci 20*, 35-46. In Chinese.

Wu, Q., (2014), New insights into the current- and past hydrology of the north-western subtropical Pacific Ocean over the past 25 kyr, based on investigations of the Nd isotopic composition of seawater and deep-sea sediments from the northern South China Sea. Geochemistry. *Université Paris Sud - Paris XI*

Xia, X.M., Li, Y., Yang, H., Wu, C.Y., Sing, T.H., & Pong, H.K., (2004), Observations on the size and settling velocity distributions of suspended sediment in the Pearl River Estuary, China. *Continental Shelf Research* 24, 1809-1826.

Xiao, Z., & Duan, A. (2016), Impacts of Tibetan Plateau Snow Cover on the Interannual Variability of the East Asian Summer Monsoon, Journal of Climate, 29(23), 8495-8514.

Xie, L., Tian, J., Zhang, S., Zhang, Y., & Yang, Q., (2011) An anticyclonic eddy in the intermediate layer of the Luzon Strait in Autumn 2005. *J. Oceanogr*.. 67. 37-46. 10.1007/s10872-011-0004-9.

Xie, X., Zheng, H.B., & Qiao, P.J., (2014), Millennial climate changes since MIS 3 revealed by element records in deep-sea sediments from northern South China Sea. *Chinese Science Bulletin*, *59*, 776-784.

Xu, F., Hu, B., Dou, Y., Liu, X., Wan, S., Xu, Z., Tian, X., Liu, Z., Yin, X., Li, A., (2017), Sediment provenance and paleoenvironmental changes in the northwestern shelf mud area of the South China Sea since the mid-Holocene. Cont. Shelf Res. 144, 21–30.

Xu, Y., Wang, S., Bai, X., Shu, D., & Tian, Y., (2018a), Runoff response to climate change and human activities in a typical karst watershed, SW China. *PloS One 13*(3), e0193073. https://doi.org/10.1371/journal.pone.0193073

Xu, Y., Liu, L., Zhou, H., Huang, B., Li, P., Ma, X., & Dong, F., (2018b), Submarine landslide identified in DLW3102 core of the northern continental slope, South China Sea. *Journal of Ocean University of China*, *17*, 147-155.

Xue, Y., Ji, J., Sun, S., Wu, G., Lau, K. M., Poccard, I., Zhang, R., Kang, H.S., Xu, G.X., Schaake, J.C., Zhang, J.Y., & Jiao, Y., (2005), Multiscale variability of the river runoff system in China and its long-term link to precipitation and sea surface temperature. *J. Hydrometeorol. 6*(4), 550-570. https://doi.org/10.1175/JHM439.1

Yancheva, G., Nowaczyk, N.R., Mingram, J., Dulski, P., Schettler, G., Negendank, J., Liu, J., Sigman, D., Peterson, L., & Haug, G., (2007), Influence of the intertropical convergence zone on the East Asian monsoon. *Nature*, 445, 74–77

Yanai, M. (1964) Formation of Tropical Cyclones. *Reviews of Geophysics, 2*, 367-414. https://doi.org/10.1029/RG002i002p00367

Yang, M.J., & Huang, H.L., (2004), Precipitation processes associated with the landfalling Typhoon Nari (2001). In *Extended Abstracts, 26th Conf. on Hurricanes and Tropical Meteorology*.

Yang, Q., Tian, J., & Zhao, W., (2010), Observation of Luzon Strait transport in summer 2007. Deep Sea Res. Part I 57, 670–676.

Yang, S.Y., Jan, C.D., & Wang, J.S., (2018), Landslides triggered by typhoon Morakot in Taiwan. *Environmental Risks*, 161-164.

Yang, T.F., Lee, T., Chen, C.H., Cheng, S.N., Knittel, U., Punongbayan, R.S., Dasdas, A.R., (1996), A double island arc between Taiwan and Luzon: consequence of ridge subduction. *Tectonophysics 258* (1), 85–101.

Yi, L., Yu, H., Ortiz, J. D., Xu, X., Qiang, X., Huang, H., Shi, X., & Deng, C., (2012), A reconstruction of late Pleistocene relative sea level in the south Bohai Sea, China, based on sediment grain-size analysis. *Sedimentary Geology*, *281*, 88-100.

Yi, S., (2011), Holocene Vegetation Responses to East Asian Monsoonal Changes in South Korea. Climate Change - Geophysical Foundations and Ecological Effects. doi: 10.5772/23920

Yin, Q., Berger, A., Driesschaert, E., Goosse, H., Loutre, M.F., & Crucifix, M., (2008), The Eurasian ice sheet reinforces the East Asian summer monsoon during the interglacial 500 000 years ago. *Climate of the Past*, *4*(2), 79-90.

Yu, H.S., & Chang, J.F., (2002), The Penghu submarine canyon off southwestern Taiwan: Morphology and origin. *Terrestrial Atmospheric and Oceanic Sciences*, *13*(4), 547-562.

Yu, H.S., & Hong, E., (2006), Shifting submarine canyons and development of a foreland basin in SW Taiwan: controls of foreland sedimentation and longitudinal sediment transport. *Journal of Asian Earth Sciences*, *27*(6), 922-932.

Yu, J., Li, L., Zhang, X., He, J., Jia, G., & Kuhnt, W., (2023), Mangrove sediment erosion in the Sunda Shelf during meltwater pulses: Insights from biomarker records. *Organic Geochemistry*, *175*, 104542.

Yu, S., Zheng, Z., Chen, F., Jing, X., Kershaw, P., Moss, P., Peng, X., Zhang, X., Chen, C., Zhou, Y., Huang, K., & Gan, H., (2017), A last glacial and deglacial pollen record from the northern South China Sea: New insight into coastal-shelf paleoenvironment. *Quaternary Science Reviews*, *157*, 114-128.

Yu, S.W., Tsai, L.L., Talling, P.J., Lin, A.T., Mii, H.S., Chung, S.H., & Horng, C.S., (2017), Sea level and climatic controls on turbidite occurrence for the past 26 kyr on the flank of the Gaoping Canyon off SW Taiwan. *Marine Geology*, *392*, 140-150.

Yu, Z., Wan, S., Colin, C., Yan, H., Bonneau, L., Liu, Z., Song, L., Sun, H., Xu, Z., & Li, T., (2016), Co-evolution of monsoonal precipitation in East Asia and the tropical Pacific ENSO system since 2.36 Ma: New insights from high-resolution clay mineral records in the West Philippine Sea. *Earth Planet. Sci. Lett. 446*, 45-55.

Yuan, D., (2002), A numerical study of the South China Sea deep circulation and its relation to the Luzon Strait transport. *Acta Oceanologica Sinica* 21 (2), 187–202.

Yuan, D., Han, W., & Hu, D., (2006), Surface Kuroshio path in the Luzon Strait area derived from satellite remote sensing data. *J. Geophys. Res.* 111, C11007. http://dx.doi.org/10.1029/2005JC003412.

Yue, Y., Yu, K., Tao, S., Zhang, H., Liu, G., Wang, N., Jiang, W., Fan, T;, Lin, W., & Wang, Y., (2019), 3500-year western Pacific storm record warns of additional storm activity in a warming warm pool. *Palaeogeography, Palaeoclimatology, Palaeoecology*, *521*, 57-71.

Yumul Jr., G.P., Dimalanta, C.B., Tamayo Jr., R.A., & Maury, R.C., (2003), Collision, subduction and accretion events in the Philippines: a synthesis. *Island Arc* 12, 77–91.

Zhang, D., Ye, Z., Yamada, K., Zhen, Y., Zheng, C., & Bu, W. (2016). Pleistocene sea level fluctuation and host plant habitat requirement influenced the historical phylogeography of the invasive species Amphiareus obscuriceps (Hemiptera: Anthocoridae) in its native range. *BMC Evolutionary Biology*, *16*(1), 1-15.

Zhang, H., Liu, C., Jin, X., Shi, J., Zhao, S., & Jian, Z., (2016), Dynamics of primary productivity in the northern South China Sea over the past 24,000 years. *Geochemistry, Geophysics, Geosystems*, *17*(12), 4878-4891.

Zhang, J., Yu, Z.G., Wang, J.T., Ren, J.L., Chen, H.T., Xiong, H., Dong, L.X., &. Xu, W.Y., (1999), The subtropical Zhujiang (Pearl River) estuary: nutrients, trace species and their relationship to photosynthesis. *Estuarine, Coastal and Shelf Science* 49: 385-400.

Zhang, L., Xiao, J., Zhou, Y., Zheng, Y., Li, J., & Xiao, H., (2016), Drought events and their effects on vegetation productivity in China. *Ecosphere*, *7*(12), e01591.

Zhang, Q., Wu, L., & Liu, Q., (2009), Tropical cyclone damages in China 1983–2006. *Bulletin of the American Meteorological Society*, *90*(4), 489-496.

Zhang, W., Wei, X.Y., Zheng, J.H., Zhu, Y.L., & Zhang, Y.J., (2012), Estimating suspended sediment loads in the Pearl River Delta region using sediment rating curves. *Continent. Shelf Res.* 38, 35–46.

Zhang, W., Leung, Y., & Chan, J.C., (2013), The analysis of tropical cyclone tracks in the western North Pacific through data mining. Part II: Tropical cyclone landfall. *J. Appl. Meteorol. Climatol., 52*, 1417–1432.

Zhang, W., Yan, H., Dodson, J., Cheng, P., Liu, C., Li, J., Lu, F., Zhou, W., An, Z., 2018. The 9.2 ka event in Asian summer monsoon area: the strongest millennial scale collapse of the monsoon during the Holocene. Clim. Dyn. 50, 2767-2782. https://doi.org/10.1007/s00382-017-3770-2

Zhang, X., Yan, Y., Dilek, Y., Chen, W.H., & Shan, Y., (2023), Mid-Miocene uplift and tectonic-sedimentary evolution of the Taiwan accretionary prism: Constraints from sedimentary records in the Hengchun Peninsula, southern Taiwan. *Marine and Petroleum Geology*, Volume 147, 105994 https://doi.org/10.1016/j.marpetgeo.2022.105994.

Zhang, Y., Liu, Z., Zhao, Y., Colin, C., Zhang, X., Wang, M., Zhao, S., & Kneller, B., (2018), Long-term in situ observations on typhoon-triggered turbidity currents in the deep sea. *Geology* 46 (8): 675–678. https://doi.org/10.1130/G45178.1.

Zhang, Z., Leduc, G., & Sachs, J.P., (2014), El Niño evolution during the Holocene revealed by a biomarker rain gauge in the Galápagos Islands. *Earth and Planetary Science Letters*, *404*, 420-434.

Zheng, Y.F., Xiao, W.J., & Zhao, G.C., (2013), Introduction to tectonics of China. *Gondw. Res*. 23, 1189–1206.

Zhao, D., Wan, S., Song, Z., Gong, X., Zhai, L., Shi, X., & Li, A., (2019), Asynchronous variation in the Quaternary East Asian winter monsoon associated with the tropical Pacific ENSO-like system. *Geophysical Research Letters*, *46*(12), 6955-6963.

Zhao, L., Fang, Q., Hou, R., & Wu, F., (2021), Effect of rainfall intensity and duration on soil erosion on slopes with different microrelief patterns. *Geoderma*, *396*, 115085.

Zhao, S., Liu, Z., Colin, C., Zhao, Y., Wang, X., & Jian, Z., (2018), Responses of the East Asian Summer Monsoon in the Low-Latitude South China Sea to High-Latitude Millennial-Scale Climatic Changes During the Last Glaciation: Evidence From a High-Resolution Clay Mineralogical Record. *Paleoceanogr. Paleoclimatology 33*, 745–765.

Zhao, W., Zhou, C., Tian, J., Yang, Q., Wang, B., Xie, L., & Qu, T. (2014), Deep water circulation in the Luzon Strait. *Journal of Geophysical Research: Oceans*, *119*(2), 790-804.

Zhao, Y., Liu, Z., Zhang, Y., Li, J., Wang, M., Wang, W., & Xu, J., (2015), In situ observation of contour currents in the northern South China Sea: Applications for deepwater sediment transport. *Earth and Planetary Science Letters* 430, 477-485.

Zhao, Y., Yang, S., Liu, J.T., Fan, D., Yang, R.J., Bi, L., & Chang, Y.P., (2017), Reconstruction of silicate weathering intensity and paleoenvironmental change during the late Quaternary in the Zhuoshui River catchment in Taiwan. *Quaternary International*, *452*, 43-53.

Zhong, G., & Peng, X., (2021), Transport and accumulation of plastic litter in submarine canyons—The role of gravity flows. *Geology*, *49*(5), 581-586.

Zhou, B., Zheng, H., Yang, W., Taylor, D., Lu, Y., Wei, G., Li, L., & Wang, H. (2012). Climate and vegetation variations since the LGM recorded by biomarkers from a sediment core in the northern South China Sea. *Journal of Quaternary Science*, *27*(9), 948-955.

Zhou, L., Yang, Y., Wang, Z., Jia, J., Mao, L., Li, Z., Fang, X., & Gao, S. (2019), Investigating ENSO and WPWP modulated typhoon variability in the South China Sea during the mid–late Holocene using sedimentological evidence from southeastern Hainan Island, China. Mar. Geol. 416, 105987. https://doi.org/10.1016/j.margeo.2019.105987

Zhou, L., Gao, S., Jia, J., Yang, Y., Tong, C., & Wang, A., (2021), Paleo-Typhoon Events as Indicated by Coral Reef Boulder Deposits on the Southern Coast of Hainan Island, China. Front. Mar. Sci. 8, 746773. https://doi.org/10.3389/fmars.2021.746773

Zhu, Y., Sun, J., Wang, Y., Li, S., Xu, T., Wei, Z., & Qu, T., (2019), Overview of the multi-layer circulation in the South China Sea. *Prog. Oceanogr*. 175, 171–182. https://doi.org/10.1016/j.pocean.2019.04.001.

Zhu, Z., Feinberg, J.M., Xie, S., Bourne, M.D., Huang, C., Hu, C., & Cheng, H., (2017), Holocene ENSO-related cyclic storms recorded by magnetic minerals in speleothems of central China. *Proceedings of the National Academy of Sciences*, *114*(5), 852-857.

Zuiderveld, K., (1994), Contrast Limited Adaptive Histogram Equalization. *In Graphics Gems IV; Academic Press: Cambridge, MA, USA*; pp. 474–485 ISBN 978012336156

Figure list

Appendix

Appendix 2-1

Table Appendix 2-1. AMS 14C ages of the upper 15 of Core MD18-3569

Core	Section	Depth (cm)	Conventional Age (yr)	error (± yr)	calendar year (95.4% prob) (yr BP)	Material	Sedimentation rate (cm/kyr)
MD18-3569	I	6	1150	30	762	G.ruber	72.9
	II	217	3670	30	3655	G.ruber	62.9
	III	401	6090	30	6579	G.ruber	39.2
	IV	471	7900	30	8363	G.ruber	50.5
	V	667	10730	30	12247	G.ruber	52.0
	VI	839	13350	40	15553	G.ruber	39.4
	VII	1006	16800	50	19790	G.ruber	34.6
	IX	1239	22630	70	26519	G.ruber	53.2
	X	1496	27920	110	31348	G.ruber	-

Appendix 2-2

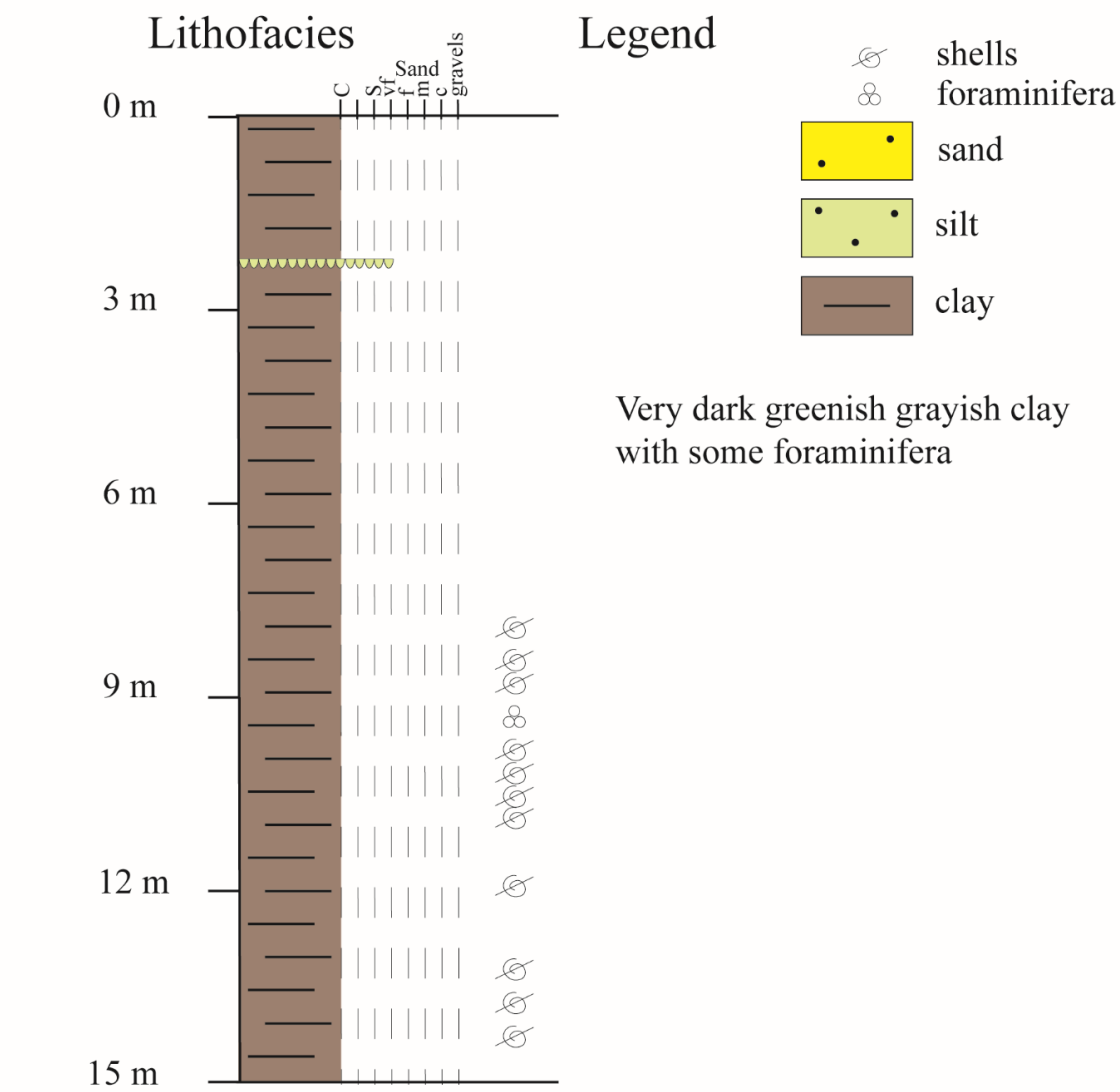

Appendix 2-2. Lithofacies schematic description of the upper 15 m of Core MD18-3569 (from Hydrosed Cruise report)

Appendix 2-3

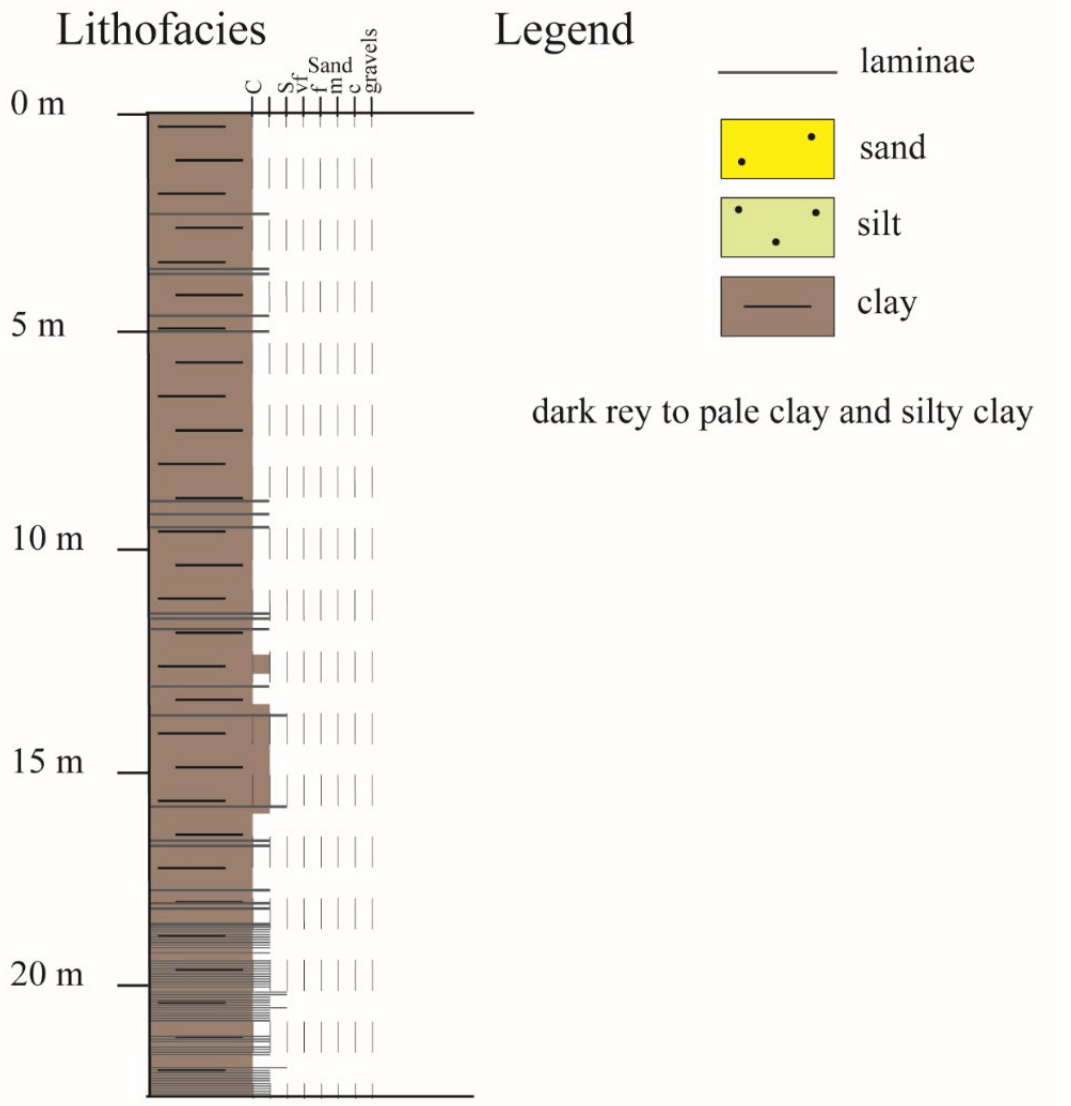

Appendix 2-3. Lithofacies schematic description of Core MD18-3574 (from Hydrosed Cruise report)

Appendix 2-4

Appendix 2-4. AMS 14C ages of Core MD18-3574

Core	Section	Depth (cm)	Material	AMS ^{14}C ages (kyr BP)	Calendar age (cal kyr BP, 1σ)	error (± kyr)
MD17-3574	1	53.5-58.5	G. ruber, G. sacculifer, O. universa	0.540 ± 0.030	0.188	0.052
	2	178-183		0.705 ± 0.030	0.347	0.044
	2	275-280		1.080 ± 0.030	0.647	0.025
	3	385.5-390.5		1.300 ± 0.030	0.849	0.043
	5	615-620		1.895 ± 0.030	1.445	0.048
	6	815-820		2.260 ± 0.030	1.864	0.043
	7	1003.5-1008.5		2.535 ± 0.030	2.216	0.055
	9	1300-1305		2.850 ± 0.030	2.636	0.061
	11	1600-1605		3.310 ± 0.030	3.154	0.054
	13	1920-1925		3.750 ± 0.030	3.670	0.054
	16	2245-2250		4.035± 0.030	4.043	0.057

Appendix 2-5

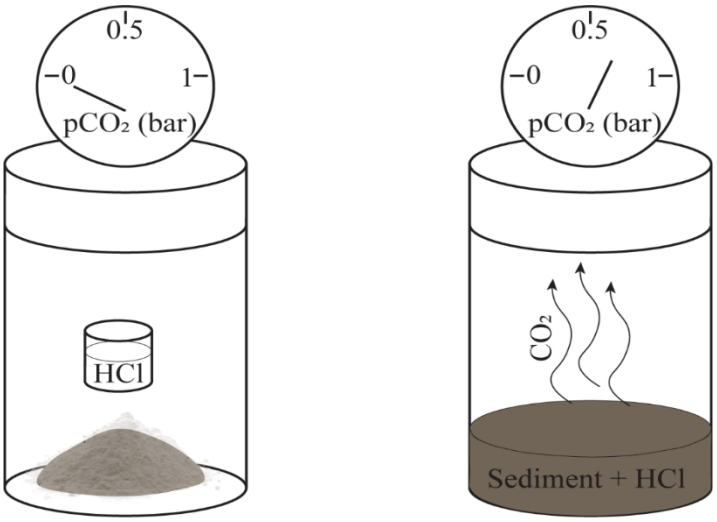

Appendix 2-5. Schematic representation of CaCO3 dissolution by HCl in vaccuum conditions and pCO2 measurement

Appendix 2-5

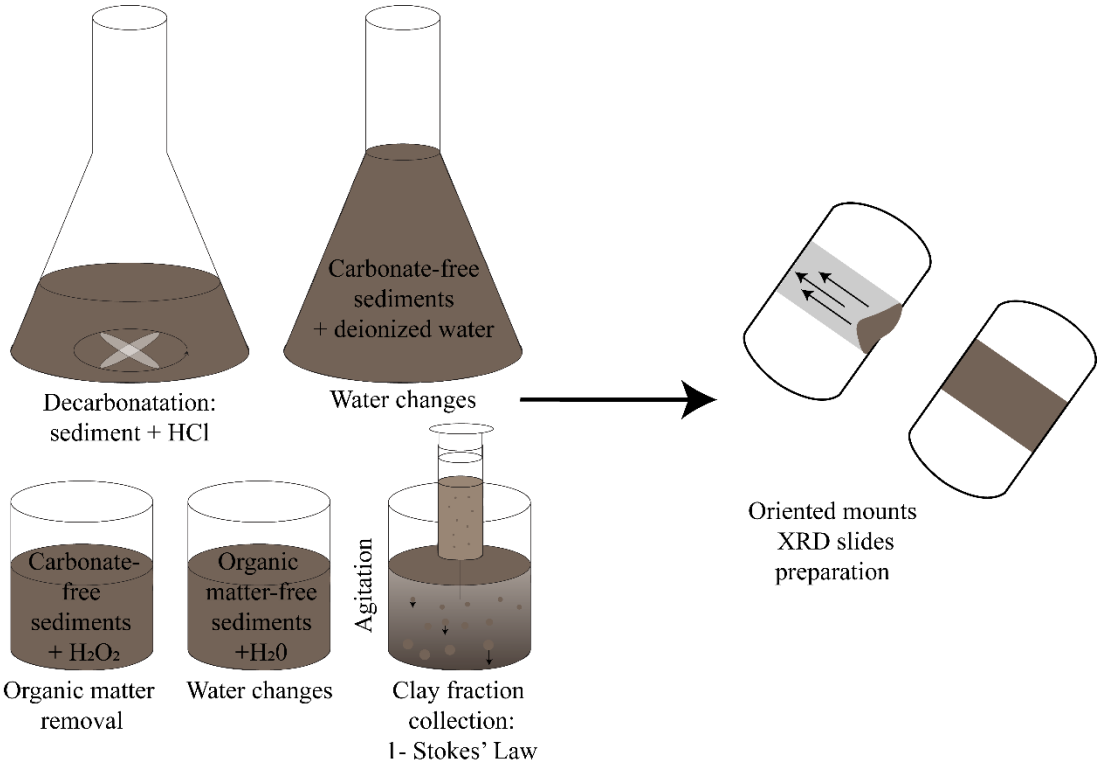

Figure 2-5. Clay mineralogy XRD prepation protocole (Liu et al., 2004)

Appendix 2-6

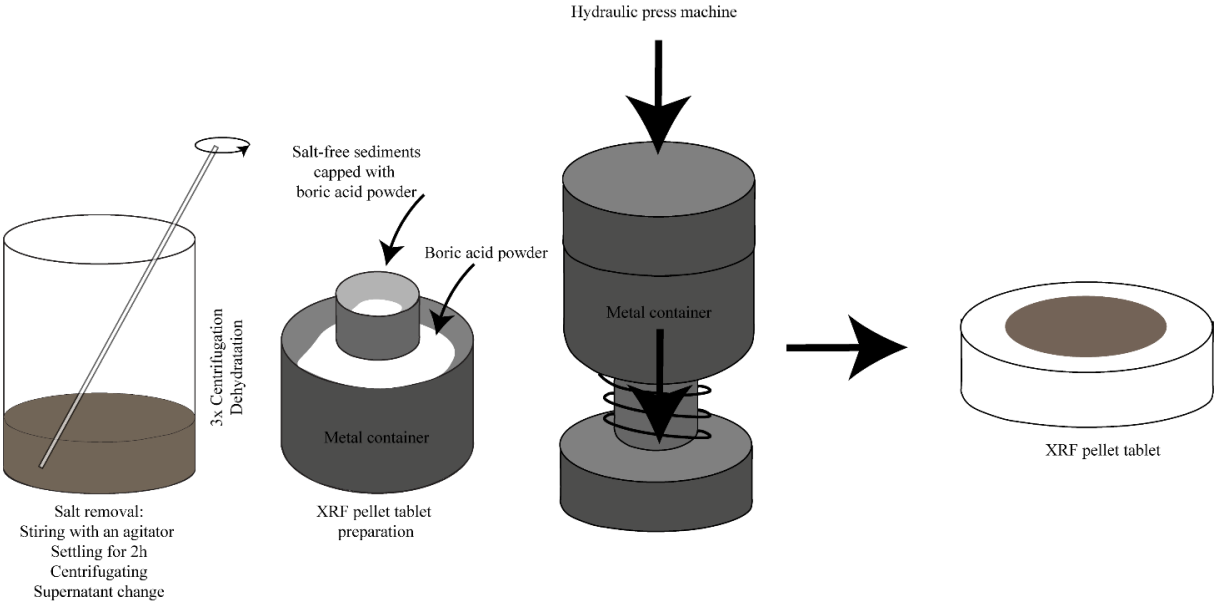

Appendix 2-6. XRF bulk geochemical composition preparation protocole (salt washing and pressure pellet tablet preparation)

Appendix 2-7

Appendix 2-7. Hyperspectral imaging proxies and their wavelength and significance used in this study

Index	Sensor	Wavelenght (mm)	Significance	Source
Rmean VNIR	VNIR		Average VNIR absorbance	Trachsel et al., 2010
d555		555	Oxides derivative reflectance	Deaton and Balsmam, 1991
Rmean SWIR	SWIR		Average SWIR absorbance	Trachsel et al., 2010
R1450		1450	H-O-H (hyrdroxyl bonds absorbance)	Viscarra Rossel et al., 2010
OM_R160		1650	Organic matter absorbance	Viscarra Rossel et al., 2010
R1935		1935	Water bonds absorbance	Viscarra Rossel et al., 2010
R1935/R140			Ratio of moisture indices	Viscarra Rossel et al., 2010
Clay R2200		2200	Clay mineral absorbance	Madejová et al., 2017

Appendix 2-8

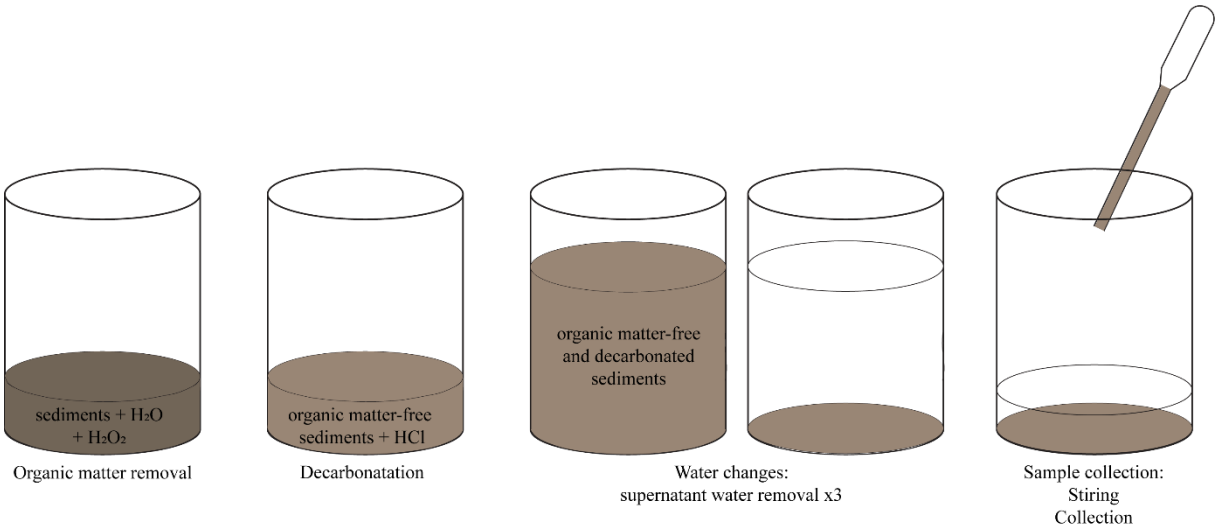

Appendix 2-8. Preparation protocole (organic matter removal and decarbonatation) of samples for laser grain size

Appendix 2-9

Appendix 2-9-1. Resin AG50W-X8 cation exchange procedure

Resin	Exchange step	Solution	Volume
AG50W-X8	Cleaning	6 N HCl	15 ml (5-5-5)
		MillI-Q water	(pH ~7)
	Pre-conditions	1 N HCl	5 ml
	Sample loading	1 N HCl	1.5 ml (1-0.5)
	Elution	2 N HCl	35 ml (1-1-3-5-5-10-10)
	Collect Sr	2 N HCl	15 ml (5-5-5)
	Elution	2.5 N HNO_3	27 ml (1-1-5-5-5-10)
	Collect REE	2.5 N HNO_3	35 ml (5-5-5-10-10)

Appendix 2-9-2. Sr-spec resin chromatography procedure

Resin	Exchange step	Solution	Volume
Sr-W	Cleaning	MillI-Q water	2 ml (1-1)
	Pre-conditions	4 N HNO_3	400 µl (200-200)
	Sample loading	4 N HNO_3	400 µl (200-200)
	Elution	4 N HNO_3	1000 µl (250-250-500)
	Collect Sr	MillI-Q water	2500 µl (500-500-500-1000)

Appendix 2-9-3. Tru and Ln-spec chromatography to elude REEs and collect and purify Nd

Resin	Exchange step	Solution	Volume
Ln-spec	Cleaning	6 N HCl	10 ml (5-5)
		Milli-Q water	(pH ~7)
	Pre-conditions	0.05N HNO3	1 ml
	Sample loading	0.05N HNO3	1ml (0.5-0.5)
	Elution	0.25N HCl	2.5 ml (0.5-0.5-0.5-0.5-0.5)
	Collect Nd	0.25N HCl	l (1-1-1.25)

Appendix 2-10

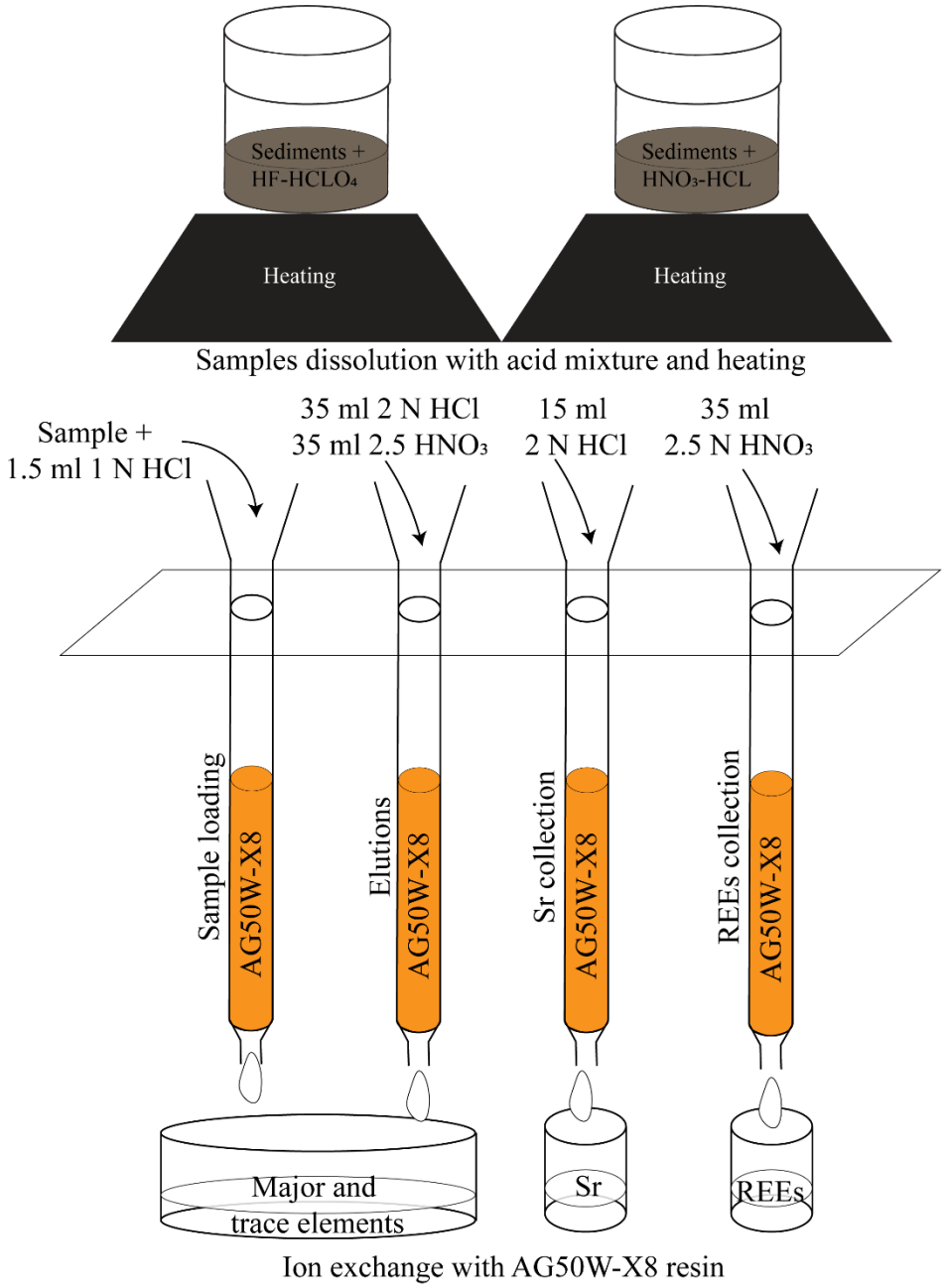

Appendix 2-10. Samples dissolution preparation and first ion exchange chromatography with AG50W-X8 resin in order to elude major and trace elements and collect Sr and REEs

Appendix 2-11

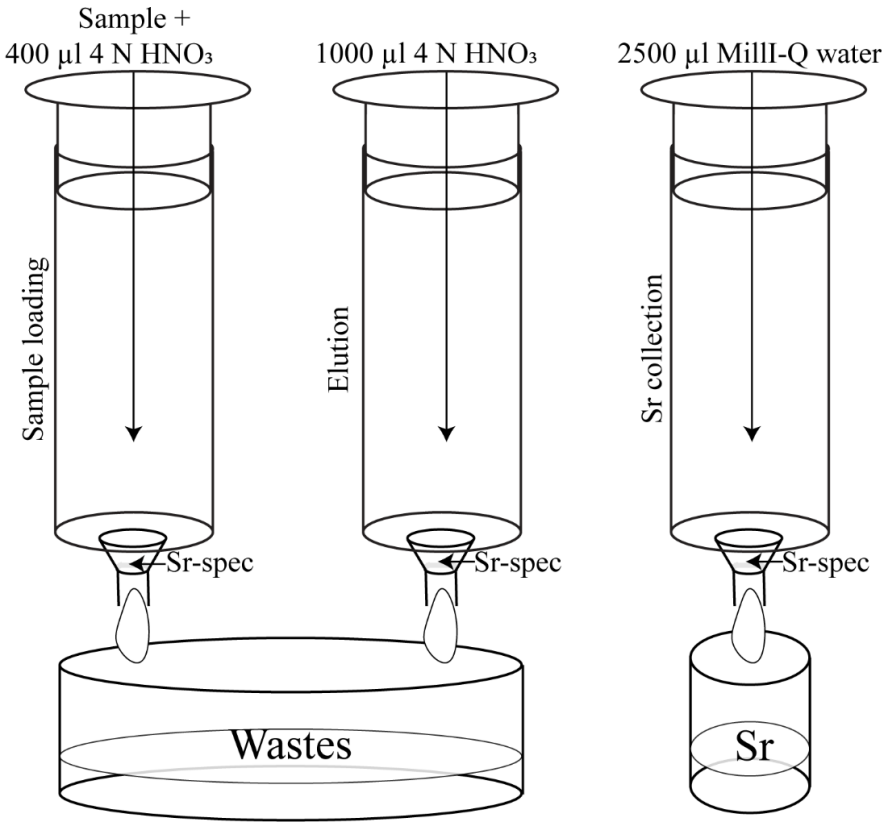

Appendix 2-11. Ion exchange chromatography with Sr-spec resin in order to purify Sr

Appendix 2-12

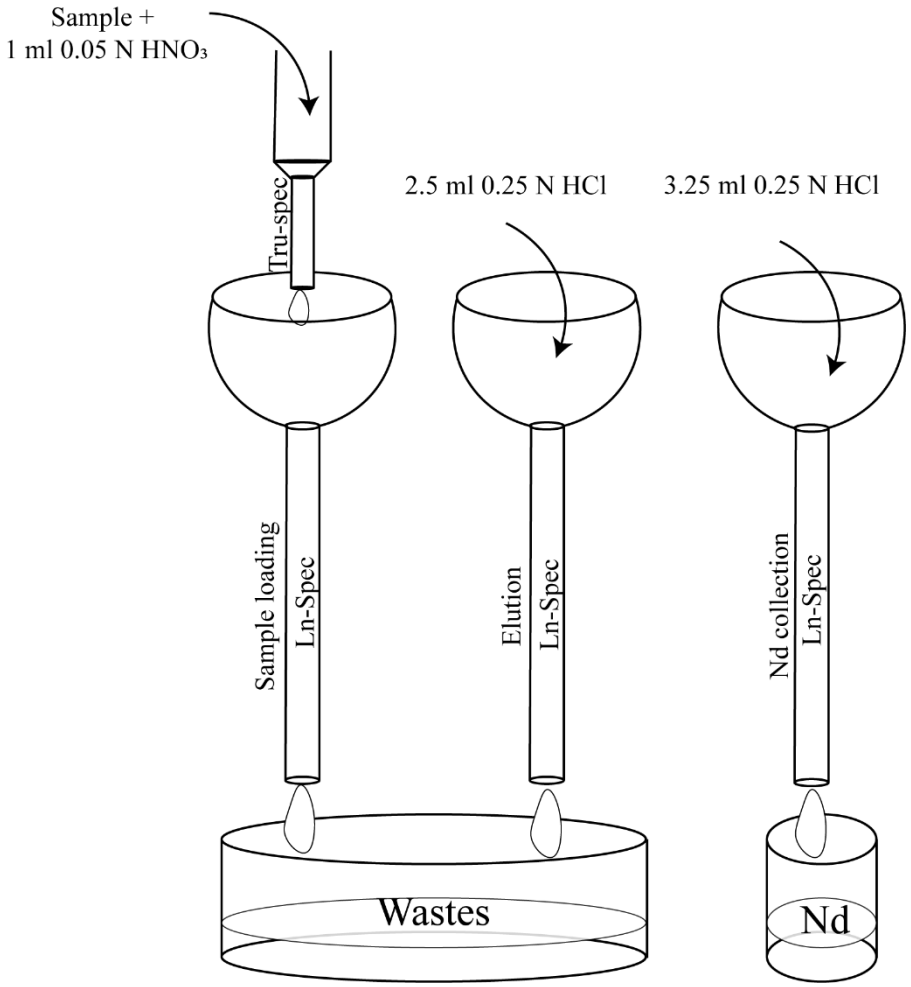

Appendix 2-12. Ion exchange chromatography with Tru and Ln-spec to purify Nd

Appendix 3-1

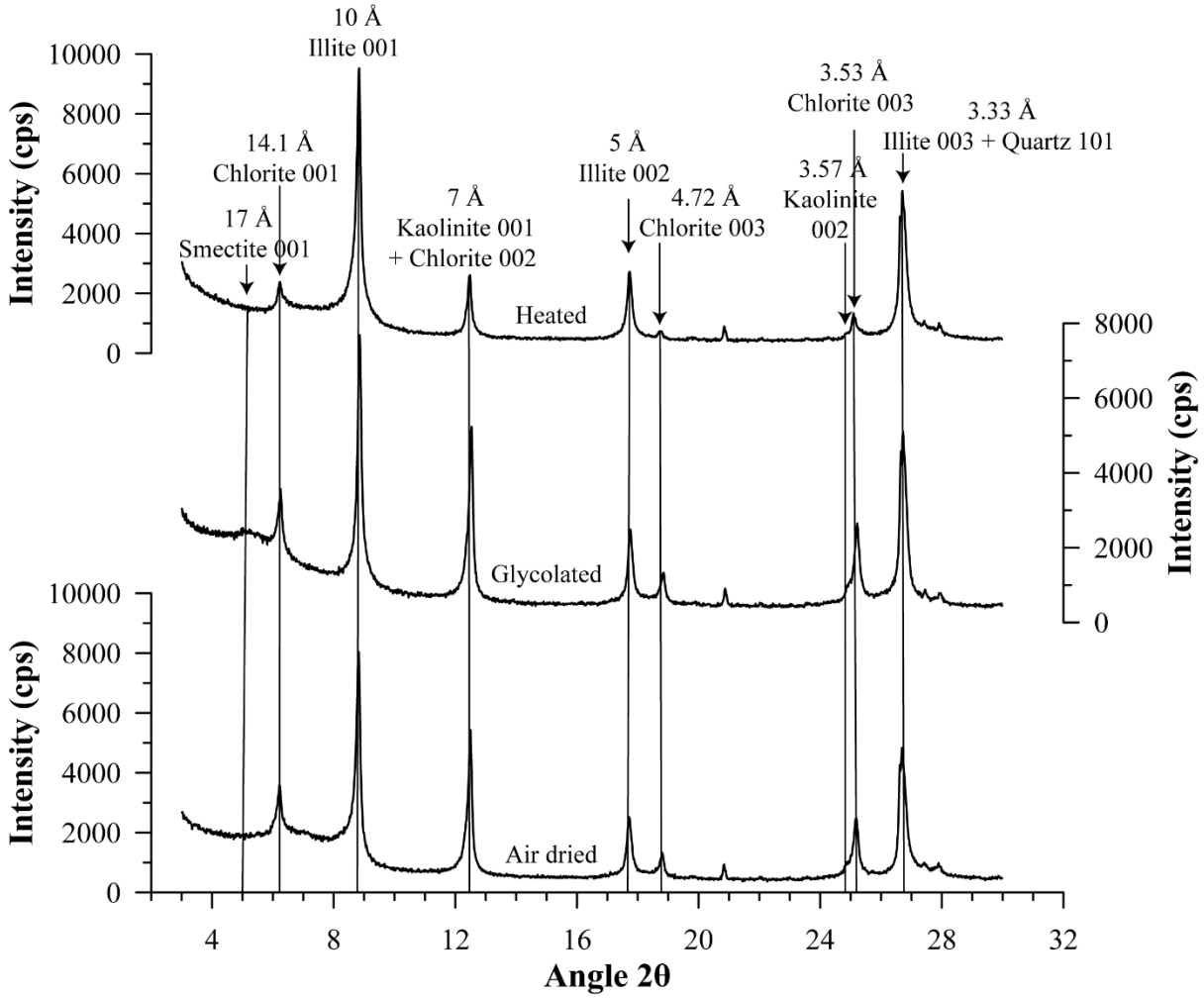

Appendix 3-1.Core MD18-3569 307 cm X-ray diffractograms of air-dried, glycolated and heated measurements showing clear 10 Å, 7 Å, 5 Å, 3.53 Å, 3.33 Å implying the presence of majority of illite and chlorite.

Appendix 5-1

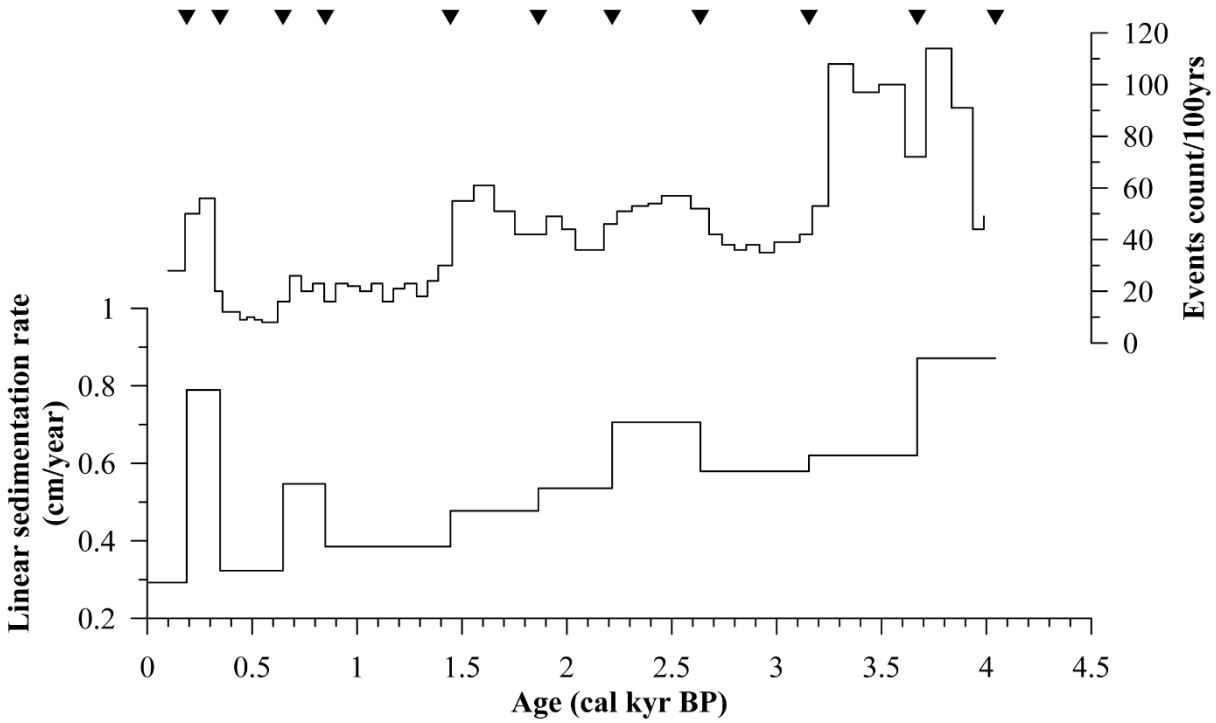

Appendix 5-1. Time variations of Core MD18-3574 linear sedimentation rate (cm/year) and turbidity deposit count per 100 years. 11 radiocarbon ^{14}C dates are also displayed

Appendix 5-2

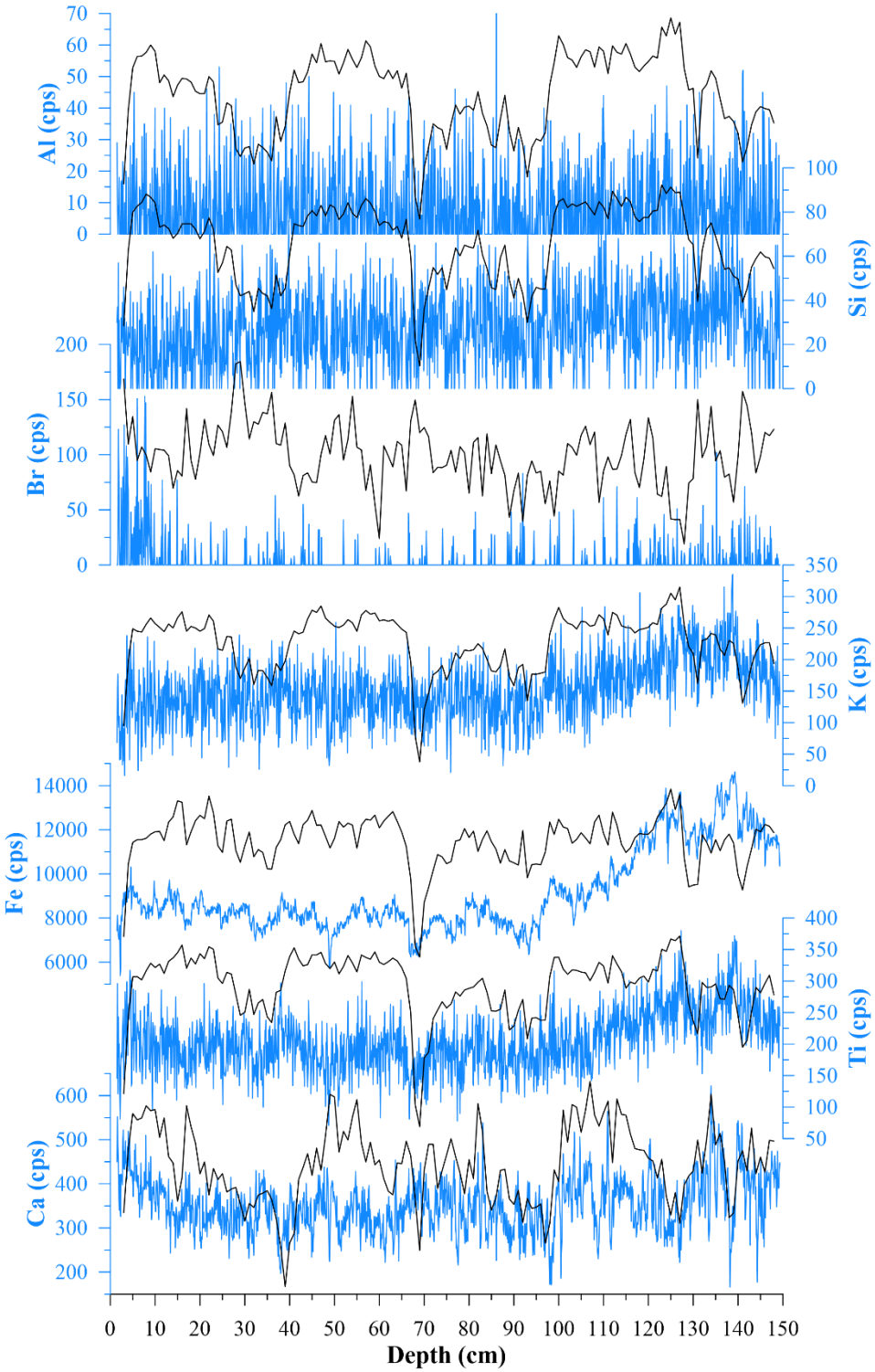

Appendix 5-2. Relative geochemical depth variations of Ca, Ti, Fe, K, Br, Si, Al at the resolutions of 1 mm (blue) and 1 cm (black)

Appendix 5-3

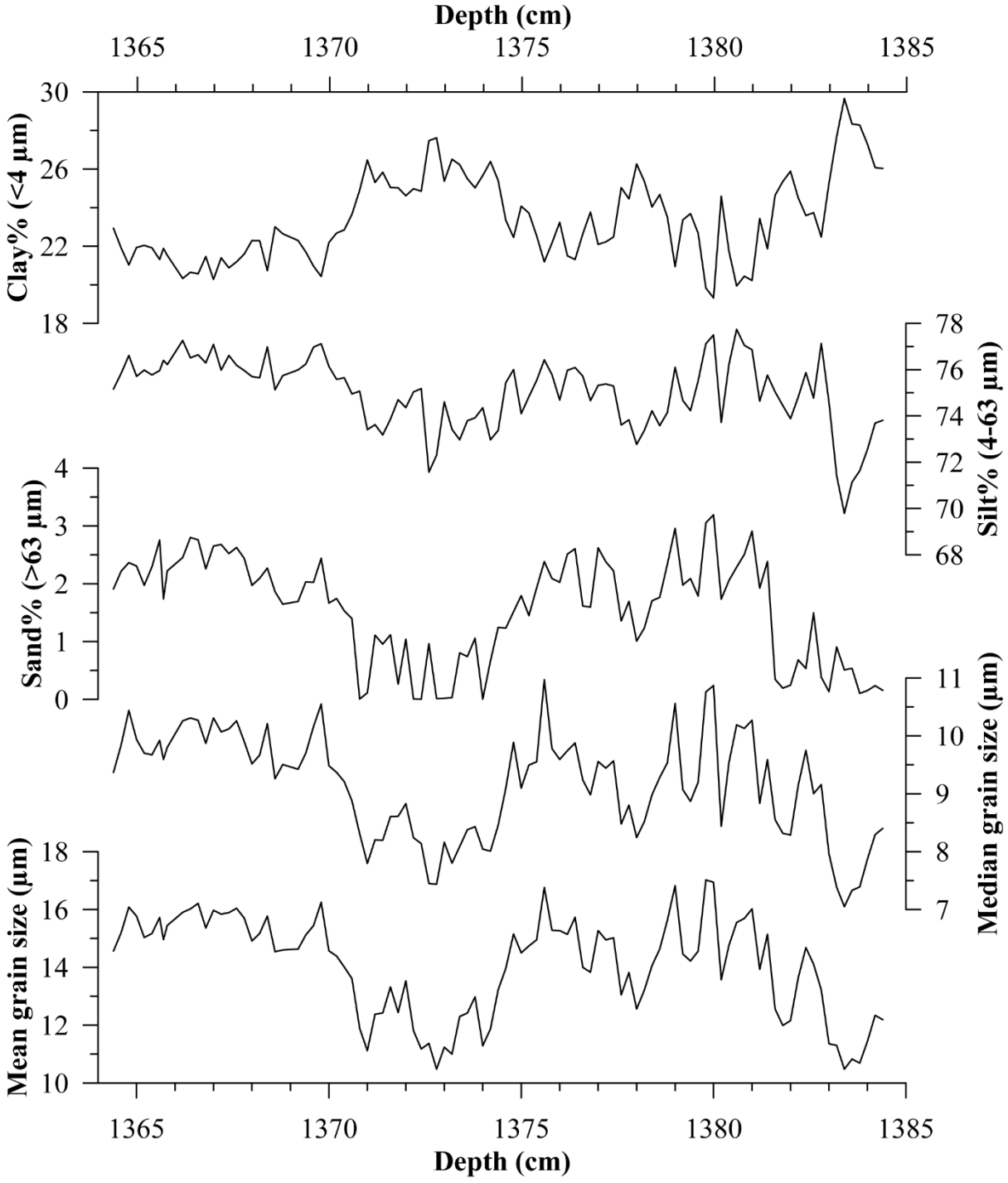

Appendix 5-3. Depth variations of the mean and median grain size and content of sand (>63 μm), silt (4-63 μm) and clay (<4 μm) fractions of Core MD18-3574 section 10.

Appendix 5-4

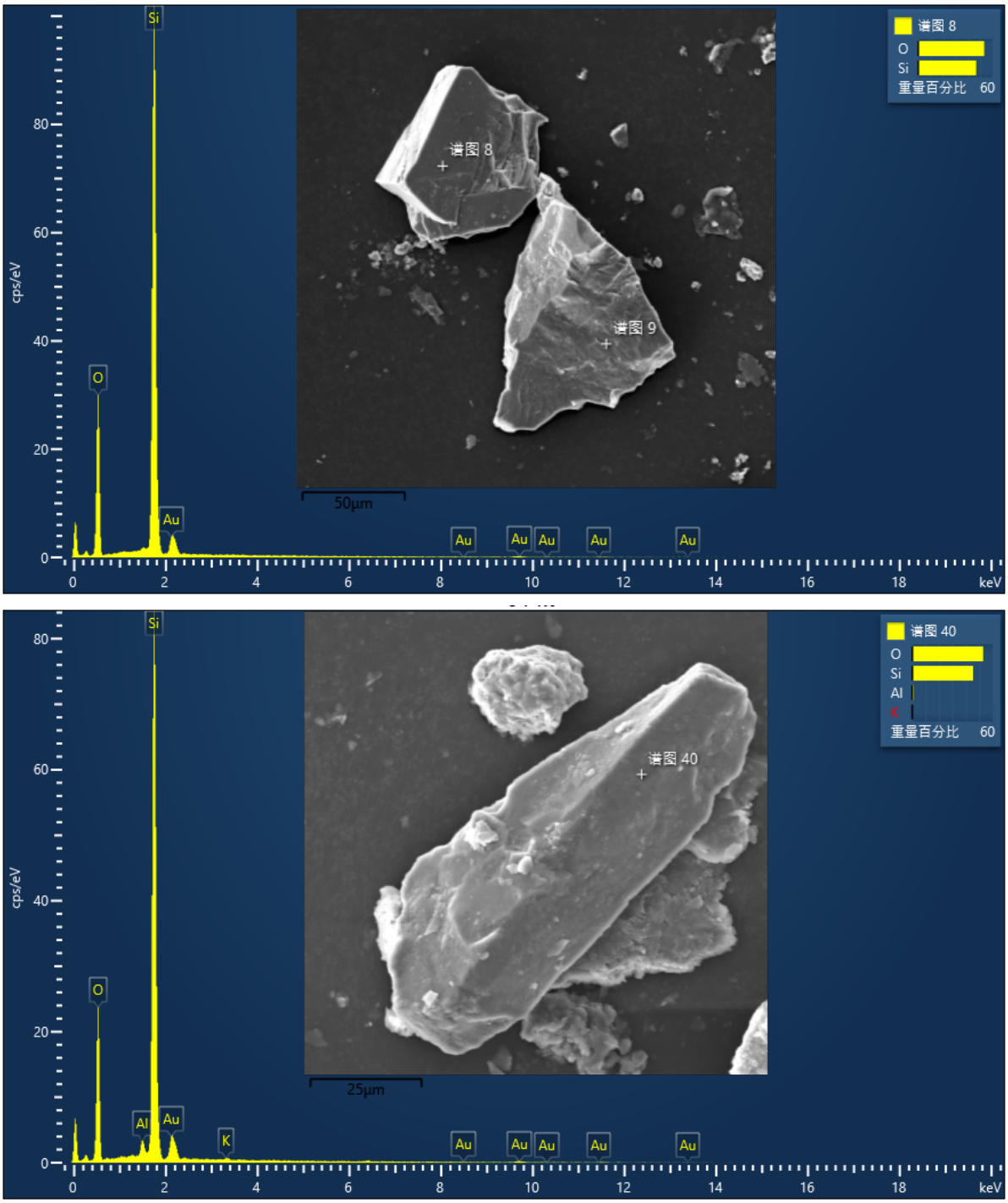

Apendix 5-4. SEM observations of quartz from coarsed-grain fraction

Appendix 5-5

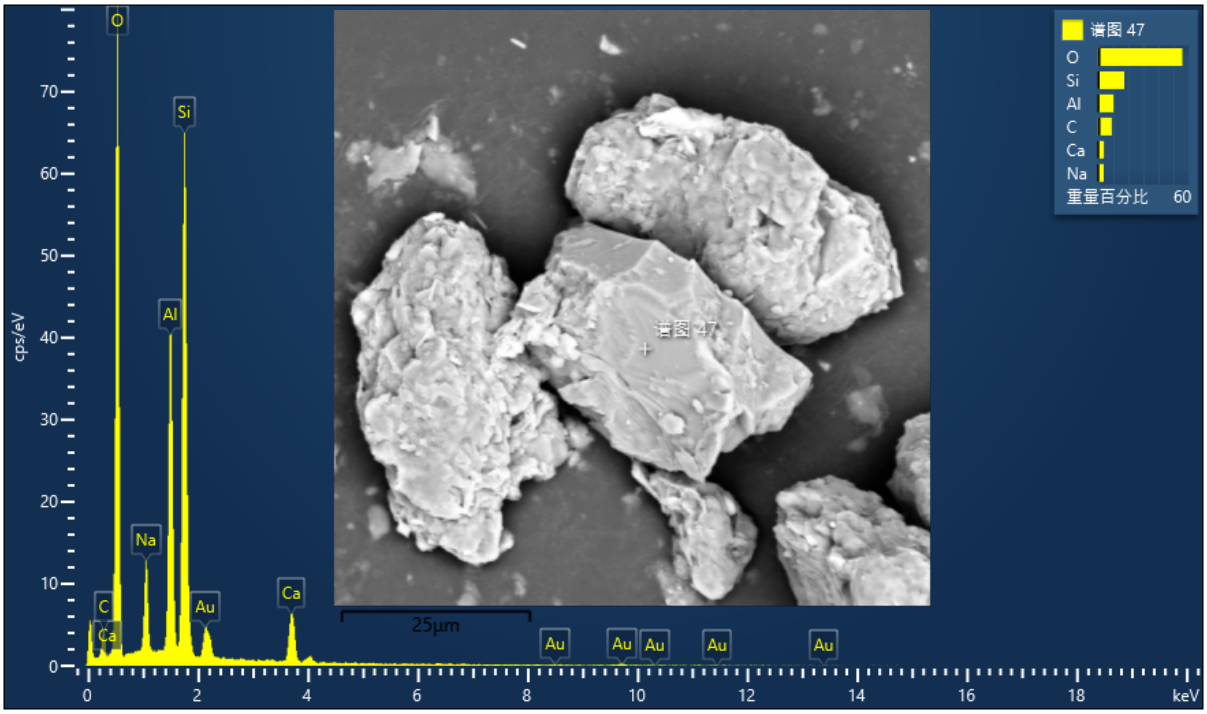

Appendix 5-5. SEM observation of coarse-grained feldspar mineral

Appendix 5-6

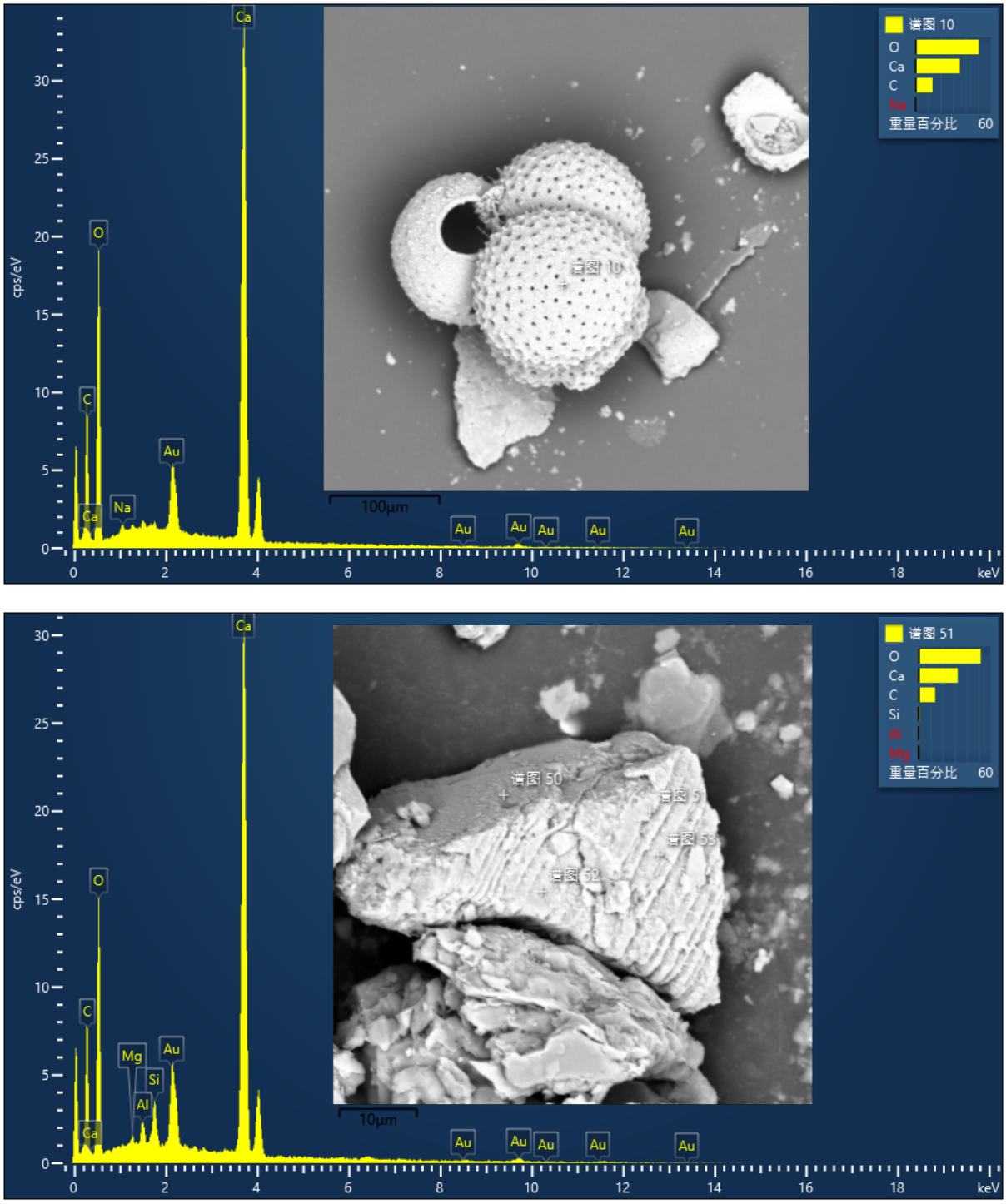

Appendix 5-6. SEM observations of calcite minerals from coarse grain fractions

Appendix 5-7

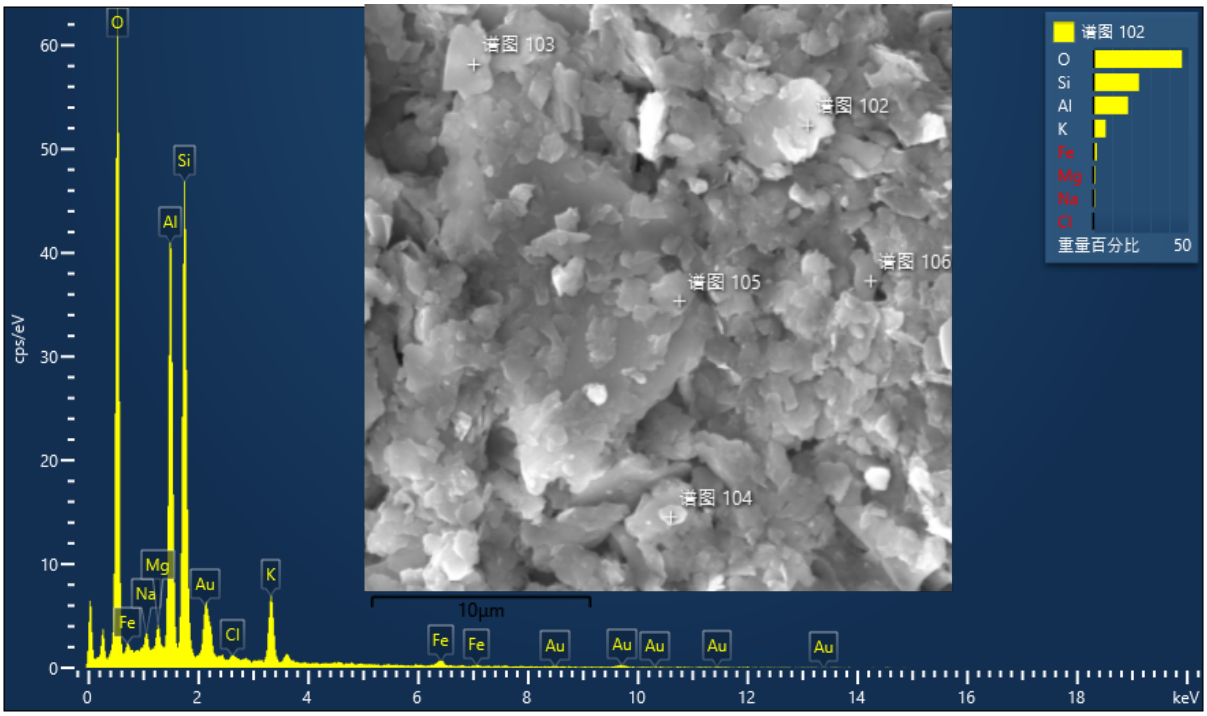

Appendix 5-7. SEM observations of fine silt and clay fraction composed of muscovite, illite and chlorite (<20 μm)

Appendix 5-8

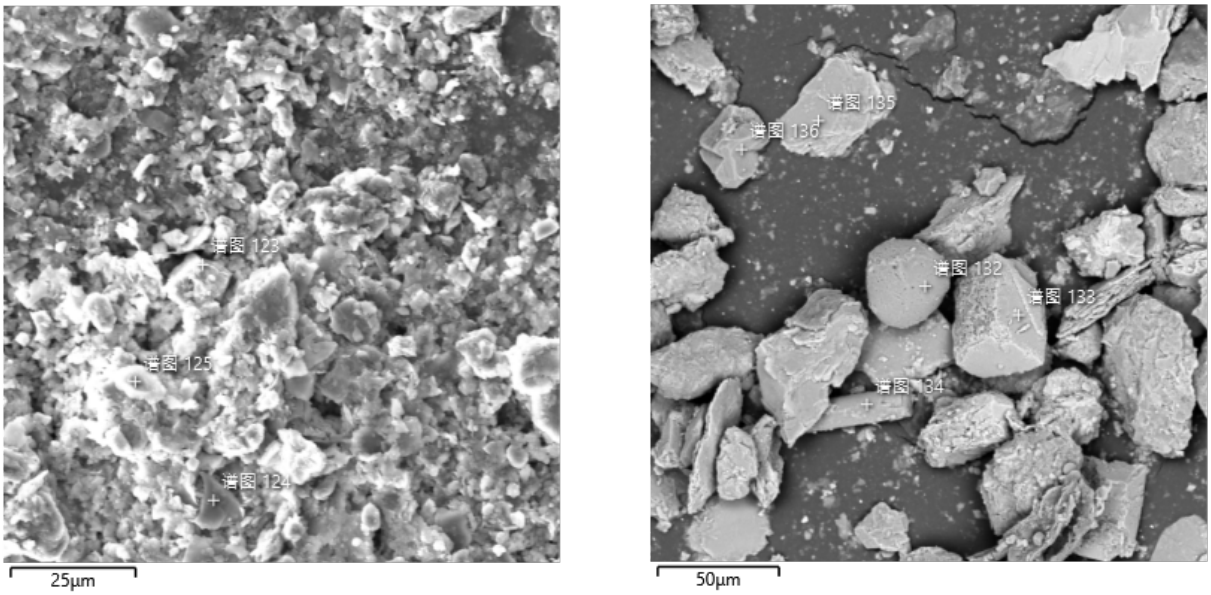

Appendix 5-8. comparison of SEM observation of <20μm and >40μm fractions

Acknowledgments

After four years of a lifetime adventure, dusk approaches on the most important chapter of my life, yet. Four years feeling like if time was flying, in the best and worst senses of the words. However, there is no place for “what if” and eventually I can close this chapter with positive emotions and satisfactions. Among the satisfactions, the most important one is the many people I met who helped going through every stage of this challenge. And I want to remember and thank them for everything they did!

First of all I would like to thank with all my heart my two supervisors, Professors Zhifei Liu and Christophe Colin. With this joint PhD, they gave me an incredible opportunity to achieve the goal of my youth and chances to live a professional and cultural experience, which helped my personal development. They were great mentors guiding me through the various steps of this PhD project. Professionally, they gave me training, encouragement and suggestions with incredible patience and kindness. Thanks to them, I truly think I improved beyond what I could imagine few years ago. But what I cherish the most is the support they provided, with comprehension, to overcome the direct and indirect impacts of the troubled period of the pandemic. From Christophe supporting me during my times in Orsay to reduce the effects of the lockdowns, optimize, and ease the conditions. To Zhifei carrying me to the hospital in a closed Shanghai and giving in total one week of his precious time in all my medical adventures. I am not exaggerating by saying that without them I would have never have the motivation and the strength to go through this. And there are no words strong enough to express my gratitude.

I had the chance to receive the help of numerous researchers to perform laboratory works and interpretations. So, I would like to thank Arnaud Dapoigny, Louise Bordier, Franck Bassinot Yanli Li, Yijie Wang, Hongchao Zhao, Serge Miska, Giuseppe Siani, Yulong Zhao, Yu Xun and Quentin Dubois-Dauphin for their expertise, suggestions, and time. I have also a special thought for Kévin Jacq and Maxime Debret who offered me an incredible opportunity and collaboration in the world of hyperspectral imaging. I would also like to thank Xavier Quidelleur,, Xu Fei, Pengfei Liu, Georgette Raboux, Mylène Viard and the many people in Tongji University, Paris-Saclay University administrations and French embassy who helped to give favourable conditions to achieve this PhD project. I am thanking warmly the jury members for accepting to review this work.

I have a very affectionate thought for all the friends I met on the way to this adventure. I would like to thank Amélie, who shared the first half of this challenge with me, Adrian, Pun, Akma, Sang, Sopheap, Salvatore, Hugo, Shu Wei, Guohui, Yi, Hongchao, Xiaodong, Mingyang, Jiaying, Jingwen, Wenzhuo, Junyuan, Wei Xie, Yijie, Zijing, Baozhi and many other work friends.

Finally, I would like to acknowledge the ones who believed in me and waited for me and whom I missed so much during these four years. First, I have no words to say how grateful I am to my rock, Anna. Thank you with all my heart for opening to me the door your wonderful world and giving me unconditional 24/7 company, support, help and motivations despite the situations. Without you I would have not succeeded. I am grateful to my childhood and university friends Anthony, Jeremy, Jésus, Rémi, William, Adrien, Lucas, Yoan, Loïc, Laetitia, Guillaume, Francis and all the others for their needed encouragements and presence during my stays in France. And last but not least, I would like to thank immensely my parents, sister and brother, grandparents and all my family who believed in me and supported me, giving optimal conditions to achieve all of this.

To all of you, thank you so much. If not for you, this work would have been impossible.

Appendix Curriculum vitae

BERTAZ Joffrey, PhD student: joint PhD at Tongji University State Key Laboratory of Marine Geology and Paris-Saclay University, GEOPS Laboratory

Education:

09.2019-09.2023: PhD program, Tongji University-Paris Saclay University

09.2017-06.2019: Master degree, Paris-Saclay University

09.2014-06.2017: B.Sc degree, Paris-Sud University

Scientific meetings:

-Bertaz J., Colin, C., & Liu, Z., (2020), Geochemical and mineralogical study of climatic and tectonic impacts on the sedimentation on the southwestern Taiwan margin since last deglaciation. *Climat et Impacts 2020*. poster

-Bertaz J., Liu, Z., Colin, C., Jian, Z., Li, Y., (2022), Climatic and environmental impacts on the sedimentation on the southwestern Taiwan margin since last deglaciation: geochemical and mineralogical investigations. *21st International Sedimentological Congress 2022.* poster

Bertaz J., Liu, Z., Colin, C., Jian, Z., & Li, Y., (2022), Climatic and environmental impacts on the sedimentation on the southwestern Taiwan margin since last deglaciation: geochemical and mineralogical investigations. *Climat et impacts 2022.* Poster

Bertaz J., Jacq, K., Colin, C., Liu, Z., Debret, M., & Zhao, H., (2022), High resolution analyses of grain-size and non-destructive hyperspectral imaging of sediments from the Gaoping canyon levee to establish past typhoon activity affecting Taiwan during the late Holocene. *Climat et impacts 2022.* Poster

Bertaz J., Jacq, K., Colin, C., Liu, Z., Debret, M., Zhao, H., & Lin, A.T.S., (2023), High-resolution grain-size analysis and non-destructive hyperspectral imaging of sediments from the Gaoping Canyon levee to establish past typhoon and monsoon activities affecting Taiwan during the late Holocene. *EGU General Assembly 2023.* Oral

Publications:

Bertaz, J., Liu, Z., Colin, C., Dapoigny, A., Lin, A.T.S., Li, Y., & Jian, Z., (under review), Climatic and environmental impacts on the sedimentation of the SW Taiwan margin since the last deglaciation: geochemical and mineralogical investigations. *Paleoceanography and Paleoclimatology*

Hunag, Y., Colin, C., Liu, Z., **Bertaz, J**., Dapoigny, A., Douville, E., Yu, Z., & Lin, A.T.S., (under review), Roles of changes in land weathering intensity in the Nd cycle of the South China Sea during the past 35 kyr as inferred from neodymium isotopic composition in foraminifera. *Chemical Geology*

Synthèse

Le climat de l'Asie de l'Est est un régime où le système de mousson de l'Asie de l'Est et l'importante activité des typhons dominent le régime des précipitations. Taïwan reçoit environ 2500 mm de précipitations par an, dont 80 % pendant la saison estivale, lorsque les fortes précipitations de la mousson d'été d'Asie de l'Est se combinent à celles des typhons. Ces précipitations intenses entraînent un ruissellement important et une décharge de sédiments des rivières d'Asie de l'Est dans les mers marginales. La mer de Chine du Sud (MCS) reçoit environ 1600 Mt de sédiments par an, ce qui représente 8 % de la décharge mondiale de sédiments aux océans. Ainsi, la mer de MCS est la mer marginale qui reçoit la plus grande quantité de sédiments terrigènes au monde. Cet apport important de sédiments se traduit par un taux de sédimentation très élevé sur les marges continentales, ce qui fait de la MCS une zone clé pour établir des enregistrements des climats passés à très haute résolution temporelle à partir des sédiments marins. La marge de Taïwan est très étroite et incisée par des canyons sous-marins profonds tels que le canyon de Gaoping et le canyon de Penghu. Les sédiments de Taiwan sont rapidement transportés vers le bassin profond de la MCS, principalement par des courants de turbidité sur le talus et à travers les canyons sous-marins profonds.

Dans ce travail deux carottes de sédiments provenant de la campagne Hydrosed, caractérisées par des taux de sédimentation très élevés (~50 cm/ka et ~5 m/ka) et couvrant l'intervalle de temps correspondant à la dernière période glaciaire et l'Holocène ont été étudiés. Ainsi, nous avons pu étudier les contrôles climatiques et environnementaux sur les processus sédimentaires dans le sud de Taïwan et la marge nord de la MCS (systèmes de canyons sous-marins) depuis la dernière période glaciaire avec une résolution temporelle très élevée.

L'objectif de cette thèse était d'étudier la dynamique sédimentaire de la marge septentrionale de la MCS ainsi que le transport et la redistribution des sédiments de Taïwan à travers deux canyons sous-marins depuis la dernière glaciation. L'étude a pour objectif d'étudier l'activité turbiditique à haute résolution dans le canyon sous-marin de Gaoping, de reconstruire l'histoire de l'altération chimique des sédiments de Taïwan et d'établir les liens avec la dynamique sédimentaire, les facteurs climatiques (EAM et typhons) et les changements hydrologiques (niveau de la mer et courants océaniques) à l'aide d'une approche source-to-sink. Les objectifs de cette étude étaient (i) de caractériser l'impact des pluies de mousson et des typhons sur l'érosion physique et l'altération chimique des sols du sud de Taiwan depuis la dernière période glaciaire ; (ii) d'établir l'activité sédimentaire du canyon sous-marin de

Penghu, y compris la provenance des sédiments, les apports terrigènes et les conditions hydrodynamiques de redistribution des sédiments, en relation avec les changements climatiques et environnementaux tels que les changements du niveau de la mer et les moussons ; et (iii) explorer les changements dans l'activité des courants de turbidité sur la levée du canyon sous-marin de Gaoping pendant la période de l'Holocène tardif, dans le but de reconstruire l'histoire des paléo-inondations provoquées par les typhons dans le bassin de la rivière Gaoping. Pour ce faire, deux carottes sédimentaires ont été prélevées sur les levées du canyon de Penghu (MD18-3569) et du canyon de Gaoping (MD18-3574) dans le sud de Taïwan. Des études minéralogiques (assemblage de minéraux argileux) et géochimiques (compositions isotopiques du Sr et du Nd, éléments majeurs) ont été réalisées pour identifier la provenance des sédiments et l'histoire de l'altération chimique du sud de Taïwan. Les conditions hydrodynamiques des canyons ont été explorées par des études sédimentologiques (granulométrie, imagerie hyperspectrale). Cette approche nous a permis de démontrer le lien existant entre les conditions climatiques et environnementales, la source et la redistribution des sédiments dans le nord de la MCS depuis 32 ka dans les rivières du sud de Taïwan et les deux systèmes de canyons.

Le canyon de Penghu est un canyon sous-marin situé sur la marge sud de Taïwan. Actuellement, la tête du canyon n'est reliée à aucune embouchure de rivière, bien qu'elle soit située près du chenal de Penghu, dans le détroit de Taïwan. Pendant les périodes où le niveau de la mer était bas, le détroit de Taïwan était émergé, et plusieurs études ont montré que le chenal de Penghu pourrait avoir été incisé par un paléo-fleuve drainant le détroit émergé. Des études minéralogiques et géochimiques ont été menées sur la carotte MD18-3569 afin d'identifier les principales sources sédimentaires des sédiments. L'assemblage de minéraux argileux est dominé par l'illite (52 %) et la chlorite (32 %) avec de petites quantités de smectite (12 %) et de kaolinite (4 %). Les compositions isotopiques du Sr et du Nd ($^{87}Sr/^{86}Sr$: 0.7187 à 0.7213 et εNd : 11.63 à 10.89) combinées aux assemblages de minéraux argileux indiquent que les sédiments proviennent probablement de rivières de Taïwan (illite : 56% ; chlorite : 36% ; $^{87}Sr/^{86}Sr$: 0.7176 à 0.7219 et εNd : 11.2 à 12.2). Les compositions isotopiques en Sr et Nd des sédiments ne présentent pas de variations temporelles. Ainsi, nous avons montré qu'il n'y a pas de changement de provenance des sources sédimentaires depuis la dernière période glaciaire, et que le sud-ouest de Taïwan est la seule source de sédiments.

Les fluctuations glaciaires-interglaciaires du niveau marin n'ont pas d'impact sur la provenance des sédiments dans le système du canyon de Penghu. Cependant, elles ont dû

affecter les conditions hydrodynamiques de la redistribution des sédiments. Des analyses granulométriques ont été effectuées sur des sédiments décarbonatés afin d'évaluer les conditions hydrodynamiques du canyon de Penghu. Les sédiments, déposés à l'est du canyon, sont principalement constitués de silts fin (~75 %) avec une granulométrie moyenne de ~13 μm (8-20 μm) et ne présentent aucune indication de dépôts turbiditiques. La granulométrie fine observée à l'est du canyon de Penghu est sensiblement différente de la granulométrie observée dans les embouchures des rivières du sud-ouest de Taïwan, qui dépasse généralement 100 μm. Cela suggère que les sédiments de la région dérivent de la circulation de surface. L'enregistrement de la granulométrie présente deux intervalles de temps principaux depuis 32 ka, séparés par une transition abrupte. De 32 à 10,7 ka, la granulométrie moyenne était plus grossière (environ 15,5 μm), avec une proportion plus élevée de silts (environ 78 %) et de sables (environ 2 %). Au cours du dernier maximum glaciaire (DMG), les dépôts de sédiments étaient plus grossiers (environ 18 μm), ce qui coïncide avec une période où le niveau de la mer était plus bas. La remontée progressive du niveau marin au cours de la déglaciation a entrainé une diminution graduelle de la granulométrie depuis le DMG à cause de l'augmentation de la distance entre les rivières et le canyon. Entre 10,7 et 10 ka, la granulométrie a brusquement diminué de 40 %, passant d'environ 15 μm à environ 9 μm, ce qui correspond à une transgression rapide connue sous le nom de "Melt Water Pulse 1C", qui a entraîné une élévation du niveau de la mer d'environ 20 m. Ce phénomène a considérablement modifié les échanges sédimentaires terre-mer, affectant la redistribution des sédiments en déconnectant le système de canyons des rivières, en inondant complètement le détroit, en influençant la circulation de surface et en piégeant les sédiments grossiers dans le détroit de Taïwan. Après 10 ka, la granulométrie des sédiments du canyon de Penghu est plus fine (~10 μm). Ceci peut être attribué à une période de haut niveau marin lorsque les sédiments du sud-ouest de Taïwan ont été transportés sur de plus longues distances à travers le détroit de Taïwan émergé.

Les assemblages de minéraux argileux et la composition en éléments majeurs présentent de petites variations qui ne sont pas liées à des changements de provenance. L'indice d'altération chimique (CIA = rapport molaire de $[Al_2O_3/(Al_2O_3+Na_2O+K_2O+CaO^*)\times100]$), $Al_2O_3{}^2/SiO_2$, Al_2O_3/NaO, smectite/(illite+chlorite) and kaolinite/(illite+chlorite) ont été utilisées pour reconstituer l'état d'altération chimique des sédiments transporté par le canyon de Penghu. Ils présentent de faibles valeurs (faible intensité de l'altération chimique) au cours du DMG. Cependant, avec la déglaciation, les valeurs des traceurs de l'altération ont augmenté

progressivement, atteignant leur maximum au début de l'Holocène, indiquant la période d'intensité maximale de l'altération chimique. Au cours de cette période, les précipitations de la mousson d'été d'Asie de l'Est se sont intensifiées, ce qui a favorisé l'installation de forêts dans les bassins versants du sud-ouest de Taïwan, entraînant une forte pédogenèse et une augmentation de l'intensité de l'altération chimique. Au cours de l'Holocène, l'intensité de l'altération chimique enregistrée par les sédiments déposés à l'est du canyon de Penghu a diminué. Les périodes sèches au cours du DMG et de l'Holocène ont entraîné une diminution des précipitations de la mousson d'été, ce qui a affaibli l'intensité de l'altération chimique des sédiments du sud-ouest de Taïwan. De plus, la faible mousson de l'Holocène a été associée aux intenses précipitations des typhons à Taïwan, ce qui a entraîné une augmentation de l'érosion physique des sols et une réduction significative du degrés l'altération chimique des sédiments transportés à la MCS. Notre étude montre une corrélation importante entre les précipitations des moussons et des typhons et l'intensité de l'altération chimique des bassins versant du sud-ouest de Taïwan.

Des méthodes d'analyses non destructives tels que l'imagerie hyperspectrale et les analyses XRF core scanning, combinées à des analyses de granulométrie et de minéralogie (DRX) ont été réalisées pour étudier la carotte MD18-3574, qui couvre les 4 derniers ka, et qui a été prélevée sur la levée ouest du canyon de Gaoping. Les niveaux sombres et grossiers, riches en matière organique, quartz, feldspaths et en calcite ont été caractérisées comme des dépôts résultant de courants de turbidité atteignant la levée du canyon de Gaoping. Ces dépôts présentent une granulométrie grossière à la base et un affinement progressif, caractéristique des dépôts de turbidites. Les systèmes d'observations in situ ont démontré que la plupart des courants de turbidités (~70%) dans le Canyon du Gaoping étaient déclenchés par d'importantes décharges sédimentaires associées à des typhons. Nous avons considéré les variations de fréquence des turbidites enregistrées comme les variations relatives des typhons affectant le sud de Taïwan. Plus de 2400 dépôts de turbidites millimétriques à centimétriques ont alors été identifiés. Nous avons ainsi calculé la fréquence des dépôts de turbidites et leur épaisseur moyenne (intensité du typhon associé) depuis la fin de l'Holocène. Nous avons observé une fréquence élevée de dépôts de turbidites entre 4 et 3 ka (60-100 par 100 ans), qui a diminué jusqu'à moins de 20 événements par 100 ans à l'heure actuelle. Cette diminution des courants de turbidité déclenchés par les typhons coïncide avec le refroidissement des températures de surface dans l'océan Pacifique tropical occidental, ce qui a entraîné une diminution du potentiel de genèse des typhons dans la région du Pacifique occidental. Après

1.5 ka, le canyon de Gaoping a présenté une plus grande variabilité dans l'intensité des typhons (comme l'indique l'épaisseur des turbidites). Cette observation est en accord avec les précédents enregistrements de typhons en Asie de l'Est. Dans tous les enregistrements, une intensification de l'intensité des typhons a été observée pendant trois intervalles de temps distincts (~1,5-1,2 ka, 1,0-0,8 ka, et 0,5-0,2 ka), tous associés à des périodes froides. Pendant les périodes froides avec des conditions similaires à La Niña, les typhons formés dans l'océan Pacifique central sont poussés vers l'ouest par la forte circulation de Walker du Pacifique, qui est associée à une mousson d'hiver plus forte et aux conditions similaires à La Niña. Les typhons s'intensifient dans la région de Taïwan, ce qui entraîne une augmentation des typhons intenses. Nos recherches révèlent que les conditions climatiques, océaniques et atmosphériques exercent une forte influence sur l'activité des typhons dans le sud de Taïwan. Ces interprétations pourraient être approfondies à l'aide de modèles climatiques afin de prévoir l'activité des typhons à la lumière des changements climatiques en cours.